Self-healing Strain-hardening Cementitious Composite As Concrete Cover Zone

He, S.

DOI
10.4233/uuid:f98bcc77-0629-4479-a17c-cba4b8d3fb2b

Publication date
2025

Document Version
Final published version

Citation (APA)
He, S. (2025). *Self-healing Strain-hardening Cementitious Composite As Concrete Cover Zone*. [Dissertation (TU Delft), Delft University of Technology]. https://doi.org/10.4233/uuid:f98bcc77-0629-4479-a17c-cba4b8d3fb2b

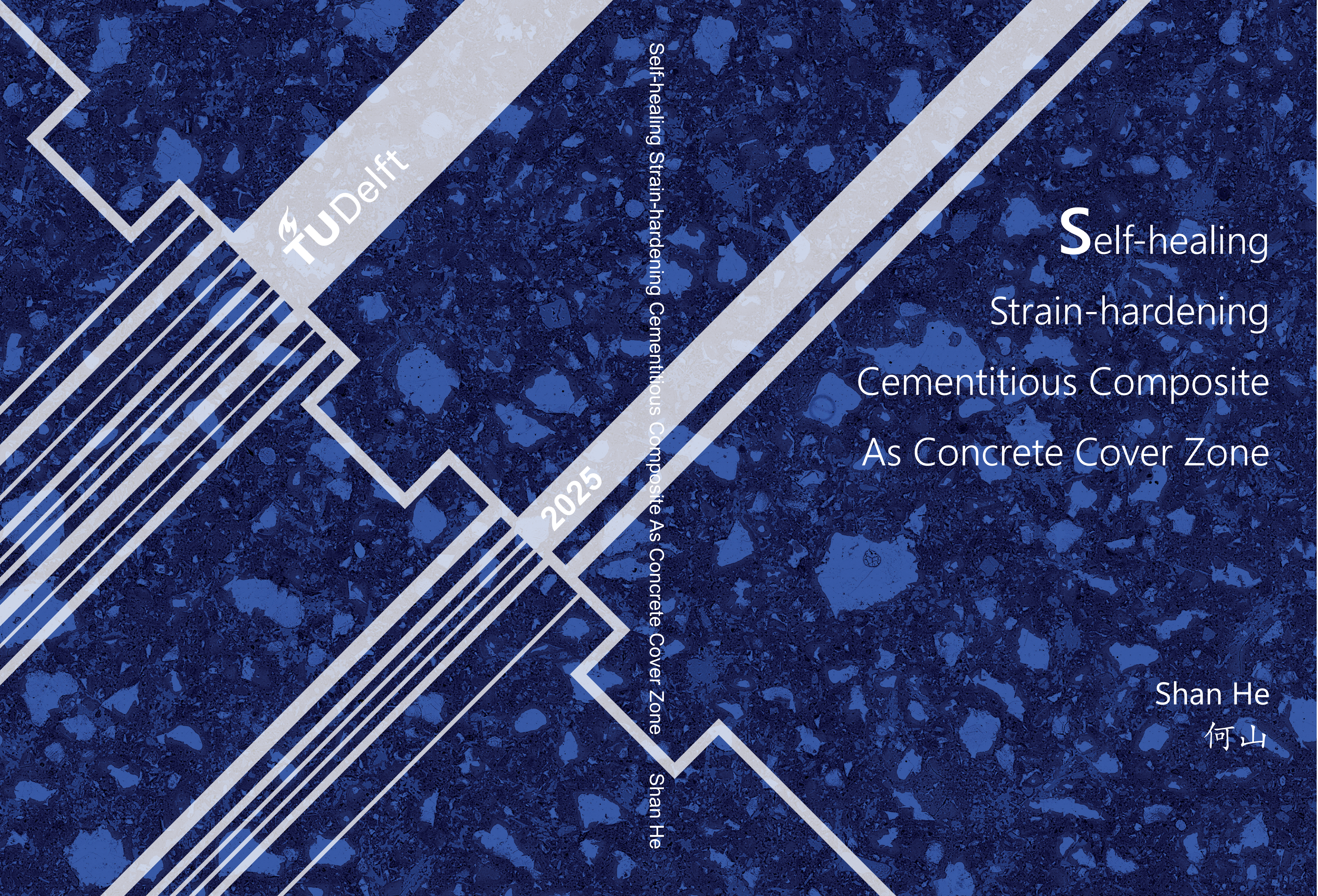

2025

Self-healing Strain-hardening Cementitious Composite As Concrete Cover Zone Shan He

Self-healing Strain-hardening Cementitious Composite As Concrete Cover Zone

Shan He
何山

Invitation

You are cordially invited
to attend the defence of
my PhD thesis

SELF-HEALING STRAIN-HARDENING CEMENTITIOUS COMPOSITE AS CONCRETE COVER ZONE

---

on
Wednesday
16th April
at
10:00
in
Senate Hall of Aula
TU Delft Campus

At 9:30, I will give a short introductory presentation on the topic of my thesis.

After the defence, there will be a reception.

Hope to see you there.

Shan He

SELF-HEALING STRAIN-HARDENING CEMENTITIOUS COMPOSITE AS CONCRETE COVER ZONE

SELF-HEALING STRAIN-HARDENING CEMENTITIOUS COMPOSITE AS CONCRETE COVER ZONE

Dissertation

for the purpose of obtaining the degree of doctor
at Delft University of Technology
by the authority of the Rector Magnificus Prof. dr. ir. T. H. J. J. van der Hagen
chair of the Board for Doctorates
to be defended publicly on
Wednesday April 16 at 10:00 o'clock

By

Shan HE
Master of Engineering in Civil Engineering,
Nanyang Technological University, Singapore,
born in Tianjin, China.

This dissertation has been approved by the promotors.

Composition of the doctoral committee:

Rector Magnificus,	chairperson
Prof. dr. ir. E. Schlangen	Delft University of Technology, promotor
Prof. dr. H. M. Jonkers	Delft University of Technology, promotor
Dr. M. Luković	Delft University of Technology, co-promotor

Independent members:

Prof.dr.ir. J.G. Rots	Delft University of Technology
Prof.dr.ir T.A.M. Salet	Eindhoven University of Technology
Prof.dr.ir. N. De Belie	University of Ghent, Belgium
Prof.dr. E.H. Yang	Nanyang Technological University, Signapore
Prof.dr.ir. M.A.N. Hendriks	Delft University of Technology, reserve member

This project has received funding from the European Union's Horizon 2020 research and innovation programme under the Marie Skłodowska-Curie grant agreement No 860006.

Keywords: Self-healing concrete, reinforced concrete, strain-hardening behaviour, crack width control, structural performance.

Cover design: Shan He

ISBN 978-94-6518-030-4

晓看天色暮看云，行也思君，坐也思君。

SUMMARY

Uncontrolled cracking in reinforced concrete structures accelerates durability issues by creating pathways for external agents to penetrate the matrix, often leading to costly repairs and reduced service life. This dissertation addresses these challenges through the development of a self-healing strain-hardening cementitious composite (SHCC) designed specifically for application in the concrete cover zone.

This thesis adopted a multi-faceted methodology. First, a self-healing SHCC material was developed, featuring bacteria-embedded polylactic acid (PLA) capsules to realize controlled microcracking and robust healing. Next, the research introduced a localized application strategy to address the cost-effectiveness of this material. By applying the self-healing SHCC exclusively to the concrete cover zone, the region most critical to durability, this approach minimizes unnecessary use of healing agents, balancing performance with economic viability. To validate the concept, experimental and numerical analyses were conducted to evaluate the performance of hybrid beams with self-healing SHCC covers. Furthermore, different manufacturing methods, including prefabrication and 3d printing, were explored. Lastly, design strategies were proposed to incorporate the self-healing benefits into structural service life models. The feasibility of the developed system was demonstrated at full scale by applying it in the construction of a tramline.

The study revealed that the incorporation of PLA capsules into SHCC significantly improved crack-healing efficiency while maintaining critical tensile properties. It was found that the fibre/matrix bond properties were enhanced by the addition of the HA. As a result, the addition of healing agents reduced residual crack widths by up to 70%, ensuring faster and more robust healing under varied conditions.

At the structural level, hybrid beams with SHCC covers exhibited enhanced performance. Beams with SHCC applied in the bottom cover zone demonstrated improved flexural behaviour, with controlled crack patterns and reduced crack widths, attributed to the optimized interface condition between the SHCC cover and concrete core. A novel type of SHCC/concrete interface that features a weakened chemical adhesion, but an enhanced mechanical interlock bonding was developed to facilitate the activation of SHCC. Similarly, hybrid beams with lateral SHCC layers showed a notable increase in shear resistance under critical loading conditions. Numerical simulations supported these experimental findings, revealing the importance of the interface condition between SHCC cover and concrete core.

For the developed self-healing cover system to be applied in structures, it is necessary to consider the implications of healing during the design process. Analysis of this thesis shows that, by refining existing engineering models to include the impact of cracks, it becomes possible to predict and design the healing effects under specific scenarios.
To further demonstrate the self-healing cover concept, the developed self-healing SHCC was applied in a full-scale construction project where stringent requirements for tensile performance

and crack healing properties are essential. The project showcased the feasibility of large-scale mixing, pumping, and application of the self-healing SHCC system.

This thesis contributes to the field of self-healing concrete by advancing material performance, structural application techniques, and design integration. By focusing on localized and practical implementations, the research bridges the gap between experimental advancements and full-scale applications where traditional solutions do not meet demands. The findings underscore the potential of self-healing concrete to extend the service life of structures without imposing substantial additional costs.

Future research should focus on scaling the developed technologies to diverse structural configurations and environmental conditions. Long-term performance evaluations and refinement of design methodologies will be critical to promoting advanced materials with added functionalities (*e.g.*, self-healing and strain-hardening) as a standard practice in construction.

SAMENVATTING

Ongecontroleerde scheurvorming in gewapende betonconstructies versnelt duurzaamheidproblemen door het creëren van paden waardoor externe stoffen de matrix kunnen binnendringen. Dit leidt vaak tot kostbare reparaties en een verkorte levensduur. Dit proefschrift gaat deze uitdagingen aan door de ontwikkeling van een zelfherstellend strain-hardening cementgebonden composiet (SHCC), specifiek ontworpen voor toepassing in de dekking van een betonconstructie.

Deze studie hanteerde een veelzijdige methodologie. Allereerst werd een zelfherstellend SHCC-materiaal ontwikkeld met polylactide (PLA) capsules met ingebedde bacteriën, die gecontroleerde microscheurvorming en effectief herstel mogelijk maken. Vervolgens introduceerde het onderzoek een lokale toepassingsstrategie om de kosteneffectiviteit van het materiaal te verbeteren. Door de zelfherstellende SHCC uitsluitend in de dekking van beton aan te brengen – de zone die het meest bepalend is voor de duurzaamheid – wordt onnodig gebruik van zelfherstelmiddelen(HA) geminimaliseerd, waardoor prestaties en economische haalbaarheid in balans blijven. Om dit concept te valideren, werden experimentele en numerieke analyses uitgevoerd om de prestaties van hybride balken met zelfherstellende SHCC-dekking zones te evalueren. Daarnaast werden verschillende productiemethoden, waaronder prefab en 3D-printen, onderzocht. Tot slot werden ontwerprichtlijnen voorgesteld om de voordelen van zelfherstel te integreren in modellen voor de levensduur van constructies. De haalbaarheid van het ontwikkelde systeem werd op ware schaal aangetoond door toepassing in de bouw van een tramlijn.

De studie toonde aan dat de opname van PLA-capsules in SHCC de scheurherstellende efficiëntie aanzienlijk verbeterde, terwijl de essentiële treksterkte behouden bleef. Het bleek dat de hechtingseigenschappen tussen vezels en matrix werden verbeterd door de toevoeging van HA De toevoeging van zelfherstelmiddelen verminderde hierdoor de resterende scheurbreedtes met maximaal 70%, wat zorgde voor sneller en robuuster herstel onder diverse omstandigheden.

Op structureel niveau vertoonden hybride balken met een SHCC-dekkingzone verbeterde prestaties. Balken met SHCC in de onderste dekking toonden een verbeterd buiggedrag, met een gecontroleerd scheurpatroon en kleinere scheurbreedtes. Dit werd toegeschreven aan de geoptimaliseerde interfaceconditie tussen de SHCC-dekking en de betonkern. Een nieuw type interface tussen SHCC en beton werd ontwikkeld, waarbij een verzwakte chemische hechting maar een verbeterde mechanische verankering de activering van SHCC faciliteerde. Evenzo vertoonden hybride balken met laterale SHCC-lagen een aanzienlijke toename in afschuifweerstand onder kritische belasting. Numerieke simulaties ondersteunden deze experimentele bevindingen en benadrukten het belang van de interfaceconditie tussen de SHCC-dekking en de betonkern.

Om het ontwikkelde zelfherstellende dekkingsysteem in de praktijk toe te passen, is het noodzakelijk om het effect van zelfherstel al in het ontwerpstadium in overweging te nemen. Analyse van dit proefschrift toont aan dat door bestaande ingenieursmodellen te verfijnen en de

impact van scheuren mee te nemen, het mogelijk wordt om de hersteleffecten onder specifieke omstandigheden te voorspellen en te ontwerpen.

Om het concept van een zelfherstellende dekking verder te demonstreren, werd de ontwikkelde zelfherstellende SHCC toegepast in een grootschalig bouwproject, waarbij strenge eisen werden gesteld aan trekprestaties en scheurherstellende eigenschappen. Dit project toonde de haalbaarheid van het op grote schaal mengen, verpompen en toepassen van het zelfherstellende SHCC-systeem aan.

Dit proefschrift levert een bijdrage aan het onderzoeksveld van zelfherstellend beton door verbeteringen in materiaaleigenschappen, structurele toepassingen en ontwerpintegratie. Door zich te richten op lokale en praktische implementaties, overbrugt het onderzoek de kloof tussen experimentele ontwikkelingen en grootschalige toepassingen waar traditionele oplossingen tekortschieten. De bevindingen onderstrepen het potentieel van zelfherstellend beton om de levensduur van constructies te verlengen zonder aanzienlijke extra kosten.

Toekomstig onderzoek zou zich moeten richten op de opschaling van de ontwikkelde technologieën naar diverse constructieve configuraties en milieufactoren. Langetermijnprestaties en verdere verfijning van ontwerpstrategieën zullen cruciaal zijn om geavanceerde materialen met extra functionaliteiten (zoals zelfherstel en strain-hardening) te bevorderen als een standaardpraktijk in de bouw.

CONTENTS

1

Introduction

In November 2022, ChatGPT, an online chatbot, was introduced. By January 2023, it had already established itself as the fastest-growing consumer software application in history. The primary function of ChatGPT is to simulate human-like conversation. Utilizing a large language model, an advanced form of artificial neural networks (ANNs), it can perform tasks like refining writing, generating text, and debugging computer programs. This tool has also played a significant role in editing and refining the language of this thesis. Reflecting on the history of ANNs, the concept was proposed in the 1940s, and initial models were developed in the 1950s. However, it was not until the 2000s, with the advent of deep learning and big data, that neural networks found widespread application in various fields like image and speech recognition, natural language processing, and more. This progression highlights how the path from technological innovation to widespread application can be long and non-linear, often requiring the convergence of multiple advancements and shifts in market or societal needs. Most likely, self-healing concrete is now navigating a similar trajectory.

This chapter seeks to describe the present standing of self-healing concrete in its developmental trajectory and explain the value of this thesis in furthering its progression.

1.1 Background

The pursuit of advancements in engineering materials has consistently aimed to mimic the qualities found in natural materials. Notably, the capacity for self-healing stands out as a highly sought-after attribute. In 1970, self-healing properties were for the first time designed inside polymeric materials [1–3]. In 1979 and 1981, publications about self-healing in thermoplastic [4] and cross-linked systems [5] appeared. Although, it was only in 2001 when White et al. [6] published their paper in Nature about self-healing in polymer-based materials that the research on self-healing materials started to attract a lot of attention. Until today, progress in this area has led to the development of various self-healing mechanisms and materials, encompassing also metals and ceramics. These innovative materials are being utilized in a wide range of sectors, from aerospace to consumer electronics, offering enhanced sustainability and performance.

Self-healing in construction materials (*e.g.*, concrete) holds significant potential as well. This is because structural concretes in service are prone to developing cracks due to various causes including mechanical loading, thermal effects, and shrinkage. In fact, reinforced concrete structures are intentionally designed to crack to activate the reinforcement. The formation of these cracks accelerates various durability issues, as they create additional pathways for external (aggressive) agents like water, chlorides, and sulphates to penetrate the cementitious matrix more deeply. Concrete with the ability to heal cracks by itself, therefore, have the prospect of exhibiting significantly improved durability performance. It is expected that structures made with self-healing concrete will have substantive extension in service life and reduction in maintenance costs.

Concrete is inherently equipped with a certain degree of autogenous healing capacity, which implies that concrete can naturally close small cracks without engineering or human intervention. However, this self-healing mechanism is only effective for cracks with limited widths. Over the past decades, extensive research has been conducted to enhance the self-healing capabilities of concrete. This includes efforts to stimulate its intrinsic autogenous healing properties (*e.g.*, via the use of mineral additives [7,8], crystalline admixtures [9,10], or superabsorbent polymers [10]), or to develop novel autonomous self-healing mechanisms (*e.g.*, via the application of micro- [11], macro- [12], or vascular-encapsulated polymers [13], minerals, or bacteria [14]). Thus far, it has been observed in several instances that key durability metrics, including but not limited to gas and water permeability, chloride diffusion, and capillary absorption, exhibit signs of positive influence. Additionally, an evident recovery in various mechanical properties such as strength, stiffness, and ductility, along with an increase in resistance to fatigue and impact have also been reported [15,16].

While self-healing techniques for concrete have been extensively studied in laboratory settings, their large-scale, real-world application remains relatively limited. In the view of the author, this can be attributed to three primary factors. The first concerns the robustness of the healing process. Although successful healing actions were reported in many studies, the likelihood of achieving consistent results depends on several variables, including crack characteristics, environmental conditions, loading conditions, and other factors. The combined influence of these factors makes the healing process insufficiently robust, rendering its performance unreliable. Furthermore, the transition from deploying self-healing in mortar to concrete further compromises the efficiency of self-healing techniques. Cracks in mortar lack preferential pathways for propagation, and thus, the probability of encountering a healing agent depends solely on the volume ratio of the healing agent within the mortar. However, when concrete is utilized instead of mortar, cracks tend to propagate primarily along the interfaces between coarse aggregates and cement pastes. As most healing agents are distributed within the cement paste, the inclusion of coarse aggregates diminishes the likelihood of cracks intersecting with embedded healing agents, thereby reducing their activation probability. This ultimately leads to a further decrease in the robustness of healing when applied to large-scale construction projects.

The second factor is related to the cost issue. The production of self-healing concrete typically requires the use of specialized components such as bacterial spores or microcapsules, which are considerably more expensive than the conventional ingredients in concrete like cement, gravel and sand. If healing agents are incorporated throughout the structure in a specific volumetric ratio to the total concrete, it can result in a notable increase in the unit cost of the concrete. While it is true that self-healing concrete could potentially offer long-term financial gains due to lower maintenance requirements and increased durability, quantifying these benefits remains a complex task. As a result, these long-term advantages are frequently overshadowed by immediate financial considerations. Especially in the current landscape of construction decision-making, there is a predominant emphasis on initial production costs over long-term savings. This requires creating a more strategic way to use self-healing concrete in regular construction.

The third obstacle lies in the lack of a methodology for incorporating self-healing capabilities into concrete design practices. Although the potential impact of crack healing on the properties of concrete can be significant, these benefits remain unrealized as long as they are not integrated into design methodologies and practices. For instance, Eurocode 2 ensures the durability of reinforced concrete structures primarily by imposing crack width limits based on exposure classes, without accounting for potential self-healing processes. Shifting the design philosophy to fully embrace healing effects may take time, but for now, the more practical approach is to incorporate these effects into existing frameworks, enabling broader adoption of the technology.

In conclusion, self-healing concrete holds great promise for improving the durability and performance of reinforced concrete structures. While significant progress has been made in enhancing self-healing capabilities, challenges such as cost considerations, healing robustness and the absence of design guideline still exist. Addressing these challenges is essential to realizing the potential benefits of self-healing concrete, which could ultimately lead to extended service life and reduced maintenance costs in construction projects.

1.2 Objective and methodology

The primary goal of this thesis is to bridge the gap between self-healing research and its industrial application. To achieve this, the focus is on developing a robust self-healing material by addressing the scientific knowledge gap around the unpredictability of healing efficiency. Additionally, the thesis aims to propose a cost-effective solution for self-healing in structural concrete, making the implementation financially viable while ensuring that the healing benefits can be incorporated into design.

The solution to the first question is to combine fibre reinforcement with self-healing technologies. By limiting crack widths, the most critical factor influencing healing efficiency, robust healing is expected to be achieved. The solution for the second issue is to apply self-healing concrete only locally, as schematically illustrated in Fig. 1.1. By applying self-healing technologies only in the concrete cover-zone, the actual zone which controls the durability of reinforced concrete structures, this approach can save unnecessary use of healing agents elsewhere and thus increase the cost-effectiveness. Furthermore, the design of healing effects can potentially be integrated into service life models with the necessary extensions.

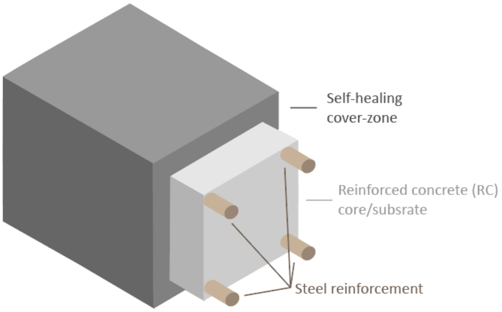

Figure 1.1: Schematic illustration of a reinforced concrete beam with self-healing cover zone

To develop the composite system which includes a reinforced concrete core and a self-healing cover zone, a 4-step strategy was adopted. The 1st step focuses on the development of an appropriate self-healing material for the structural cover, with a specific emphasis on creating a strain-hardening cement-based material capable of effectively ensuring cracks with minimal width, providing rapid and robust healing (Chapter 2 and 3). The second part of this study aims to explore the optimal integration of this self-healing cover into structural members (Chapter 4 and 5). In this regard, the research investigates the impact of applying such a cover on flexural and shear resistance of the hybrid beams through a combination of experimental testing and numerical simulations. Additionally, the study seeks to devise practical methods for applying the self-healing cover to new structures, encompassing both traditional mould casting and additive manufacturing techniques like 3D printing (Chapter 6). Then, an essential objective of this research is to propose methodologies for incorporating the benefits of the self-healing cover into existing design codes (Chapter 7), thereby facilitating broader adoption of self-healing in the construction industry. Finally, the technology will be examined and validated through a full-scale demonstrator (Chapter 8). A roadmap can be seen in Fig. 1.2.

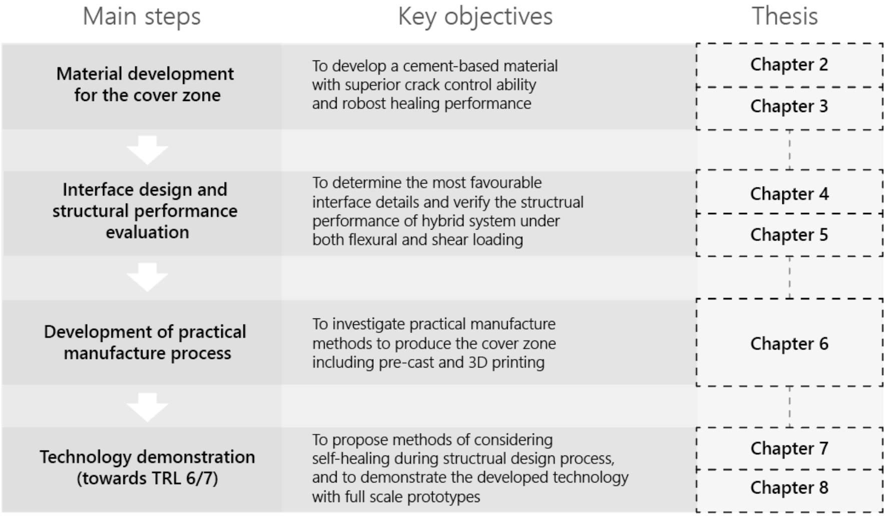

Figure 1.2: Roadmap for reaching the objectives

1.3 Scope of the research

The thesis is conducted within the framework of the EU-funded project SMARTINCS (Self-healing – Multifunctional – Advanced Repair Technologies in Cementitious Systems) [17], whose primary aim is to pioneer innovative approaches for extending the service life of concrete infrastructure, including both new and existing structures, through the utilization of self-healing technologies. This initiative encompasses 15 doctoral studies, organized into 4 work packages (WPs) with specific targets:

- WP1: Development of optimized self-healing methods and tailored concrete mix designs for various applications.
- WP2: Conceptualization of localized applications for self-healing technologies.
- WP3: Assessment and demonstration of durability improvements and increased service life of structures equipped with self-healing systems under realistic, aggressive conditions.
- WP4: Identification and utilization of drivers for commercializing self-healing concrete and local (self-)repair solutions.

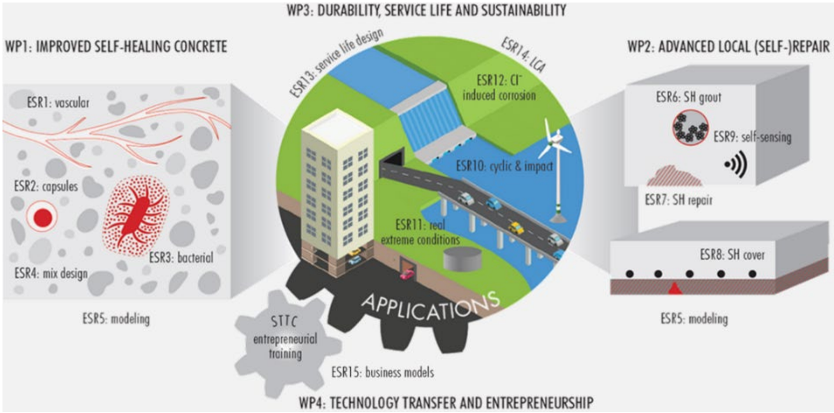

Figure 1.3: Overview of the topics for all the Early Stage Researchers (ESRs) in Smartincs

Fig. 1.3 gives an overview of all the doctoral studies within the project. This thesis, as ESR 8 of Work Package 2 (WP2), focuses on developing strategies for localized self-healing concrete applications to improve its cost-effectiveness. This study specifically aims to apply self-healing techniques to the outer layer of reinforced concrete structures (*i.e.*, the cover zone), which plays a crucial role in determining the overall durability of the structure. The research focus spans two critical dimensions: firstly, the formulation of materials for the cover zone to enhance healing properties, and secondly, the design of the hybrid structural elements with tailored interface between the self-healing cover and the concrete core. At both material and structural levels, mechanical and cracking properties are the focus. This thesis does not address the development of new healing mechanisms or the assessment of durability enhancements arising from adopting the healing cover, as these aspects are the focus of other work packages.

1.4 Outline of the thesis

The thesis discusses the development of a methodology to apply self-healing technology only in reinforced concrete cover zone. It is divided into 9 chapters, including an introduction (Chapter 1) and conclusions (Chapter 9). An overview of all the chapters as well their relation can be found in Fig. 1.4. Due to the breadth of subjects covered in this thesis, such as multiscale material characterization and structural analysis of reinforced concrete beams, a dedicated literature review chapter has not been included. Instead, relevant literature is reviewed within each respective chapter, providing context and background directly related to the specific subjects addressed.

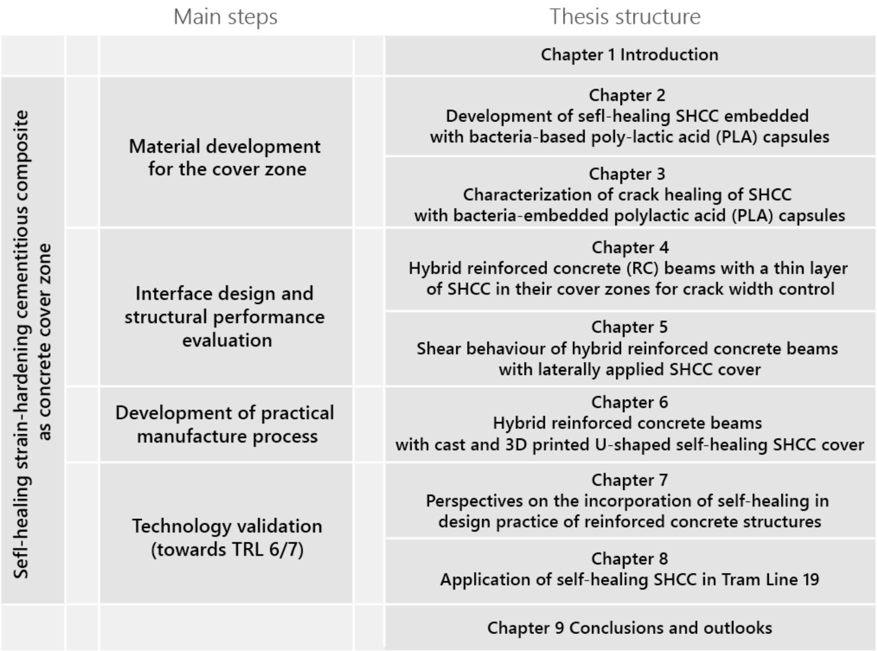

	Main steps	Thesis structure
		Chapter 1 Introduction
Sefl-healing strain-hardening cementitious composite as concrete cover zone	Material development for the cover zone	Chapter 2 Development of sefl-healing SHCC embedded with bacteria-based poly-lactic acid (PLA) capsules
		Chapter 3 Characterization of crack healing of SHCC with bacteria-embedded polylactic acid (PLA) capsules
	Interface design and structural performance evaluation	Chapter 4 Hybrid reinforced concrete (RC) beams with a thin layer of SHCC in their cover zones for crack width control
		Chapter 5 Shear behaviour of hybrid reinforced concrete beams with laterally applied SHCC cover
	Development of practical manufacture process	Chapter 6 Hybrid reinforced concrete beams with cast and 3D printed U-shaped self-healing SHCC cover
	Technology validation (towards TRL 6/7)	Chapter 7 Perspectives on the incorporation of self-healing in design practice of reinforced concrete structures
		Chapter 8 Application of self-healing SHCC in Tram Line 19
		Chapter 9 Conclusions and outlooks

Figure 1.4: Thesis structure

Chapter 1 Introduction

This chapter presents the background and motivation for the research, as well as the scope and structure of the current thesis.

Chapter 2 Development of strain hardening cementitious composite (SHCC) embedded with bacteria-based poly-lactic acid (PLA) capsules

This chapter documents the development of a material suitable to be used in the cover zone. The objective is to develop a fibre-reinforced, strain-hardening cement-based composite with enhanced cracking performance and to examine the effects of incorporating healing agents on its multiscale properties, such as tensile stress-strain behaviour, fracture toughness, and fibre/matrix bonding.

Chapter 3 Characterization of crack healing of SHCC with bacteria-embedded polylactic acid (PLA) capsules

This chapter verifies the healing efficiency of the developed material by means of microstructural characterization. This includes an examination of both short-term and long-term healing behaviour under various conditions, including ideal laboratory settings and more realistic environmental scenarios. The study investigates changes in the microstructure along the depth of cracks, utilizing backscattered electron (BSE) imaging and energy dispersive X-ray spectroscopy (EDS) on cross-sections of the cracks. This chapter does not cover the recovery of mechanical properties or durability post-healing.

Chapter 4 Hybrid reinforced concrete (RC) beams with a thin layer of SHCC in their cover zones for crack width control

This chapter delves into the creation of hybrid beams that incorporate a thin layer of SHCC in the bottom cover zone (as shown in Fig. 1.5). The primary focus is on identifying the optimal interface conditions that promote favourable crack patterns, ensuring small crack width control and thereby enhancing the efficiency of self-healing. The chapter provides a comprehensive analysis of the flexural behaviour of the hybrid beams, using a combination of experimental and simulation approaches.

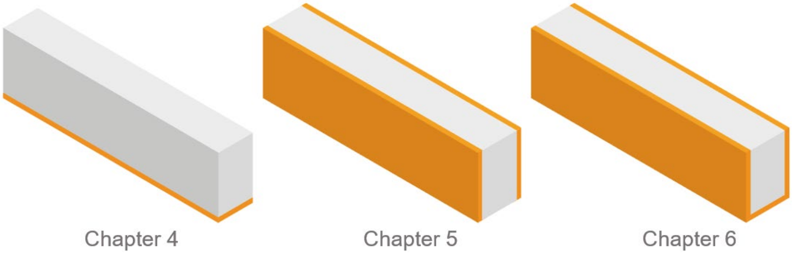

Figure 1.5: An overview of structural specimens prepared in this thesis.

Chapter 5 Shear behaviour of hybrid reinforced concrete beams with laterally applied SHCC cover

This chapter investigates whether a hybrid beam with thin SHCC layers on its lateral surfaces can maintain the structural integrity under critical shear loading. The contribution of SHCC cover to shear resistance was assessed with varying boundary condition (supporting at full width versus supporting only at the concrete core). Lattice model was also applied to investigate the responses of the hybrid beams under different combination of loading/supporting condition.

Chapter 6 Hybrid reinforced concrete beams with cast and 3D printed U-shaped self-healing SHCC cover

This chapter examines the structural integrity and healing efficacy of reinforced concrete beams equipped with U-shaped self-healing cover. It also details the fabrication of U-shaped self-healing SHCC covers, which were created using both traditional mould casting and 3D printing techniques, serving as lost formwork for the reinforced concrete beams. Special attention is paid to the characterization of crack branching between the concrete core and the cover. Additionally, the chapter also includes a microscopic examination of the healing process within these cracks.

Chapter 7 Perspectives on the incorporation of self-healing in design practice of reinforced concrete structures

This chapter discusses the possibility of integrating self-healing concepts into structural concrete design practice. To facilitate the design of the developed system, emphasis is given to the role of self-healing in reducing chloride penetration into cracked concrete. In specific, this chapter first review related research progress and then suggest modifications to existing predictive models to accommodate various healing approaches.

Chapter 8 Application of SH-SHCC in Tram line 19

This chapter documents a demonstrator project to apply the developed SH-SHCC in a full-scale construction project where stringent requirements for tensile performance and crack healing properties are essential. It highlights insights from scaling up the self-healing system, involving the casting of approximately 1,800 cubic meters of SH-SHCC. Key technical considerations, including shrinkage reduction, production optimization, and pumpability verification, will be discussed.

Chapter 9 Conclusions and outlook

This chapter presents conclusion and recommendation for future research.

Appendix-A: Characterization of porosity in the interfacial transition zone (ITZ) between microfibre and cement paste

In the development of fibre-reinforced composites, comprehending the interface or interphase between the fibre and matrix is pivotal. However, characterizing this region in cement-based materials surrounding micro-polymeric fibres poses a significant challenge, leading to limited quantitative data availability. To tackle this issue, a novel method has been devised to characterize this ITZ and offer valuable insights for future engineering endeavours.

References

[1] Y.M. Malinskii, V. V. Prokopenko, N.A. Ivanova, V.A. Kargin, Investigation of self-healing of cracks in polymers - I. Effect of temperature and crosslinks on self-healing of cracks in polyvinyl acetate, Polymer Mechanics 6 (1970) 240–244. https://doi.org/10.1007/BF00859196/METRICS.

[2] Y.M. Malinskii, V. V. Prokopenko, N.A. Ivanova, V.S. Kargin, Investigation of self-healing of cracks in polymers - 2. Effect of molecular weight of a polymer and the environment on self-healing of cracks in polyvinyl acetate, Polymer Mechanics 6 (1970) 382–384. https://doi.org/10.1007/BF00858197/METRICS.

[3] Y.M. Malinskii, V. V. Prokopenko, V.A. Kargin, Investigation of the self-healing of cracks in polymers - 3. Effect of medium and layer thickness on self-healing in polyvinyl acetate, Polymer Mechanics 6 (1970) 969–972. https://doi.org/10.1007/BF00856916/METRICS.

[4] R.P. Wool, Crack healing in semicrystalline polymers, block copolymers and filled elastomers., Polymer Science and Technology 12 A (1980) 341–362. https://doi.org/10.1007/978-1-4613-3093-6_22/COVER.

[5] R.P. Wool, K.M. O'Connor, R.P. Wool, K.M. O'Connor, A theory of crack healing in polymers, J Appl Phys 52 (1981) 5953–5963. https://doi.org/10.1063/1.328526.

[6] S.R. White, N.R. Sottos, P.H. Geubelle, J.S. Moore, M.R. Kessler, S.R. Sriram, E.N. Brown, S. Viswanathan, Autonomic healing of polymer composites, Nature 2001 409:6822 409 (2001) 794–797. https://doi.org/10.1038/35057232.

[7] H. Huang, G. Ye, D. Damidot, Effect of blast furnace slag on self-healing of microcracks in cementitious materials, Cem Concr Res 60 (2014) 68–82. https://doi.org/10.1016/J.CEMCONRES.2014.03.010.

[8] Y. Yang, M.D. Lepech, E.H. Yang, V.C. Li, Autogenous healing of engineered cementitious composites under wet–dry cycles, Cem Concr Res 39 (2009) 382–390. https://doi.org/10.1016/J.CEMCONRES.2009.01.013.

[9] C. de Nardi, S. Bullo, L. Ferrara, L. Ronchin, A. Vavasori, Effectiveness of crystalline admixtures and lime/cement coated granules in engineered self-healing capacity of lime mortars, Materials and Structures 2017 50:4 50 (2017) 1–12. https://doi.org/10.1617/S11527-017-1053-3.

[10] L. Ferrara, V. Krelani, M. Carsana, A "fracture testing" based approach to assess crack healing of concrete with and without crystalline admixtures, Constr Build Mater 68 (2014) 535–551. https://doi.org/10.1016/J.CONBUILDMAT.2014.07.008.

[11] J.Y. Wang, H. Soens, W. Verstraete, N. de Belie, Self-healing concrete by use of microencapsulated bacterial spores, Cem Concr Res 56 (2014) 139–152. https://doi.org/10.1016/J.CEMCONRES.2013.11.009.

[12] T. Van Mullem, G. Anglani, M. Dudek, H. Vanoutrive, G. Bumanis, C. Litina, A. Kwiecień, A. Al-Tabbaa, D. Bajare, T. Stryszewska, R. Caspeele, K. Van Tittelboom, T. Jean-Marc, E. Gruyaert, P. Antonaci, N. De Belie, Addressing the need for standardization of test methods for self-healing concrete: an inter-laboratory study on concrete with macrocapsules, Sci Technol Adv Mater 21 (2020) 661–682. https://doi.org/10.1080/14686996.2020.1814117.

[13] Y. Shields, N. de Belie, A. Jefferson, K. van Tittelboom, A review of vascular networks for self-healing applications, Smart Mater Struct 30 (2021) 063001. https://doi.org/10.1088/1361-665X/ABF41D.

[14] H.M. Jonkers, A. Thijssen, G. Muyzer, O. Copuroglu, E. Schlangen, Application of bacteria as self-healing agent for the development of sustainable concrete, Ecol Eng 36 (2010) 230–235. https://doi.org/10.1016/J.ECOLENG.2008.12.036.

[15] V. Cappellesso, D. di Summa, P. Pourhaji, N. Prabhu Kannikachalam, K. Dabral, L. Ferrara, M. Cruz Alonso, E. Camacho, E. Gruyaert, N. De Belie, A review of the efficiency of self-healing concrete technologies for durable and sustainable concrete under realistic conditions, International Materials Reviews 68 (2023) 556–603. https://doi.org/10.1080/09506608.2022.2145747.

[16] N. De Belie, E. Gruyaert, A. Al-Tabbaa, P. Antonaci, C. Baera, D. Bajare, A. Darquennes, R. Davies, L. Ferrara, T. Jefferson, C. Litina, B. Miljevic, A. Otlewska, J. Ranogajec, M. Roig-Flores, K. Paine, P. Lukowski, P. Serna, J.-M. Tulliani, S. Vucetic, J. Wang, H.M. Jonkers, A Review of Self-Healing Concrete for Damage Management of Structures, Adv Mater Interfaces 5 (2018) 1800074. https://doi.org/10.1002/admi.201800074.

[17] The MSCA-ITN project SMARTINCS, homepage available at www.smartincs.eu, (2020).

2

Development of self-healing SHCC with bacteria-embedded polylactic acid (PLA) capsules[1]

This chapter outlines the development of a self-healing cement-based material for the cover zone, emphasizing two key requirements: 1) microcracking performance to enhance healing efficiency, and 2) minimal impact on other material properties. A strain-hardening cementitious composite (SHCC), known for its high tensile ductility through tight crack formation, is formulated with locally sourced materials to meet these criteria. To achieve this, the study investigates how adding a commercial healing agent (HA) affects SHCC's multiscale properties. Experiments were performed to study composite performance, matrix properties, and single fibre pullout behaviour, with microscopy used for fibre/matrix interface analysis. Results show that adding up to 5% HA slightly reduced tensile performance but significantly lowered residual crack widths. A higher HA dosage increased matrix toughness, enhanced fibre/matrix bonding, and improved fibre bridging energy, sustaining SHCC's tensile strain capacity as confirmed by a micromechanical model

.

---

[1] Part of this chapter has been published in:

He, S., Zhang, S., Luković, M., & Schlangen, E. (2022). Effects of bacteria-embedded polylactic acid (PLA) capsules on fracture properties of strain hardening cementitious composite (SHCC). Engineering Fracture Mechanics, 268, 108480.

2.1 Introduction

A critical factor governing the effectiveness of all self-healing materials lies in the magnitude of damage. Within the domain of concrete, this factor manifests chiefly through crack width. Research has evidenced that the rate and degree of crack healing are significantly influenced by the crack width.

In conventional reinforced concrete structures, achieving crack widths as small as a hundred micrometres requires a significant volume of steel reinforcement. This requirement may result in too dense reinforcement configuration for certain applications, thereby escalating execution problems. Instead, fibres present a viable means to reduce crack widths. Among the various fibre-reinforced cementitious composites (FRCCs) available, the strain hardening cementitious composite (SHCC) or Engineered Cementitious Composite (ECC) [1] stands out as particularly promising. The material was initially developed in the 1990s based on the micro-mechanics theory [2]. It possesses the most desirable crack control ability as it can exhibit multiple microcracking behaviour (*i.e.*, average crack width of 60–80 microns) with strain-hardening response even at a tensile strain over 3%. The unique cracking performance of SHCC is a result of careful tailoring of matrix, fibre, and matrix/fibre interface [3,4].

Due to the featured tight crack width, autogenous self-healing of SHCC has been the subject of extensive study. The recovery of both transport properties (*e.g.*, permeability, diffusivity, and absorptivity) and mechanical properties (*e.g.*, tensile strength, flexural strength, and strain capacity) of SHCC upon self-healing of microcracks has been experimentally confirmed under a variety of exposure environments [5]. It has been reported that the degree of autogenous healing in SHCC is still highly affected by the crack width. Yang et al. [6] found that the maximum allowable crack width to obtain complete resonant frequency recovery was around 50 μm; partial recovery was observed for cracks between 50 and 150 μm; cracks beyond 150 μm did not show any recovery. Fan et Li [7] studied the crack volume filling monitored by 3D X-ray computed microtomography and reported that, for cracks with width of around 30 μm, the crack volume decreased by 73% after exposure to 10 wet-dry cycles. For cracks having a width of 75 μm, the reduction of crack volume under the same conditions fell to only 11%. Therefore, to achieve a more robust self-healing behaviour, it would be desirable to enable SHCC the ability for healing beyond the autogenous capacity.

Incorporation of encapsulated bacterial healing agent (HA) can be one of the approaches to enable SHCC with autonomous self-healing. Among the various HA developed, the use of bacteria-embedded poly-lactic-acid (PLA) capsules as HA has proven its potential to satisfy both mechanical and functional requirements of the resulting self-healing system [9,10]. The main benefit of using PLA is that it reduces the volume of required healing particles, as PLA serves not only to protect the bacterial HA as a shell but also to provide the carbon source. Previous research [10,11] has also shown promising results towards full scale application and commercialization. Nevertheless, the addition of PLA capsules can largely alter the fracture properties of the materials [12] by introducing new interfacial transition zone (ITZ) and by deviating crack path, possibly even increasing the crack widths and therefore having conflicting effects on self-healing ability. In addition, PLA capsules are by nature biodegradable and will partially hydrolyses in alkaline environments. It is therefore plausible that some PLA capsules may release some bacterial spores and nutrient medium into the fresh paste during the mixing, which may affect the mechanical properties of the cement paste. Since the tensile performance of the SHCC is the prerequisite of adequate healing, it is important to understand the influence of HA and above-mentioned factors on the matrix and fibre/matrix bond properties of SHCC.

To address the research gaps mentioned above, this chapter investigates the effect of bacteria-embedded PLA capsules on the mechanical properties of SHCC. The current study does not aim to determine the optimum dosage of HA with respect to healing efficiency but focuses on understanding how the addition of the HA can affect the tensile and cracking performance of the SHCC. For this purpose, self-healing SHCC mixtures with a wide range of dosages of PLA capsules were developed; and their mechanical properties at the SHCC, matrix and fibre-matrix bond levels were tested and compared with control SHCC without any HA. Micromechanics-based models were used to calculate the fibre bridging capacity and to assess the strain-hardening potential of the resulting self-healing SHCCs.

2.2 Materials and tests

2.2.1 Mix design and materials

Table 2.1 shows the mixture compositions of SHCCs with varying dosages of HA (*i.e.*, 0%, 1.25%, 2.5% and 5% by weight to binder). The mix design of the control SHCC was tailored based on a SHCC mix developed in the group previously [13]. The modified SHCC matrix has a water-to-binder ratio of 0.4 and a filler-to-binder ratio of 0.5, which were determined experimentally for improved tensile strain capacity and tight crack width. Blast furnace slag (BFS) cement CEM III/B 42.5 N from ENCI (the Netherlands), consisting of 20-34 % clinker and 66-80% BFS [14], was used as binder to enable good matrix rheology and low matrix fracture toughness. Finely grinded limestone powder Calcitec® from Carmeuse (Belgium) with a particle size distribution similar to that of cement was used as filler to further reduce the matrix fracture toughness and to facilitate uniform fibre dispersion. A polycarboxylate-based superplasticizer MasterGlenium 51 produced from BASF (Germany) with 35.0% solid content by mass was used to reach desired workability. The fibre used in this study is polyvinyl alcohol (PVA) fibre from Kuraray (Japan) with 1.2% by weight oiling coating, the mechanical and physical properties of which are presented in Table 2.2.

Table 2.1: Mixture compositions of SHCCs [unit in kg/m3].

Mixture ID	CEM III/B	Limestone powder	Water	SP	PVA fibre (2.0 vol%)	Healing agent
SHCC	1060	530	424	2	26	0
SHCC-1.25HA	1048	524	419	2	26	13
SHCC-2.5HA	1036	518	415	2	26	26
SHCC-5HA	1014	507	406	2	26	51

Table 2.2: Physical and mechanical properties of PVA fibres.

Length (mm)	Diameter (µm)	Density (kg/m3)	Nominal tensile strength (MPa)	Young's modulus (GPa)	Surface oil-content (wt.%)
8	39	1300	1640	41.1	1.2

The HA adopted in the current study is the self-healing bio-polymeric particles (Fig. 2.1a) produced by Basilisk (the Netherlands). It is composed of a poly-lactic acid (PLA) derivate matrix, bacterial spores of *Bacillus cohnii*-related strains and growth-required nutrient inorganic salts. The capsules have a particle size distribution between 0.1 to 1.0 mm (Fig. 2.1b).

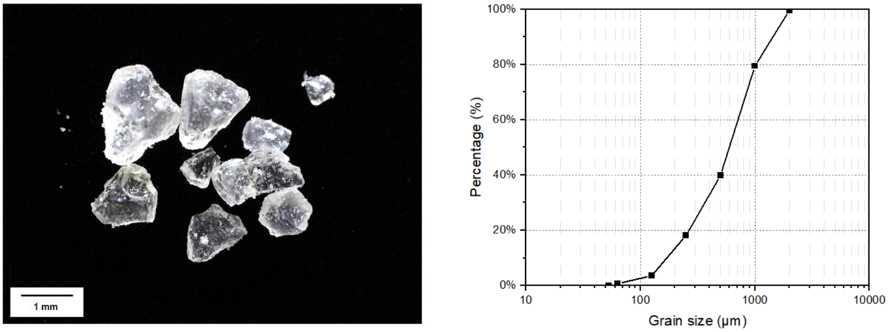

(a) (b)

Figure 2.1: (a) Photograph of bacteria-embedded PLA capsules and (b) its particle size distribution.

2.2.2 Specimen preparation

To prepare the SHCC specimens, BFS cement and limestone powders were first dry mixed by a Hobart® mixer at low speed for 5 min. Water pre-mixed with 80% of SP was slowly added into the mixture and mixed until the fresh paste was homogenous and consistent. HAs were then gradually added and mixed for another 2 min, followed by the addition of fibres within a duration of 5 min. Meanwhile, the remaining 20% SP was added into the mixture to compensate for the rheological loss due to the addition of fibres. Afterward, the fresh SHCC was cast into polystyrene prism (40 × 40 × 160 mm^3) moulds and dog-bone (80 × 30 × 13 mm^3 in gauge length volume) moulds, while moderate vibration was applied to remove entrapped air and to improve consolidation. The moulds were then covered with plastic sheets and cured at room temperature for one day, after which the hardened specimens were removed from the moulds and cured in a climate room (20 °C and ≥98% RH) for another 27 days before testing. The preparation of SHCC matrix specimens for fracture toughness test and elastic modulus test followed the same procedure except that no fibre was added into the fresh paste.

Preparation of single fibre pullout specimens followed the suggestion of reference [15]. A long PVA fibre was cut into about 150 mm in length and embedded into the SHCC matrices (same mix composition as in Table 2.1 but without the addition of PVA fibre). The hardened specimen was demoulded after one day and cured under the same condition as SHCC specimens. The specimens were sawed into thin specimens having 1 mm in thickness with a single fibre extruding out from one side.

2.2.3 Tests

The compressive strength of the SHCC was measured in accordance with NEN EN 196-1 [16] by using 40 × 40 × 40 mm^3 cube specimens. Uniaxial tension tests were performed by using a servo-hydraulic testing machine (Instron® 8872) under displacement control at a rate of 0.005 mm/s. Dogbone-shaped specimens recommended by the Japan Society of Civil Engineers (JSCE) [17] with a cross-section of 13 × 30 mm at the test zone were adopted. The deformations were measured with a gauge length of 80 mm with two Linear Variable Differential Transformers (LVDTs) fixed on both sides of the specimens as shown by Fig. 2.2. Tests were stopped by releasing the applied tensile load after the tensile load drops to 80% of the maximum load. Immediately after the tensile test, the residual crack width of unloaded specimens was measured by using a pre-calibrated digital microscope. The maximum tensile stress is regarded as ultimate tensile strength (σ_{ult}), and the corresponding strain value is called the tensile strain capacity (ε_{ult}). At least 4 samples were tested for each mixture. The average and the standard deviation of the results were reported.

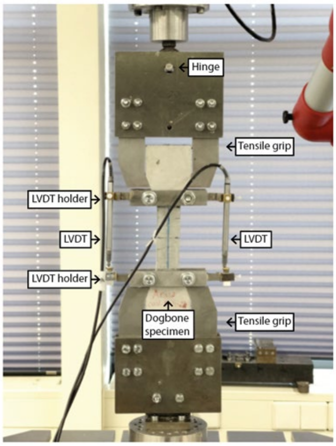

Figure 2.2: Experimental set-up for uniaxial tensile test of SHCC dog-bone specimens

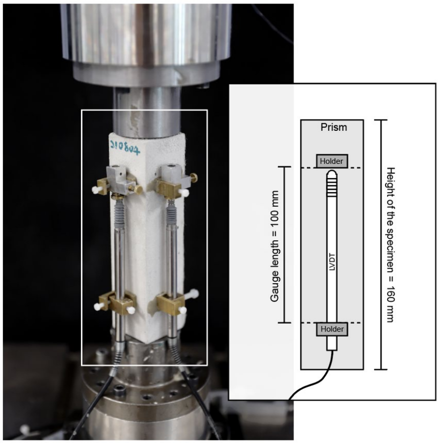

Figure 2.3: Experimental set-up for elastic modus test of prismatic specimens

The matrix properties (*i.e.*, elastic modulus and fracture toughness) of the SHCC mixtures without fibre were tested by using 40 × 40 × 160 mm^3 prismatic specimens. For each matrix property, at least 6 samples from each mixture were tested. Elastic modulus test was carried out in accordance with NEN-EN 12390-13 [18] with prism specimens as shown by Fig. 2.3. Four LVDTs were arranged at each side of the prism along central axis of the specimen with a gauge length of 10 cm. The tests were carried out under load control at a rate of 0.1 N/s for measuring the stabilized secant modulus of elasticity. Three loading cycles were carried out after preloading.

The fracture toughness of SHCC matrices was determined by performing three-point bending tests on pre-notched prism specimens in accordance with the Extended Round Robin Testing program (RRT+) of COST ACTION TU1404 [19]. The notches with a thickness of 1.5 mm and a depth of

12 mm were prepared by using a cutting saw. Bending tests were performed under crack mouth opening displacement (CMOD) control at a rate of 0.01 mm/min, which was monitored by two LVDTs on both sides of the notch. The prism was supported over a load span of 120 mm. Since SHCC matrix formulations do not contain coarse aggregates, the fracture process zone size is expected to be small compared with all relevant specimen dimensions. The fracture toughness of the brittle SHCC matrices (without fibre) is thus determined using linear elastic fracture mechanics (LEFM) considerations, as has been widely used in previous studies and recommendations [1,3,20,21]. The stress intensity factor, K_{Ic}, is given by Eqs. (2.1) – (2.5):

$$K_{Ic} = \frac{1.5 \cdot F_{max} \cdot S\sqrt{\pi a}}{BW^2} f(a) \tag{2.1}$$

where F_{Max} is the highest applied load [N], B is the specimen width [mm], W is the specimen depth [mm], S is the loading span [mm], a is the notch depth and $\alpha = a/W = 0.3$ $(0.05 \leq \alpha \leq 0.8)$ is the relative notch depth ratio. The geometry dependent function *f(a)* is determined using two-dimensional plane stress analysis and is given by:

$$f(a) = f_1(a) + f_2(a) \tag{2.2}$$

Where:

$$f_1(a) = \frac{0.68 - 0.744\alpha}{1 - 2.155\alpha + 1.161\alpha^2} \tag{2.3}$$

$$f_2(a) = 0.36 - 2.088\alpha + 4.611\alpha^2 - 6.499\alpha^3 + 4.233\alpha^4 \quad \textit{(for } 0.05 \leq \alpha \leq 0.8\textit{)} \tag{2.4}$$

Additionally, crack tip toughness J_{tip} (*i.e.*, the critical strain energy release rate) should also be calculated to provide insights from an energy perspective:

$$J_{tip} = \frac{{K_m}^2}{E_m} \tag{2.5}$$

where E_m is the elastic modulus of the paste [GPa].

The interface properties were determined using single fibre pullout tests following previous studies by Redon et al. [22]. A micromechanics-based model proposed by Lin et al. [23] was adopted to describe the bond properties through the notions of : (1) chemical bond strength G_d quantified by interfacial fracture toughness, (2) constant frictional bond strength τ_0 for small sliding and (3) slip hardening coefficient β that characterizes the increasing effective frictional bond during large sliding (pullout) stage. The tests were performed by using a micro tension-compression testing device from Kammrath & Weiss GmbH as shown in Fig. 2.4. During the test, both the bottom surface of the thin specimen and the free end of the PVA fibres were glued to two small metal blocks, which were then clamped with the actuator and the load cell (50 N capacity), respectively. The pull-out process was carried out at a displacement rate of 0.005 mm/s, which is the same as in the tensile test. At least 10 specimens were tested for each mixture, the results of which were then analysed to determine the interface properties (*i.e.*, chemical bond G_d, frictional bond τ_0, and slip-hardening coefficient β) according to Eqs. 2.6 – 2.8:

$$G_d = \frac{2(P_a - P_b)^2}{\pi^2 E_f d_f^3} \tag{2.6}$$

$$\tau_0 = \frac{P_b}{\pi d_f L_e} \tag{2.7}$$

$$\beta = \frac{d_f}{L_e}\left(1 + \frac{1}{\pi \tau_0 d_f} \cdot \frac{\Delta P}{\Delta u'} \Bigg|_{u' \to 0}\right) \tag{2.8}$$

where E_f, d_f and L_e are the elastic modulus [GPa], diameter [mm], and embedded length of PVA fibre [mm], respectively. $\Delta P/\Delta u$ is the initial slope of the pullout load vs displacement. P_a is the load up to full debonded length and P_b is the load when the fibre begins to slip.

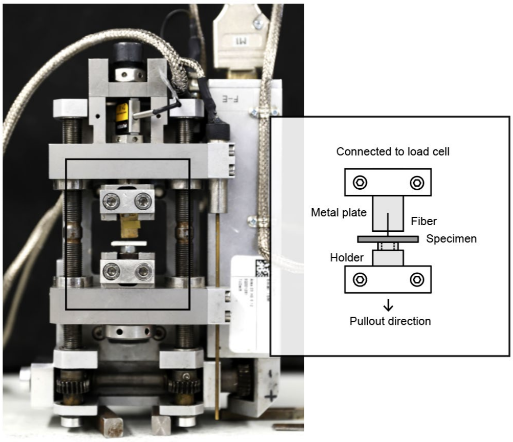

Figure 2.4: Experimental set-up for single fibre pullout test.

Optical microscope (OLYMPUS BX51) and environmental scanning electron microscope (SEM, QUANTA FEG 450) were used to study the microstructure of interface between PVA fibre and SHCC matrices. The specimens were prepared by cleaving through the fibre so that the fibre/matrix interface was exposed longitudinally.

2.2.4 Micromechanics-based modelling

Micromechanical modelling based on fracture mechanics provides an opportunity of tailoring micro-parameters and thus modification of the failure mode, the tensile strength, and ultimate tensile strain of composite material [24]. In this study, the micromechanical modelling was performed using a modified fibre bridging constitutive law developed by Yang et al. [25]. The model links the single fibre/matrix interaction to the fibre bridging behaviour of a single crack (σ–δ relationship), and the simulated results are used to evaluate the potential for PSH of composite material as described in the following paragraphs. The most important simulated results from the model are the σ-δ relationships of single fibre bridging.

Tensile strain hardening of cement-based material is a result of sequential development of steady-state cracks. The condition for steady-state cracking was quantitatively analysed by Marshal and Cox based on the J-integral method, which can be expressed as Eq. 2.9.

$$\frac{{K_m}^2}{E_m} = J_{tip} \leq \sigma_0\delta_0 - \int_0^{\delta_0} \sigma(\delta)d\delta \equiv J_b' \tag{2.9}$$

It indicates that the complementary energy of fibre-bridging J_b' must exceed the crack tip toughness J_{tip}. By assuming the size of the break down zone of the matrix is small, J_{tip} can be interpreted as the amount of energy consumed in the fracture process G_f and therefore can be calculated by ${K_m}^2/E_m$ at small fibre content as shown in Eq. 2.9, where K_m is the matrix fracture toughness and E_m is the matrix Young's modulus. The $\sigma(\delta)$ curve, which can be viewed as the constitutive law of fibre-bridging behaviour, can be expressed as a function of a set of micromechanics parameters including interface frictional bond strength τ_0 and snubbing coefficient f accounting for the interaction between fibre and matrix when pulled at an inclined angle. Besides interfacial properties, the $\sigma(\delta)$ curve is also governed by the matrix Young's modulus E_m, fibre content V_f, fibre diameter d_f, fibre length L_f, and fibre Young's modulus E_f. In addition, the fibre-bridging strength σ_0 along the crack plane must be higher than the matrix cracking strength σ_c to allow the initiation of crack propagation from a matrix flaw. This consideration leads to the second criterion for strain hardening as Eq. 2.10.

$$\sigma_c \leq \sigma_0 \tag{2.10}$$

Eqs 2.11 and 2.12 are referred to as the energy criterion and the strength criterion of pseudo strain hardening, respectively. Satisfaction of both is necessary to achieve tensile strain hardening behaviour. The pseudo strain hardening (PSH) performance indices are often used to quantitatively evaluate the likelihood and robustness of strain hardening behaviour [2].

$$PSH_{energy} = \frac{J_b'}{J_{tip}} \tag{2.11}$$

$$PSH_{strength} = \frac{\sigma_0}{\sigma_c} \tag{2.12}$$

Theoretically, if both PSH indices are larger than 1, strain hardening behaviour would occur. However, large margins are preferred to ensure saturated multiple cracking and high tensile strain capacity because of the material heterogeneity. In this study, the measured interface bond properties from the single fibre pullout tests and measured matrix properties were used to calculate fibre-bridging constitutive law and to determine the PSH indices of the SHCC with and without HA.

2.3 Results and discussion

2.3.1 Composite performance of SHCC with and without healing agent

Table 2.3 summarizes the mechanical properties of SHCCs with different amount of HA and the corresponding control mix where no HA was added. Fig. 2.5 shows the development of compressive strength of the mixtures. As can be seen, the inclusion of HA resulted in strength reductions at all ages. The degree to which the strength was reduced depends on the dosage of HA and the maturity of the specimens. In general, higher dosage of HA leaded to more strength reduction; and the reduction was more pronounce at early ages. One of the possible reasons for this detrimental effect can be due to the hydrolytic degradation of PLA. It has been reported that in aqueous solutions PLA can experience hydrolytic degradation via random cleavage of the ester bond [26]. Depolymerization via hydrolysis leads to the formation of lactic acid, which is likely to consume alkalinity when the HA is mixed with the fresh paste. Since the hydration of slag also demands hydroxyl and alkali ions, a competition may have occurred. It is therefore expected that the use of a higher HA content will lead to greater competition, resulting in a more significant strength reduction.

Table 2.3: Results of uniaxial compression and tension tests.

Mixture ID	28-day compressive strength (MPa)	First cracking strength (MPa)	Ultimate tensile strength (MPa)	Ultimate tensile strain (MPa)	Residual crack width (µm)
SHCC-0HA	62.8±4.5	3.5±0.2	4.8±0.2	4.8%±0.5%	44.4±33.6
SHCC-1.25HA	59.3±2.1	3.4±0.2	4.4±0.3	4.7%±0.4%	33.6±25.2
SHCC-2.5HA	52.3±1.5	3.4±0.3	4.3±0.3	4.4%±0.3%	25.9±22.5
SHCC-5HA	41.1±2.4	3.0±0.1	4.6±0.2	5.1%±0.7%	13.2±5.3

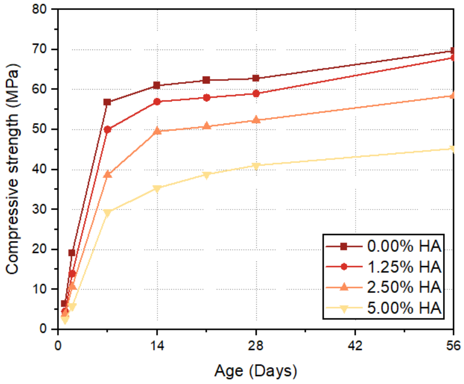

Figure 2.5: Compressive strength of SHCCs with different amount of healing agent.

Fig. 2.6 shows the tensile stress-strain curves of SHCCs without HA and with the highest dosage of HA (*i.e.*, 5% by weight of binder). As can be seen, both mixes exhibited pronounced tensile strain hardening behaviour. Three distinctive phases can be observed in the tensile stress-strain curves. The first phase is the initial elastic phase. The second phase starts from the formation of the first crack, after which the load continues to increase without damage localization. The sequential formation of multiple parallel cracks (as shown in Fig. 2.7) results in the transitory load drops and contributes to the inelastic deformation during the strain hardening stage. The third phase begins with the occurrence of the final fracture when the fibre-bridging capacity is exhausted, which defines the ultimate strength of the composite. The corresponding strain value is the tensile strain capacity of the composite.

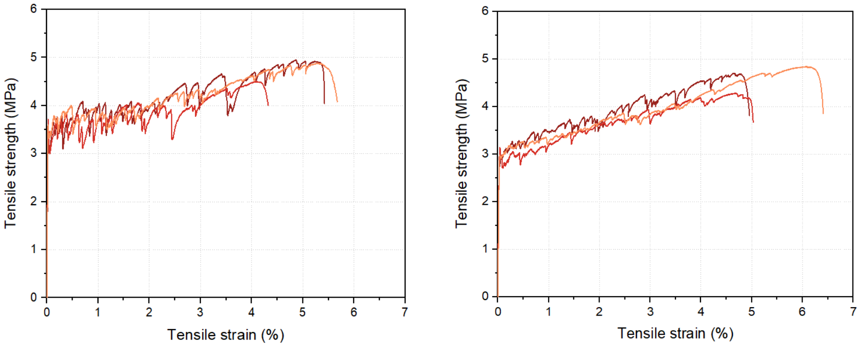

(a) (b)

Figure 2.6: Representative tensile stress-strain curves of SHCCs (a) without HA and (b) with 5% HA.

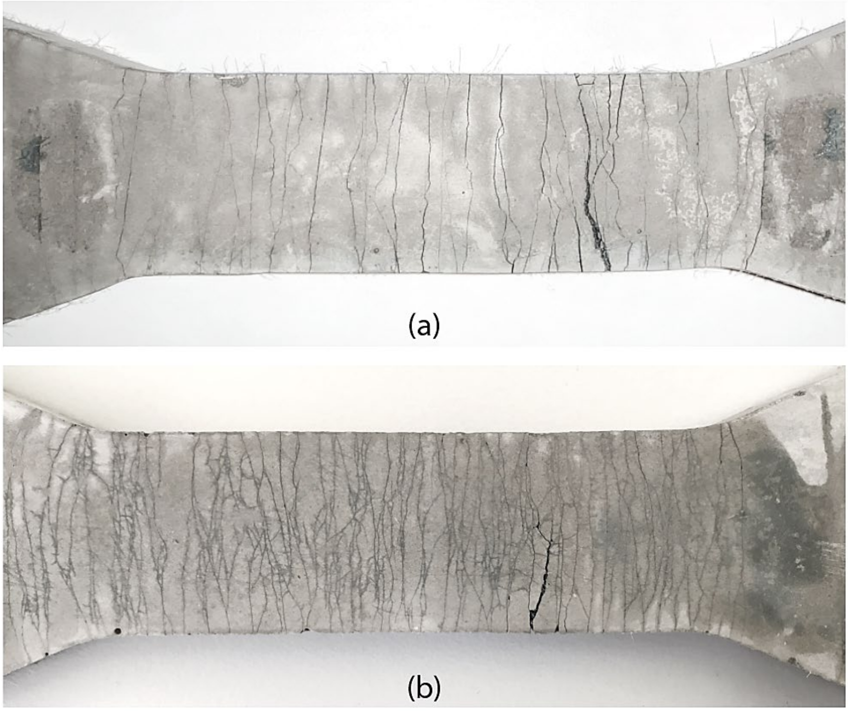

Figure 2.7: Typical crack pattern of SHCCs (a) without HA and (b) with HA (gauge length: 8 cm).

As shown in Fig. 2.8a, different from the effect of adding HA to the compressive strength, the tensile strengths (*i.e.*, the first cracking strength and the ultimate tensile strength) were only slightly altered by the addition of HA. When 5% of HA was added, the first cracking strength and the ultimate tensile strength decreased by only 14% and 4%, respectively. The first cracking strength is dependent on the flaw size distribution and the matrix fracture toughness. It is therefore possible that the HA may have served as artificial flaws, for that both the strength and stiffness of PLA are much lower than that of the cement matrix. Once the cracks form, the load shed by the matrix is taken over by the bridging fibres on each crack plane. Therefore, the increase in ultimate tensile strength should be a direct consequence of having enhanced fibre bridging capacity, indicating the formation of stronger fibre/matrix bond. Similarly, the tensile strain capacity of SHCC was also found to be insensitive to the addition of HA. With increasing amount of HA, the tensile strain capacity fluctuated between 4.4% and 5.1%. In fact, the tensile strain was the largest (*i.e.*, 5.1%) when the dosage of HA was the highest. It is therefore concluded that the addition of HA up to 5% by weight to binder did not pose any detrimental effect to the desired tensile properties of SHCC. In the design of self-healing SHCC, the optimal dosage of HA can then be decided purely based on the healing performance.

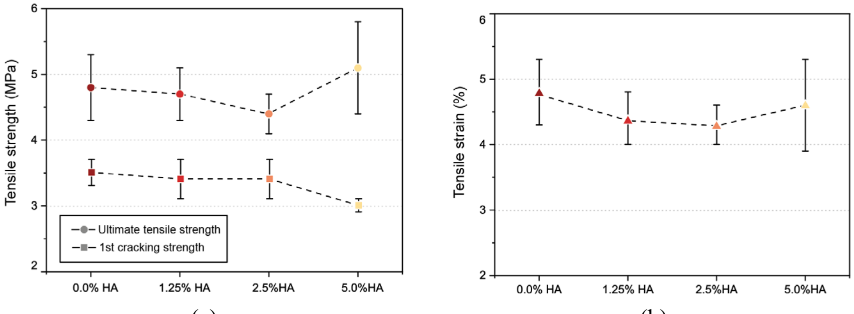

(a) (b)

Figure 2.8: Results of uniaxial tensile tests of SHCCs.

Furthermore, residual crack width of SHCC was found to decrease with increasing amount of HA as shown by Fig. 2.9. As summarized in Table 2.3, compared with the control SHCC without HA, the average residual (*i.e.*, crack width after unloading) crack width of SHCC with 5% HA decreased by 70% from 44.4 µm to 13.2 µm, indicating that the interface frictional bond strength may have been enhanced, which restrains the slippage of the fibre during pullout [4,27]. The observed reduction in crack width is in line with the tensile stress-strain curves as shown in Fig. 2.6, which show smaller drops when a crack occurs in the case of HA. This unforeseen effect of adding HA is expected to be extremely beneficial to the healing performance of the composite, for which the tight crack width can largely promote the speed and the extend of cracking healing.

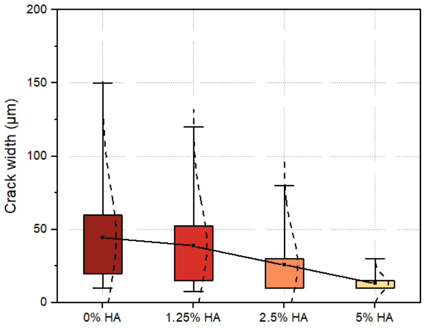

Figure 2.9: Residual crack width of SHCCs with different amount of HA.

2.3.2 SHCC matrix properties with and without healing agent

Based on the design theory of SHCC as explained in Section 2.4, the tensile strain capacity is determined by both matrix and fibre/matrix interface properties when the same type of fibre is used. Therefore, the effects of HA on the matrix properties were also investigated and the results are summarized in Table 2.4. Figs. 10 and 11 show the change of fracture toughness and elastic modulus of the SHCC matrices with increasing amount of HA. As can be seen, when the amount of HA was no more than 2.5%, both matrix properties were not noticeably modified. When the dosage was increased to 5%, however, the elastic modulus of the matrix decreased by 31.5% and the fracture toughness increased by 60.1%, as compared to the control SHCC without HA. The reduction in elastic modulus is as expected, as the elastic modulus of PLA itself is significantly lower than that of cement hydration products and aggregates. Also, since the addition of HA will inevitably introduce an ITZ between the particle and the matrix, the formation of porous ITZ will also reduce the stiffness of the resulting composite. The increase in fracture toughness can be attributed to the relatively large particle size of the HA as compared to that of cement and limestone powder. The inclusion of particles of millimetre size can significantly increase the tortuosity of a crack path, leading to higher fracture resistance. In addition, since surface of some HA will experience alkali hydrolysis, the chemical compositions of the hydration product may also be modified. In fact, it has been reported that a strong positive correlation was identified between the Ca/Si ratio of calcium aluminate silicate hydrate (CASH) and its fracture properties [28]. Therefore, since the addition of HA also brings in extra calcium ions, the increase in fracture toughness can also be partially attributed to the increase of Ca/Si ratio of hydration products. It should be noted that the current calculation of the matrix fracture toughness was made under assumption that the LEFM holds true for the brittle SHCC matrices. Therefore, although these fracture data are generally consistent with expected trends, they are probably not the true fracture toughness and should be regarded as indicative values only.

Table 2.4: Matrix and interface bond properties of the SHCCs.

Mixture ID	Matrix properties				Fiber/matrix interface properties		
	Peak force (kN)	Fracture toughness ($kPa\cdot m^{1/2}$)	Elastic modulus (GPa)	Crack tip toughness (J/m^2)	Chemical bond energy Gd (J/m^2)	Frictional bond τ_0 (MPa)	Slip-hardening coefficient β
SHCC-0HA	0.260±0.036	0.143±0.018	16.5±1.4	1.21	4.98±2.42	1.98±0.54	0.302±0.07
SHCC-1.25HA	0.263±0.029	0.144±0.015	17.4±0.3	1.18	5.65±2.38	2.04±1.01	0.235±0.13
SHCC-2.5HA	0.253±0.042	0.139±0.025	17.2±1.1	1.13	6.60±2.31	3.59±1.31	0.241±0.09
SHCC-5HA	0.416±0.013	0.229±0.007	11.3±0.1	4.6	7.20±3.12	3.69±1.49	0.281±0.11

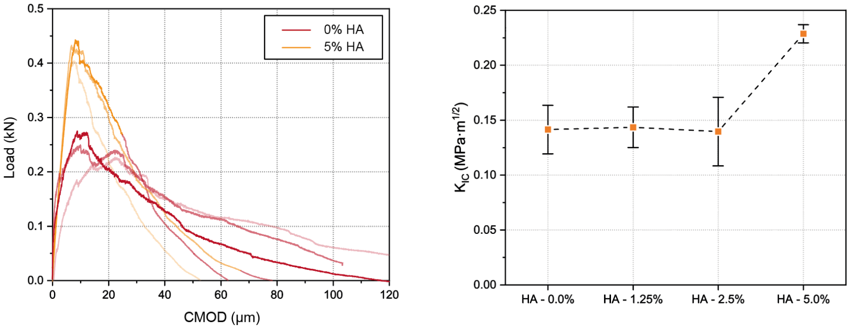

(a) (b)

Figure 2.10: Results of 3-Point-Bending test: (a) representative Load vs CMOD curves and (b) fracture toughness of SHCC matrices with different amount of HA.

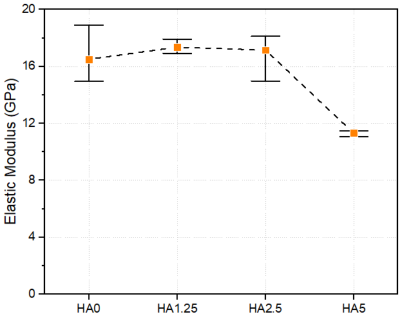

Figure 2.11: Young's modulus of SHCC matrix properties.

2.3.3 Fibre/matrix interface properties

Besides matrix properties, the fibre/matrix interface properties are also critical to the tensile strain-hardening performance of SHCC. Fig. 2.12 presents the typical single fibre pullout curve of PVA fibre from SHCC matrix, from which the interface bond properties including chemical bond (G_d), frictional bond strength (τ_0), and slip-hardening coefficient (β) can be derived. The results are summarized in Table 2.4. As can be seen, both chemical bond and frictional bond increased with increasing HA content. The addition of 5% HA resulted in a 45% enhancement of the chemical bond energy and an 86% enhancement of frictional bond strength. The increase of the bond properties is line with the reduction trend of the residual crack width as measured. The slip-hardening coefficient was not significantly influenced.

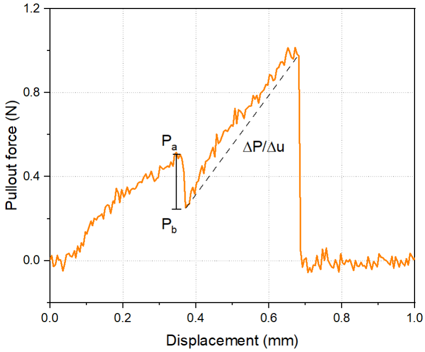

Figure 2.12: Representative results of single fibre pullout test. $\Delta P/\Delta u$ is the initial slope of the pullout load vs displacement. P_a is the load up to full debonded length and P_b is the load when the fibre begins to slip.

To investigate the mechanism for the bond improvement, specimens containing a single fibre were prepared and cleaved at the fibre plane. A longitudinal section of the fibre/matrix ITZ can then be exposed for SEM analysis. Figs. 2.13a and b show the resulting, representative micrographs of SHCC matrices having 0% and 5% HA with a fibre partially embedded in the middle (horizontally). As can be seen, the microstructure of the ITZ for specimen with HA is dense, while for the specimen without HA, a very porous zone filled with hexagonal calcium hydroxide (CH) crystals near the fibre can be identified. An ITZ with higher stiffness and compactness will result in more of the contact area and damage tolerance during fibre pullout and therefore lead to increased frictional bond strength. The formation of less CH may be attributed to the hydrolytically degradable nature of the PLA. The hydrolysis of a polyester such as PLA produces shorter chains with acid and alcohol terminal groups. The chain cleavage results in a shorter polymer chain and an increasing carboxylic acid-end group concentration, which may have consumed the CH and delayed its precipitation. Further study should be carried out to investigate this densification process. Furthermore, the surface condition of fibre in the two specimens were also very different. In the specimen with HA, a layer of hydration product on the surface of PVA fibre can be easily identified, while the fibre in specimen without HA had a very smooth and clear surface. This suggests that the matrix with HA have possessed higher chemical affinity with the PVA fibre, which may have contributed to the enhanced chemical bond energy.

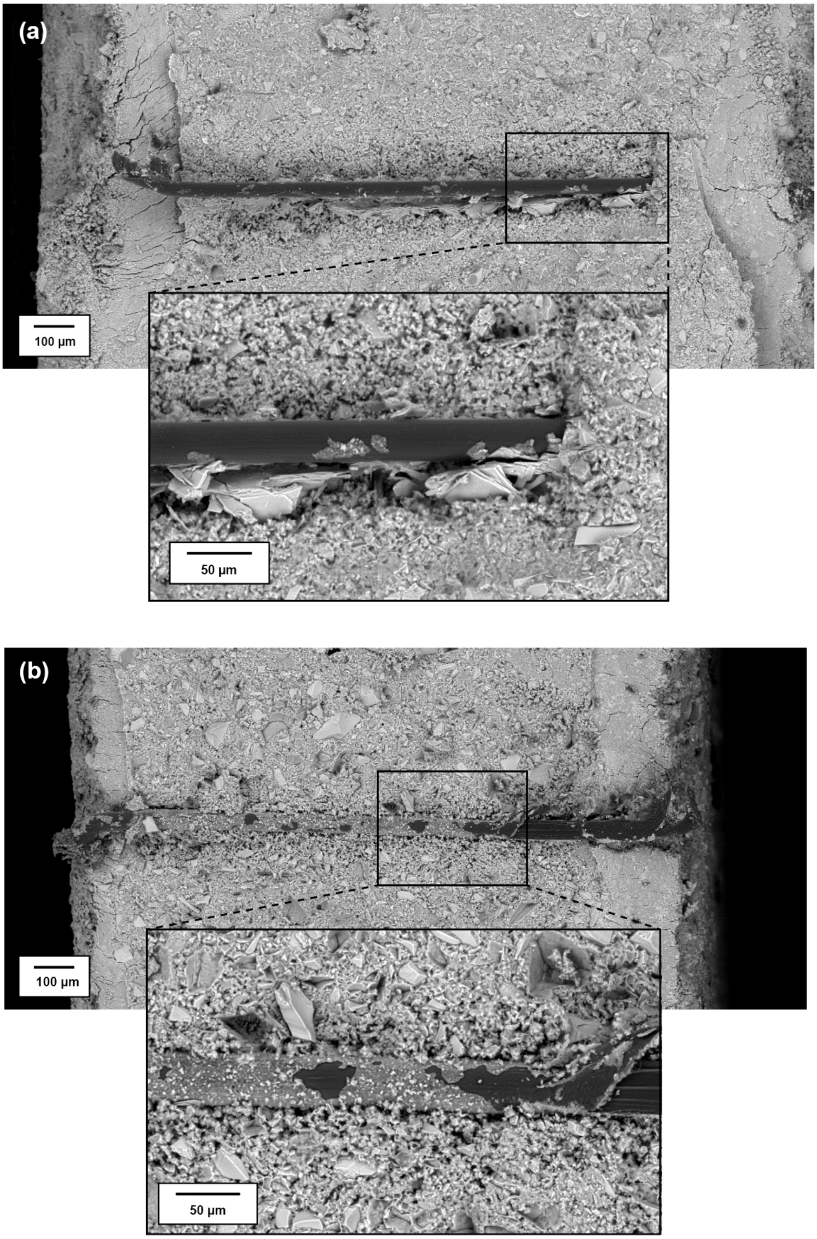

Figure 2.13: SEM micrographs of ITZs between fibre and SHCC matrix: (a) without HA and (b) with 5% HA.

2.3.4 Micromechanics-based modelling of strain hardening potential

The fibre bridging behaviour of SHCC with different amount of HA can be calculated based on the measured micromechanical parameters (Table 2.4) and the fibre parameters provided by the manufacturer (Table 2.2). Model results of the calculation of complementary energy J'_b, peak fibre-bridging strength σ_0 and two *PSH* indices based on the micromechanical model are reported in Table 2.5. As can be seen, all SHCC mixtures possessed *PSH* indices larger than one regardless the amount of HA. This suggests that all materials satisfied the criteria of achieving the strain hardening performance. However, with increasing amount of HA, the two *PSH* indices exhibited opposite trends. While the *PSH* strength index increased with increasing amount of HA, the PSH energy index decreased significantly from 15 to 3.8. In theory, high indices (*i.e.*, large margins between J'_b and J_{tip} and between σ_0 and σ_c) are often necessary to accommodate expected variability and inhomogeneity of the material. Therefore, the decreasing trend of PSH energy index suggests that the addition of HA can deplete the potential of having pronounced strain-hardening behaviour. The reason why the SHCCs developed in the current study did not experience any strength and ductility losses with increasing amount of HA is because the potential was not exhausted. But it is possible that tensile properties of SHCC can be attenuated when too much of HA is added. It should be noted that the required amount of HA may depend on specific application and the required level of healing performance. Even if a strong self-healing performance is demanded, the required dosage of HA may not exceed the highest dosage as adopted in the current study. When the amount of HA is 5% by weight of binder, the equivalent dosage of HA is 51 kg/m^3, whereas the typical dosage used in commercial self-healing concrete is only between 5 to 7.5 kg/m^3. Therefore, it can be concluded that a robust self-healing function can indeed be realized in SHCC without sacrificing its superior tensile properties.

Table 2.5: Results of micromechanical model calculation.

Mixture ID	J_b’ (J/m^2)	σ_0 (MPa)	J_{tip} (J/m^2)	σ_c (MPa)	PSH strength (J'_b/J_{tip})	PSH energy (σ_0/σ_c)
HCC-0HA	18.16	5.89	1.21	3.5	1.68	15.0
SHCC-1.25HA	16.58	5.78	1.18	3.4	1.70	14.1
SHCC-2.5HA	14.15	6.58	1.13	3.4	1.93	12.5
SHCC-5HA	17.64	6.48	4.6	3.0	2.16	3.8

It should be noted that the discovered ITZ strengthening effect of the HA may not always be beneficial to the tensile properties of the SHCC. Especially for SHCC adopting hydrophilic fibres, a perfect bond does not necessarily lead to improved tensile performance because this increases the risk of having extensive fibre rupture. Since fibre pullout rather than rupture confers a larger ductility to the fibre reinforced composites, the bond properties should always be carefully tailored based on the fibre properties and matrix properties to minimize fibre rupture during pullout. For the current study, the reason why the improved bond properties contributed to improved tensile performance of the SHCC is because, for the SHCC mixtures without HA, the strength of the fibre was not fully utilized. For the group of SHCC utilizing hydrophobic fibres, adding HA into the mixture can always be an effective solution to enable the self-healing functionalities while at the same time improve the tensile and cracking performance of the resulting composites.

2.4 Conclusions

In this study, the effects of adding bacteria-embedded PLA capsules on mechanical properties of SHCC were investigated. Self-healing SHCC mixtures with different dosages of PLA capsules ranging from 1.25% to 5% by weight of binder were developed; and their mechanical properties were tested and compared with control SHCC without HA. Tests considering behaviours of SHCC mixtures at multiple scales (*i.e.,* at composite, matrix, and fibre/matrix bond level) were performed. The main findings of the current study are:

1. The inclusion of the PLA-HA up to 5% by weight to binder did not influence the tensile properties (*i.e.*, tensile strength and ductility) of SHCC. All mixtures exhibited pronounced strain-hardening behaviour.
2. The residual crack width was found to reduce with increasing HA content. Compared with the control SHCC without HA, the average crack width of SHCC with 5% HA decreased by 70% from 44.4 µm to 13.2 µm. Having smaller crack widths in an SHCC with HA should also result in a better healing capacity.
3. The matrix properties (*i.e.*, fracture toughness and elastic modulus) of the SHCC were found to be insensitive to the addition of small and moderate amounts of HA but can change dramatically when the dosage was high. The crack tip toughness of the matrix containing 5% of HA is 3.8 times of that without any HA.
4. Single fibre pullout results show that the fibre/matrix bond properties were enhanced by the addition of the HA, which can be attributed to the formation of a denser ITZ with reduced calcium hydroxide crystals.

References

[1] V.C. Li, Engineered Cementitious Composites (ECC), Engineered Cementitious Composites (ECC) (2019). https://doi.org/10.1007/978-3-662-58438-5.

[2] V.C. Li, C.K.Y. Leung, SteadyState and Multiple Cracking of Short Random Fiber Composites, J Eng Mech 118 (1992) 2246–2264. https://doi.org/10.1061/(ASCE)0733-9399(1992)118:11(2246).

[3] V.C. Li, D.K. Mishra, H.-C. Wu, Matrix design for pseudo-strain-hardening fibre reinforced cementitious composites, Materials and Structures 1995 28:10 28 (1995) 586–595. https://doi.org/10.1007/BF02473191.

[4] V.C. Li, C. Wu, S. Wang, A. Ogawa, T. Saito, Interface Tailoring for Strain-Hardening Polyvinyl Alcohol-Engineered Cementitious Composite (PVA-ECC), Materials Journal 99 (2002) 463–472. https://doi.org/10.14359/12325.

[5] G. Yildirim, Ö.K. Keskin, S.B.I. Keskin, M. Şahmaran, M. Lachemi, A review of intrinsic self-healing capability of engineered cementitious composites: Recovery of transport and mechanical properties, Constr Build Mater 101 (2015) 10–21. https://doi.org/10.1016/J.CONBUILDMAT.2015.10.018.

[6] Y. Yang, M.D. Lepech, E.H. Yang, V.C. Li, Autogenous healing of engineered cementitious composites under wet–dry cycles, Cem Concr Res 39 (2009) 382–390. https://doi.org/10.1016/J.CEMCONRES.2009.01.013.

[7] S. Fan, M. Li, X-ray computed microtomography of threedimensional microcracks and self-healing in engineered cementitious composites, Smart Mater Struct 24 (2015). https://doi.org/10.1088/0964-1726/24/1/015021.

[8] J. Qiu, H.S. Tan, E.H. Yang, Coupled effects of crack width, slag content, and conditioning alkalinity on autogenous healing of engineered cementitious composites, Cem Concr Compos 73 (2016) 203–212. https://doi.org/10.1016/j.cemconcomp.2016.07.013.

[9] R.M. Mors, H.M. Jonkers, Feasibility of lactate derivative based agent as additive for concrete for regain of crack water tightness by bacterial metabolism, Ind Crops Prod 106 (2017) 97–104. https://doi.org/10.1016/j.indcrop.2016.10.037.

[10] E. Tziviloglou, V. Wiktor, H.M. Jonkers, E. Schlangen, Selection of nutrient used in biogenic healing agent for cementitious materials, Front Mater 4 (2017). https://doi.org/10.3389/fmats.2017.00015.

[11] R. Mors, H. Jonkers, Effect on concrete surface water absorption upon addition of lactate derived agent, Coatings 7 (2017). https://doi.org/10.3390/coatings7040051.

[12] L. Mercuri, C. Romero Rodriguez, Y. Xu, S. Chaves Figueiredo, R. Mors, E. Rossi, G. Anglani, P. Antonaci, B. Savija, E. Schlangen, On the role of soft inclusions on the fracture behaviour of cement paste, in: G. Pijaudier-Cabot, P. Grassl, C. la Borderie (Eds.), 10th International Conference on Fracture Mechanics of Concrete and Concrete Structures (FraMCoS-X), Bayonne, 2019. https://doi.org/10.21012/FC10.235271.

[13] J. Zhou, S. Qian, M.G.S. Beltran, G. Ye, K. van Breugel, V.C. Li, Development of engineered cementitious composites with limestone powder and blast furnace slag, Materials and Structures/Materiaux et Constructions 43 (2010) 803–814. https://doi.org/10.1617/s11527-009-9549-0.

[14] European committee for standardization, NEN-EN 197-1. Cement - Part 1: Composition, specifications and conformity criteria for common cements, 2011.

[15] B. Carl Redon, V.C. Li, C. Wu, H. Hoshiro, T. Saito, A. Ogawa, MEASURING AND MODIFYING INTERFACE PROPERTIES OF PVA FIBERS IN ECC MATRIX, (n.d.).

[16] European committee for standardization, NEN-EN 196-1. Methods of testing cement - Part 1: Determination of strength, 2016.

[17] K.A. Rokugo Tetsushi Kanda AE Hiroshi Yokota AE Noboru Sakata, Applications and recommendations of high performance fiber reinforced cement composites with multiple fine cracking (HPFRCC) in Japan, (n.d.). https://doi.org/10.1617/s11527-009-9541-8.

[18] European committee for standardization, NEN-EN 12390-13. Testing hardened concrete - Part 13: Determination of secant modulus of elasticity in compression, 2021.

[19] COST Action TU 1404, Main phase of the Extended Round Robin Testing programme for TU1404 - Tseting protocols, 2016. https://www.tu1404.eu/wp-content/uploads/2017/12/RRT-Main-phase_Protocols_06112017.pdf (accessed February 28, 2022).

[20] C. Sonat, S. He, J. Li, C. Unluer, E.-H. Yang, Strain hardening magnesium-silicate-hydrate composites (SHMSHC) reinforced with short and randomly oriented polyvinyl alcohol microfibers, Cem Concr Res 142 (2021). https://doi.org/10.1016/j.cemconres.2021.106354.

[21] S. Zhang, V.C. Li, G. Ye, Micromechanics-guided development of a slag/fly ash-based strain-hardening geopolymer composite, Cem Concr Compos 109 (2020). https://doi.org/10.1016/j.cemconcomp.2020.103510.

[22] B. Carl Redon, V.C. Li, C. Wu, H. Hoshiro, T. Saito, A. Ogawa, Measuring and Modifying Interface Properties of PVA Fibers in ECC Matrix, Journal of Materials in Civil Engineering 13 (2001) 399–406. https://doi.org/10.1061/(ASCE)0899-1561(2001)13:6(399).

[23] Z. Lin, T. Kanda, V. Li, On interface property characterization and performance of fiber reinforced cementitious composites, Concrete Science and Engineering 1 (1999) 173–184. https://deepblue.lib.umich.edu/bitstream/handle/2027.42/84718/zlin_CSE99.pdf?sequence=1 (accessed March 1, 2022).

[24] V.C. Li, Tailoring ECC for Special Attributes: A Review, Int J Concr Struct Mater 6 (2012) 135–144. https://doi.org/10.1007/S40069-012-0018-8.

[25] E. Yang, S. Wang, Y. Yang, V.L.-J. of advanced concrete, undefined 2008, Fiber-bridging constitutive law of engineered cementitious composites, Jstage.Jst.Go.Jp 6 (n.d.) 181–193. https://www.jstage.jst.go.jp/article/jact/6/1/6_1_181/_article/-char/ja/ (accessed March 1, 2022).

[26] M.A. Elsawy, K.H. Kim, J.W. Park, A. Deep, Hydrolytic degradation of polylactic acid (PLA) and its composites, Renewable and Sustainable Energy Reviews 79 (2017) 1346–1352. https://doi.org/10.1016/J.RSER.2017.05.143.

[27] S. He, J. Qiu, J. Li, E.-H. Yang, Strain hardening ultra-high performance concrete (SHUHPC) incorporating CNF-coated polyethylene fibers, Cem Concr Res 98 (2017) 50–60. https://doi.org/10.1016/j.cemconres.2017.04.003.

[28] S. Zhang, Z. Li, B. Ghiassi, S. Yin, G. Ye, Fracture properties and microstructure formation of hardened alkali-activated slag/fly ash pastes, Cem Concr Res 144 (2021). https://doi.org/10.1016/j.cemconres.2021.106447.

3

Characterization of crack healing of SHCC with bacteria-embedded polylactic acid (PLA) capsules[2]

This chapter investigates short-term and long-term crack-healing behaviour of the SHCC developed in the previous chapter. Two sets of specimens were prepared and subjected to different healing regimes, with the first set kept in a mist room for varying short durations (i.e., 1 week, 2 weeks, 3 weeks and 8 weeks) and the second set placed in an unsheltered outdoor environment for a long-term healing process (i.e., 1 year). Alteration of microstructure because of self-healing was characterized by backscattered electron (BSE) imaging and energy dispersive X-ray spectroscopy (EDS) measurement across crack cross-sections. Results show that visible crack healing enabled by bacteria began after 2 weeks in a humid environment. The healing products initially precipitated at the crack mouth and gradually moved deeper into the cracks, with the precipitated calcium carbonate crystals growing larger over time. After 8 weeks, healing products can be found a few millimetres deep inside the crack. Observations of crack healing in a realistic environment revealed significant differences compared to healing under controlled conditions. While healing products can be found at the crack mouth, a substantial healing process was observed throughout the entire crack depth. It is likely that the environmental actions such as rainfall and/or freeze and thaw cycles may have worn away the healing products at the crack mouth and thus led to a deeper ingress of oxygen into cracks, which promoted the activation of healing agents and associated calcium carbonate precipitation deep inside a crack.

---

[2] Part of this chapter has been published in:

He, S., Wan, Z., Chen, Y., Jonkers, H. M., & Schlangen, E. (2023). Microstructural characterization of crack-healing enabled by bacteria-embedded polylactic acid (PLA) capsules. Cement and Concrete Composites, 105271.

3.1 Introduction

Despite the prevalence of results on the performance of bacteria-based self-healing concrete, several key questions remain unanswered. Firstly, previous investigations have primarily evaluated crack healing by measuring the closure rate of surface-level cracks, with little attention paid to the extent of healing deeper within the cracks. Some researchers have even suggested that self-healing occurs only at the crack mouth [2–4], which appears inconsistent with the documented improvements in concrete durability resulting from bacteria-mediated limestone formation [5,6]. Secondly, as bacteria can only induce precipitation of calcium carbonate under specific environmental conditions, previous investigations have typically been conducted under the conditions that are ideal for bacterial growth but not realistic for most concrete structures. Research is thus necessary to evaluate the efficacy of self-healing under realistic environmental conditions. Thirdly, it is crucial that the healing agents containing bacteria should protect the bacteria during concrete mixing and hardening, while also being able to release the bacteria when cracking occurs. In the case of the PLA capsule, it functions through alkaline hydrolysis of PLA capsule to release bacteria when water enters a crack. However, the presence of water during concrete mixing also triggers the hydrolysis process, which may potentially damage the properties of concrete and therefore needs to be determined. This is important to ensure that the healing agent does not negatively affect the structural integrity of the concrete while at the same time can function as intended to promote self-healing.

To answer the above-mentioned questions, the current chapter investigates the crack-healing behaviour of mortar embedded with bacterial healing agents (*i.e.*, PLA capsules), in both short-term and long-term, under both ideal and realistic environmental conditions. Two sets of specimens were thus prepared and subjected to different healing regimes, with the first set kept in a mist room for varying short durations (*i.e.*, 1 week, 2 weeks, 3 weeks and 8 weeks) and the second set placed in an unsheltered outdoor environment for one year as a long-term healing investigation. Each set contained specimens with and without healing agents. To enable the observation of crack healing along crack depth, evolution of microstructure due to self-healing was characterized by BSE and EDS via the crack cross-sections, which also allows the examination of the PLA particles embedded in the mortar matrix. In the following sections, the design of the experimental program will first be introduced, followed by a detailed explanation of the sample preparation procedure, and the methods used to observe crack healing. Then, the progression of crack healing along crack depth for specimens with and without healing agents will be presented, starting with the short-term results, and concluding with the long-term results. Finally, the behaviour of individual PLA capsules during the healing process will also be discussed.

3.2 Materials and tests

3.2.1 Design of experiments

To study the crack healing behaviour of the developed SHCC materials, SHCC dogbone specimens were prepared and loaded under uniaxial tension to generate cracks. The multiple cracking behaviour of SHCC typically leads to the formation of closely spaced fine cracks with parallel crack walls. Unlike the V-shaped cracks created by bending tests, the parallel-wall cracks are ideal for the investigation of healing due to the constant crack width along its depth. Figs. 3.1a and 3.1b show dogbone specimens before and after healing. In addition, because of the inherent variability of the tensile properties, the cracks formed in the dogbone specimens usually have varied crack widths. The range of crack width that can be observed in a single dogbone specimen can be from a few microns to several hundreds of microns (Fig. 3.1c) and thus allows the observation of crack healing from the same specimen but at different crack width.

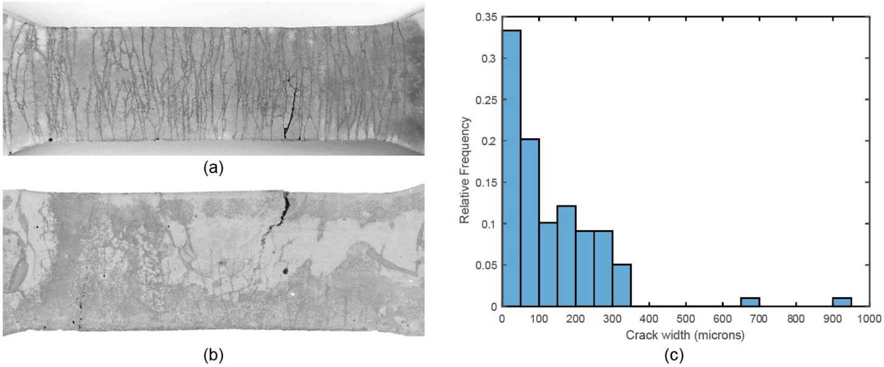

Figure 3.1: Photograph of (a) a dogbone specimen of SHCC after uniaxial tension test and (b) a self-healed dogbone specimen; and (c) crack width distribution of the SHCC material adopted in the current study (calculated based on more than 8 specimens).

To study the crack-healing process under varying conditions, two sets of dogbone specimens were prepared as illustrated in Fig. 3.2. After cracking the specimens, the first set was kept in a mist room with saturated moisture and allowed to heal for various durations (ranging from one week to two months) as a short-term healing study. The second set was placed in an unsheltered outdoor environment and allowed to undergo a long-term healing process for one year. Based on the meteorological history of the city (Delft) in which the experiments were carried out, there were 110 days with precipitation more than 1 mm and 20 days with daily low temperature below zero degree Celsius (Fig. 3.3). The specimens for long-term healing have thus experienced a considerable number of wet-dry cycles and freeze-thaw cycles. Specimens with and without healing agent were both prepared for each set of experiments.

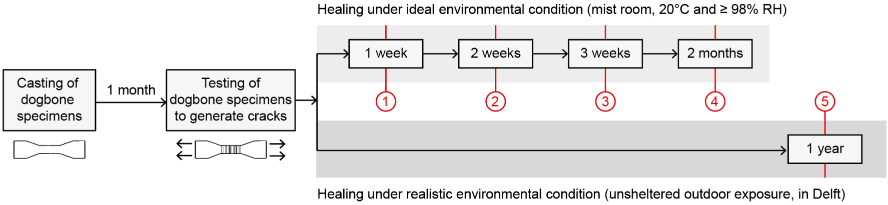

Figure 3.2: Schematic illustration of experimental program (course of healing for SHCC specimens with and without HA).

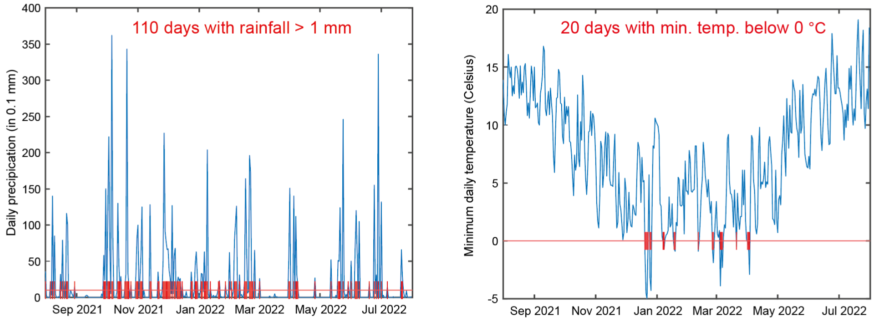

Figure 3.3: Meteorological history of Delft from Aug 01, 2021, to July 31, 2022. Data were obtained from the climate archive of Royal Netherlands Meteorological Institute (KNMI) data portal.

3.2.2 Mix design and materials

Table 3.1 shows the mixture compositions of reference SHCC and the self-healing SHCC, both of which were formulated in the preceding chapter. A healing agent dosage of 2.5% by weight of cement was chosen as it demonstrated the most balanced mechanical performance, encompassing both compressive and tensile behaviours.

Table 3.1: Mixture compositions of SHCCs [unit in kg/m^3].

Mixture ID	CEM III/B	Limestone powder	Water	SP	PVA fibre	PLA capsule
Reference SHCC	1060	530	424	2	26 (2.0 vol%)	0
Self-healing SHCC	1036	518	415	2	26 (2.0 vol%)	26

3.2.3 Specimen preparation

The SHCC material and the dogbone specimens were prepared using the same method as explained in the previous chapter. To generate the cracks in the dogbone specimens, uniaxial tensile tests were performed by using a servo-hydraulic testing machine (Instron® 8872) under displacement control at a rate of 0.005 mm/s. The tests were stopped when the applied tensile load dropped to 80% of the maximum load, and the load was then released. Directly after the generation of cracks by tensile test, the specimens were sawed into segments and then stored in different environments to initiate healing. The sawing process was carried out with great care to prevent secondary damage to the cracked specimen. Crack width measurement of selected cracks before and after sawing demonstrated that the sawing had minimal influence on the formed micro-cracks. At the end of their respective healing program, the specimens were removed from their designated environment and then dried in an oven at 40 °C for 2 days. Next, the segments were epoxy impregnated and coated to preserve the healing products precipitated both inside the cracks and at the sample surface and. To expose the cross-sectional surfaces, the epoxy-coated specimen was cut by a diamond saw from its middle. The exposed cross-section was then epoxy impregnated again to aid surface finishing. Afterward, the sample was first ground by 4000 grit abrasive papers for 5 minutes and then polished with a synthetic silk polishing cloth (MD-Dac from Struers) charged with 3 μm and 1 μm diamond paste for 2 separate 10-minute-long sessions. An oil-based lubricant (DP-Lubricant Brown from Struers) was used to dissipate any heat built-up. Between each grinding/polishing interval, the sample was immersed in an ultrasonic bath for 30 seconds to remove debris from the surface.

3.2.4 Characterization

As explained above, microstructural characterization of crack healing was carried out with segmented dogbone specimens as shown in Fig. 3.4a, with each segment having 3-5 penetrating cracks. The segments were epoxy impregnated and coated to preserve the healing products precipitated both at the sample surface and inside the cracks. Characterization of crack healing along crack depth was then performed at the cross-sectional surfaces by cutting the epoxy coated segment from its middle (Fig. 3.4b).


(a) (b)

Figure 3.4: Photograph of (a) cut segments from a dogbone specimen (gauge zone: 8 cm × 3 cm × 1.3 cm) and (b) epoxy impregnated specimens (3 cm × 1.3 cm × 1 cm).

The polished cross-sections were then characterized by backscattered electrons (BSE) imaging and energy dispersive X-ray spectroscopy (EDS). BSE analyses were carried out with the concentric backscattered (CBS) detector in an FEI QUANTA FEG 650 environmental scanning electron microscope (SEM) at high vacuum chamber condition. All specimens were coated with a layer of carbon of roughly 10 nm thick before BSE examination. Stitched BSE images of large area were taken with a commercial software (Maps 3 from Thermo Fisher Scientific). EDS elemental mapping was performed with the same SEM equipped with a silicon drift detector (SDD) with a NORVAR® light element window. The EDS maps were acquired by using the Pathfinder X-ray Microanalysis Software (Thermo Fisher Scientific). The combination of 50 μs dwell time per pixel with an averaging over 50 frames was found to provide good results. The resulting acquisition time of a map is around 30 minutes per area. All analyses (*i.e.*, BSE and EDS) were carried out at a working distance of 10 mm and at an accelerating voltage of 15 kV.

3.3 Results and discussion

3.3.1 Microstructural features of the specimens

Fig. 3.5 shows the typical appearance of a cross-section of the specimens under BSE. In the BSE images, the brightness of each pixel depends on the mean atomic number of the underlying phases. This allows different phases to be distinguished based on their grayscale. The epoxy filled cracks can be easily identified in the graph as dark lines penetrating the whole specimen horizontally. The left and right sides of the specimen are respectively the top and bottom exposing surfaces of the original dogbone specimen as shown in Fig. 3.4a. In addition to cracks, epoxy filled pores could be seen also in dark black, leading to shadowy appearance in areas with a high porosity. Embedded fibres and PLA capsules, which both contain mainly the element of carbon, can also be found as regions in dark back. They can be distinguished by their shape, with fibres appearing as either circular or oval and PLA capsules appearing an irregular shape. Some large black circles can also be seen, which are epoxy filled air voids.

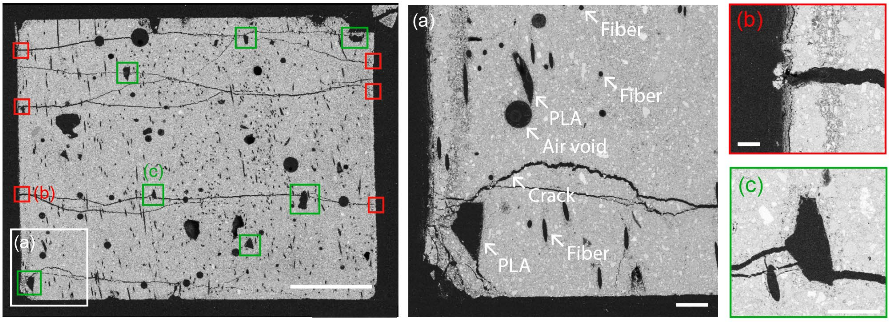

Figure 3.5: Stitched BSE micrograph of a cross-section (scale bar = 3 mm) of a cracked and healed SHCC segment: (a) the bottom left corner (scale bar = 300 µm), (b) a crack mouth (scale bar = 100 µm) and (c) a bacteria-embedded PLA particle (scale bar = 200 µm).

In the following sections, characterization of the crack healing will first focus on the crack mouths located at either left or right side of the specimens (marked as red squares, such as Fig. 3.5b). The extent to which healing occurred along crack depth will be determined by shifting the focus from the crack mouths to the middle of the specimen. Moreover, the microstructure of matrix that surrounds crack-passing PLA particles (marked as green squares, such as Fig. 3.5c) will be analysed to reveal the mechanism by which the PLA particles contribute to the healing of cracks.

3.3.2 Process of crack-healing over time

3.3.2.1 Short-term healing under controlled climate

Fig. 3.6 shows the BSE images taken at crack mouth from specimens amended with healing agent. These specimens were kept in a mist room after cracking and were incubated for various short durations (ranging from 1 week to 8 weeks). As can be seen, no trace of healing was observed after the 1st week, even for cracks as small as 7 µm. At the end of the 2nd week, precipitates began to form near crack mouths, preferably covering the entrance of the cracks instead of filling them. The precipitates formed presumably due to bacterial conversion of PLA-derived calcium lactate to calcium carbonate. At this moment, only cracks smaller than 20 µm were observed to experience certain degree of healing (Fig. 3.6d). Deposition of minerals around crack mouths of larger cracks were also observed; but these minerals mainly accumulated near the tips of crack walls instead of bridging over the crack (Fig. 3.6c). At the end of the 3rd week, the extent of crack healing was noted to progress considerably, with cracks as large as 80 μm being covered fully by precipitates (Fig. 3.6e). The size of the individual precipitate was also found to increase from roughly 20-30 μm at the end of the 2nd week to around 70-80 μm at the end of the 3rd week. The observation by now is in line with our understanding on the characteristic of the aerobic bacterial activity, which is that this biochemical reaction through which calcium lactate is converted to calcium carbonate depends on the availability of oxygen. Therefore, the precipitation of minerals should start at the locations where oxygen abounds.

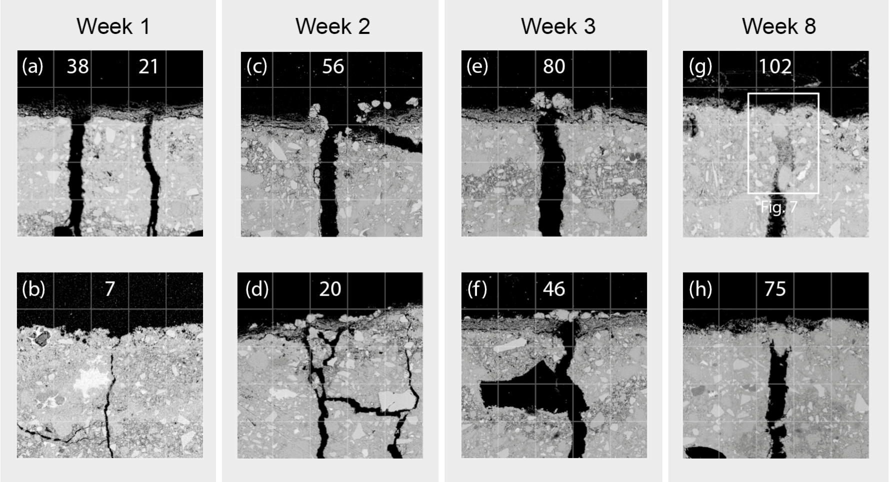

Figure 3.6: Progress of crack healing over time at crack mouth in specimens with healing agents. Each image captures a region of 500 μm × 500 μm. Grids are provided for easy estimation of crack width and precipitate size. Each cell in grids is 100 μm × 100 μm. The number in each figure is the crack width in the unit of micron.

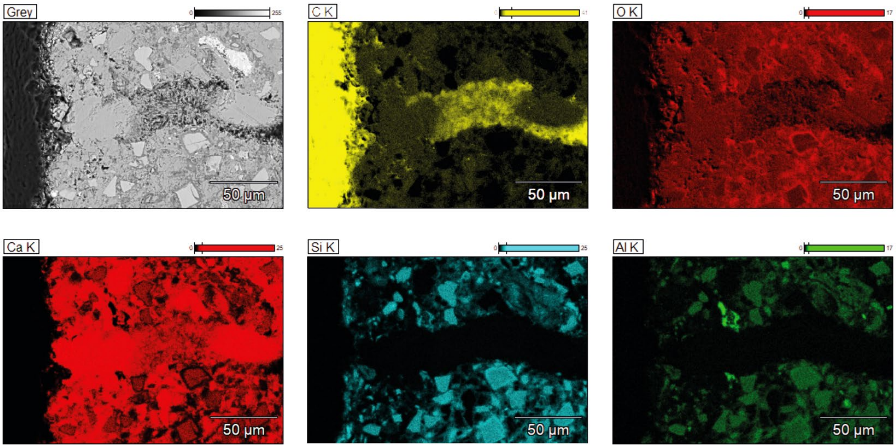

Figure 3.7: EDS elemental mappings of a healed crack mouth after 8 weeks of healing in mist room from a specimen with healing agents. The location of this mapping is marked in Fig. 3.6 as a white rectangle.

Significant changes were noticed after longer incubation duration (*i.e.*, 8 weeks). Not only even larger cracks were found to heal (Fig. 3.6g), but also the precipitates which were previously only grouping over crack mouths started to form inside the cracks. As showed by Fig. 3.7, EDS element mappings reveal that the formed precipitate inside the cracks was an association of calcium, oxygen and carbon elements, which suggests that mineral precipitates were indeed calcium carbonate based. Fig. 3.8 shows a comparison of the crack cross-sections after 3-week healing and 8-week healing (extended view of Fig. 3.6f and 3.6h). As can be seen, at the end of the 3rd week, the crack walls were still smooth and barely any crystals or healing products can be found inside the crack; on the contrary, the cracks after 8-week healing appeared to have crystals precipitated at both crack walls as deep as 1.5 mm inside the crack. EDS element mappings indicate that the precipitates were likely calcium carbonate, since no silicon, sulphur and aluminium were detected, which rules out the possibility of CSH, ettringite or AFm. The precipitates appeared to be a mixture of calcite and aragonite, displayed primarily as rhombohedra and needle in shape. To further investigate the morphology of the precipitates, a healed specimen without epoxy impregnation was opened through a crack to examine the crystals formed inside. Fig. 3.9a shows the BSE image of one crack surface with the bottom edge being the entrance of the crack. Fibres can also be found protruding out from the matrix. As can be seen, a large number of crystals can be found on the crack surface (Fig. 3.9b). Rhombohedral crystals with somewhat rounded edges and surface indentations of bacteria encased within the growing crystals (Fig. 3.9c) were observed closer to crack mouth. Further away from the crack entrance, needle-shape crystals were found to dominate (Fig. 3.9d). Similar to what was seen in Fig. 3.8, the depth to which the precipitates were found inside a crack was within 2 mm. It also appears that the size of crystals was larger when they were close to the crack mouth.

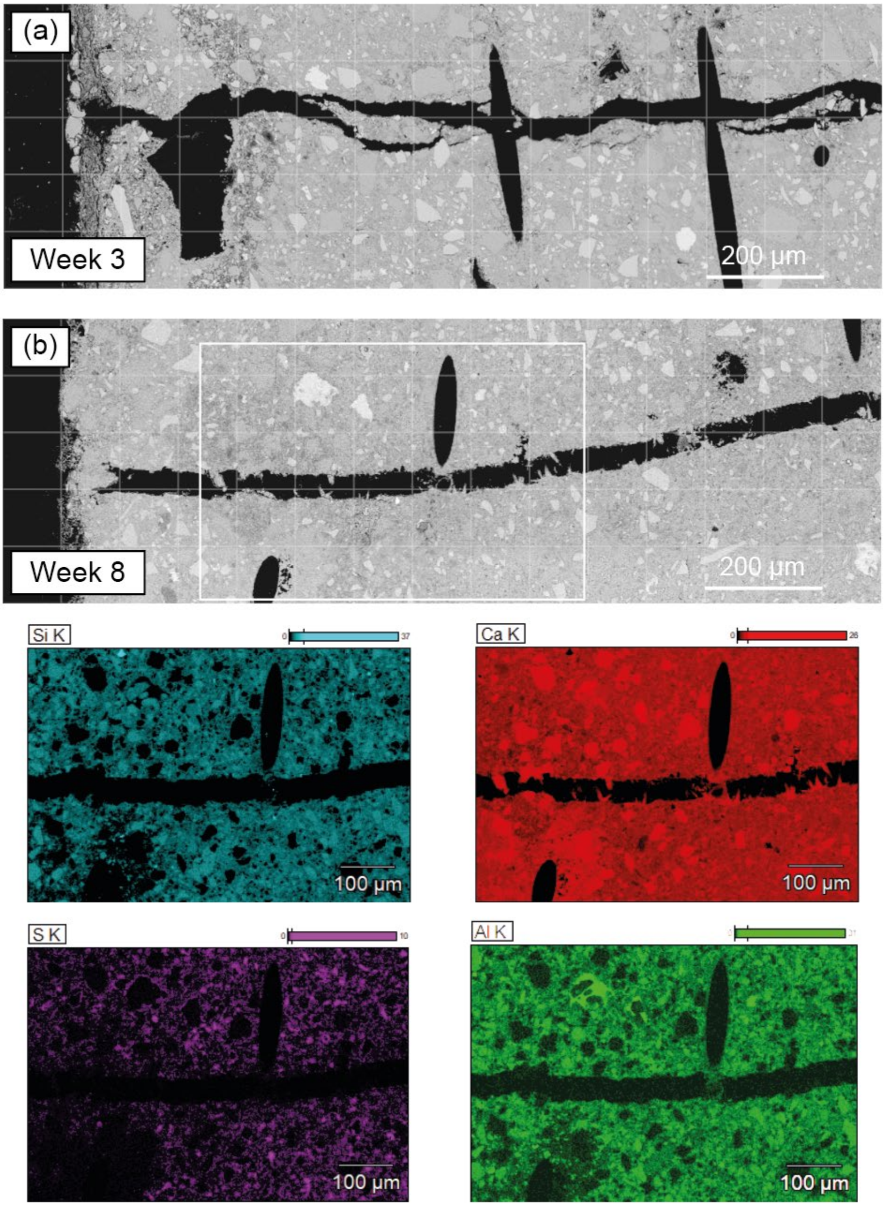

Figure. 3.8: Comparison of the depth of healing occurred inside a crack after a period of (a) 3 weeks and (b) 8 weeks in mist room for specimens with healing agent (width of field = 1.5 mm).

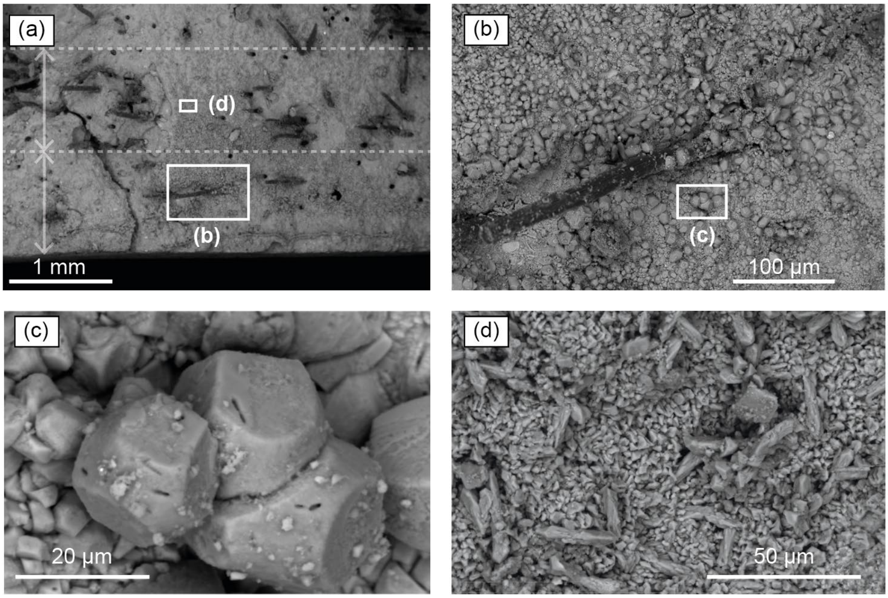

Figure 3.9: Morphology of precipitated healing products inside a crack after an 8-week-long healing.

The delayed formation of calcium carbonate inside a crack as compared to the calcium carbonate formed at crack mouth again highlights the importance of the availability of oxygen. Since bacteria and organic carbon are embedded inside the healing agent capsules, one would have expected that healing should occur first inside a crack, preferably close to a healing particle. However, as what has been shown by the BSE images, the formation of healing products inside a crack occurred several weeks later than the healing at crack mouth. The underlying cause may be attributed to a dual-factor phenomenon. Firstly, the initial oxygen content inside a crack is limited due to the fact that the oxygen can only be supplied via cracks and that the slag containing cement-based matrix itself also consumes oxygen when a crack forms. This is because that the formation of metal sulphides such as FeS and MnS during hydration under anoxic conditions will also react with oxygen whenever oxygen becomes available, through which the S^{2-} ions are oxidized into $S_2O_3{}^{2-}$ (intermediate) and $SO_4{}^{2-}$ (stable) ions [7]. Secondly, the formation of the calcium carbonate at the crack mouth will inevitably block the ingress of oxygen, which further limits oxygen availability in cracks and decreases the rate of calcium carbonate precipitation.

Figs. 10 and 11 document the autogenous crack healing process of the reference SHCC specimens without healing agent. As can be seen, evident crack closure occurred after a period of 3 weeks in a humid environment. Similar to the bacteria-enabled healing process, healing products started to precipitate from the two sides of a crack mouth and then gradually bridged over the crack mouth by accumulating more crystals. At the end of the 8th week, cracks around 100 microns wide were observed to heal completely. The healing product is expected to be also calcium carbonate but was formed due to carbonation with the carbon dioxide from the environment. By comparing Fig. 3.10 and Fig. 3.6, it can be seen that autogenous healing happens slower than the bacteria-enabled healing. The size of the crystals formed due to autogenous healing also appear to be smaller than the crystals formed in bacterial samples. Crack width was found to be a controlling factor for both autogenous and bacteria-enabled healing, as smaller cracks always healed faster than larger ones. However, crack width does not seem to influence the size and the morphology of the precipitated crystals. Another distinction between the two types of healing is the healing condition inside the crack. Unlike the specimens with healing agent (Fig. 3.8), no crystals can be observed inside a crack in specimens without healing agent (Fig. 3.12). This agrees with previous study which utilized X-ray computed microtomography to study autogenous healing of cementitious material [8]. It was found that, even under the condition of wet–dry cycles, the crack is closed by calcium carbonate formation only near the crack mouth.

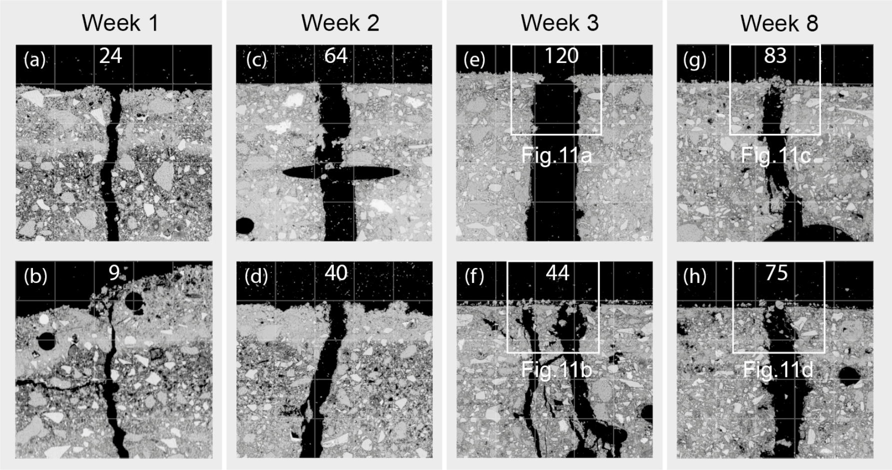

Figure 3.10: Process of autogenous crack healing at crack mouth in refence specimens without healing agents. Each image captures a region of 500 µm × 500 µm. The number in each figure is the crack width in the unit of micron.

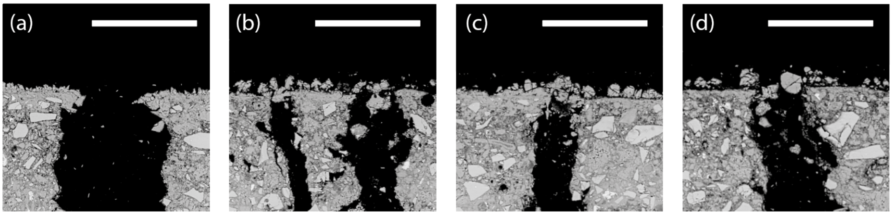

Figure 3.11: Zoom-in views of autogenous healing at crack mouth of reference specimens at (a-b) week 3 and (c-d) week 8 (scale bar = 100 µm).

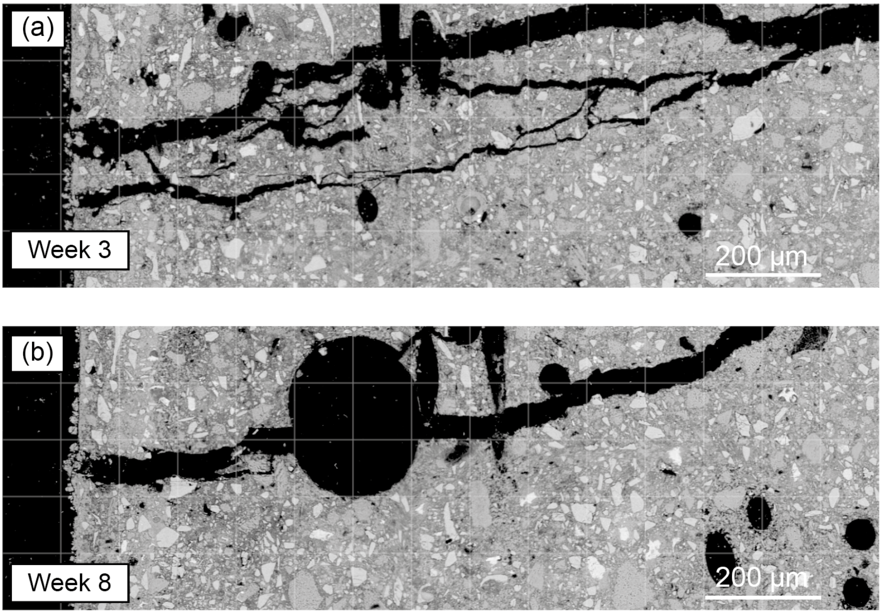

Figure 3.12: Comparison of the autogenous healing occurred inside a crack after a period of (a) 3 weeks and (b) 8 weeks in mist room for the reference specimens without healing agent (width of field = 1.5 mm).

3.3.2.2 Long-term healing under natural exposure

Fig. 3.13 shows the microstructure of a specimen with healing agent after one year exposure in an unsheltered outdoor environment. As can be seen, the distribution of healing products in Fig. 3.13 is essentially different than in specimens that have undergone short-term healing. While the most obvious crack closure happened close to crack mouth after short-term healing, the precipitation of healing products after a long-term healing is found to occur predominantly near a healing particle. As can be seen from the BSE image, epoxy filled cracks gradually disappeared when approaching a healing agent particle. If the healing process can only result in the relocation of calcium element, the microstructure of an area before and after the precipitation of calcium carbonate can then be compared by assessing the silicon mapping and the calcium mapping. From the silicon mapping, it can be seen that the original boundary of the healing agent was smooth and that several cracks passed through the healing agent; and the calcium mapping revealed that the outer layer of the particle was consumed and converted to a calcium-rich rim, resulting in a rough boundary of healing agent. Also, the cracks which were originally passing through the particles were filled and even air voids were partially filled by the precipitates. This microstructural change indicates that, after one year of outdoor exposure, oxygen seems to have entered so deep that there is enough oxygen for the bacteria around a particle to become active. The availability of oxygen is thus no longer governing the metabolic activities of the bacteria in this case. In addition, it can also be found that no healing products can be seen at crack mouth. Since the specimens were placed outdoor for a whole year in a climate where temperature can drop below freezing point in winter, it is possible that the environmental actions such as rainfall and freeze and thaw cycles may have worn away the healing products at the crack mouth [5] and thus led to a deeper ingress of oxygen into cracks, which promoted the bacteria to precipitate preferably near a healing agent.

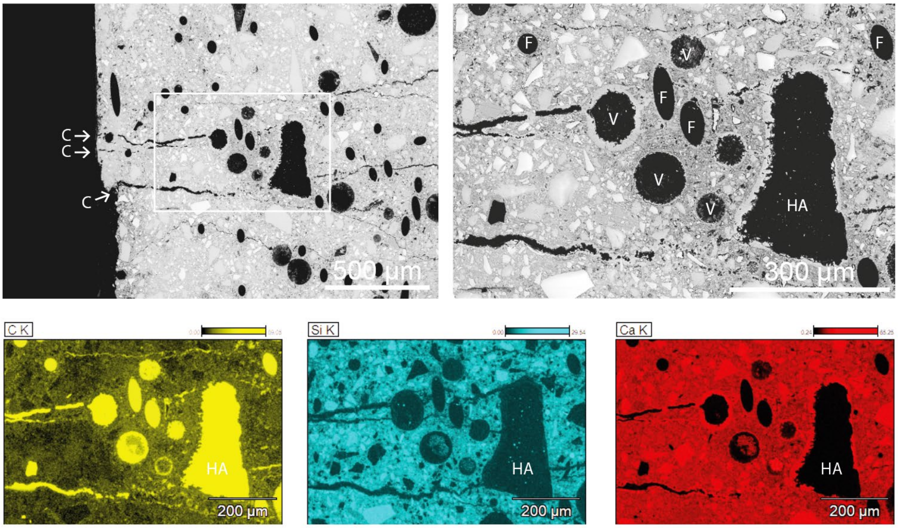

Figure 3.13: BSE images and EDS mappings of a specimen with healing agents after 1-year outdoor exposure. (Abbreviation: C – crack; F – fibre; V – void; HA – healing agent).

Fig. 3.14 shows BSE images of 2 different locations in the bacterial specimens after long-term healing, both of which show evident healing along the crack walls extending several millimetres deep inside the cracks. As the thickness of the specimen is 13 mm, the observed 6-mm-deep healing from one side of the specimen means that the entire crack path has undergone certain degree of healing. By comparing the silicon mapping and calcium mapping, it can be seen that the precipitated calcium carbonates have filled the small cracks, and partially filled larger ones and even some voids. It is also interesting to notice that all the healing agent particles which were activated by cracks had the outer layer converted into calcium carbonate, which may have restricted the further hydrolysis of the PLA and thus limited the discharge of bacterial spores. This self-limiting feature can have both negative and positive consequences. At one hand, it will certainly impede the pace of crack-healing by limiting the amount of spores and nutrients released by each particle. On the other hand, the preservation of certain portion of the particle can produce a repeated healing, when the material is damaged again. Therefore, the particle size of healing agent can be an important factor and should be designed according to the expected crack width and the specific working condition.

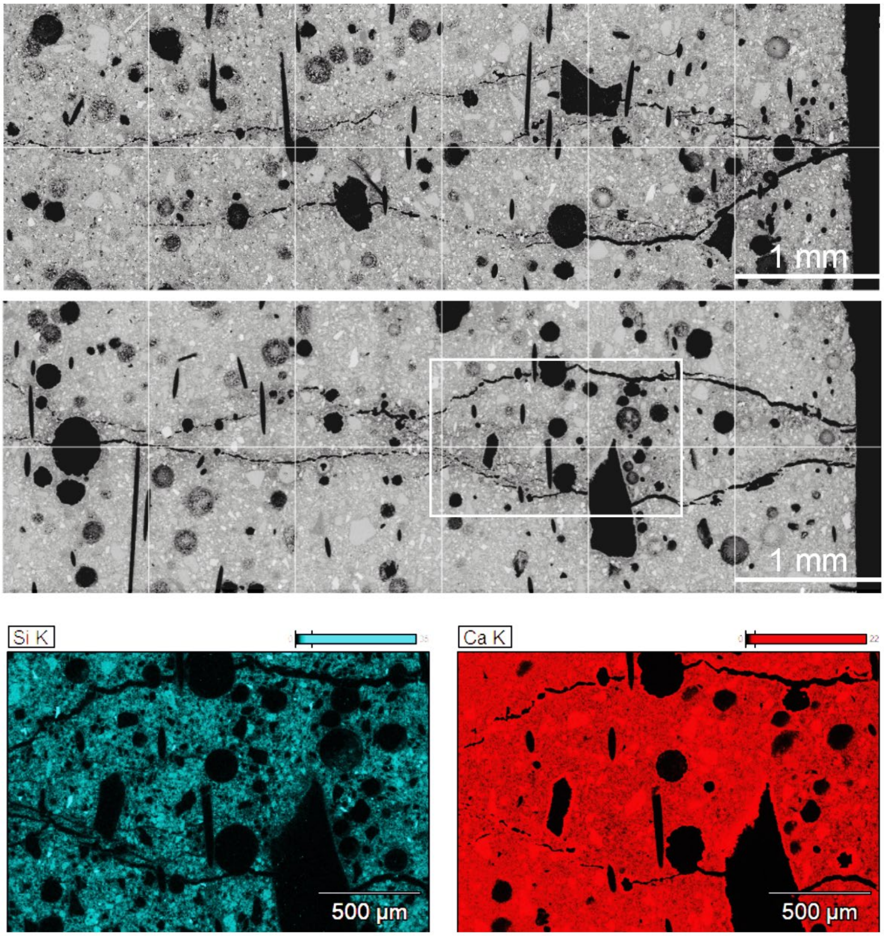

Figure 3.14: BSE images of 2 different locations in a specimen with healing agents after 1-year outdoor exposure showing evident healing along crack depth (width of field = 6 mm).

Fig. 3.15a shows the microstructure of a reference specimen after 1-year autogenous healing. The autogenous healing capacity of SHCC is evident from the observed crack closure near the crack exit on both the smaller and larger cracks. Similar to the specimens with healing agent, no precipitates were observed at the crack mouth. This may also because of the environmental effects acting upon the healing products. However, a key difference between autogenous and autonomous healing is the depth to which the crack can be healed. In the bacterial specimen (Fig. 3.14), precipitation of calcium carbonate along the crack walls was clearly visible, while obvious narrowing of cracks due to calcium carbonate precipitation occurred only within 0.5 mm deep in the reference specimen (Fig. 3.15b). This may be because even if the precipitates at the crack mouth were gone, the ingress of carbon dioxide would still be blocked by the calcium carbonate formed slightly deeper in the cracks, as long as this affected zone is within the carbonation front. Consequently, the availability of carbon dioxide for autogenous healing was still limited, resulting in only a very thin layer of calcium-rich precipitates along the crack walls, as shown in Fig. 3.15c (processed calcium mapping depicting only high-intensity calcium signals).

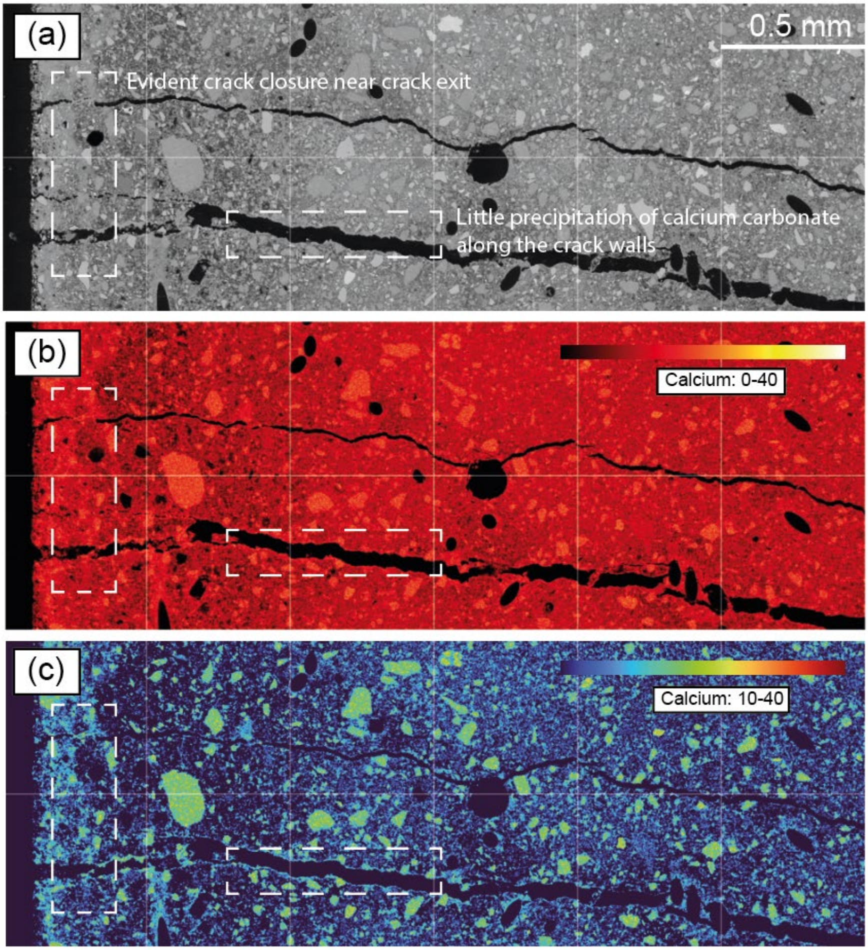

Figure 3.15: (a) BSE image of a reference specimen without healing agents after 1-year outdoor exposure showing limited healing along crack walls (width of field = 6 mm) and (b) EDS mapping of calcium element and (c) processed calcium mapping showing only locations where high intensity calcium signal was detected.

By comparing the extend of healing observed in specimens with and without healing agent, it can be concluded that the use of aerobic bacteria is highly beneficial in terms of crack healing. The bacteria have changed the governing factor for the formation of calcium carbonate from the availability of carbon dioxide to the availability of oxygen. And since oxygen diffuses more easily in concrete than carbon dioxide [8], this change of limiting factor increases the likelihood of calcium carbonate precipitation in deeper cracks. Moreover, the metabolic activities of aerobic bacteria also produce carbon dioxide, which can react with calcium hydroxide minerals in locations that are not accessible to carbon dioxide from the outside atmosphere.

Another conclusion that can be drawn from this study is that relying solely on the observation of the crack mouth to evaluate crack sealing or healing may not be a reliable method. This is evident from the BSE images of the crack cross-sections, which show that a complete closure of the crack mouth can occur even when there is essentially no healing occurring inside the crack. Conversely, the absence of healing products at the crack mouth does not necessarily indicate a lack of healing inside the crack.

3.3.3 Behaviour of bacteria-embedded PLA capsules in cement-based matrix

In the development of all types of self-healing concrete, it is important to ensure that the healing agent does not affect too much the properties of concrete and at the same time can still function as intended to promote self-healing. The PLA capsule adopted in the current study functions through hydrolysis of the PLA to release bacteria when water enters a crack. However, the presence of water during concrete mixing is expected to trigger the hydrolytic degradation of PLA already from the start. Depolymerization via hydrolysis leads to the formation of lactic acid, which consumes some alkalinity in concrete close to the PLA capsule. It is therefore necessary to verify if PLA particles can modify the microstructure of cement-based matrix surrounding it.

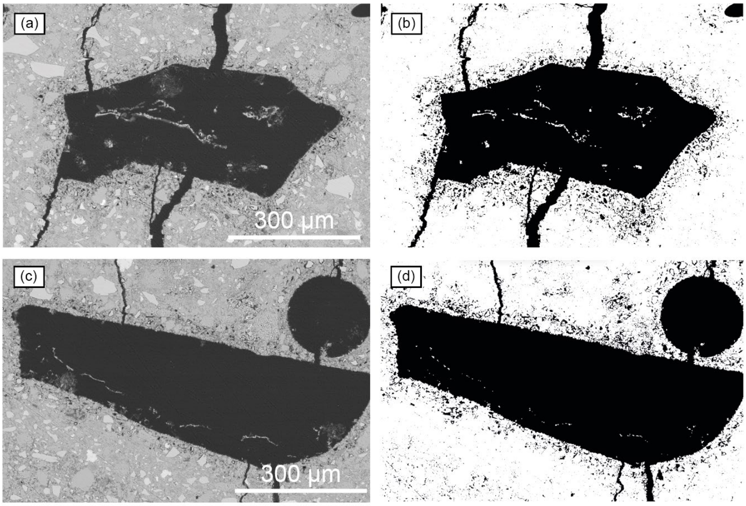

Figure 3.16: BSE images of crack-bridging PLA particles after a period of 1 week in mist room as well as their respective binary images highlighting porosity after grayscale segmentation.

Fig. 3.16 shows the BSE images of two PLA particles embedded in the specimens at a very early stage after cracking (*i.e.*, at the end of the 1st week). As can be seen, a porous zone can indeed be noticed surrounding the particles. The thickness of this zone is around 50 microns, which is the typical thickness of the interfacial transition zone (ITZ) between a bigger inclusion and cement-based matrix [9,10]. In fact, similar porous zone can also be seen around the circular air void at the top right corner of Figs. 16c and 16d, which suggests that the influence of the PLA to its surrounding matrix is only minor, and that the hydrolytic degradation of PLA may have only happened to a very limited extent. Conversely, the hydrolysis of PLA during the self-healing process is quite noticeable. As shown by Fig. 3.17, 3 weeks in a mist room has led to the formation of a calcium-rich rim around the particle. It is likely that the reaction between the lactic acid and the calcium hydroxide in the matrix has led to the formation of calcium lactate, which might have been metabolically converted into calcium carbonate and filled the cracks next the particle. At this moment, the ITZ between the particle and the cement-based matrix also appeared to be less porous, probably also due to the precipitated calcium carbonate. Fig. 3.18 shows the typical appearance of a PLA particle inside a crack after 8 weeks of healing. By comparing the silicon mapping and the calcium mapping, it can be seen that almost 1/3 of the particle has now been consumed and converted into calcium rich precipitates either around the particle or close to the crack mouth. The porous zone surrounding the particle is also no longer visible. It is thus concluded that the bacteria-embedded healing particles can indeed function as intended to promote self-healing, while posing no threat to the concrete properties.

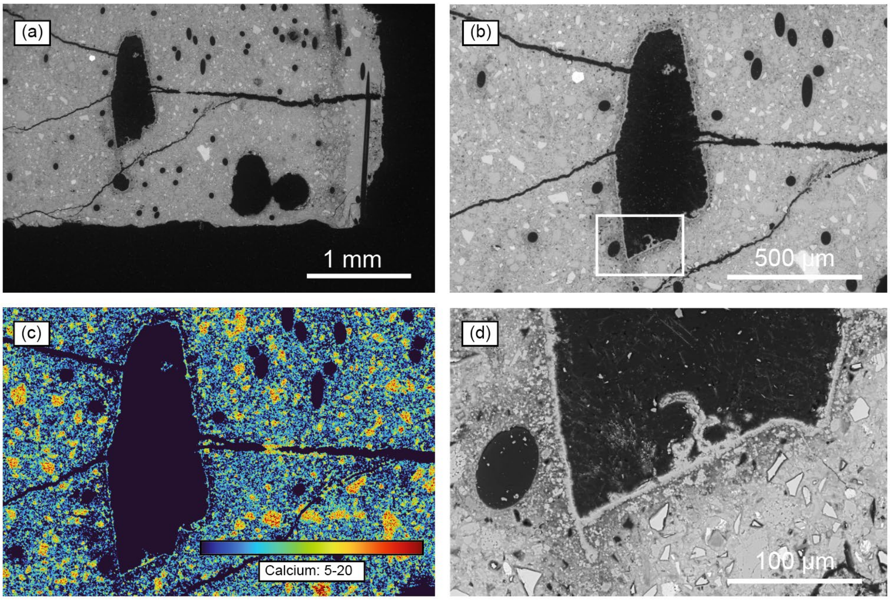

Figure. 3.17: BSE images of a crack-bridging PLA particle after a period of 3 weeks in mist room as well as its EDS calcium mapping.

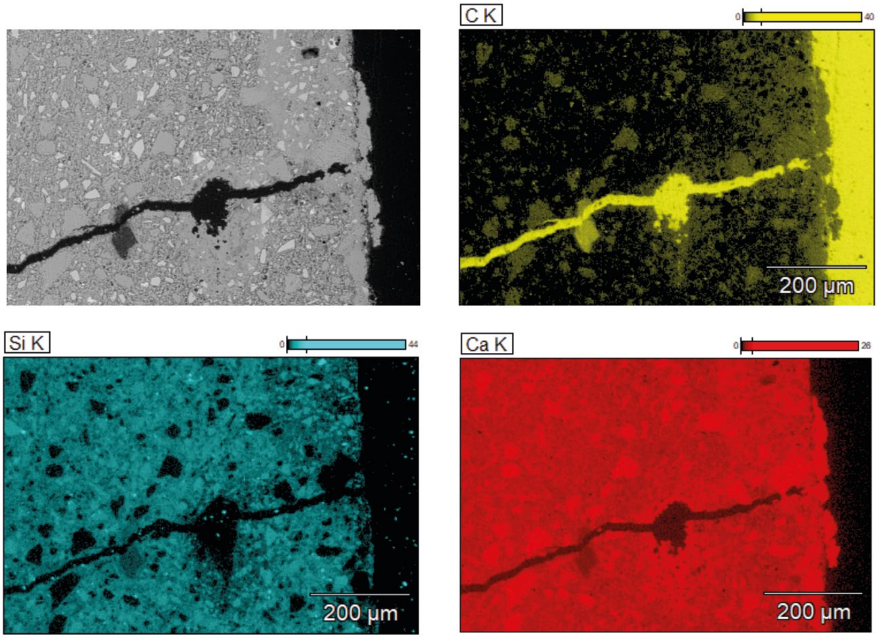

Figure 3.18: BSE image and EDS mappings of a crack-bridging PLA particle after 8 weeks in mist room.

3.4 Conclusions

An experimental study was carried out to characterize the bacteria-enabled crack-healing behaviour of mortar by BSE and EDS. Healing under both short-term ideal condition and long-term realistic condition were investigated. Unlike previous studies which usually quantify healing by examining the formation of healing products at crack mouth, the current study documented the process of both autogenous and autonomous healing process along crack depth. The behaviour of individual PLA capsules during the healing process was also studied. The main findings of the current study are:

1. Apparent crack healing enabled by bacteria began after 2 weeks in a humid environment. The healing products initially precipitated at the crack mouth and gradually moved deeper into the cracks, with the precipitated crystals growing larger over time. After a period of 8 weeks, cracks as wide as 100 microns were fully filled with healing products at the crack mouth. Healing products were also found to form a few millimetres deep inside the crack.
2. Autogenous healing happened slower than the bacteria-enabled healing. Only after the end of the 3rd week, healing products started to precipitate from the two sides of a crack mouth and then gradually bridged over the crack mouth by accumulating more crystals. Despite a slower speed, cracks of 100 microns wide were also observed to heal completely at the end of the 8th week. However, hydration products were only found at crack mouth, leaving the crack depth largely unhealed.
3. Long-term crack healing in realistic environment was observed to differ from healing under short-term controlled conditions. Specimens with healing agent were found to have no healing products formed at the crack mouth but a high degree of healing through the

entire crack depth. It is likely that the environmental actions such as rainfall and freeze and thaw cycles may have worn away the healing products at the crack mouth and thus led to a deeper ingress of oxygen into cracks, which promoted the aerobic metabolic activity of the bacteria inside the cracks.

4. Autogenous healing after long-term outdoor exposure was found to possess similar characteristics, with the depth of healing increased and a loss of healing products at surface. However, the depth to which a crack can heal because of autogenous healing is significantly less than bacterial healing, which is probably due the limited ingress of carbon dioxide inside the cracks.
5. The cement-based matrix surrounding a healing particle was found to be porous. However, this porous zone appeared to be similar to the ITZ commonly formed between the matrix and big inclusions such as fibres and aggregates, which suggests that the hydrolytic degradation of PLA may have only happened to a very limited extent during concrete mixing and hardening.
6. During to the healing process, the PLA particles were found to be consumed and converted into calcium-rich precipitates, potentially calcium carbonate. The formed calcium carbonate can not only heal the cracks but also densify the matrix surrounding the healing agents.
7. Relying solely on the observation of the crack mouth to evaluate crack sealing or healing may not be a reliable method. This is evident from the BSE images of the crack cross-sections, which show that a complete closure of the crack mouth can occur even when there is essentially no healing occurring inside the crack. Conversely, the absence of healing products at the crack mouth does not necessarily indicate a lack of healing inside the crack.

References

[1] K. Sisomphon, O. Copuroglu, E.A.B. Koenders, Self-healing of surface cracks in mortars with expansive additive and crystalline additive, Cem Concr Compos 34 (2012) 566–574. https://doi.org/10.1016/J.CEMCONCOMP.2012.01.005.

[2] R. Roy, E. Rossi, J. Silfwerbrand, H. Jonkers, Self-healing capacity of mortars with added-in bio-plastic bacteria-based agents: Characterization and quantification through micro-scale techniques, Constr Build Mater 297 (2021) 123793. https://doi.org/10.1016/J.CONBUILDMAT.2021.123793.

[3] E. Rossi, R. Roy, O. Copuroglu, H.M. Jonkers, Influence of self-healing induced by polylactic-acid and alkanoates-derivates precursors on transport properties and chloride penetration resistance of sound and cracked mortar specimens, Constr Build Mater 319 (2022) 126081. https://doi.org/10.1016/J.CONBUILDMAT.2021.126081.

[4] V.G. Cappellesso, T. Van Mullem, E. Gruyaert, K. Van Tittelboom, N. De Belie, Bacteria-based self-healing concrete exposed to frost salt scaling, Cem Concr Compos 139 (2023) 105016. https://doi.org/10.1016/J.CEMCONCOMP.2023.105016.

[5] V. Cappellesso, D. di Summa, P. Pourhaji, N. Prabhu Kannikachalam, K. Dabral, L. Ferrara, M. Cruz Alonso, E. Camacho, E. Gruyaert, N. De Belie, A review of the efficiency of self-healing concrete technologies for durable and sustainable concrete under realistic conditions, International Materials Reviews (2023) 1–48. https://doi.org/10.1080/09506608.2022.2145747.

[6] D. Le Cornec, Q. Wang, L. Galoisy, G. Renaudin, L. Izoret, G. Calas, Greening effect in slag cement materials, Cem Concr Compos 84 (2017) 93–98. https://doi.org/10.1016/J.CEMCONCOMP.2017.08.017.

[7] D. Snoeck, J. Dewanckele, V. Cnudde, N. De Belie, X-ray computed microtomography to study autogenous healing of cementitious materials promoted by superabsorbent polymers, Cem Concr Compos 65 (2016) 83–93. https://doi.org/10.1016/J.CEMCONCOMP.2015.10.016.

[8] Y.F. Houst, F.H. Wittmann, Influence of porosity and water content on the diffusivity of CO2 and O2 through hydrated cement paste, Cem Concr Res 24 (1994) 1165–1176. https://doi.org/10.1016/0008-8846(94)90040-X.

[9] K.L. Scrivener, A.K. Crumbie, P. Laugesen, The Interfacial Transition Zone (ITZ) Between Cement Paste and Aggregate in Concrete, Interface Science 2004 12:4 12 (2004) 411–421. https://doi.org/10.1023/B:INTS.0000042339.92990.4C.

[10] S. He, Z. Li, E.-H. Yang, Quantitative characterization of anisotropic properties of the interfacial transition zone (ITZ) between microfiber and cement paste, Cem Concr Res 122 (2019) 136–146. https://doi.org/10.1016/j.cemconres.2019.05.007.

4

Hybrid reinforced concrete (RC) beams with a thin layer of SHCC in their cover zones for crack width control[3]

This chapter delves into the creation of hybrid beams that incorporate a thin layer of SHCC in the bottom cover zone. The primary focus is on identifying the optimal interface condition that fosters favourable crack patterns conducive to healing, though the healing process itself is not explored here. The chapter provides a comprehensive analysis of the flexural behaviour of hybrid beams in terms of its structural performance and crack development, employing a combination of experimental and simulation approaches. A novel type of SHCC/concrete interface that features a weakened chemical adhesion, but an enhanced mechanical interlock bonding was developed to facilitate the activation of SHCC. Results show that hybrid beams possessed similar load bearing capacity but exhibited a significantly improved cracking behaviour as compared to the reference beam without SHCC. With a 1-cm-thick layer of SHCC, the maximum crack width of the best performing hybrid beam exceeded 0.3 mm at 53.3 kN load, whereas in the control beam the largest crack exceeded 0.3 mm at only 32.5 kN load. The hybrid beam with the proposed new interface formed 10 times more cracks in SHCC than a hybrid beam with a smooth interface and had an average crack width less than 0.1 mm before failure. The simulation result from lattice model suggests that, while the mechanical interlocking is provided, a weak interface bond can indeed promote the controlled cracking behaviour of SHCC and thus results in a delayed development of maximum crack width. As the volume ratio of SHCC used in the hybrid beams is only 6%, the current study highlights the strategic use of minimum amount of SHCC in the critical region to efficiently enhance the performance of hybrid structures.

---

[3] Part of this chapter has been published in:

He, S., Mustafa, S., Chang, Z., Liang, M., Schlangen, E., & Luković, M. (2023). Ultra-thin Strain Hardening Cementitious Composite (SHCC) layer in reinforced concrete cover zone for crack width control. Engineering Structures, 292, 116584.

4.1 Introduction

As discussed in previous chapters, the multiple microcracking and strain-hardening behaviour of SHCC provides an effective crack-control strategy without using excessive reinforcement [1,2]. While SHCC presents promise for enhancing resilience and durability, its high material cost limits complete replacement of reinforced concrete (RC), making localized application a potential solution.

To investigate the possibility of combining SHCC and conventional concrete, various studies have developed hybrid systems using SHCC and RC for different structural members. These include the use of SHCC on the tension side for flexural strengthening [3–5], or as a permanent formwork by pre-casting SHCC for the strengthening of both shear and flexural resistance [6]. SHCC has also been applied to produce composite slab for improved crack width control under flexural loads [7]. In a very recent study, the crack width control ability of SHCC/RC hybrid beams is investigated [8]. The study adopted a 7-cm-thick layer of SHCC in the tensile zone of a 20-cm-high beam with reinforcement embedded in the SHCC and confirmed that the use of SHCC can sufficiently reduce crack width, thereby rendering the reinforcement design independent of the SLS criterion. However, the amount of SHCC used in this hybrid system is still relatively large, comprising 35% of the whole beam by volume. Given that the material cost of SHCC is roughly 3 times of the cost of reinforced concrete [9], a 35% concrete replacement ratio by SHCC will incur a significant amount of additional cost. For the other related research, the replacement ratio of the SHCC is even higher than 35% and can sometimes go to more than 50%, which is even less economically attractive. It is, therefore, desirable to investigate the effectiveness of a SHCC/RC hybrid system with much reduced thickness of SHCC layer.

Therefore, in the present investigation, a combined experimental and numerical study was carried out to investigate the cracking behaviour of reinforced concrete beams consisting of a very thin layer (*i.e.*, 1 cm in thickness) of SHCC in the concrete cover zone. A particular attention was paid to the design of the interface between the SHCC and the concrete. This is because the preservation of structural integrity and the activation of SHCC have conflicting demand on the properties of the interface. While a strong interface is usually preferred to prevent delamination between the two layers, the formation of multiple cracks in SHCC favours a certain degree of laterally unrestrained deformation, which often demands a weak interface [10,11]. To balance this conflicting demand, a new type of interface which consists of a pattern of protruding teeth (shear-keys) from the SHCC and a surface treatment with Vaseline was thus developed (Fig. 4.1). The idea behind is that the presence of the shear-keys can provide sufficient mechanical interlocking and thus ensures the overall structural integrity of the hybrid beams, while the Vaseline treatment can make sure that, locally, the SHCC material in between 2 lines of shear-key can deform freely with respect to the concrete above it. In this way, a new interface condition which allows a controlled extent of partial delamination between the two layers can be achieved. For comparison purposes, interfaces with only the shear-key pattern but not the Vaseline treatment, as well as a smooth interface without any modification, were also made and applied to produce hybrid beams. The three hybrid SHCC/concrete beams with different interfaces were then tested and compared with a control reinforced concrete beam without SHCC. The beams were tested in four-point bending configuration, while Digital Image Correlation (DIC) was used to monitor the development of crack pattern and crack width. Furthermore, a fracture model (*i.e.*, a discrete type of lattice model [12]) was also used to acquire insight into the influence of the interface strength on the crack width and crack pattern of the hybrid beam and to provide insights in how to further optimize the interface and thereby the behaviour of the hybrid system.

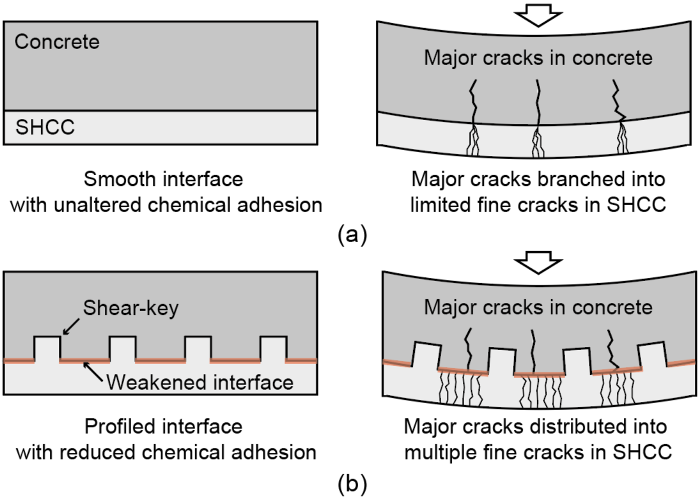

Figure 4.1: Schematic illustration of (a) the smooth interface and (b) the proposed new interface with strong mechanical bond but weak chemical adhesion.

4.2 Materials and tests

4.2.1 Experimental design

The test program consists of four 1.9-meter-long beams, including one conventional reinforced concrete beam as a reference specimen and three hybrid beams consisting of a 1-cm-thick SHCC layer in the tensile zone. The geometry and reinforcement details of the beams are given in Fig. 4.2. One hybrid beam has a smooth interface between SHCC and reinforced concrete, while the other two hybrid beams have a profiled interface, which is made of a pattern of protruding teeth (shear-key) from the SHCC layer. The interface pattern consists of equally sized and evenly spaced cylindrical keys, which have a diameter of 2.5 cm and a height of 1 cm. The clear distance between 2 adjacent keys is 2.5 cm, which is selected such that the largest aggregate in the concrete can fill into the gap. The shear-keys are designed to provide adequate mechanical interlocking between the SHCC and the concrete layers so to ensure the structural integrity of the hybrid system. The image at the bottom of Fig. 4.2 shows the design of the shear-key pattern. Furthermore, within the two hybrid beams having profiled interface, one beam has a purposely weakened interfacial bond, which is realized by applying a thin layer of liquid Vaseline on the profiled side of the SHCC laminate. This treatment is to reduce the chemical adhesion between SHCC and concrete and to promote local debonding. The aim for combining the Vaseline treatment and the shear-key profile is to fully utilize the tensile strain capacity of the SHCC by allowing a controlled degree of differential deformation between the SHCC and the concrete, as schematically illustrated by Fig. 4.1. In the following text, the reference beam is referred as Ref and the hybrid beams with smooth interface, profiled interface and Vaseline treated profiled interface are referred as Smooth, Profile and Vaseline, respectively.

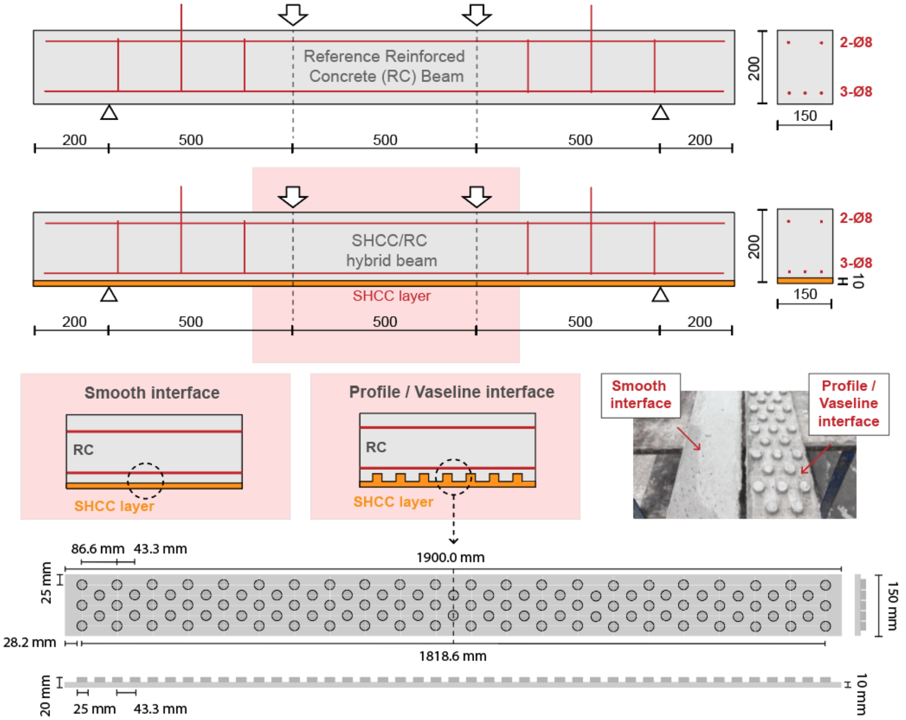

Figure 4.2: Geometries and reinforcement details of the reference beam and the hybrid beams with different interface types. All dimensions are in mm.

The geometry of the beams was adopted from previous studies [4,8]. The beams are 1900 mm long, 150 mm wide and 200 mm high. For the hybrid beams, the bottom 10 mm of concrete is replaced by SHCC. The reason why the hybrid beams in the current study only have the SHCC layer in the bottom cover is for easy examination of the different crack patterns in SHCC and in concrete. Cracks on the front and back sides of the beams are not considered to govern the durability, because the SHCC layer will eventually be applied in the entire cover zone of the beam for an all-around protection. All the beams have the same reinforcement configuration with 3 Φ8 ribbed rebars at the bottom and 2 Φ8 ribbed rebars at the top (as shown in Fig. 4.2). To allow the development of cracks in the constant moment region, the percentage of longitudinal reinforcement was kept low (0.61%). The stirrups of Φ8@150 are provided in the shear span to ensure that the beams fail in flexure. The central stirrup on both sides is extended upward for easy handling of the beams.

4.2.2 Materials and sample preparation

Table 4.1 presents the mixture compositions of SHCC and concrete utilized in this chapter. The design philosophy and constituents of SHCC have been elaborated upon in Chapters 2 and 3. Furthermore, the preparation procedure of SHCC, along with the methods employed for its mechanical performance testing, are addressed in preceding chapters. The same procedure is used herein.

Table 4.1: Mixture compositions of SHCC and concrete [unit in kg/m3].

Material	SHCC	Concrete
CEM I 52.5 R	-	260
CEM III/B 42.5 N	1060	-
Limestone powder	530	-
Sand (0.125-4 mm)	-	847
Gravel (4-16 mm)	-	1123
PVA fibre	26	-
Water	424	156
Superplasticizer	2.00	0.26

All the hybrid beams were casted in 2 steps. In the first step, SHCC laminates were casted vertically by using a plywood mould (Fig. 4.3a) having pockets/slots with an opening of 10 mm. As comparing to casting the SHCC laminates in the lie-flat manner, casting a thin laminate vertically allows a more precise control on the thickness of the laminate, which is vital to the current study. The SHCC laminates with shear-keys were prepared by a similar mould but with an opening of 20 mm (Fig. 4.3b). The 20-mm-thick slot contains a 10-mm-thick silicon rubber glued to one side wall having a reverse shape of the desired shear-key pattern (Fig. 4.3c). By casting the SHCC into the remaining gap, the fresh material will fill into the holes of the rubber sheet and then form the resulting protruding keys as shown by Fig. 4.3d. All the laminates were cured for 14 days in a climate room (20◦C and ≥98% RH) before casting of concrete. In the second step, SHCC laminates were taken out from the climate room and placed into plywood mould. On top of the SHCC laminates, reinforcement cages were placed with appropriate spacers. After the preparation, the concrete was cast and compacted using a vibration needle. The hybrid beams were then cured for 28 days in sealed conditions before testing. The reference reinforced concrete beam was cast along with this second phase.

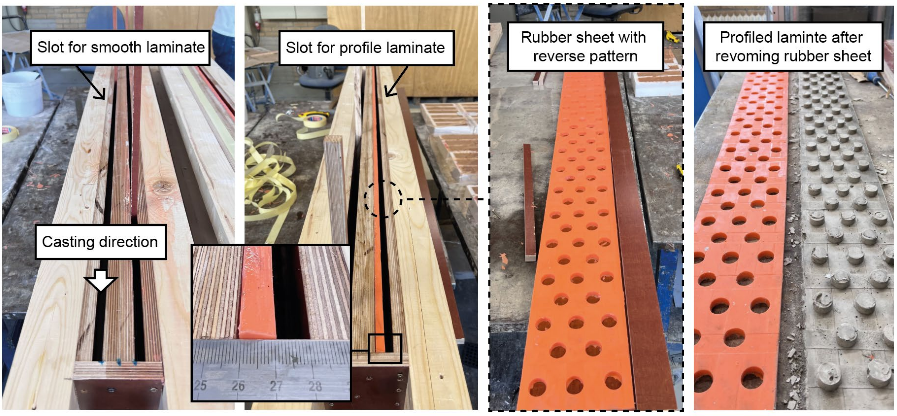

(a) (b) (c) (d)

Figure 4.3: Wooden mould for the preparation of (a) SHCC laminate with smooth surface and (b)-(c) SHCC laminate with a profiled surface, as well as (d) a SHCC laminate.

4.2.3 Testing

All the beams were tested in a four-point bending test setup (Fig. 4.4a) under displacement control at a rate of 0.01 mm/s. The deformation of the beams was monitored within the constant bending moment region by using Digital Image Correlation (DIC) from both sides, while the relative vertical mid-point deflection of the beams with reference to the supports was measured by a Linear Variable Differential Transformer (LVDT). DIC is a measurement technique that processes pictures taken from cameras to track and record the surface motion of a deforming solid. The regions of the beam for DIC measurement were first painted in white and sprayed with a black speckle pattern by using an air gun. Images for DIC were captured throughout the loading at 10-second intervals at a resolution of 0.08 mm/pixel. Post-processing of DIC results was carried out with a free version of GOM Correlate software.

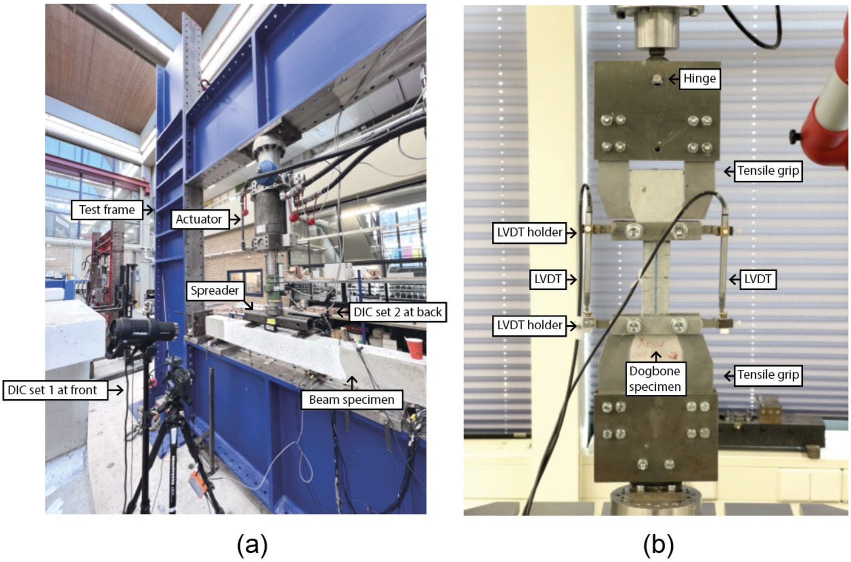

Figure 4.4: Experimental set-up for (a) four-point-bending test of beam specimens with DIC measurement on both sides and (b) uniaxial tensile test of SHCC dog-bone specimens.

The compressive strength of the SHCC was measured in accordance with NEN EN 196-1 [13] by using 40 mm × 40 mm × 40 mm cube specimens cut from prism specimens. Uniaxial tension tests were performed by using a servo-hydraulic testing machine (Instron® 8872) under displacement control at a rate of 0.005 mm/s. Dog-bone shaped specimens recommended by the Japan Society of Civil Engineers (JSCE) [14]with a cross-section of 13 mm × 30 mm at the test zone were adopted. During tests, the specimens were placed inside of a pair of tensile grips and then slightly pre-stressed before testing. The deformations were measured with a gauge length of 80 mm with two LVDTs fixed on both sides of the specimens as shown by Fig. 4.4b. Tests were stopped after the tensile load dropped to less than 50% of the maximum load. The maximum tensile stress experienced by the specimen during this experiment is called the ultimate tensile strength (σ_{ult}), and the strain value when the load drops to 90% of the ultimate value is taken as the tensile strain capacity (ε_{ult}). Four samples were tested for the determination of the tensile properties of SHCC. The average and the standard deviation of the results are reported.

4.3 Experimental results

4.3.1 Material properties

Fig. 4.5 shows the typical tensile stress-strain curves of SHCC dog-bones cured comparably to the SHCC laminates in the hybrid beams. The tensile testing process of SHCC consists of three phases. In the first phase, the material undergoes a linear elastic phase, with a slope equal to its elastic modulus. In the second phase, cracks begin to successively form while load continues to increase. This phase is characterized by the sequential formation of multiple parallel cracks, which results in temporary load drops and contributes to the inelastic deformation. The final phase is marked by the occurrence of the final fracture, which signals the exhaustion of the fibre-bridging capacity of the composite and defines its ultimate strength. As can be seen, the mixture exhibited pronounced tensile strain hardening behaviour with the formation of multiple fine cracks as shown by the inset of Fig. 4.5. Table 4.2 summarizes the mechanical properties of SHCC and concrete. The average tensile strain capacity of SHCC is 3.2% and the average tensile strength is 4.1 MPa. The average compressive strengths of SHCC and concrete are 67.5 MPa and 47.5 MPa respectively. The adoption of a relatively stronger SHCC as compared to concrete is to ensure that the thin laminates can withstand the loads caused by demoulding, handling and beam casting. A stronger cover zone with dense microstructure is also expected to be favourable to the durability of a structural element.

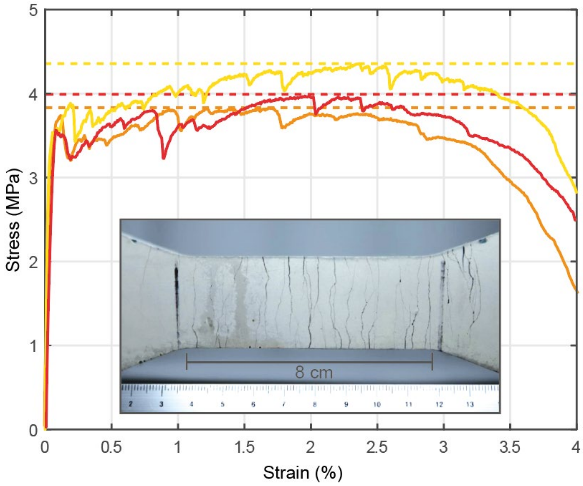

Figure 4.5: Stress-strain curves of SHCC under direction tension with an inset image showing a typical crack pattern of a dog-bone specimen after test.

Table 4.2: Results of uniaxial compression and tension tests.

Mixture	Compressive strength (MPa)	First cracking strength (MPa)	Ultimate tensile strength (MPa)	Ultimate tensile strain
SHCC	67.5±0.7	3.7±0.3	4.1±0.4	3.2%±0.7%
Concrete	47.9±2.0	-	-	-

4.3.2 Structural behaviour

Fig. 4.6 shows the comparison of load deflection response and maximum crack width development between the beams. As can be seen from the solid lines, load-deflection curves of the hybrid beams were in general similar to the curve of reference reinforced concrete beam. Only that the first-cracking loads of all the hybrid beams were slightly higher than that of the reference beams, which is expected given the higher strength of SHCC compared to concrete and the fact that the SHCC can provide additional bridging force even after the concrete is cracked. After cracking, the stiffness of the beams was reduced and no significant difference between the stiffness of the hybrid beams and the reference beam can be noticed. The next turning point is when the load ceased to increase linearly with increasing deflection, which marks the starting point of reinforcement yielding. In this stage, a slightly more pronounced tension hardening behaviour can be noticed for the hybrid beams compared to reference beam due to the contribution of SHCC in tension. The last stage is when the load started to decrease as marked by the square markers on the curves, which indicates the onset of the failure stage of the beams. As can be seen, all the tested beams have similar load carrying capacity. While the maximum load for the Ref beam is 58.9 kN, the load bearing capacity for the Smooth, Profile and Vaseline hybrid beams are 58.2 kN, 59.7 kN and 57.7 kN, respectively. The difference is only 3 percent over the highest load value. This is as expected because all the beams have the same reinforcement and the contribution from the 1-cm-thick SHCC layer to the resistance moment is small.

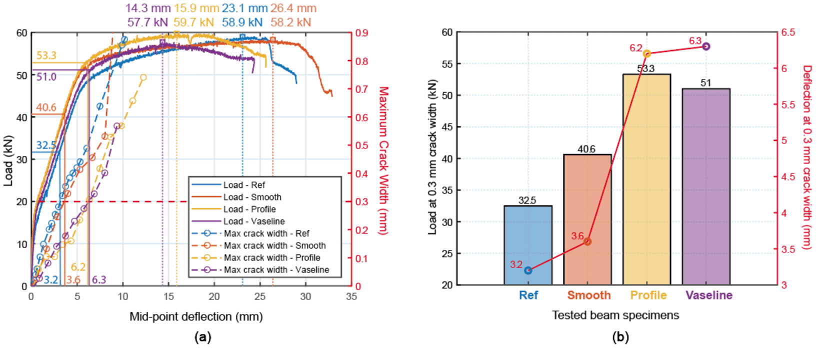

Figure 4.6: (a) Load-deflection-crack width response of all tested beams and (b) summary of load and deflection values when the maximum crack width exceeds 0.3 mm for each beam.

Still, the load-deflection curves for hybrid beams are noticeably different depending on the interface type. Vaseline beam exhibited the smallest tension stiffening. Furthermore, for the Ref and Smooth beams, after reinforcement yielding, the loads increased monotonously with increasing deflection, following by a quick drop after reaching the ultimate load. On the contrary, the loads of the Profile and the Vaseline beams first increased and then decreased at an almost identical speed for a similar amount of deflection. This difference means that the Profile and Vaseline beams reached their maximum loads at much smaller deflections than the Ref and Smooth beams. As compared to the Smooth beam whose mid-point deflection is 26.4 mm when the load is at its maximum, the equivalent deflection for the Vaseline beam is only 14.3 mm. In the beams with a profiled interface, cracks in concrete may have developed at lower loads, since the shear-keys might have provided a splitting force to open up a crack, resulting in an early crack localization and an accelerated elongation of the reinforcement. Also because of the presence of the shear-key, the crack patterns in the SHCC are much more complex in the hybrid beams with profiled interface as shown by Fig. 4.7. It is thus possible that due to geometry discontinuity there is stress concentration and final crack localized earlier in SHCC.

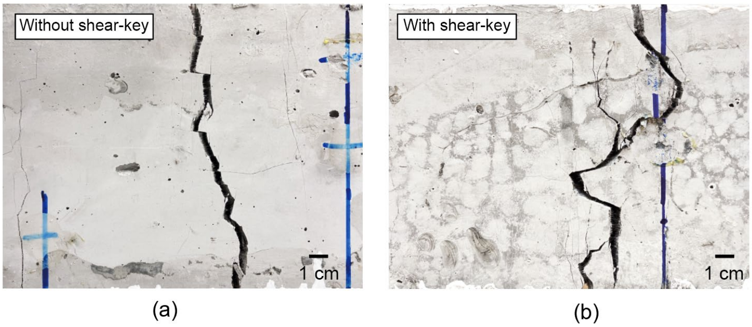

(a) (b)

Figure 4.7: Crack pattern of the bottom side of (a) Smooth beam and (b) Vaseline beam.

More importantly for the aim of this study, it can be seen from the dashed lines in Fig. 4.6a that all hybrid beams show improved crack width control ability. The dashed lines in Fig. 4.6a show the development of the maximum crack widths along the bottom edge of the beams with increasing deflection as calculated from the DIC results from both the front and back sides of the same beam. The maximum values were taken from the side with larger crack widths. As can be seen, the reference beam showed maximum crack widths exceeding 0.3 mm at a load of 32.5 kN. In contrast, the hybrid beams with smooth, profiled, and Vaseline-applied profiled interfaces were able to refrain crack widths below 0.3 mm until loads of 40.6 kN, 51.0 kN and 53.3 kN, respectively. In this thesis, a surface crack width limit of 0.3 mm is adopted, which is the prescribed critical value in Eurocode 2 for reinforced concrete under quasi-permanent load across all exposure classes, except for X0 and XC1. For the best performing hybrid beam (*i.e.*, the Profile beam), the load when 0.3 mm crack width is reached is 89.3% of its ultimate capacity. Fig. 4.6b summarizes the loads and deflections for the tested beams when the maximum crack widths reached 0.3 mm. Though the hybrid beams all exhibited a deferred opening of cracks in SHCC, it is obvious that the hybrid beams with a profiled interface (*i.e.*, the Profile and Vaseline beams) have a superior crack width control ability. Not only the loads at 0.3 mm crack width of the Profile and Vaseline beams were higher than the Smooth beam, a 0.3-mm-wide crack also happens at a much larger deflections for the Profile and Vaseline beams (*i.e.*, at 6.2 mm and 6.3 mm respectively) as compared to the Smooth beam which reached the 0.3 crack width at only 3.6mm. This deflection value is only slightly higher than that of the Ref beam, showing that the crack width control ability of the SHCC material was only marginally activated in the Smooth beam.

To further investigate the different behaviours of the hybrid beams in terms of the crack development, the evolution of crack pattern in the constant bending moment region at 30 kN, 50kN and ultimate load for all the tested beams are shown in Figs. 4.8-10. The moments at which the crack patterns were recorded are showed by the circle markers at the load-deflection curves next to the respective crack pattern image. As shown by the crack patterns, all beams exhibited first flexural cracking, followed by crack opening and then a final failure of concrete in the compression zone. By comparing Figs. 4.8a and 4.8b, it is found that the SHCC layer has very little influence on the cracking behaviour of the beam when a smooth interface is adopted. Branching of cracks from concrete to SHCC was observed only to a very limited extent as shown in Figs. 4.11a and 4.11b, which are zoom-in images of the strain field at the SHCC/concrete interface. The locations from where the images were captured are marked in the crack pattern of Smooth beam (Fig. 4.8b) at 50 kN. As can be seen from the zoom-in images, cracks from concrete can be spread into only 2-3 smaller cracks in SHCC and no delamination can be observed between the 2 layers, resulting in an extremely narrow cracked zone in the SHCC. This indicates that the adhesion between SHCC and concrete at smooth interface is so strong that the debonding is thoroughly resisted, causing only a small portion of SHCC to be activated and an early localization of cracks in SHCC. This restricted crack-distributing behaviour also explains the limited crack width control ability of the SHCC layer in the hybrid beam with a smooth interface.

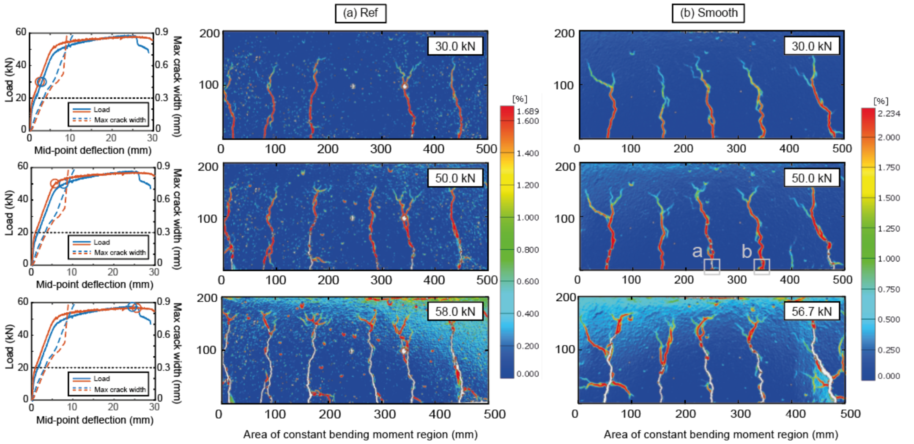

Figure 4.8: Crack pattern development at 30 kN, 50kN and ultimate load for (a) Ref beam and (b) Smooth beam.

Fig. 4.9 and Fig. 4.10 show the crack pattern of the hybrid beams with profiled interface (*i.e.*, Profile and Vaseline beams). The vertical lines in white colour in the crack pattern images show the positions of the cracks in the SHCC along the length of the constant bending moment of a beam. As can be seen, both beams exhibited considerably more cracks in the SHCC as compared to the Smooth beam. The zoom-in images at the Concrete/SHCC interface (Figs. 4.11c, 4.11d and 4.11e) also show that the cracks from concrete were largely arrested in both the Profile and Vaseline beams and that the branching of cracks were much more obvious than that of the Smooth beam. The reason for the better crack performance of the SHCC with a profiled interface is probably because the presence of shear-keys can lead to a non-uniform load transfer between the concrete and the SHCC layer. In such a case, stresses may have concentrated around the shear-keys even at a low load level and thus led to a relatively early local delamination near shear-keys as shown by the crack patterns at 30 kN, which then facilitated the activation of SHCC and the formation of microcracks. It might also be that, due to interlocking profiles, more cracks in concrete can be triggered and thus results in smaller crack width in concrete, which will ease SHCC to distribute the concrete cracks locally. Furthermore, because of the additional shear stress taken by the shear-key, the tensile stress in the SHCC layer is expected to be higher than that of a smooth interface, which may have further encouraged cracking in the SHCC.

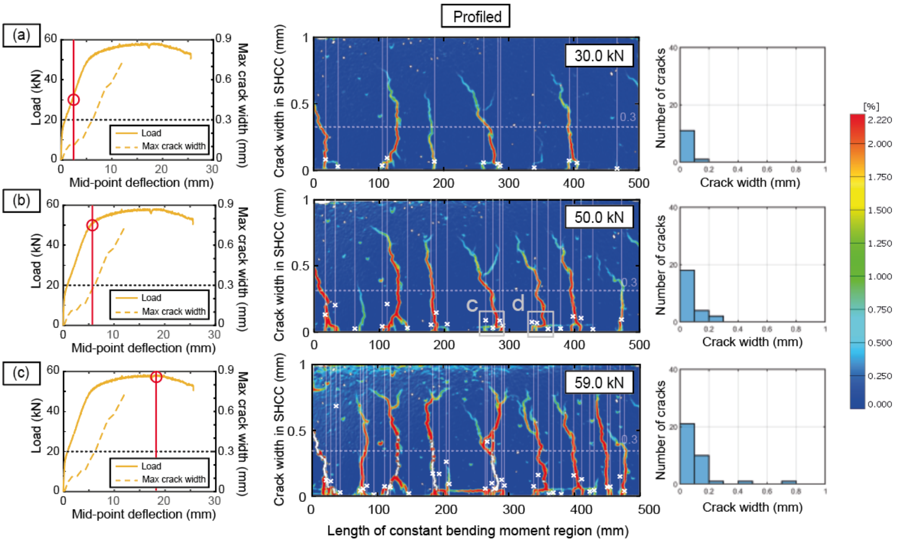

Figure 4.9: Crack pattern development of the Profile beam at 30 kN, 50kN and ultimate load as well as the crack width distribution at each load levels. The vertical lines in white colour show the positions of cracks in the SHCC; and the y-value of each '×' marker is the crack width of each individual crack.

By comparing the crack patterns between the Profile beam and the Vaseline beam, it can also be found that a higher portion of the SHCC was activated in the Vaseline beam than the Profile beam. By comparing the zoom-in images of the Profile beam (Fig. 4.11c and 11d) and the Vaseline beams (Fig. 4.11e), it can be found that delamination between SHCC and concrete is more pronounced in the Vaseline beam than in the Profile beam, which might have led to the activation of a wider portion of SHCC and the formation of more cracks. As can be seen from the histograms right to the crack pattern in Figs. 4.9 and 4.10, the number of cracks in the SHCC layer of the Vaseline beam is almost two times that of the Profile beam for all the three load levels. This demonstrates that a purposely weakened interface can indeed facilitate the activation of SHCC in a hybrid structure by allowing differential deformation between the SHCC and concrete layers.

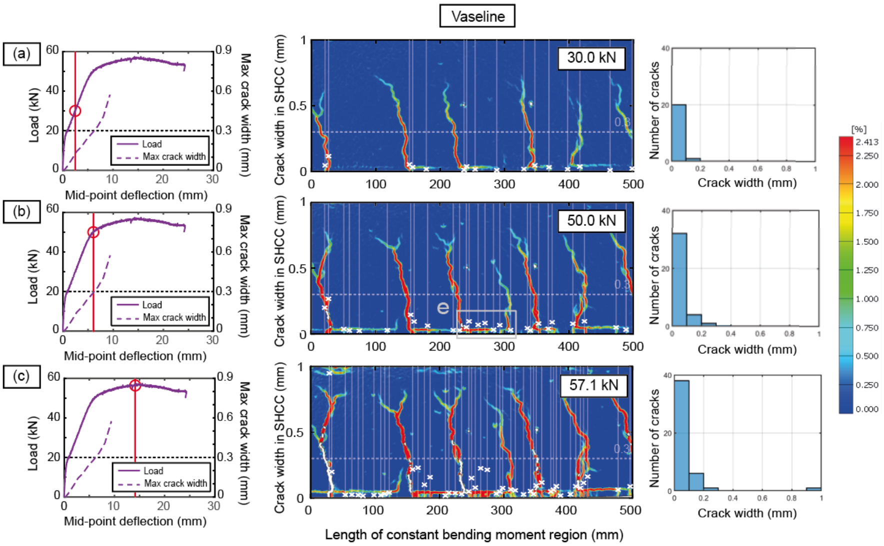

Figure 4.10: Crack pattern development of the Vaseline beam at 30 kN, 50kN and ultimate load as well as the crack width distribution at each load levels. The vertical lines in white colour show the positions of cracks in the SHCC; and the y-value of each × marker is the crack width of each individual crack.

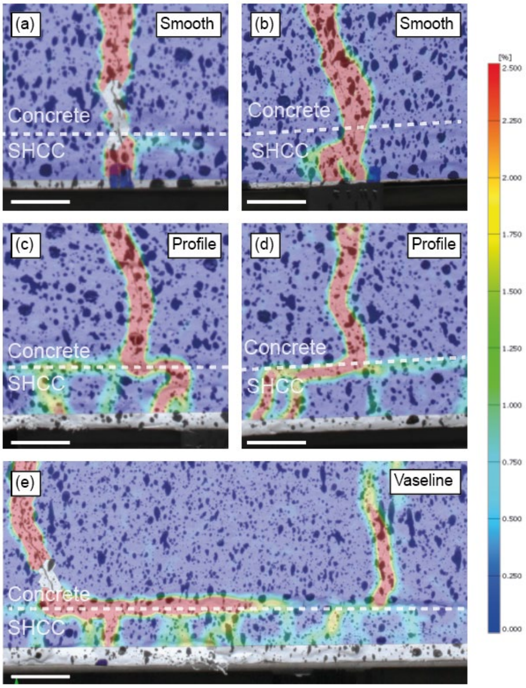

Figure 4.11: Zoom-in images of the crack pattern at interface between concrete and SHCC for all the hybrid beams at 50 kN load. Scale bar = 1 cm.

The width of the cracks formed in the SHCC layer of the hybrid beams were also calculated and overlapped over the crack pattern images as the cross makers in Figs. 4.9 and 4.10. The y-values of the makers represent the individual crack width while the x-values correspond to the locations of each crack along the beams. From the figures, it can be clearly seen that the majority of cracks formed in SHCC are microcracks having a crack width smaller than 0.3 mm even at the ultimate loads. Also, it can be found that even though the localized cracks were widened significantly at high loads, most of the cracks formed in SHCC stayed small (*i.e.*, to well below 0.3 mm) for all load levels. Figs. 4.12a and 4.12b quantitatively show the distribution of crack width in the Profile and the Vaseline beams with increasing deflection. As can be seen, though the maximum crack width increased quickly with increasing deflection, the average crack widths stayed low and almost constant (around 0.1 mm). Except for only a few crack that went larger than 0.3 mm, most of the cracks remained below 0.2 mm width.

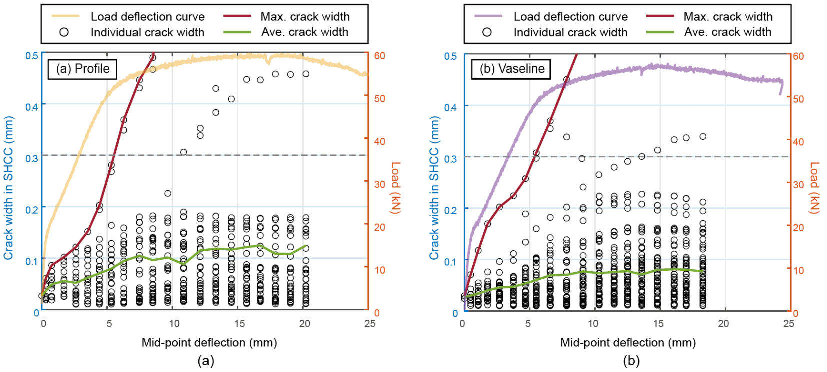

Figure 4.12: Crack width distribution for (a) Profile beam and (b) Vaseline beam.

Fig. 4.13a shows a comparison of average crack width between all the tested beams. Unlike the Profile and Vaseline beams, the average crack widths for the Ref and Smooth beams increased almost linearly with increasing deflection, which again proves that a smooth interface in a SHCC/RC hybrid system is not desirable as the crack control ability of SHCC cannot be sufficiently triggered. Besides, it can be seen that the Vaseline beam has the lowest average crack width among the 4 tested beams, which should be a direct result of having more cracks. Fig. 4.13b shows the change of crack number with increasing deflection for all the beams. As expected, the Vaseline beam has the highest number of cracks for almost the entire test period. The number of cracks in the Vaseline beam is about 160% of that in the Profile beam and 10 times more than that in the Smooth and Ref beams. Furthermore, it can also be seen that the number of cracks for Vaseline beam kept increasing until a much larger deflection than in the rest of the beams. While the Ref and the Smooth beams stopped forming more cracks at a deflection around 3 mm, the Vaseline beam reached its maximum crack number at a deflection of 15 mm, which is also much larger than the 10-mm-deflection at which the Profile beam stopped generating more crack. The superior performance of the Vaseline beam again demonstrates the advantage of having a chemically debonded but mechanically connected bond behaviour to the crack width control performance of SHCC/RC hybrid structural elements.

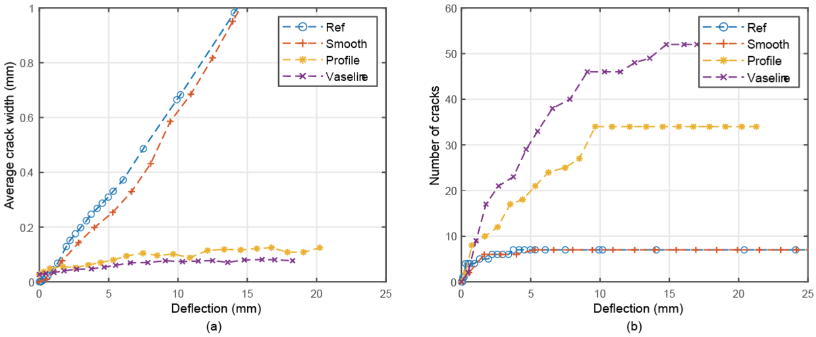

Figure 4.13: Comparison of (a) average crack widths and (b) number of cracks between all tested beams.

One possible issue with the use of a purposely weakened interface for a hybrid structure is the risk of having complete delamination, which might severely damage the structural integrity. To investigate the extent to which the delamination was influenced by the Vaseline treatment, the deformation of the Profile and Vaseline beams in y-direction from the DIC analysis at different load levels are presented in Figs. 4.14. To highlight the delamination degree, only the lower parts of beam near the interface, instead of the full height of the beam, are presented. The relative y-direction displacement between the 2 layers at several critical sections (as marked by the dashed lines) are also given in the line plot below the respective DIC images. As can be seen from the DIC strain fields in Figs. 4.14a and 4.14b, the Vaseline treatment has indeed led to a wider range of delamination even at lower deformation. However, a full delamination did not occur as the two layers were still tightly bonded at some locations along the interface, where the shear-keys might stay. Fig. 4.14b shows the opening of interface at several critical sections as marked by the dashed line, as referred by P1-5 and V1-5 in the Profile and the Vaseline beam, respectively. As can be seen, both beams exhibited a controlled degree of delamination, *i.e.*, the opening of the interface remained stable with increasing deflection. However, it can be seen that the maximum opening of interfacial crack of the Vaseline beam experienced an abrupt increase when deflection reached around 16 mm. This is because at this moment the beam has already passed it ultimate load and the crack in SHCC has started to localize fast. Still, it can be observed that, as long as the Vaseline beam did not reach its ultimate load (ULS scenario), the opening of interface crack was restricted below 0.3 mm, securing the structural integrity of the hybrid system.

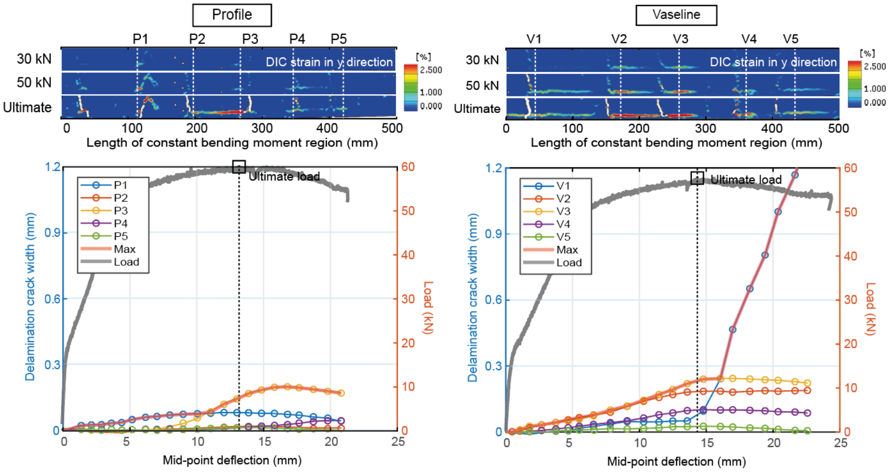

(a) (b)

Figure 4.14: DIC strain in vertical direction near the RC/SHCC interface at 30kN, 50kN and ultimate load as well as the vertical opening of delaminated positions for (a) Profile beam and (b) Vaseline beam.

Based on the above experimental results, it can be concluded that a 1-cm-thick SHCC layer can be very effective in controlling the crack width of a hybrid beam, as long as the interface is properly designed. The new interface type of having a shear-key pattern and a layer of Vaseline is also successfully demonstrated to enable a tailored bonding mechanism. However, it is still not clear to what extent has the Vaseline treatment reduced the interface bond and whether it is beneficial for the interface properties to be as weak as possible. Application of numerical testing, validated with experimental observations, might be beneficial as it can provide insights into the influence of a single parameter which is difficult to precisely control in an experimental study. It is thus decided to conduct numerical study to answer the above-mentioned questions.

4.4 Numerical simulations

4.4.1 Introduction

The lattice modelling approach has been extensively utilized in material research to simulate various phenomena in cement-based systems, including fracture [12,15], moisture transport [16], chloride diffusion [17] and 3D printing process [18]. Recently, the lattice model was also extended to simulate the structural behaviour of reinforced concrete structural elements [8,19]. Adopting a similar approach, the lattice model was also used in the current study to examine the cracking behaviour of the SHCC/RC hybrid beams. The aim of this numerical study is to quantitatively investigate the influence of interface properties on the activation of SHCC and on the crack width development.

In a lattice model, the material is discretized as a network of truss or beam elements connected at the ends. In most cases, elements have linear elastic properties. In each loading step, the element having the highest stress-to-strength ratio is removed from the system. The system is then updated due to the damage of losing one element. The analysis procedure is repeated until a pre-determined failure criterion (*i.e.*, in term of either load or displacement) for the simulated specimen is achieved. In certain situations where plasticity has to be introduced (*e.g.*, elements of reinforcement, the interface between steel and concrete, and SHCC), multi-linear constitutive relationship is assigned to those elements as pairs of stiffness and strengths. Each pair represents a point on the stress–strain curve of the material and is referred to as a segment. For those elements, the stiffness decreases gradually when the stress in an element reaches its strength. This occurs by moving from one segment to the next, in contrast to the complete removal from the mesh for (brittle) materials having single segment. In this way, stress-strain responses and realistic crack patterns of both brittle and ductile material can be obtained. For a detailed description on the procedure of constructing a lattice model for structural application, please consult [8].

To build lattice models of hybrid beam with a profiled interface, SHCC laminates with shear-keys were firstly modelled. Due to the limitation of the mesh size (*i.e.*, 10 mm), the cylindrical shear-keys were modelled as prisms following an equivalent pattern as shown in Fig. 4.15a. The resulting lattice model of a profiled SHCC laminate can be seen as Fig. 4.15b. The length of the simulated SHCC laminate is 1.5 meter so that only the effective span of the beam is modelled. Fig. 4.15c shows the resulting model of a hybrid beam. The model consists of 5 types of elements, namely Concrete, SHCC, Reinforcement, SHCC/Concrete Interface and Concrete/Reinforcement Interface. A total of six simulations were carried out in this study, including one reference reinforced concrete beam (designated as R) and five hybrid beams. Within the five hybrid beams, one beam is with a smooth interface (designated as S), while the remaining four beams are with a profiled interface but with different SHCC/Concrete interface properties (designated as P75, P50, P25 and P10, with reducing strength of interface elements). A list of the simulated models can be found in Table 4.3.

Table 4.3: Interface properties of performed six lattice simulations.

Simulation models	Mechanical properties of SHCC-concrete interface elements, given as a fraction to those of concrete elements		
	Modulus E	Compressive strength f_c	Tensile strength f_t
R	-	-	-
S75	100%	100%	75%
P75	100%	100%	75%
P50	100%	100%	50%
P25	100%	100%	20%
P10	100%	100%	10%

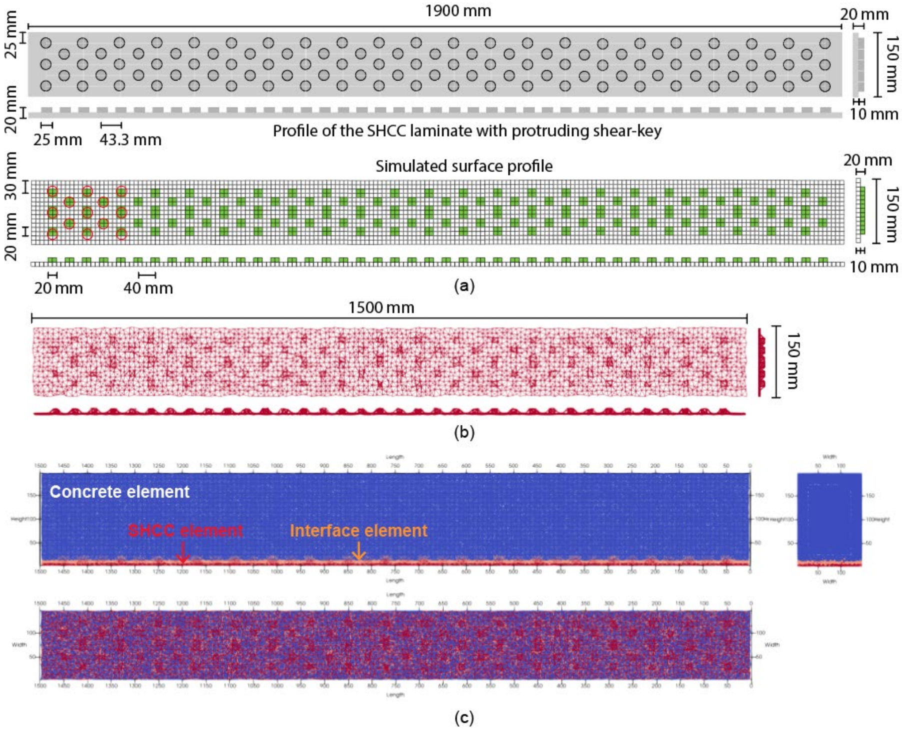

Figure 4.15: *(a) Comparison of the real profile and the simulated profile of the SHCC laminate with shear-key, (b) lattice model of a SHCC laminate with shear-key profile and (c) lattice model of the resulting hybrid beam with a profiled interface.*

4.4.2 Model inputs

The lattice elements are assigned mechanical properties (*i.e.*, stiffness and strengths) based on the materials they represent. In this study, all lattice elements are cylindrical and have a circular cross-section. The radius of these elements is determined iteratively to match the global elastic modulus obtained in the lattice simulation with the input of elastic modulus in a direct tension test. This iterative process ensures that the stiffness of the members is simulated accurately. The strength in the lattice model is determined by inverse modelling, which means that they are adjusted such that the response of the simulated material tests matches the experimental results [20]. Table 4.4 shows a list of input properties for lattice simulation. The determination of material properties, except for that of SHCC and the SHCC/Concrete interface, can be found in [8,19], in which same material properties were used for the simulation of hybrid beams.

Table 4.4: Material properties as inputs for lattice simulations.

Materials	Segment	Modulus E (GPa)	Tensile strength f_t (MPa)	Compressive strength f_c (MPa)
Concrete	-	32.00	4.0	70.0
SHCC	1	17.00	4.0	100.0
	2	10.00	3.5	0.1
	3	0.30	2.5	0.1
	4	0.20	2.5	0.1
	5	0.15	3.0	0.1
	6	0.12	4.0	0.1
	7	0.10	4.0	0.1
Reinforcement	1	200.00	500.0	500.0
	2	22.00	525.0	525.0
	3	12.00	550.0	550.0
Reinforcement/Concrete Interface	1	47.00	6.0	6.0
	2	9.00	12.0	12.0
	3	4.44	17.0	17.0
	4	2.00	23.0	23.0
	5	1.00	29.0	29.0
	6	0.70	35.0	35.0
	7	0.50	40.0	40.0
	8	0.40	46.0	46.0
	9	0.30	52.0	52.0
	10	0.20	58.0	58.0
	11	0.10	58.0	58.0
	12	0.05	48.0	48.0
	13	0.03	39.0	39.0
	14	0.02	29.0	29.0
	15	0.01	20.0	20.0

The input properties of SHCC were determined from a simulated direct tension test on a 10 mm × 100 mm × 200 mm thin plate model (Fig. 4.16a), which has the same thickness of the SHCC layer in the hybrid beam model. SHCC is defined using 7 segments such that the modelled SHCC exhibits similar stress-strain response as obtained experimentally (Fig. 4.16b) with realistic multiple cracking behaviour (Fig. 4.16b). The modelled SHCC also has good crack width control as shown by Fig. 4.16b, where the maximum crack width in SHCC at ultimate strain level is below 50 µm, as commonly observed in experiments. However, the simulated SHCC has lower ductility (blue line) as compared to experiments (orange line), which might be because of the relatively large mesh size adopted in the study. As this study focuses more on analysing the maximum crack width in SHCC rather than ductility, the modelling approach described earlier has been selected. However, it is worth noting that this approach may underestimate the ductility of the simulated hybrid beams.

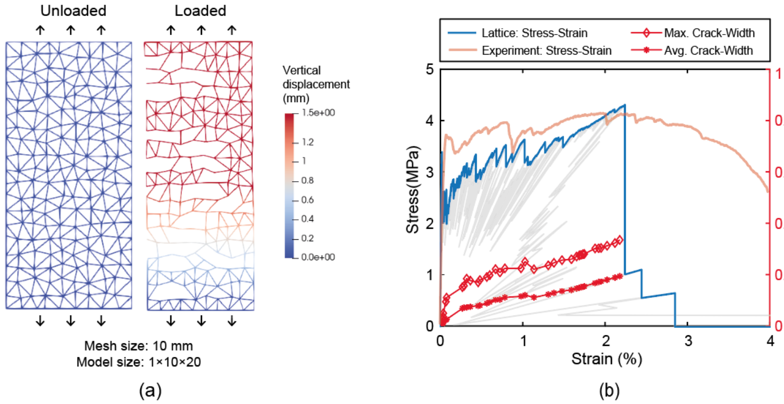

Figure 4.16: (a) Lattice model of a uniaxial tensile test for the calibration of SHCC material properties and (b) comparison of simulated and tested stress-strain response.

In order to simplify the inputs for the SHCC/Concrete interface, the strength values of the interface elements are expressed as a percentage of the strengths of concrete elements. The stiffness of the interface is kept the same as that of concrete. For simulation of the hybrid beams with smooth (S75) and untreated profiled interface (P75), the tensile strength of interface elements is assigned as 75% of the concrete properties. The remaining three hybrid beams have interface elements with decreasing tensile strength of 50% (P50), 25% (P25) and 10% (P10) of the tensile strength of concrete elements, while the compressive strength of interface elements in all simulated beams is assigned as 100% of the concrete properties. Assigning higher strength in compression is to simulate the condition of a physical contact, in which the interface is, in theory, able to transfer infinite load, as long as the materials on both sides do not fail.

4.4.3 Simulation results

The results of the simulation for reference reinforced concrete (R) are considered for verification of the model. The load-deflection-maximum crack width response of tested and simulated reinforced concrete beam is compared in Fig. 4.17a. It can be seen, the selected modelling choices are in general able to simulate the load deformation response, despite that the model has slightly overestimated the stiffness of the beam after concrete cracking. Also, the simulated maximum crack widths are in good agreement as compared to experimental observations throughout the loading. Since crack width prediction and general insight into fracture behaviour are the aims of this study, the described modelling approach was thus adopted. Because of the same reason, the simulations were only continued until the deflection reached 15 mm, as the max crack widths always exceed 0.3 mm at a deflection smaller than 15 mm. Fig. 4.17b shows the load-deformation results of all simulated beams. It can be seen that the influence of the SHCC layer and the interface properties can hardly be noticed, which is in agreement with the experimental observation as shown by Fig. 4.6a. Figs. 4.18 show the damage patterns from the lattice simulation for the reference beam R (Fig. 4.18a) and for the hybrid beam with the weakest profiled interface P10 (Fig. 4.18b). If these patterns are compared with the DIC results of Ref beam and Vaseline beam, it can be seen that the lattice simulations are able to develop similar crack pattern, with accurate crack spacing and crack number in the constant moment region. The debonding between the concrete and the SHCC in the Vaseline beam as observed by DIC is also well captured by the lattice simulation (Fig. 4.18b). Furthermore, the formation of multiple cracks in SHCC as observed from the bottom of the simulation is also consistent with the large number of cracks (Fig. 4.13a) as counted by DIC, which again proves the applicability of the current modelling approach.

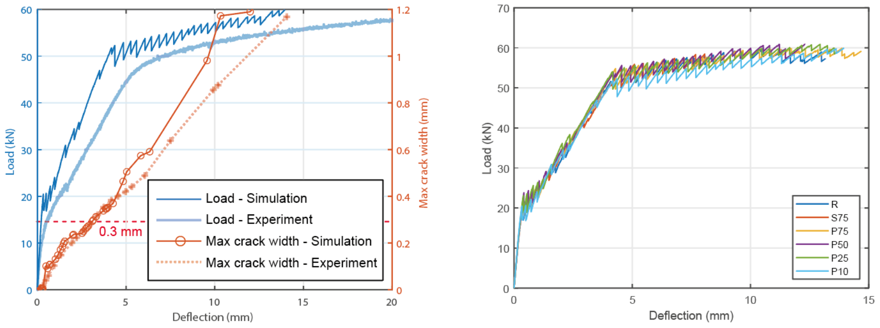

(a) (b)

Figure 4.17: (a) Comparison of simulation results and experimental results for the reference beam and (b) load deflection responses of all simulated beams.

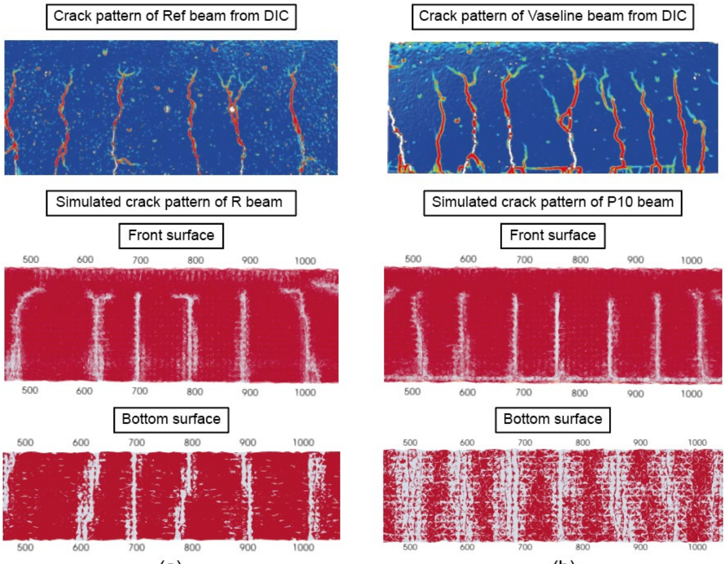

(a) (b)

Figure 4.18: Comparison of crack patterns from DIC and lattice model for (a) Ref beam and (b) Vaseline hybrid beam.

Fig. 4.19 shows the development of maximum crack width for all the simulations. The reference beam R has the largest crack widths for all the deformations, followed the by the hybrid beam with smooth interface. The simulation results of the profiled hybrid beams (P75-P10) demonstrate clearly that, by reducing the tensile strength of the interface elements, the development of the maximum crack width can be delayed. The profiled hybrid beam with the lowest tensile strength has the best crack width control performance among the six simulated beams. Fig. 4.20 shows the crack pattern of the simulated beam. A clear trend can be seen that, by gradually reducing the tensile strength of the interface elements, the degree of delamination increases, leading to the formation of more cracks in the SHCC. Fig. 4.21 shows the damage condition of only the interface elements and the SHCC elements. It can be found that a lower tensile strength results in the damage of more interface elements, and the number of cracks formed in SHCC increases with decreasing strength of the interface. To conclude, the simulation results demonstrate that, when the mechanical interlocking is provided, a weak interfacial bond between SHCC and concrete can indeed promote the activation of more SHCC and thus results in the formation of more cracks and a delayed development of maximum crack width.

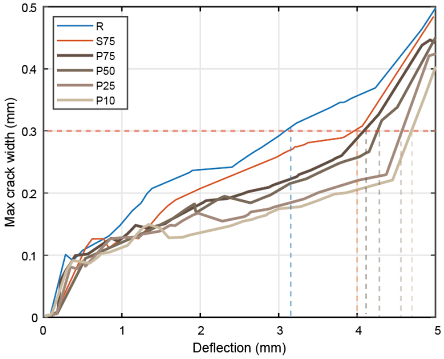

Figure 4.19: Development of the maximum crack width for all the simulated beams.

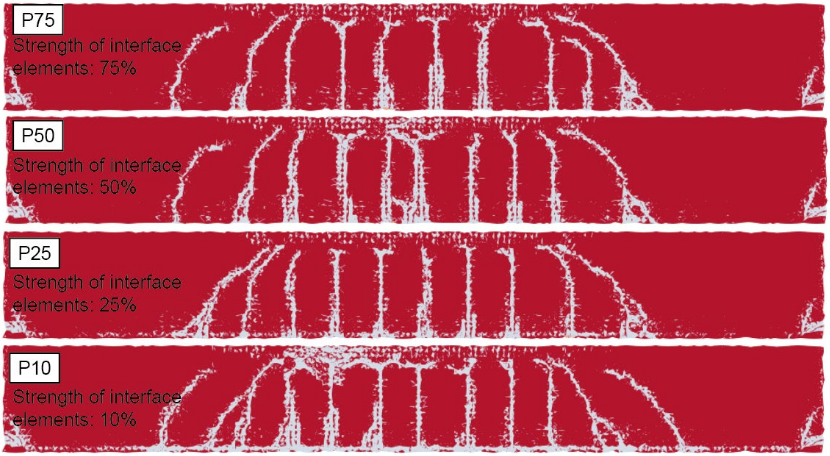

Figure 4.20: Simulated crack pattern of hybrid beams with interface element having different tensile strength.

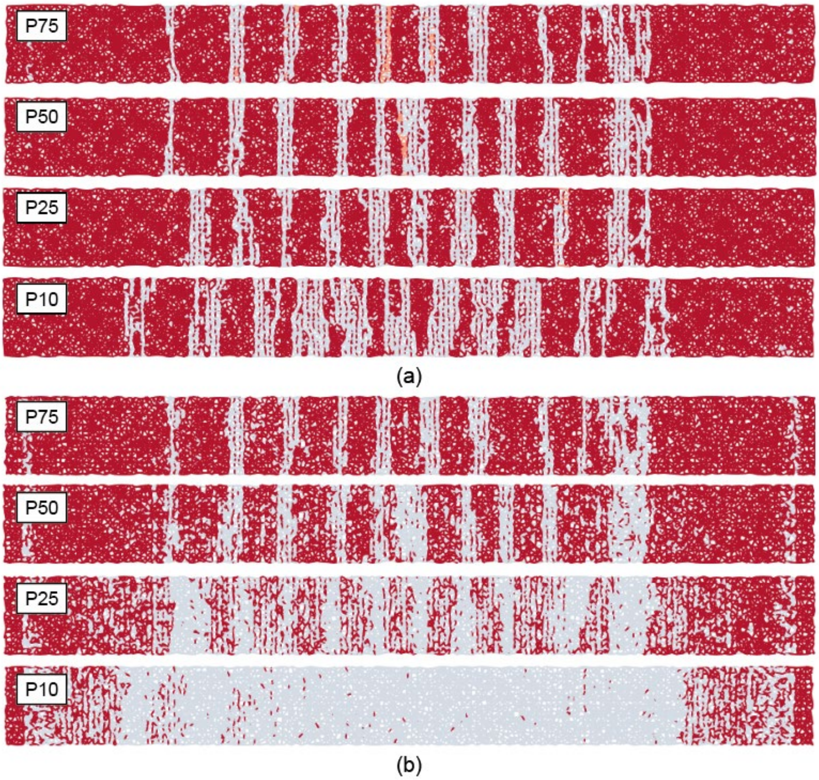

Figure 4.21: Simulated damage condition of (a) SHCC elements and (b) interface elements of hybrid beams with interface element having different tensile strength.

4.5. Conclusions

A combined experimental and numerical study was performed aiming to investigate the cracking behaviour of hybrid reinforced concrete beams enhanced with a very thin layer of SHCC in the cover zone, and also to develop interface profile such that the performance of a thin SHCC overlay is optimized with respect to its cracking behaviour. Structural behaviour, crack pattern and crack width development of the hybrid beams with different interfaces were tested and compared to the control reinforced concrete beams. The main findings of the current chapter are:

1. A 1-cm-thick SHCC layer can be very effective in controlling the crack width of a hybrid beam, as long as the interface is properly designed. As the volume ratio of SHCC used in the hybrid beams is only 6%, the current study demonstrates the feasibility of using minimum amount of SHCC in the critical region to efficiently enhance the performance of hybrid structures.
2. With a 1-cm-thick layer of SHCC, the maximum crack width of the best performing hybrid beam exceeded 0.3 mm at 53.3 kN load, whereas in the control beam the largest crack exceeded 0.3 mm at only 32.5 kN load. This 64% increase in load at the critical crack width means that the amount of reinforcement, possibly required for crack width control can be omitted/reduced.

3. A smooth interface is not desirable as it can only marginally delay the crack width development. The hybrid beams with profiled interface have much improved crack width control ability. The proposed new SHCC/concrete interface, that features a weakened chemical adhesion but an enhanced mechanical bonding, can successfully lead to a controlled extent of partial delamination between the two layers, which promotes the activation of SHCC. The hybrid beam with the proposed new interface formed 10 times more cracks in SHCC than a hybrid beam with a smooth interface and have an average crack width less than 0.1 mm until final capacity is reached.
4. The lattice model provided more systematic insight into the fracture behaviour of hybrid systems with varying interface properties. The simulation results suggest that, when the mechanical interlocking is provided, a weaker interface bond can indeed promote the activation of more SHCC and thus results in the formation of more cracks as well as a delayed development of maximum crack width.
5. The hybrid beams developed in the current study possess an improved crack control ability at the expense of minimal additional cost. The reduced crack width is expected to increase durability and the self-healing potential of the structural elements, which may eventually lead to an extended service life of the whole structure and more optimal design.

References

[1] M. di Prisco, G. Plizzari, L. Vandewalle, Fibre reinforced concrete: New design perspectives, Materials and Structures/Materiaux et Constructions 42 (2009) 1261–1281. https://doi.org/10.1617/S11527-009-9529-4/FIGURES/15.

[2] V.C. Li, On Engineered Cementitious Composites (ECC) a review of the material and its applications, Journal of Advanced Concrete Technology 1 (2003) 215–230. https://doi.org/10.3151/JACT.1.215.

[3] A.E.H. Khalil, E. Etman, A. Atta, M. Essam, Behavior of RC beams strengthened with strain hardening cementitious composites (SHCC) subjected to monotonic and repeated loads, Eng Struct 140 (2017) 151–163. https://doi.org/10.1016/J.ENGSTRUCT.2017.02.049.

[4] M. Luković, D.A. Hordijk, Z. Huang, E. Schlangen, Strain hardening cementitious composite (SHCC) for crack width control in reinforced concrete beams, Heron 64 (2019) 189–206. https://doi.org/10.2/JQUERY.MIN.JS.

[5] M.I. Khan, S.U. Sial, G. Fares, M. ElGawady, S. Mourad, Y. Alharbi, Flexural performance of beams strengthened with a strain-hardening cementitious composite overlay, Case Studies in Construction Materials 17 (2022). https://doi.org/10.1016/J.CSCM.2022.E01645.

[6] C.K.Y. Leung, Q. Cao, Development of Pseudo-ductile permanent formwork for durable concrete structures, Materials and Structures/Materiaux et Constructions 43 (2010) 993–1007. https://doi.org/10.1617/S11527-009-9561-4/FIGURES/17.

[7] B.Y. Deng, D. Tan, L.Z. Li, Z. Zhang, Z.W. Cai, K.Q. Yu, Flexural behavior of precast ultra-lightweight ECC-concrete composite slab with lattice girders, Eng Struct 279 (2023) 115553. https://doi.org/10.1016/J.ENGSTRUCT.2022.115553.

[8] S. Mustafa, S. Singh, D. Hordijk, E. Schlangen, M. Luković, Experimental and numerical investigation on the role of interface for crack-width control of hybrid SHCC concrete beams, Eng Struct 251 (2022). https://doi.org/10.1016/j.engstruct.2021.113378.

[9] S.Z. Qian, V.C. Li, H. Zhang, G.A. Keoleian, Life cycle analysis of pavement overlays made with Engineered Cementitious Composites, Cem Concr Compos 35 (2013) 78–88. https://doi.org/10.1016/J.CEMCONCOMP.2012.08.012.

[10] M. Kunieda, T. Kamada, K. Rokugo, Localized fracture of repair material in patch repair systems, in: Proceedings of FRAMCOS-5, Vail, Colorado, USA, 2004. http://www.framcos.org/FraMCoS-5/Kunieda.Localized.pdf (accessed February 13, 2023).

[11] Luković Mladena, Influence of interface and strain hardening cementitious composite (SHCC) properties on the performance of concrete repairs, Delft University of Technology, 2016.

[12] E. Schlangen, J.G.M. van Mier, Simple lattice model for numerical simulation of fracture of concrete materials and structures, Mater Struct 25 (1992) 534–542. https://doi.org/10.1007/BF02472449/METRICS.

[13] European committee for standardization, NEN-EN 196-1. Methods of testing cement - Part 1: Determination of strength, 2016.

[14] Japan Society of Civil Engineers, Recommendations for Design and Construction of High Performance Fiber Reinforced Cement Composites with Multiple Fine Cracks (HPFRCC), 2008.

[15] E. Schlangen, M&S highlight: Schlangen and van Mier (1992), Simple lattice model for numerical simulation of fracture of concrete materials and structures, Materials and Structures/Materiaux et Constructions 55 (2022). https://doi.org/10.1617/S11527-022-01932-W.

[16] B. Šavija, M. Luković, E. Schlangen, Influence of Cracking on Moisture Uptake in Strain-Hardening Cementitious Composites, J Nanomech Micromech 7 (2017). https://doi.org/10.1061/(ASCE)NM.2153-5477.0000114.

[17] B. Šavija, J. Pacheco, E. Schlangen, Lattice modeling of chloride diffusion in sound and cracked concrete, Cem Concr Compos 42 (2013) 30–40. https://doi.org/10.1016/J.CEMCONCOMP.2013.05.003.

[18] Z. Chang, Y. Xu, Y. Chen, Y. Gan, E. Schlangen, B. Šavija, A discrete lattice model for assessment of buildability performance of 3D-printed concrete, Computer-Aided Civil and Infrastructure Engineering 36 (2021) 638–655. https://doi.org/10.1111/MICE.12700.

[19] D. Gu, S. Mustafa, J. Pan, M. Luković, Reinforcement-concrete bond in discrete modeling of structural concrete, Computer-Aided Civil and Infrastructure Engineering (2022). https://doi.org/10.1111/MICE.12937.

[20] Z. Chang, H. Zhang, E. Schlangen, B. Šavija, Lattice Fracture Model for Concrete Fracture Revisited: Calibration and Validation, Applied Sciences 2020, Vol. 10, Page 4822 10 (2020) 4822. https://doi.org/10.3390/APP10144822.

5

Shear behaviour of hybrid reinforced concrete beams with laterally applied SHCC cover

Chapter 5 delves into the shear resistance of hybrid elements under shear loading. Specifically, hybrid beams with laterally applied SHCC covers were prepared and subjected to 3-point-bending tests, while the deformation and crack pattern of the beams, along with delamination between SHCC and concrete, were monitored. The profiled interface developed in the previous chapter (without Vaseline treatment) was adopted. The contribution of SHCC cover to shear resistance was assessed with varying boundary condition (supporting at full width versus supporting only at the concrete core). Lattice model was also applied to investigate the responses of the hybrid beams under different combination of loading/supporting condition. Results showcased that the profiled interface effectively mitigates interfacial delamination under shear loading, thereby ensuring the structural stability of the hybrid system. The SHCC cover can arrest the dominate critical inclined cracks formed in concrete and dissipate cracks from concrete into multiple fine cracks in the SHCC. This featured cracking behaviour has led to an increased post-cracking ductility and an enhanced energy absorption capacity in the hybrid beams. The structural performance of the hybrid beams was found not sensitive to the boundary condition.

As an extension of the current study, a hybrid beam without shear reinforcement was also prepared. The contribution from SHCC was assessed. It was found that the contribution of SHCC cover was larger in case when shear reinforcement was present, affecting both the peak load and the developed crack pattern.

5.1 Introduction

In the design of reinforced concrete beam, the consideration of shear resistance often takes precedence over flexural resistance due to several reasons. Shear failure in concrete beams tends to be brittle, posing significant safety concerns as it can occur without warning. Moreover, shear forces are influenced by various factors such as loading conditions, beam geometry, and support conditions, making their prediction and management crucial for structural integrity. This significance is further accentuated in composite systems, such as beams with SHCC cover layers, where the introduction of new interfaces and discontinuities may perturb shear flow paths and redistribute shear forces, thus heightening the risk of delamination between layers. Addressing shear resistance is important to enable the structural stability and safety of reinforced concrete beams.

Despite the significance of shear behaviour within a composite system, studies investigating the shear performance of SHCC/RC hybrid members are rare, with only two relevant sources of literature having been identified. Hossain et al. [1] evaluated the shear response of novel SHCC/RC composites beam by applying SHCC on the tensile side in hybrid beams. The results showed that due to the bridging action in SHCC tension zone, the composite beam showed an improved shear strength and ductility compared to full RC or SHCC beams. Zhang et al. [2] studied the shear behaviour of SHCC/RC hybrid beams made with precast U-shaped SHCC formwork. The influences of the formwork thickness and the interface treatment methods were investigated. It was found that the SHCC layers were able to improve the shear resistance and deformational ability. The bond at the interface has found to have little influence on the shear strength. However, both studies adopted a relatively large volume of SHCC.

To evaluate the performance of the hybrid beams with self-healing SHCC cover under shear, precast thin SHCC cover (*i.e.*, 1 cm in thickness, same to previous chapter) were placed laterally before casting concrete core to produce SHCC/RC hybrid beams. The shear behaviour of the SHCC/RC hybrid beams under 3-point bending test is investigated. The primary objective of this study is to investigate the reliability of the connection between the cover and the core under shear loading and to evaluate the influence of the cover layer on the shear resistance of the beams. In the following sections, the manufacturing process of the hybrid beams with laterally applied cover zone will be introduced. Then, the shear resistance of the beams and final failure mode are reported. Emphasis will be placed on the shear crack development in SHCC and the interfacial behaviour between SHCC and conventional concrete.

5.2 Materials and tests

5.2.1 Experimental design

The main structural test program consists of three 1.4-meter-long beams with a height of 200 mm and a width of 120 mm, including one reference beam and two hybrid beams with profiled interface. It should be noted that Vaseline was not applied with the profiled interface, as controlling crack width was not the primary objective of the lateral SHCC cover application. All beams have a minimal amount of shear reinforcement; only four stirrups with nominal diameter of 6 mm are designed within the shear span.

In order to induce the most critical loading conditions and investigate its role on resistance, two different boundary conditions are varied. One beam was fully supported across its entire width, while the other was supported only at the inner concrete core in order to create the most critical scenario for evaluating the bond between SHCC and concrete. The geometry and reinforcement details of the beams can be found in Fig. 5.1.

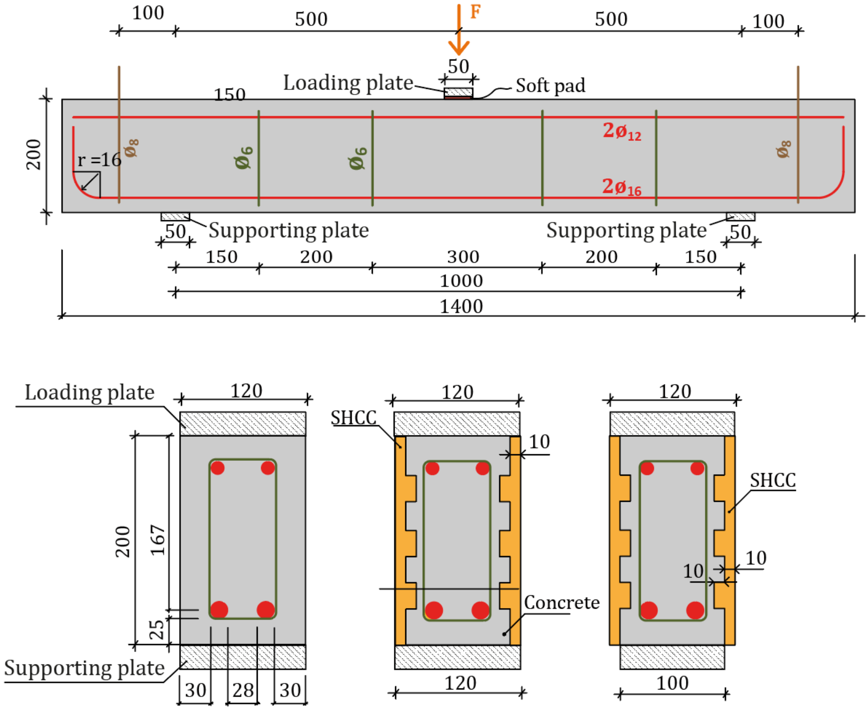

Beam No. 1
Reference beam
(Ref)

Beam No. 2
Hybrid beam
supported at full width
(Hybrid - 120120)

Beam No. 3
Hybrid beam
supported at concrete
(Hybrid - 120100)

Figure 5.1: Geometry and reinforcement details of the specimens.

5.2.2 Materials and sample preparation

Table 5.1 shows the mixture compositions of SHCC and concrete used in the current study. The SHCC has the same mix design as have reported in the previous chapter, while the concrete is different. To assure shear failure of the beams, a C20/25 grade conventional concrete having a water-to-binder ratio of 0.6 and a maximum aggregate size of 16 mm has been selected.

Table 5.1: Mixture compositions of SHCC and concrete [unit in kg/m3].

Material	SHCC	Concrete
CEM I 42.5 N	-	260
CEM III/B 42.5 N	1060	-
Limestone powder	530	-
Sand (0.125-4 mm)	-	847
Gravel (4-16 mm)	-	1123
PVA fibre	26	-
Water	424	156
Superplasticizer	2	0.26

Similar to the previous chapter, all the hybrid beams were casted in 2 steps. In the first step, SHCC cover were cast with custom-made moulds and cured for 14 days in a climate room (20ºC and ≥ 98% RH) before casting of concrete beams. In the second step, SHCC covers were taken out from the climate room and vertically placed into plywood moulds. In between the SHCC cover, reinforcement cages were placed with appropriate spacers. After the preparation, the concrete was cast in between the SHCC covers on a vibration table. Finally, the hybrid beams were then cured for 28 days in sealed conditions before testing. The reference RC beam was cast along with this second phase. For detailed information on material preparation and SHCC cover fabrication, please refer to Section 4.2 of Chapter 4.

5.2.3 Testing

All the beams were tested in a three-point bending test setup (Fig. 5.2) under displacement control at a rate of 0.01 mm/s. During each test, the deformation of the beams was captured within the effective span by using DIC; and the mid-point deflection of the beams was measured by LVDTs. In addition, the interface condition between the cover and the core was monitored during each test by measuring the interfacial opening and sliding at four different locations via eight LVDTs as shown in Fig. 5.3.

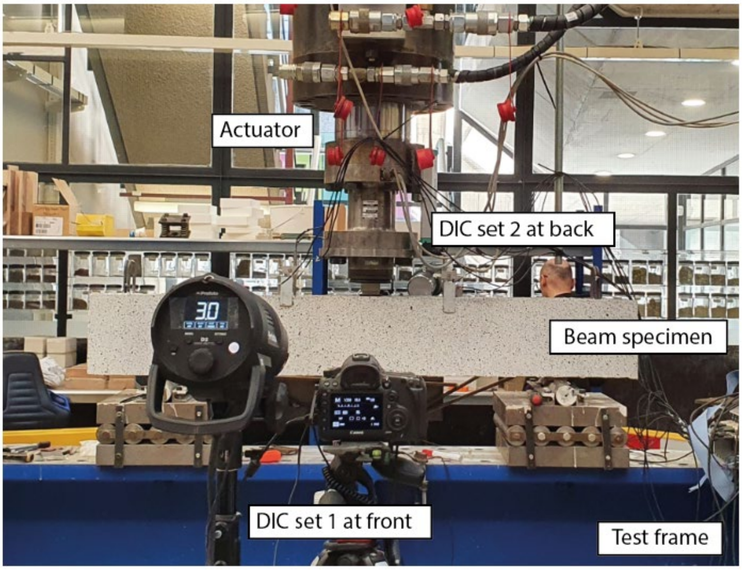

Figure 5.2: Experimental set-up for 3-point-bending test of beam specimens with DIC measurement on both sides.

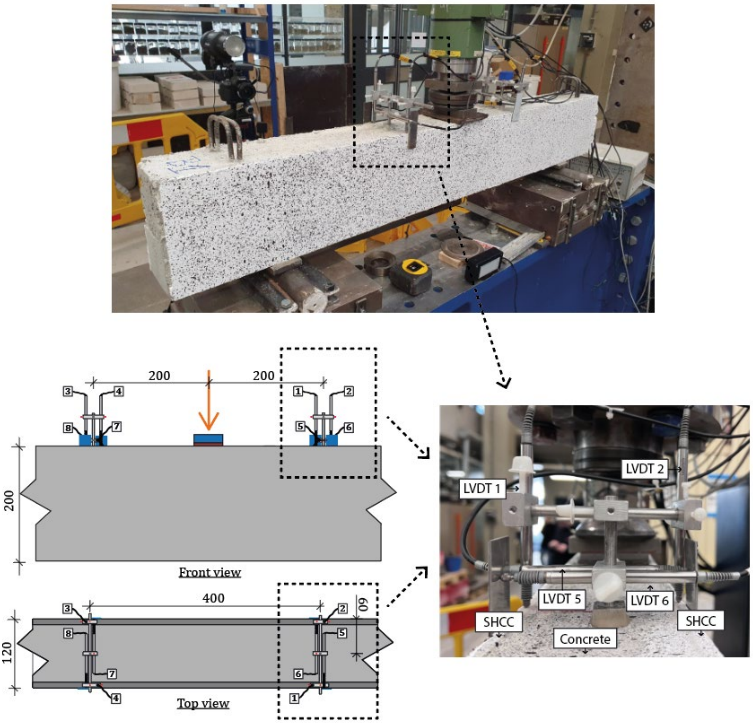

Figure 5.3: Design of LVDT set for measuring interfacial opening and sliding.

5.3 Experimental results

5.3.1 Load-deflection response

Fig. 5.4 shows the load versus mid-span deflection curves for the beams. The load-deflection curves for the three tested specimens exhibit a similar trend. Initially, the beams behave elastically, but as flexural cracks form, the slope of the curves decreases. This is followed by a further reduction in stiffness due to the development of major shear cracks. Finally, beam failure is characterized by a sudden drop in load. The peak load of the reference beam is 101.8 kN, while the two hybrid beams reach 124.5 kN and 124.2 kN, respectively, indicating an approximate 25% increase in shear strength. This additional load-carrying capacity arises from the higher tensile (and compressive) strength of SHCC matrix and the crack-bridging force provided by the PVA fibres. Additionally, the stiffness in all hybrid beams decreases less than in the reference beam after the formation of flexural cracks, which can be attributed to the post-cracking stiffness of SHCC. The hybrid beams also demonstrate enhanced deformational capacity, with more than a 16% improvement in deflection, further proving the effectiveness of SHCC.

Furthermore, it is found that the boundary condition (*i.e.*, loading over the whole width or only the concrete core part) has no influence on the shear behaviour of the hybrid beams. The profiled interface provides sufficient bond strength between the SHCC and the concrete, allowing the composite beams to behave monolithically.

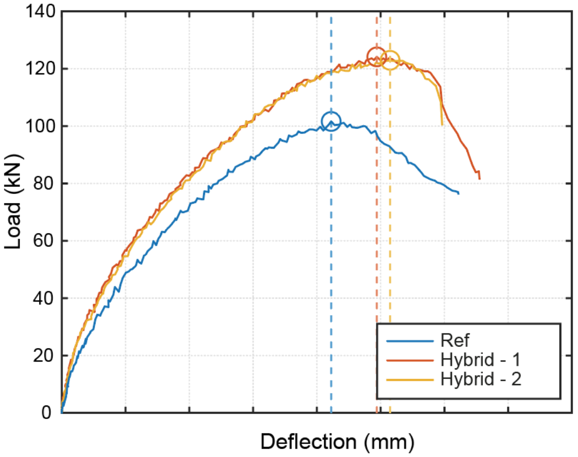

Figure 5.4: Load-deflection behavior of tested beams.

Post-cracking shear ductility is the ability of RC beam to continue deforming and absorbing energy after the initiation of major shear crack [3]. It is an index to measure the capacity of the beam to resist sudden shear failure and to sustain large deformations without collapsing. High post-cracking shear ductility enables beams to deform and absorb energy after cracking, reducing the risk of sudden failure and enhancing the overall structural performance and safety. The post-cracking shear ductility of the beams can be expressed in terms of ductility factor (DF) as per Eq. 5.1. The DF has been defined as the ratio of the deflection at failure load to the deflection at first diagonal crack load.

$$DF = \frac{\Delta_u}{\Delta_f} \tag{5.1}$$

where Δ_u is the deflection at the peak load, Δ_f is the deflection at the initiation of major shear crack.

Table 5.2: Summary of structural responses of tested beams.

Beam ID	Flexural crack formation		Major shear crack initiation		Ultimate point		Ductility factor	Energy absorption (kN·mm)
	Load (kN)	Deflection (mm)	Load (kN)	Deflection (mm)	Load (kN)	Deflection (mm)		
Ref	22.9	0.5	50.0	1.1	101.6	4.2	3.8	287.26
Hybrid – 1	32.6	0.5	57.6	0.9	124.1	4.9	5.4	423.28
Hybrid - 2	30.4	0.5	56.4	0.9	122.9	5.1	5.7	444.13

The DF values of the tested beams are summarized in Table 5.2. As can be seen, all hybrid beams exhibited higher DF than their reference beams. The shear resistance of concrete elements depends on aggregate interlock mechanism, dowel action of the longitudinal reinforcement, and uncracked compression zone. When SHCC is applied on the lateral surface of the beams, the fibre bridging stresses in the SHCC can be considered as an additional source of post-cracking shear resistance and thus contributed to enhanced DF values. Energy absorption was calculated by measuring area under the load-deflection curves up to the peak load, and is shown in Table 5.2. The hybrid beams in both groups exhibited significantly higher energy absorption capacities than the reference beam.

5.3.2 Cracking behaviour and failure pattern

To capture the damage process of the beams, the evolution of crack pattern within the effective span at three critical moments (*i.e.*, the formation of the first flexural crack, the initiation of major shear crack, and the ultimate state) for all the tested beams are exported based on DIC principal strain analysis and are shown in Fig. 5.5. In addition, the visualized final failure pattern of the beams together with the plotted shear crack angle is also presented. In the current study, the shear crack angle is defined as the angle between the longitudinal axis of beams and the inclined compressive strut; and the direction of compressive strut is obtained by simply connecting the two points where the dominate shear crack intersects with the longitudinal tensile and compressive reinforcement. The representative fracture stages are also indicated in the load-deflection curves by the circle markers.

Fig. 5.5a shows the crack pattern development of the reference beam. Firstly, fine vertical flexural cracks formed around the mid-span of the beam, indicating the ending of uncracked stage for beam specimens. As the applied load was further increased, diagonal major shear cracks initiated and propagated towards the loading point and the supports. Finally, the beams failed in shear at the peak load, characterized by the formation of a full-grown dominant shear crack crossing through top and bottom longitudinal reinforcement.

The crack development of the hybrid beams is presented in Figs. 5.5b and 5.5c. As can be seen, the crack patterns are different than that in the reference beam. Instead of forming sparsely spaced diagonal shear cracks, the hybrid beams with SHCC layer exhibited a unique crack pattern, which is characterized by the formation of bundles of fine cracks. It is possible that the dominate shear cracks formed in conventional concrete core were arrested by the SHCC layer and turned into multiple fine cracks in the SHCC. Although the crack width is not crucial for shear cracks, the hybrid beams can still benefit from the increased ductility conveyed by the formation of multiple micro-cracks. In consistence with the load-deflection curves, the boundary condition was found to have little influence on the crack pattern of the beams. The load and deflection levels at which the first flexural crack formed, the shear crack initiated, and the peak load are all similar between the two hybrid beams with different boundary conditions.

Additionally, it is noteworthy that the shear angles in the two hybrid beams differ significantly, even though their shear resistance is nearly identical. The shear angle is a crucial parameter in calculating the shear resistance of the SHCC in engineering models (*i.e.*, shear reinforcement equivalent theory [4] and JSCE model [2,5]), as the shear angle decides the cross-sectional area of the SHCC that can be activated to resist the shear loading.

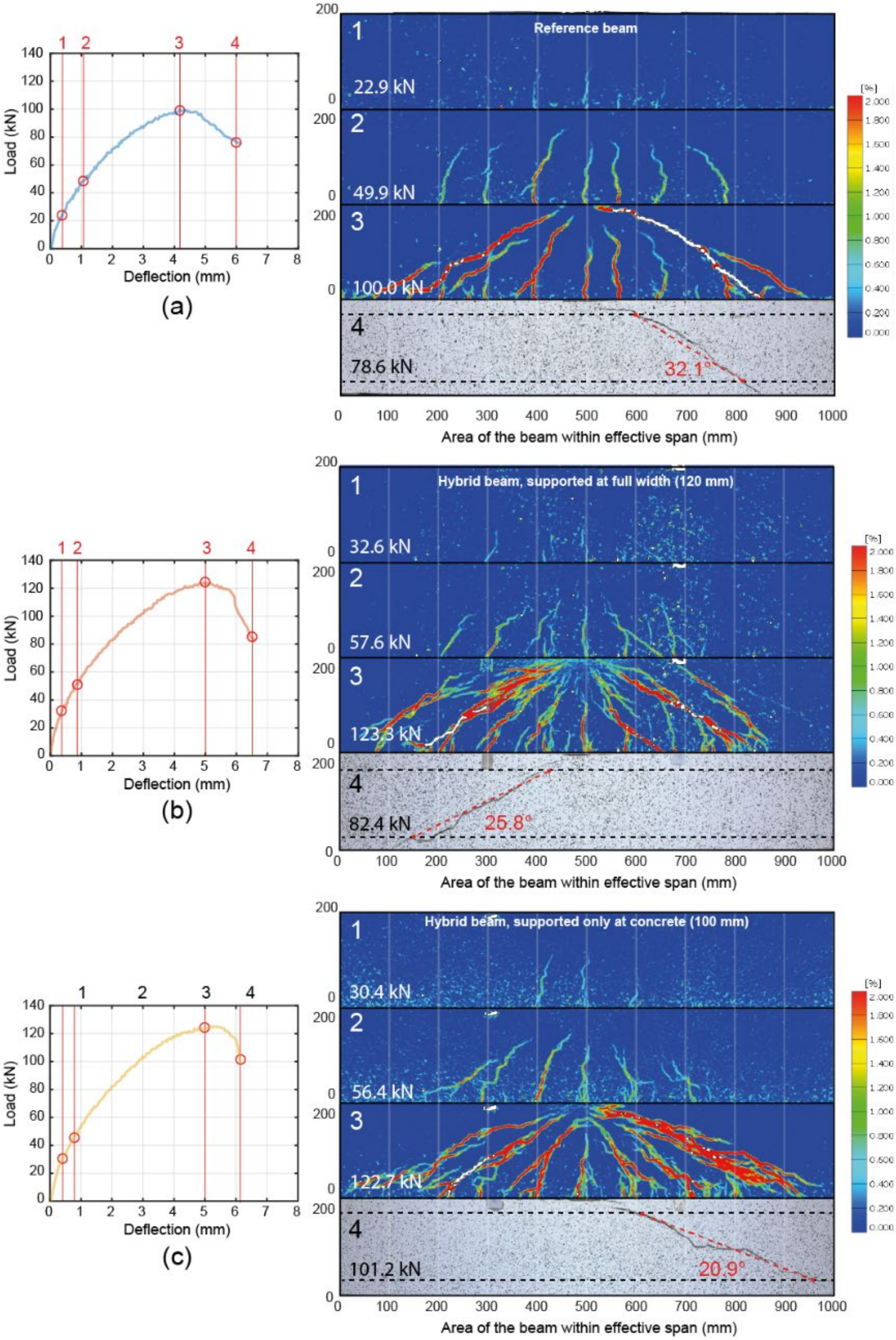

Figure 5.5: Crack pattern development within the effective span of (a) reference beam, (b) hybrid beam supported at full width, and (c) hybrid beam supported at concrete core.

In terms of the calculation of V_{SHCC} by shear reinforcement equivalent theory, the SHCC layer can be treated as additional shear reinforcement in hybrid beams since SHCC exhibits strain-hardening properties, similar to steel reinforcement. Therefore, the shear resistance of SHCC V_{SHCC} can be expressed as:

$$V_{SHCC} = \frac{A_{SHCC} \cdot f_t \cdot z}{s_f} \cdot \cot\theta \tag{5.2}$$

$$A_{SHCC} = 2 \cdot t_{SHCC} \cdot w_{SHCC} \tag{5.3}$$

where t_{SHCC}, w_{SHCC} are the total thickness and length of SHCC panel respectively, f_t is the ultimate tensile strength of SHCC, s_f is the spacing of SHCC strip and taken as 1 for continuous SHCC panels, θ is the angle between compression strut and the beam axis perpendicular to the shear force.

As for the other calculation method, as specified in JSCE, V_{SHCC} is the sum of the shear resistance provided by the fibres V_f and the matrix V_{cc}, and can be expressed by the following equations:

$$V_f = \frac{f_{ty}}{\tan\alpha} \cdot t_{SHCC} \cdot z \tag{5.4}$$

$$V_{cc} = 0.14 \cdot \sqrt[3]{f_{SHCC}} \cdot \sqrt[4]{1000/d} \cdot \sqrt[3]{100\rho_{sl}} \cdot t_{SHCC} \cdot d \tag{5.5}$$

where, f_{ty} is tensile yield strength of SHCC, f_{SHCC} is the compressive strength of SHCC, and if $\sqrt[4]{1000/d}\ or\ \sqrt[3]{100\rho_{sl}} > 1.5$, then taken as 1.5, α is the angle of shear crack to the member axis, generally $\alpha = 45°$ is recommended but in this case can used the observed shear angle from experiments.

Based on the above-mentioned equations, the shear contribution from V_{SHCC} are calculated with the two methods. Comparison between experimental results and theoretical calculation are summarized in Table 5.3. As can be seen, the calculated shear resistance from the two models varies significantly due to the difference of shear angle, while their experimental contribution is almost the same. This implies that while the method of determining the shear angle graphically from the dominant shear crack is well accepted for RC, such method may not be applicable to SHCC. This is due to the trajectory of the dominate shear crack formed in SHCC with multiple cracking characteristics can be influenced by inherent variability of the material. It has been well accepted that the tensile properties of fibre reinforced cementitious composite like SHCC has a large variability [6,7], which is caused by the scattering of matrix properties (*e.g.*, initial flaw distribution) and fibre properties (*e.g.*, fibre distribution). As shown by Fig. 5.5, the formation of the dominant shear crack in concrete resulted in the development of a bundle of micro-cracks in SHCC, which collectively cover a wide area. Due to the intrinsic variability of the matrix and fibre properties, the exact path of the final failure can be quite random within this band. This is probably the reason why the two hybrid beams possessed almost identical peak loads but had different shear angles (*i.e.*, 25.8° versus 20.9°).

Table 5.3: Comparison between theoretical calculation and experimental results.

Test beam	Ultimate shear resistance V_{test} (kN)	Addition from SHCC (kN)	Shear crack angle α	Shear reinforcement equivalent theory (kN)	JSCE code (kN)		
				V_{SHCC}	V_{cc}	V_f	V_{SHCC}
Ref	101.8	-	32.10 °	-	-	-	-
Hybrid-1	124.6	22.8	25.80 °	21.9	3.4	18.0	21.4
Hybrid-2	124.2	22.4	20.90 °	27.8	3.4	22.8	26.2

5.3.4 Interface behaviour between SHCC and concrete

Since the benefits of hybrid beams can be realized only if the structural integrity of the element is maintained over its design life, the interface condition between SHCC and concrete is crucial. Therefore, in the current study, eight LVDTs were placed on top of each beam to monitor the interfacial opening and sliding between the SHCC layers and the concrete core at four symmetric locations as shown by Fig. 5.6. These measurement points are all 200 mm away from the loading point.

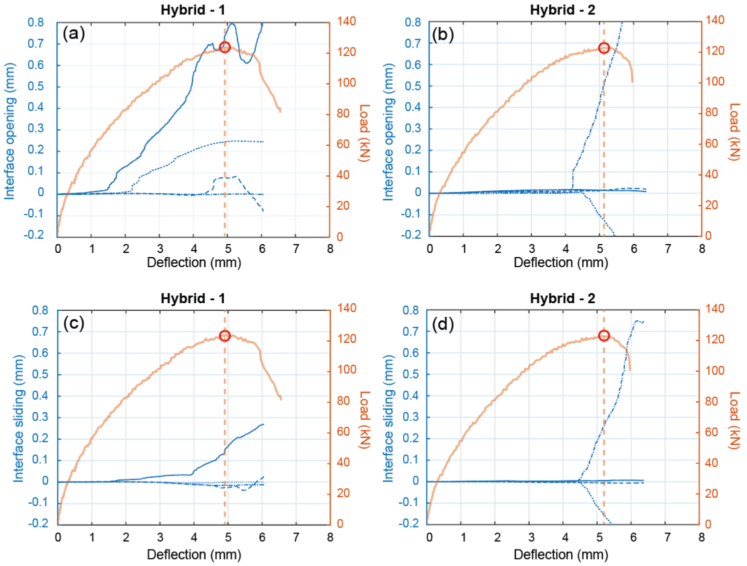

Figure 5.6: Interface opening (a) and (b), and sliding (c) and(d) at four inspection points as measured by LVDTs for hybrid beams.

Fig. 5.6 shows the interfacial opening and sliding for all hybrid beams. The four blue lines with different line style represent the measurements at the four different locations for either interfacial opening or sliding. To associate the interface behaviour with the structural response of the beam, the interface conditions were plot against the deflection of beam with the load-deflection curve superimposed in orange colour.

As can be seen, although both hybrid beams had the same interface profile and exhibited similar load-deflection response, the interfacial response were quite different. As shown by Figs. 5.6a and

5.6c, SHCC layer at one side of Hybrid-1 started to debond from the concrete core at 1 mm beam deflection. Despite that the opening values were larger than the sliding values. On the contrary, Hybrid-2 exhibited almost no debonding before reaching its peak load. This difference is not expected as both beams had the same profiled interface which is designed to provide adequate interface mechanical interlock and thus resist early-stage debonding. However, upon closer inspection of the beam after the test, it was found that the part of SHCC lamella under the loading point in the Hybrid-1 was damaged severely as shown by Fig. 5.7b. The reason might be that, during the concrete casting, the top surface of the beam was not properly levelled, resulting in an uneven surface where the top surface of SHCC cover were slightly higher than that of concrete. As a result, the SHCC cover right beneath the loading point may have exhibited an excessive compressive stress, which leads to the localized debonding as observed near the loading point. In fact, the trace of being excessively compressed can be observed in the DIC strain field (Fig. 5.5b and c), where a significant amount of microcracking in radial pattern can be seen near the loading point. Fig. 5.7a shows the top view of the Hybrid-2 beam after testing. It was found that, even though the smashing of SHCC under the loading point (Fig. 5.7b) has caused an interface crack as wide as 1 mm (Fig. 5.7c) roughly 12 cm away from the loading point, this interfacial crack disappeared around 24 cm away from the loading point (Fig. 5.7d). This suggests that the interface profile is able to resist the propagation of an interface crack even when the SHCC lamellae were unproportionally loaded. The same phenomenon can be observed also on one side of the Hybird-2 beam (Figs. 5.8), where the SHCC under the loading point experienced noticeable damage (Fig.5.8b) but the propagation of interfacial crack was arrested within short propagation path (Figs. 5.8c and d).

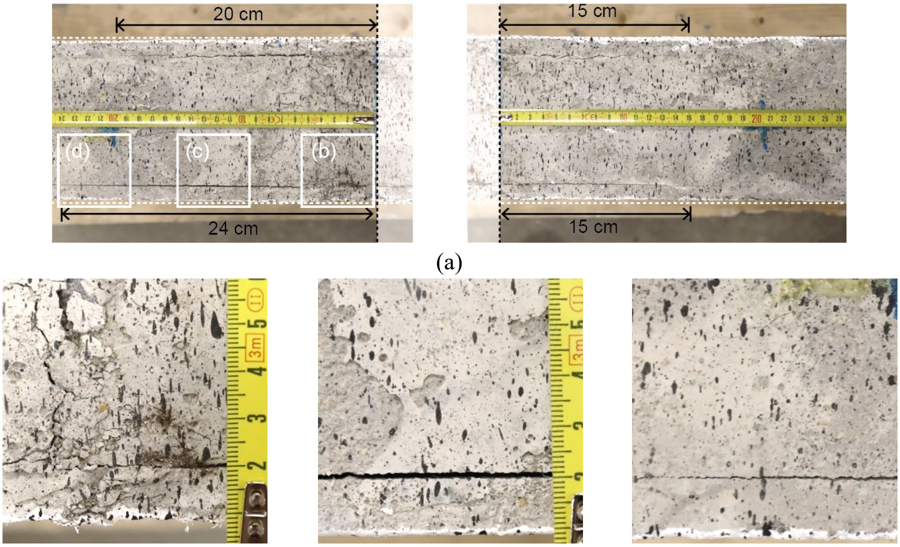

(a)

(b) (c) (d)

Figure 5.7: Top view of hybrid beam loaded at full width (Hybrid-1) after test.

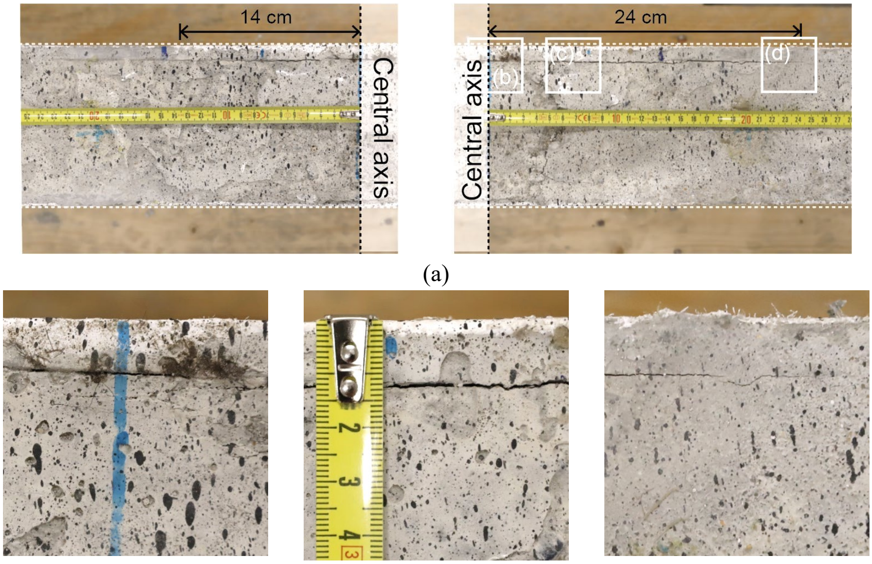

(a)

(b) (c) (d)

Figure 5.8: Top view of hybrid beam loaded at core (Hybrid-2) after test.

5.4 Numerical simulations

To further investigate the impact of boundary conditions on the shear behaviour of hybrid beams, the lattice model introduced in the previous chapter was applied to simulate three-point bending tests under different loading and support configurations. A detailed overview of the lattice model's background and capabilities is provided in the previous chapter.

Fig 5.9 shows the lattice model of a hybrid beam with thin SHCC covering the lateral surfaces. The beam model spans one meter in length, representing its effective span, and uses a mesh size of 10 mm, consistent with the previous chapter. The model comprises five element types: Concrete (blue), SHCC (red), Reinforcement (yellow), SHCC/Concrete Interface (white), and Concrete/Reinforcement Interface (also yellow). Although the experiment utilized a profiled interface, in the simulation this was simplified by assuming a smooth surface, whereas the mechanical interlocking effect of the shear-key profile was accounted for by assigning strong mechanical properties to the interface elements. Four simulations of hybrid beams were conducted in this study under different boundary conditions: loading and supporting across the full width (Hybrid-120120), loading and supporting only at the core (Hybrid-100100), loading only at the core with support across the full width (Hybrid-100120) and loading across the full width with support only at the core (Hybrid-120100).

All input parameters from the previous chapter (as shown in Table 4.4) were applied in the simulation, with the exception of the SHCC/Concrete interface elements. These elements were assigned the same modulus as concrete but only 25% of its compressive and tensile strength. The aim of this simulation is not to precisely replicate experimental behaviour but to explore the influence of various support and loading conditions.

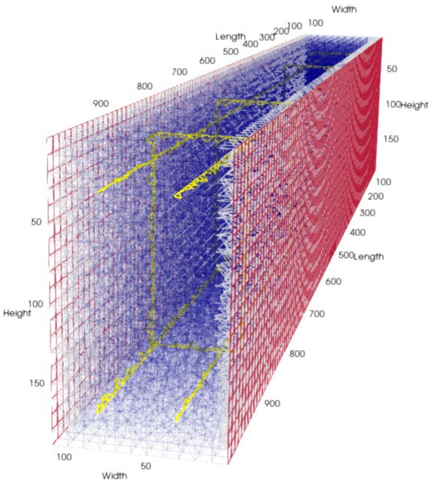

Graphical projection

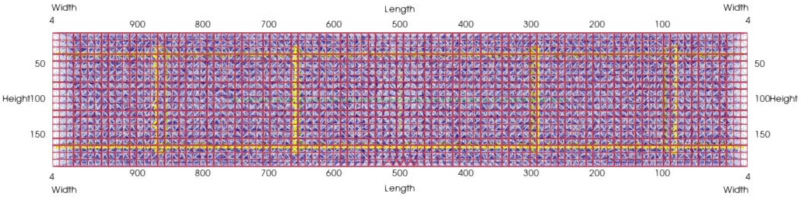

Front view

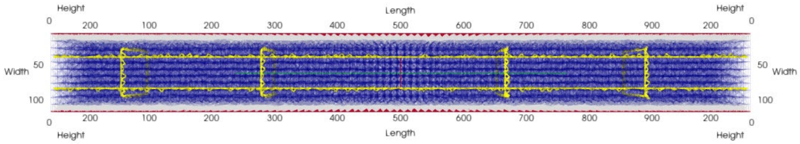

Top view

Figure 5.9: The lattice model for hybrid beams.

The simulation results for the hybrid beam under full width loading and support were used to verify the model. Fig. 5.10 compares the load-deflection response of the tested and simulated reinforced concrete beam. Overall, the chosen modelling approach successfully replicates the load-deformation behaviour. Although the model slightly overestimates the maximum capacity, it accurately captures the reduction in stiffness due to the formation of flexural and shear cracks, as well as the rapid load drop after reaching peak capacity.

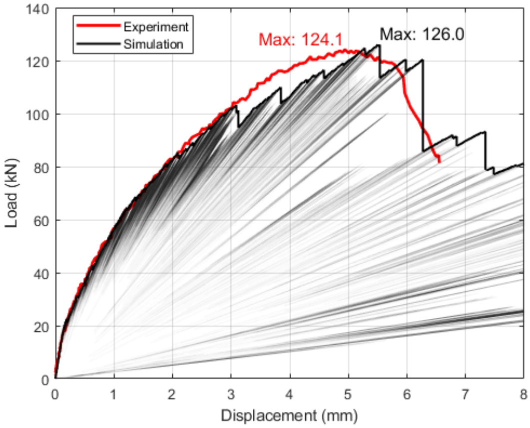

Figure 5.10: Comparison of results from simulation and experiment for the hybrid beam loading and supporting across the full width (Hybrid-120120)

Fig. 5.11 presents the crack patterns of the simulated hybrid beam at various load levels. A significant advantage of numerical modelling is its ability to visualize internal damage, which goes beyond what surface observations can reveal. To provide clearer analysis, the crack patterns in the SHCC and concrete cores are presented separately. As can be seen, the simulated crack patterns closely resemble those observed in the experiments (as shown in Fig. 5.5b), further validating the accuracy of the model. Interestingly, the crack patterns of both the cover and the core align well, indicating that the cover was effectively engaged through a strong interface bond.

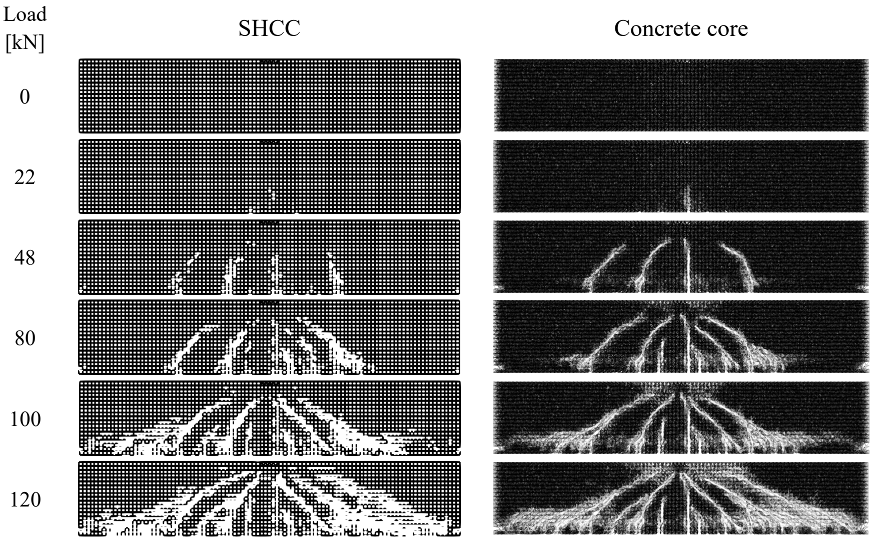

Figure 5.11: Simulated crack pattern of the hybrid beam loading and supporting across the full width (Hybrid-120120).

Fig. 5.12 presents the load-deflection results of all simulated beams. As observed, hybrid beams under different combinations of loading and support conditions exhibited nearly identical behaviour, consistent with the experimental results shown in Fig. 5.4. The additional two scenarios considered in the simulation do not appear to cause interfacial delamination. Fig. 5. 13 compares the crack pattern at peak load for the four simulated beams. Again, no significant difference can be found between the models. It can therefore be concluded that the SHCC cover was effectively engaged in all simulated models, regardless of the loading and support conditions. This further demonstrates that the interface bond between the SHCC and concrete is strong enough to transfer shear loads, ensuring the structural integrity of the hybrid systems even under the most critical conditions.

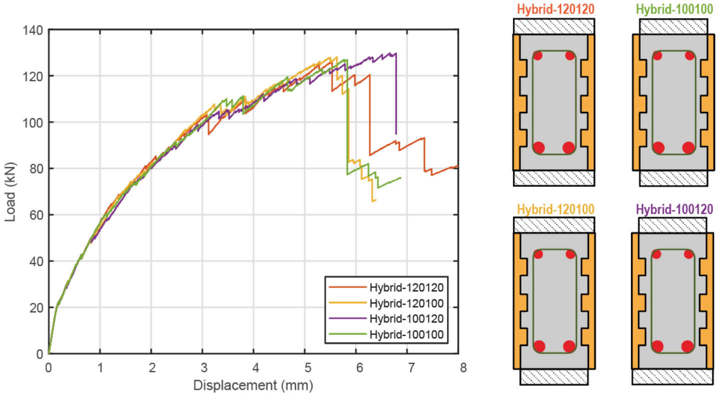

Figure 5.12: Simulated load deflection responses of hybrid beams under different loading/supporting conditions.

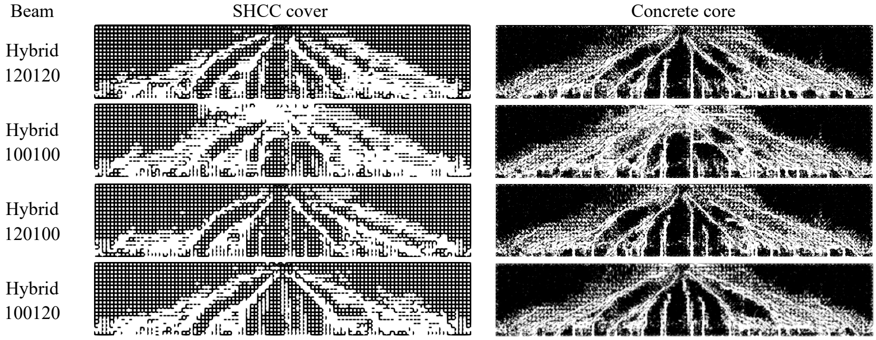

Figure 5.13: Comparison of simulated crack patterns at peak load for hybrid beams under varying loading and support conditions.

5.5 Conclusions

An experimental and numerical study was performed aiming to investigate the shear behaviour of reinforced concrete beams with laterally applied SHCC cover. The main objective of this chapter is to investigates whether the hybrid beams with thin SHCC layers on its lateral surfaces can maintain the structural integrity under shear loading. The influence of boundary condition was particularly analysed. The main findings of the current study are:

1. Applying 1-cm-thick SHCC cover can be an effective way to enhance the shear resistance of RC beams. A profiled interface can effectively mitigate interfacial delamination under shear loading, thereby ensuring the structural stability of the covered system. The contribution of SHCC to the peak load of hybrid beams is 21.9 kN.
2. The SHCC cover can arrest the dominate shear cracks formed in concrete and turned the crack in concrete into multiple fine cracks in the SHCC. This featured cracking behaviour has led to an increased post-cracking ductility and an enhanced energy absorption capacity in the hybrid beams.
3. Both experimental and numerical analysis shows that the boundary conditions, i.e., the width at which the hybrid beams were loaded and supported, did not influence the effect of the SHCC cover. This indicates that the profiled interface is strong enough to resist interfacial delamination, even under the most critical loading and support conditions.

Additional discussion: Effects of stirrup on SHCC contribution

Since SHCC has been demonstrated to significantly enhance the shear resistance of reinforced concrete beams, it is worthwhile to investigate whether SHCC alone can serve as effective shear reinforcement and to evaluate how this application influences the strengthening properties of SHCC. To extend the main testing program, two shear-deficient beams without stirrups were prepared and tested: one as a reference reinforced concrete beam (SD-Ref) and the other as a hybrid beam (SD-Hybrid). Fig. 5.14 presents the geometry and reinforcement details of these beams. The two beams were tested using the same procedure as the other beams.

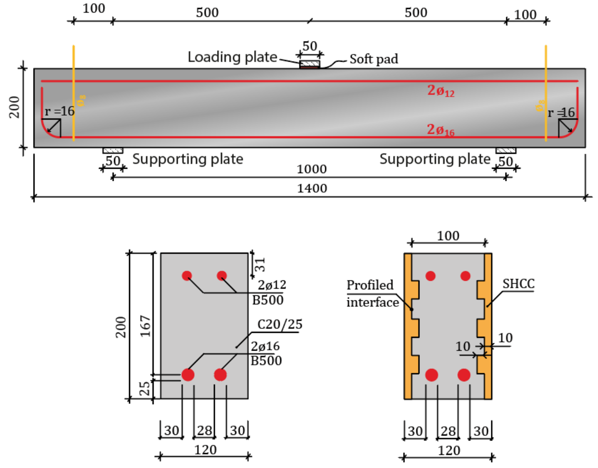

Shear-deficient
reference beam

Hybrid beam with
profiled interface

Figure 5.14: Geometry and reinforcement details of the shear deficient beams.

Fig. 5.15 shows the load-deflection curves for the beams without stirrup. The reference beam (SD-Ref) experienced a sudden load drop when the load continued to increase steadily, while the hybrid beams exhibited substantial ductility and had around two times higher deflection than that of reference specimen when reaching its ultimate state. While the peak load of the reference beam is 53.5 kN, the hybrid beams reached 65.6 kN. Interestingly, although the used SHCC layers were identical in beams with stirrups and beams without stirrups, the contribution of the SHCC layers to the peak loads is different. While for the beams with stirrups, the average increase in load is 21.9 kN, the contribution of SHCC here is only 12.1 kN, which indicates that the activation of SHCC may be influenced by the presence of stirrups. Similarly, as in the first group, part of the strength gain comes from higher compressive strength of concrete (around 5% or 8%, considering that the shear capacity is proportional to $f_{ck}^{1/3}$ or $f_{ck}^{1/2}$, respectively), and remaining contribution is from crack bridging force provided by PVA fibres in SHCC. It is possible that the addition of stirrups led to a decrease of shear angle and thus activated more SHCC in the shear plane.

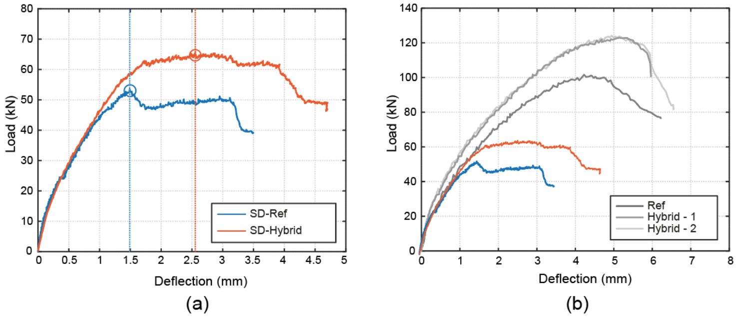

Figure 5.15: Load-deflection behaviour of tested beams in (a) shear deficient beams only, and (b) shear deficient beams along with results on beams with stirrups in grey.

Fig. 5.16a shows the crack pattern development of the reference beams without stirrups. By comparing Fig. 5.5a and Fig. 5.16a, it can be seen that the initial crack pattern until the initiation of shear crack in the beams with shear reinforcement was observed to be similar to that observed in the beams without shear reinforcement. However, after the formation of diagonal shear cracks, the stirrups started to play a key role in transferring the shear. As a result, dominant shear cracks formed on both side of the shear span in the reference beam with stirrups, unlike the reference beam without stirrups in which major shear crack is only clearly exhibited on one side of the specimen.

Fig. 5.16b shows the crack pattern development of the hybrid beams without stirrups. In contrast to Fig. 5.5b, the hybrid beams without stirrup exhibited very limited multiple cracking behaviour. This is in consistent with our previous observation from Fig. 5.15 that SHCC may have not been fully activated. It is possible that, when no stirrups existed in the tested specimens, the rapid formation of the major shear crack led to localized high strain rate in SHCC, therefore leading to unsaturated multiple cracking. Still, the crack pattern between the hybrid and reference beams are different. In the reference beam, dominant shear cracks formed only on one side of the shear span, while the hybrid beams developed visible shear cracks on both sides. This proves that SHCC had a similar effect as that of stirrups in modifying the crack pattern.

To conclude this discussion, it is important to highlight that the contribution of SHCC to the peak load of hybrid beams varies significantly between those with stirrups (21.9 kN) and those without (12.7 kN). This discrepancy suggests that the inclusion of stirrups may have reduced the shear angle, thereby activating a greater amount of SHCC in the shear plane. Future research is essential to further explore this relationship and to understand the underlying mechanisms at play. Investigating the interactions between stirrups and SHCC will provide valuable insights that could inform design practices and enhance the performance of hybrid beam systems.

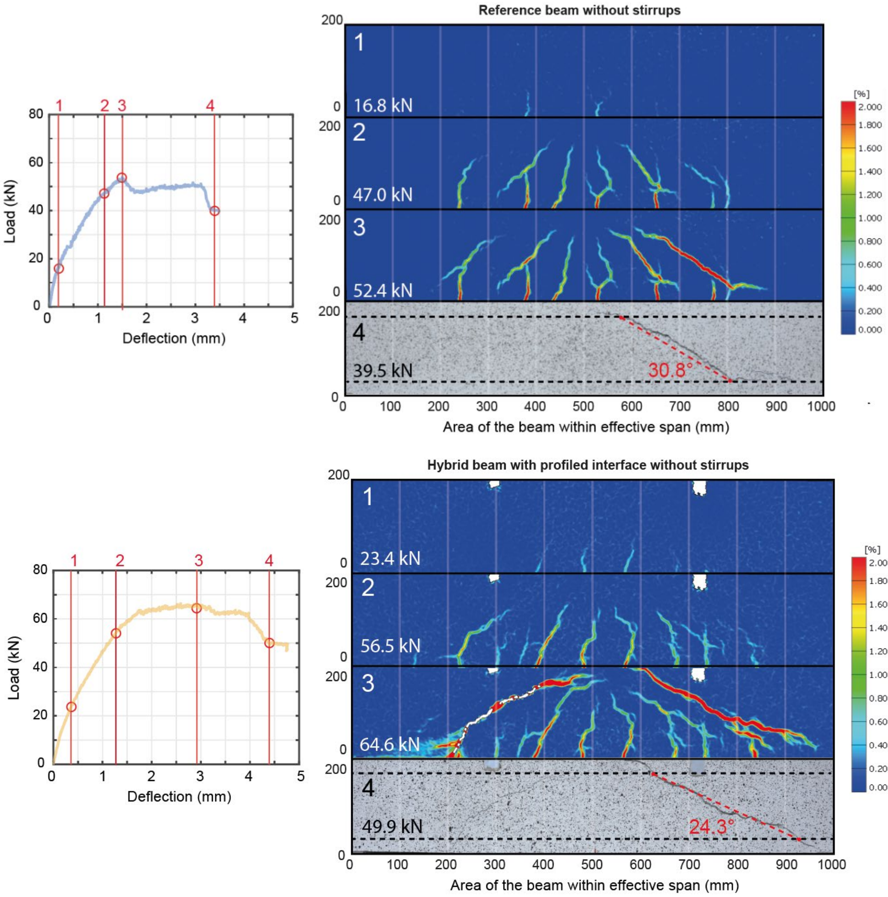

Figure 5.16: Crack pattern development within the effective span of (a) reference beam without stirrups and (b) hybrid beam without stirrups.

References

[1] K.M.A. Hossain, S. Hasib, T. Manzur, Shear behavior of novel hybrid composite beams made of self-consolidating concrete and engineered cementitious composites, Eng Struct 202 (2020) 109856. https://doi.org/10.1016/J.ENGSTRUCT.2019.109856.

[2] R. Zhang, P. Hu, X. Zheng, L. Cai, R. Guo, D. Wei, Shear behavior of RC slender beams without stirrups by using precast U-shaped ECC permanent formwork, Constr Build Mater 260 (2020) 120430. https://doi.org/10.1016/J.CONBUILDMAT.2020.120430.

[3] J. Qi, Z.J. Ma, J. Wang, Y. Bao, Post-cracking shear behaviour of concrete beams strengthened with externally prestressed tendons, Structures 23 (2020) 214–224. https://doi.org/10.1016/J.ISTRUC.2019.09.009.

[4] S.W. Kim, W.S. Park, Y. Il Jang, L. Feo, H. Do Yun, Crack damage mitigation and shear behavior of shear-dominant reinforced concrete beams repaired with strain-hardening cement-based composite, Compos B Eng 79 (2015) 6–19. https://doi.org/10.1016/J.COMPOSITESB.2015.04.020.

[5] Japan Society of Civil Engineers, Recommendations for Design and Construction of High Performance Fiber Reinforced Cement Composites with Multiple Fine Cracks (HPFRCC), 2008.

[6] S. He, E.H. Yang, Non-normal distribution of residual flexural strengths of steel fiber reinforced concretes and its impacts on design and conformity assessment, Cem Concr Compos 123 (2021) 104207. https://doi.org/10.1016/J.CEMCONCOMP.2021.104207.

[7] S.H.P. Cavalaro, A. Aguado, Intrinsic scatter of FRC: an alternative philosophy to estimate characteristic values, Materials and Structures/Materiaux et Constructions 48 (2015) 3537–3555. https://doi.org/10.1617/S11527-014-0420-6/FIGURES/17.

6

Hybrid reinforced concrete beams with cast and 3D printed U-shaped self-healing SHCC cover[4]

Following the initial assessment of hybrid beams incorporating self-healing SHCC layer on their bottom or lateral surfaces, this chapter aims to advance the concept by introducing hybrid beams with an U-shaped cover zone. It also details the fabrication of U-shaped self-healing SHCC covers, which were created using both mould-casting and 3D printing techniques, serving as lost formwork for the reinforced concrete beams. Specifically, the experiments involve testing the structural and healing characteristics of eight beams, comprising two reference beams and six hybrid beams, among which four feature precast covers and two incorporate 3D-printed covers. The research focuses on the performance under both flexural and shear loading, examining aspects such as load-bearing capacity, surface crack pattern, crack propagation between layers, and healing effectiveness. Findings reveal that mould-casted SH-SHCC covers enhance crack control and sealing without compromising beam properties, offering comparable or improved load capacity and ductility under shear and flexure. Although 3D-printed covers are slightly less effective in crack control, they still improve overall performance and offer advantages in manufacturing efficiency. Both cover types effectively prevent delamination and disperse major cracks into finer, healable cracks, facilitating crack healing observed after one-month moist curing.

---

[4] Part of this chapter has been published in:

He, S., Nuri, M., Jonkers, H. M., Luković, M., & Schlangen, E. (2024). Structural behaviour of reinforced concrete beams with self-healing cover zone as lost formwork. Developments in the Built Environment, 18, 100458.

6.1 Introduction

The development of novel high-performance cement-based materials has opened new possibilities in designing more resilient and versatile concrete structures. The new materials can offer improved mechanical properties, such as higher tensile strength [1], better ductility [2,3], and enhanced durability [4], which can improve the structural performance of concrete structures under different loading and environmental conditions. However, while advanced materials offer promising advantages, they typically come at a higher cost and demand specialized production processes. This renders them economically and technically impractical for fully replacing conventional concrete. To address this challenge, researchers have devised hybrid structural elements, merging high-performance concrete with conventional concrete to minimize the use of costly materials in individual structural components [5–8]. An illustrative instance of this innovation is the creation of SHCC/RC hybrid elements, the specifics of which are outlined in Chapters 4 and 5.

As emphasized in the previous chapters, the interface between distinct constituents holds paramount importance in designing composite elements to guarantee optimal performance. A robust interface ensures effective stress transfer, prevents delamination, and minimizes the risk of premature failure [9]. In the case of hybrid RC elements with SHCC, various methods have been proposed to ensure the integrity of the interface between the layers. Aside from the shear-key pattern proposed in the prior chapter, conventional practices encompass surface preparation to eliminate contaminants, application of bonding agents to bolster adhesion [10], and integration of mechanical interlocking features such as grooving [11] or steel anchorages [12]. However, most of these methods entail multiple procedural steps and the requirement of intricate moulds for production, occasionally proving impractical and inefficient.

The extrusion-based 3D concrete printing (3DCP) technology provides another possibility to tackle the delamination issue. 3D printing of concrete is effective at producing desired surface texture due to its precise layer-by-layer deposition process, allowing for customizable patterns and textures to be easily integrated into the printed structure [13]. Therefore, additional efforts in treating the interface may be avoided when 3D printing technology is used to fabricate permanent formworks, into which fresh concrete is cast to build composite structural members [14].

The aim of the current chapter is to assess the structural response and healing performance of hybrid reinforced concrete beams with 3D-printed U-shaped cover, and to compare the performance with hybrid elements made with precast U-shaped cover. This cover zone is made of self-healing strain-hardening cementitious composite (SH-SHCC), designed to control crack width and promote crack healing. A total of 8 beams were prepared and tested, including 2 reference RC beams, 4 hybrid beams with mould-cast cover, and 2 hybrid beams with 3D-printed cover. These beams were divided into 2 groups for testing, one subjected to flexural loading and the other to shear loading. Subsequent to testing, the beams were cut into smaller segments. Certain segments underwent epoxy impregnation to investigate crack propagation from the core to the cover, while others underwent one month of moisture curing, and subsequently also epoxy impregnation. Surface crack patterns before and after healing were then compared to qualitatively assess the healing performance.

6.2 Materials and tests

6.2.1 Experimental design

The testing protocol comprises two sets of beams: one exposed to flexural loading in a 4-point bending setup, and the other exposed to shear loading in a 3-point bending setup. In addition to investigating the load-deflection behaviour, each set of beams is tailored to address different testing objectives. For the beams subjected to flexural loading, the primary objective was to assess the potential of the SH-SHCC cover in enabling the development of fine cracks, thereby facilitating rapid healing. In the case of beams undergoing shear, emphasis is placed on evaluating the capacity, post-peak ductility and the energy dissipation ability.

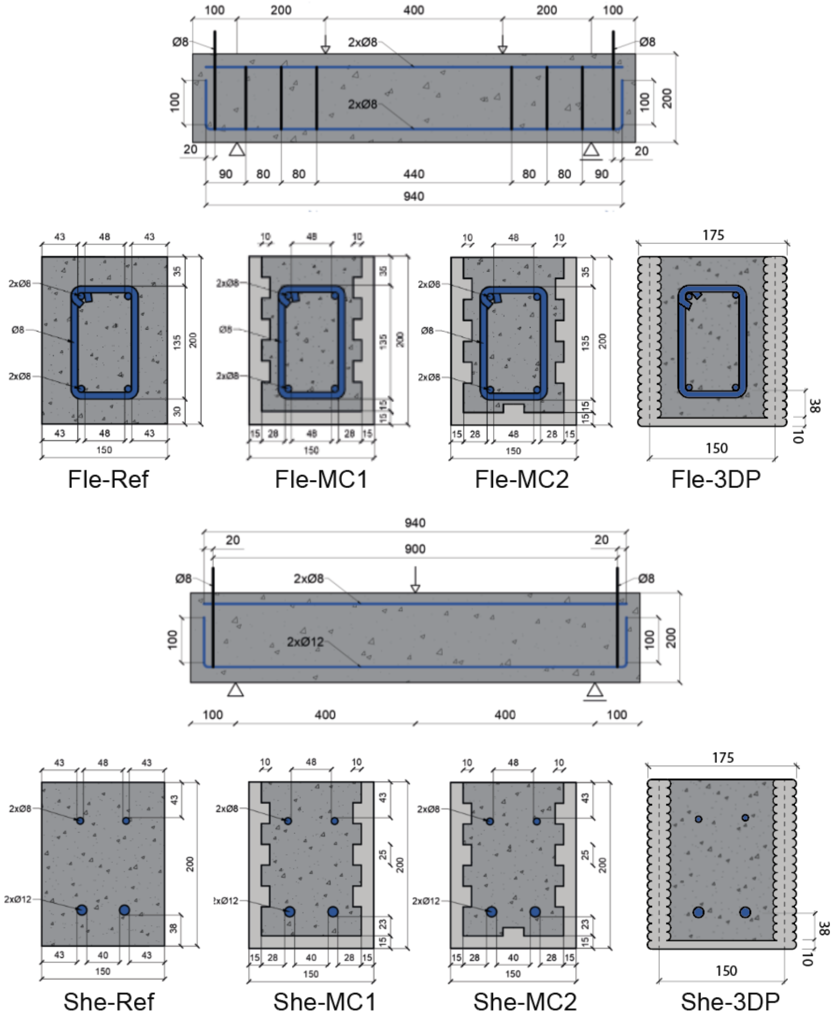

Figure 6.1: Design details of the beams [unit in mm].

Each set of beams contains 4 specimens, including 1 conventional reinforced concrete beam as a reference specimen, 2 hybrid beams consisting of a mould-cast (MC) U-shaped cover, and 1 hybrid beam with a 3D-printed (3DP) cover. The reference beams are denoted as ‘Fle-Ref’ and ‘She-Ref’. The reinforcement details were designed to ensure that the reference beams would fail in flexure and shear, respectively. The geometry and reinforcement details of all the beams are given in Fig. 6.1. All side surfaces of one group of hybrid beams (Fle-MC2 and She-MC2) have a profiled interface which is made of a line of protruding shear-key from the SHCC layer, while in the second group (Fle-MC1 and She-MC1), the bottom surface of SHCC has a smooth interface All interfaces between the cover and the core have been treated with a thin layer of Vaseline. The design principles and geometric details of the Vaseline-treated shear-key pattern are discussed in Chapter 4.

The reference beams and the hybrid beams with mould-cast cover have a cross-section of 150 mm × 200 mm. The beams with 3D-printed cover (Fle-3DP and She-3DP) feature a slightly larger cross-sectional area, due to a thicker printed cover layer and the applied nozzle size. Our preliminary trials indicate that, to prevent fibre jamming, the nozzle diameter must exceed 1.5 cm, resulting in an average cover thickness of approximately 2.5 cm. Still, as depicted in Fig. 6.2, the printed cover zone exhibited satisfactory shape retention ability as small variation in the average thickness of the cover along the height of the beam was observed. In addition, the hybrid beam with printed cover maintains identical reinforcement details and consistent cover depth between the longitudinal rebar and the bottom surface (*i.e.*, 38 mm).

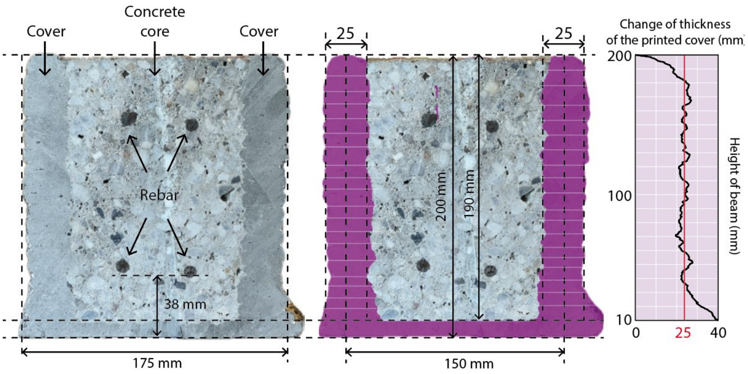

Figure 6.2: Cross-section of hybrid beam with 3D-printed cover zone with highlighted area of the cover zone.

6.2.2 Materials and sample preparation

Table 6.1 shows the mixture compositions of SH-SHCC and concrete used in the current study. The mix design of the SH-SHCC from previous chapters was modified for 3D printing. The main difference is that the SH-SHCCs adopts an ultra-high-molecular-weight polyethylene (PE) fibre instead of Polyvinyl alcohol (PVA) fibre used in previous chapters. The PE fibre, being thinner and stronger compared to the PVA fibre, leads to a decrease in the required volume and thus enhances the pumpability of the material during 3D printing. Only 1% by volume of PE fibre is incorporated into the mix, contrasting with the 2% typically used for PVA fibre. The physical and geometrical properties of the PE fibre are provided in Table. 6.2.

Table 6.1: Mixture compositions of SH-SHCC and concrete [unit in kg/m3].

Material	SHCC-MC	SHCC-3DP	Concrete
CEM I 52.5 R	-	-	260
CEM III/B 42.5 N	842	807	-
Silica fume	94	115	-
Limestone powder	468	448	-
Sand (0.125-4 mm)	-	-	847
Gravel (4-16 mm)	-	-	1123
PE fibre (vol.%)	10 (1%)	10 (1%)	-
Healing agent	20	20	-
Water	374	359	156
Superplasticizer	3	3	0.3

Table 6.2: Physical and mechanical properties of PE fibres.

Length (mm)	Diameter (µm)	Density (kg/m3)	Nominal tensile strength (MPa)	Young's modulus (GPa)	Elongation at break
6	20	980	3000	110	3%

Specifically, the modified SH-SHCC matrix has Blast furnace slag (BFS) cement CEM III/B 42.5 N and silica fume as binder. Silica fume was added to enhance the bond strength between PE fibre and cement-based matrix and to improve the fresh properties of the mix. Finely grinded limestone powder was used as filler. Two different SH-SHCCs were used to prepare mould-cast cover (SHCC-MC) and 3D-printed cover (SHCC-3DP), as can be seen in Table 6.1. The main difference between the mixes is the amount of silica fume used, as silica fume controls the workability of the fresh materials.

All the hybrid beams in the current study were casted in two steps. In the first step, SH-SHCC covers were prepared either by mould-casting or by 3D-printing. In the second step, reinforcement cages were placed in, and conventional concrete was poured. The mould-cast covers were made with a plywood mould having a piece of foam fixed at the bottom of the mould (Fig. 6.3). The foams were glued with 10-mm-thick silicon rubber sheets having a reverse shape of the desired shear-key pattern at both side walls. By casting the SH-SHCC into the remaining gap, the fresh material will fill into the holes of the rubber sheet and then form the resulting protruding keys as shown in Fig. 6.3.

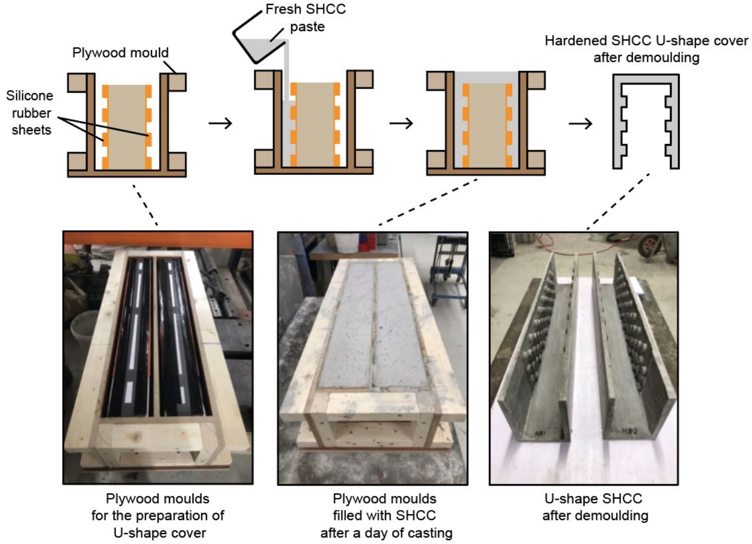

Figure 6.3: Preparation procedure of the SH-SHCC cover.

Extrusion-based 3D printing was employed to prepare U-shaped SH-SHCC covers. The 3DCP set-up consists of three primary components: a 3-degree of freedom Computer Numerical Control (CNC) system, a PFT Swing-M type material conveying pump, and a nozzle (Fig. 6.4). The CNC machine can operate within an area of 1100 mm length, 720 mm width, and 290 mm height. The material conveying pump (also known as progressive cavity pump) that provided primary forces for pumping, and the extrusion of fresh mixtures was based on a rotor and stator configuration. A 5-metre-long hose with an inner diameter of 25 mm was used to connect the pump and the nozzle. This study selected a down-flow nozzle featuring a circular 10 mm diameter opening, chosen for its distinctive capability to produce a rougher surface texture. This is because, as each new layer is extruded out from the nozzle, it compresses the underlying substrate, thereby generating a textured vertical surface during deposition. Fig. 6.5 shows the appearance of the casted and printed covers as well as a close shot of the vertical surface. The resulting texture of printed cover (Fig. 6.5d) is poised to improve interface integrity, akin to the shear-key pattern in mould-cast covers (Fig. 6.5c).

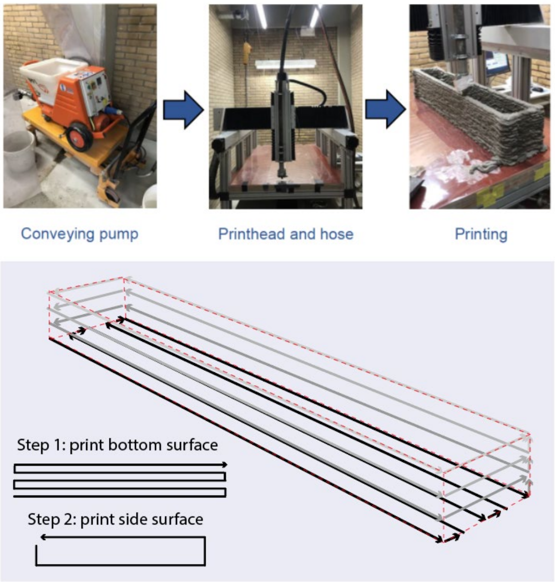

Figure 6.4: Set-up for the fabrication of the 3D-printed cover as well as the printing path map.

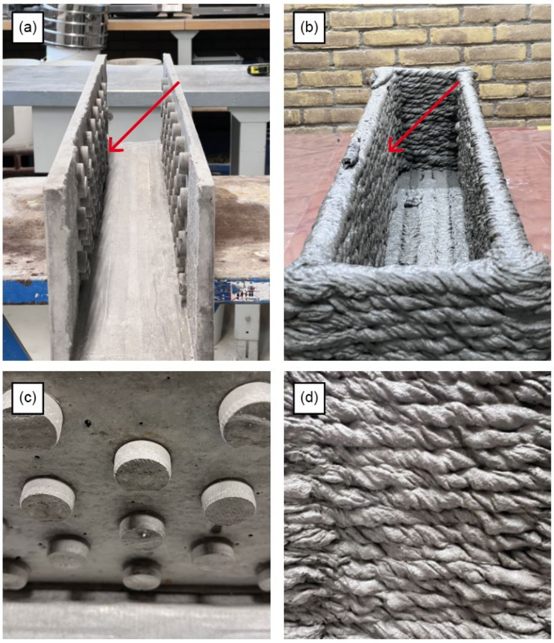

Figure 6.5: Pictures of (a) mould-cast cover and (b) 3D-printed cover, as well as their detailed surface textures.

Roughly 1 day after printing and casting, all covers were moved to a climate room (20◦C and ≥98% RH) for curing of 14 days before casting of concrete. Then, SH-SHCC covers were taken out from the climate room and placed into plywood mould. On top of the SH-SHCC covers, reinforcement cages were placed with appropriate spacers. Subsequently, the concrete was cast and compacted using a vibration needle. The hybrid beams were then cured for 28 days in sealed conditions before testing.

6.2.3 Testing

The beams underwent testing in a four- or a three-point-bending configuration, as depicted in Fig. 6.6a. Both tests were conducted under displacement control at a rate of 0.01 mm/s. The relative vertical mid-point deflection of the beams with respect to the supports was measured using a LVDT while deformation of the beams was tracked using DIC on both sides. Prior to DIC measurement, specific regions of the beam were painted white and adorned with a black speckle pattern applied using an air gun. Images for DIC were captured at 10-second intervals throughout the loading process, with a resolution of 0.08 mm/pixel. Subsequently, post-processing of DIC results was performed using a freely available version of GOM Correlate software. Given that interfacial delamination typically poses a concern for layered systems, LVDTs were arranged atop the hybrid beams to detect the interfacial opening between the core and the cover. For beams subjected to 4-point bending, the measuring points were positioned at the mid-span, whereas for beams undergoing 3-point bending, two sets of LVDTs were installed 10 centimetres away from the loading point as shown in Fig. 6.6b.

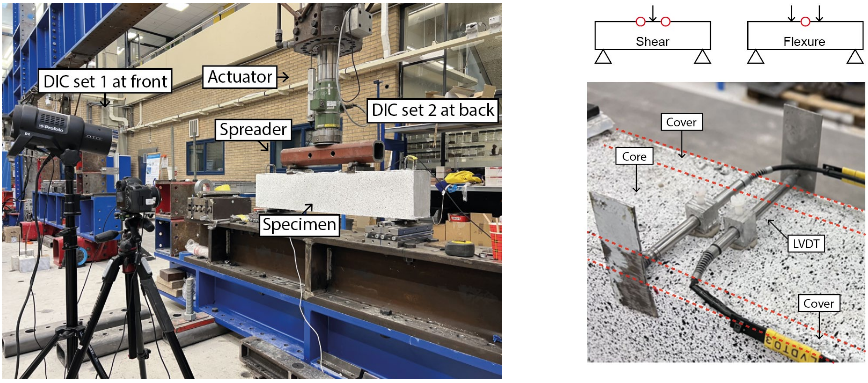

(a) (b)

Figure 6.6: (a) Experimental set-up for beam specimens with DIC measurement on both sides and (b) LVDT sets for the measurement of interfacial opening.

The corresponding compressive and tensile properties of the SH-SHCC were assessed at the same testing age. Details of the testing method can be found in ‘Materials and Tests’ section of Chapter 2 and Chapter 4. The results are presented in Table 6.3.

6.3 Results and discussion

6.3.1 Material properties

Fig. 6.7 presents the stress-strain curves for the two types of SH-SHCC materials. As previously emphasized, the tensile properties of SH-SHCC play a pivotal role in the overall functionality of hybrid beams. The ductile nature of this material not only accommodates differential deformations between the cover and the core but also facilitates the development of small cracks, which enables prompt and robust healing. Notably, both mixtures exhibit significant tensile strain hardening behaviour. Although the 3D-printed mixture contains a slightly higher content of silica fume aimed at enhancing buildability, no noticeable changes in tensile behaviour are observed. Therefore, both mixtures can be considered to possess similar mechanical properties. Table 6.3 provides a summary of the mechanical properties of SH-SHCCs and concrete. The compressive strengths of SHCC are around 25% higher than that of concrete. As mentioned also in previous chapters, opting for a relatively stronger SHCC over traditional concrete is intended to ensure the cover can function as lost formwork to produce precast elements. Additionally, a stronger cover zone with a dense microstructure is anticipated to enhance the durability of the structural element.

Table 6.3 Results of uniaxial compression and tension tests.

Mixture	Compressive strength (MPa)	First cracking strength (MPa)	Ultimate tensile strength (MPa)	Ultimate tensile strain (MPa)
SHCC-MC	59.4±0.7	1.9±0.3	2.8±0.26	2.6%±0.4%
SHCC-3DP	60.2±0.9	2.0±0.2	2.6±0.21	3.1%±0.8%
Concrete	48.4±2.0	-	-	-

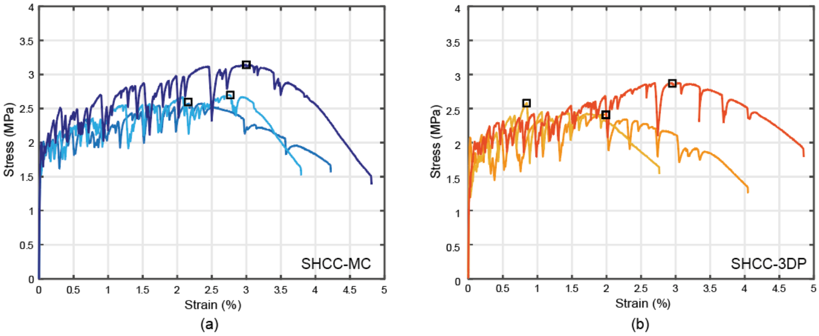

Figure 6.7: Stress-strain curves of SHCC under direction tension for (a) mould-cast cover and (b) 3D-printed cover.

6.3.2 Flexural performance of the hybrid beams

Fig. 6.8a illustrates the comparison of load versus mid-span deflection responses for the beams tested under flexural loads. As can be seen, the load-deflection relationship of the hybrid beams (*i.e.*, Fle-MC1, Fle-MC2 and Fle-3DP) differed significantly from that of the reference beam (Fle-Ref). The hybrid beams exhibited a higher tension stiffening in the stabilized cracking stage, and a higher load-bearing capacity compared to the reference beam. Strain hardening capacity of the cover played a significant role in contributing to the bending moment resistance of the beam.

Moreover, it is found that the interface properties between the cover and the core influenced the structural response of the hybrid beams with mould-casting cover. The presence of a line of shear-keys at the bottom interface provided additional mechanical resistance, resulting in 10% (14kN) increase in load-carrying capacity. This enhancement probably stemmed from a more synchronized behaviour between the cover and the core, leading to the activation of more SH-SHCC to bear the tensile load. This is in line with interface opening detected at Fig. 6.8b. Besides, despite the larger cross-section and thicker cover of the Fle-3DP beam, its load capacity remained lower than that of the hybrid beam with bottom shear-key. This underscores the critical significance of the interface condition to the load bearing capacity of the hybrid elements.

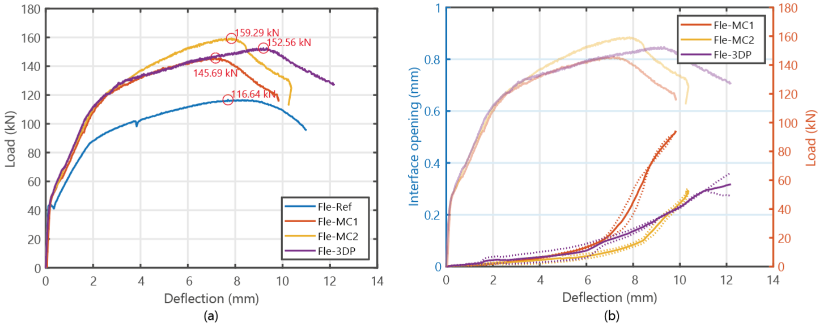

Figure 6.8: (a) Load-deflection response of the tested beams under flexural loading and (b) interface opening between cover and core (each solid lines are averaged values from 2 LVDTs, while dotted lines are results from individual LVDTs).

Fig. 6.8b illustrates the evolution of interface opening, measured by LVDTs on the top surface of the hybrid beams. Dotted lines represent readings from individual LVDTs, whereas solid lines depict the averaged results for each beam. It is evident that the average opening values for all hybrid beams remained consistently below 0.1 mm throughout the tests. Despite concerns regarding interfacial delamination in layered systems, all hybrid beams exhibited robust structural integrity throughout the testing. Furthermore, it is evident that the hybrid beam with a 3D-printed cover displayed an interface profile comparable to that of hybrid beams with mould-cast covers. This similarity suggests that the texture resulting from the printing process may have served a similar function to resist interfacial delamination as the shear-key pattern at the mould-cast covers.

Fig. 6.9a depicts the crack patterns based on DIC principal strain analysis in the constant bending moment region for four key stages. These stages correspond to 1) crack formation stage, 2) stabilized cracking stage, 3) reinforcement yielding stage, and 4) ultimate stage of the reference beams. As can be seen, all beams failed as per design, exhibiting flexural tension failure characterized by flexural cracks on the tension side and concrete crushing on the compression side. The crack patterns reveal that all hybrid beams developed significantly more cracks compared to the reference beam. Unlike the reference beam, which exhibited only a few large cracks, the hybrid beams, equipped with either mould-cast or 3D-printed covers, displayed closely spaced fine cracks across the constant bending moment region. Moreover, the hybrid beam with bottom shear-keys displayed an increased occurrence of cracks, which were also more evenly distributed across all deflection levels. This phenomenon helps to elucidate its previously observed higher peak load capacity.

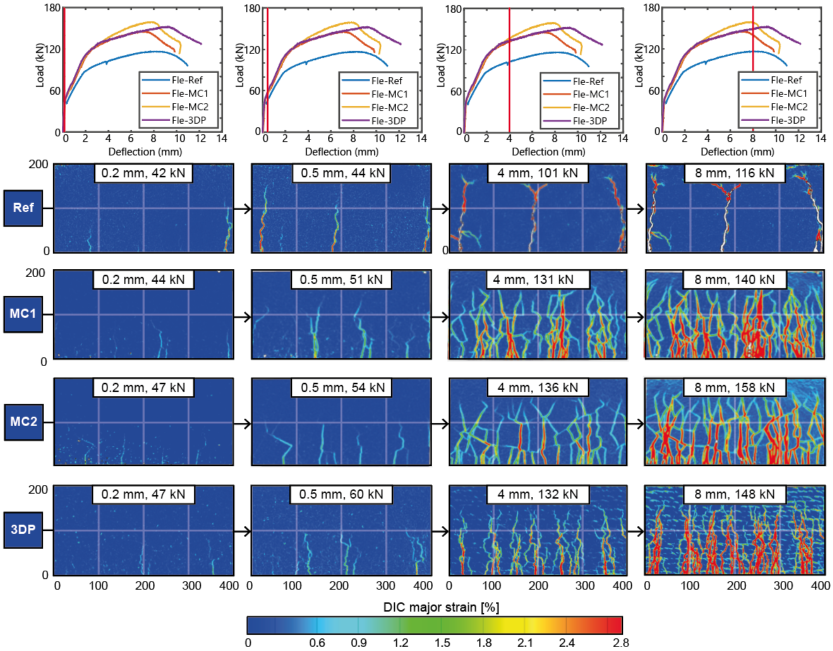

Figure 6.9: Crack pattern development at critical stages (i.e., crack formation stage, stabilized cracking stage, reinforcement yielding stage, and ultimate stage of the reference beams)

All hybrid beams demonstrated enhanced control over crack widths as a result of forming more cracks. In Fig. 6.10a, the development of the maximum crack widths along the bottom edge of the beams, as a function of deflection, is depicted. The maximum values correspond to the maximum crack width observed from the two side of beams by DIC. It is clear that the maximum crack width of the reference beam increased linearly with deflection. In contrast, for the hybrid beams, a distinct pattern of delayed crack width development was observed due to the generation of more cracks rather than the widening of existing ones. Consequently, the hybrid beams achieved higher load capacities while maintaining smaller crack widths (Fig. 6.10b). If a surface crack width limit of 0.3 mm is adopted as a benchmark, in line with the prescribed threshold in Eurocode 2 for reinforced concrete under quasi-permanent load across most exposure classes (excluding X0 and XC1), the reference beam exhibited maximum crack widths surpassing 0.3 mm at a load of 59.8 kN. The hybrid beams with mould-cast cover managed to confine crack widths below 0.3 mm until reaching loads of 124.7 kN and 137.3 kN, which is after reinforcement already yielded. The hybrid beam with 3D-printed cover exhibited 100.05 kN when its maximum crack width reached 0.3 mm. Despite overall enhancements, hybrid beams with mould-cast covers surpassed those with printed covers in terms of their ability to control crack width.

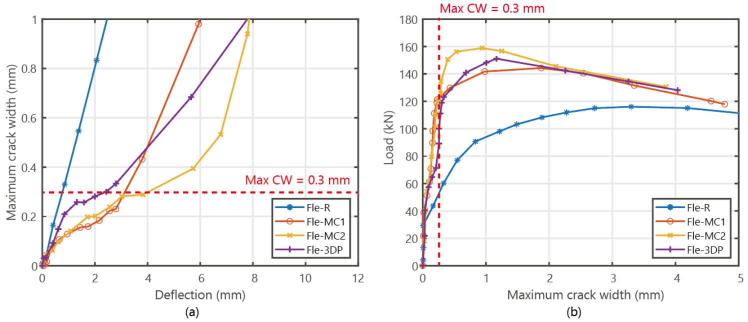

Figure 6.10: Interface opening expressed as (a) development of maximum crack width versus mid-point deflection, and (b) relation between load and maximum crack width.

Nevertheless, since all load levels were achieved after reinforcement yielding, the quantity of reinforcement can be determined solely by the structural capacity required under the ultimate limit state. Therefore, no additional reinforcement is required to control crack widths. Moreover, this approach facilitates the efficient utilization of high-strength steel, where crack control is governing for design.

6.3.3 Shear performance of the hybrid beams

Fig. 6.11a illustrates the load versus mid-span deflection curves for the beams subjected to shear. The purpose was to evaluate the reliability of the hybrid beams under shear. Therefore, shear-deficient beams without stirrups were made for the most critical situation where a very brittle failure is expected. As can be seen, in addition to the increase in peak load, hybrid beams with the SH-SHCC cover exhibited higher stiffness after cracking and displayed a more ductile post-peak behaviour, characterized by a gradual decrease in load. Among the hybrid beam, the one with 3D-printed cover has the highest load capacity and the most ductile post-peak behaviour, which can be attributed to the relatively larger amount of SH-SHCC in contributing the shear resistance.

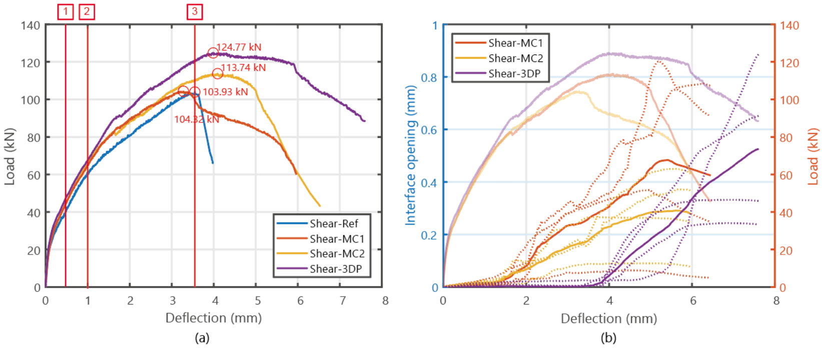

Figure 6.11: (a) Load-deflection response of the tested beams under shear and (b) interface opening between cover and core (each solid lines are averaged values from 4 LVDTs, while dotted lines are results from individual LVDT).

Crucially, the experiment revealed no delamination between the cover and the core. This is evidenced by Fig. 6.11b, where the measured interface opening from four locations near the loading point remained consistently below 1 mm throughout the test duration. Despite slight variability in individual measurements, the average values consistently stayed below 0.3 mm before reaching peak load. Similarly, as observed in flexural tests, higher capacity was observed in sample with the shear key pattern on the bottom, in which also crack opening at the interface stayed smaller throughout the test (She-MC2). The Hybrid beam with 3D-printed cover demonstrated the most superior structural integrity, for that basically no interfacial opening was observed before the peak load was reached. This proves that the surface texture of the printed cover can improve the interfacial bond, similar to the shear-key profile.

Energy absorption capacities of all tested beams are shown in Fig. 6.12. A higher energy dissipation capacity implies greater ductility, which is desirable as it allows the structure to undergo substantial deformation without sudden collapse. This property was calculated by measuring the area under the load-deflection curves until the load drops to 85% of the peak load. All hybrid beams exhibited higher energy absorption capacities than the reference beam. The increase of energy absorption of hybrid beams was achieved due to higher deformation capacity and strain hardening characteristics of SH-SHCC. In addition, it was noticed that the shear key pattern at the bottom led to higher energy absorption increase. The hybrid beam with 3D-printed cover demonstrated the most significant improvement in energy dissipation ability because of higher peak load and a more ductile post-peak behaviour.

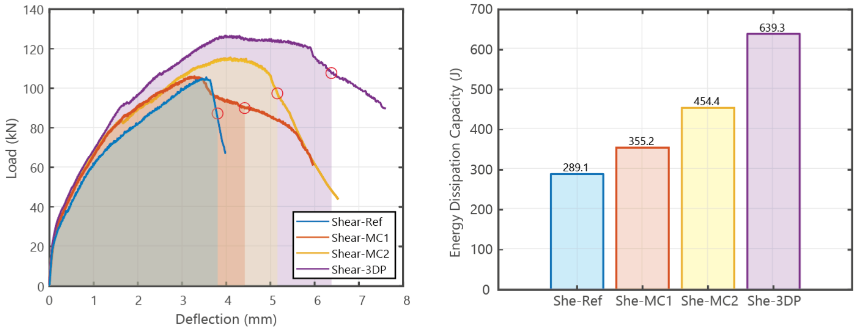

(a) (b)

Figure 6.12: Visualization of the area representing energy dissipated during tests for all the shear beams as well as the calculated results.

To capture the damage process of the beams, the evolution of crack pattern within the effective span at 3 critical moments (*i.e.*, the initiation of flexural cracks, the initiation of major shear crack, and the ultimate state) for all the tested beams are exported. DIC principal strain distribution is shown in Fig. 6.13. The representative cracking moments are also indicated in the load-deflection curves by the vertical red lines in Fig. 6.11a. As can be seen, the crack patterns of the hybrid beams are largely different than the reference beam. Instead of forming a main diagonal shear crack, the hybrid beams with cover exhibited a unique crack pattern, which is characterized by the formation of bundles of fine cracks. The dominate shear cracks formed in conventional concrete core were arrested by the cover layer and turned into multiple fine cracks. Additionally, the hybrid beam with a 3D-printed cover displayed a noticeable 'stepwise' cracking pattern (Fig. 6.14a). Given that interlayer bonding often constitutes the weakest points in printed materials, it is plausible that cracks may predominantly propagate along these interfaces. Consequently, these weaker interfaces may serve as stopgaps, mitigating stress concentration at the crack tip. Ultimately, the layered configuration may have significantly strengthened the fracture resistance of the cover, resulting in an enhanced peak load, a more ductile post-peak behaviour, and increased energy dissipation capacity.

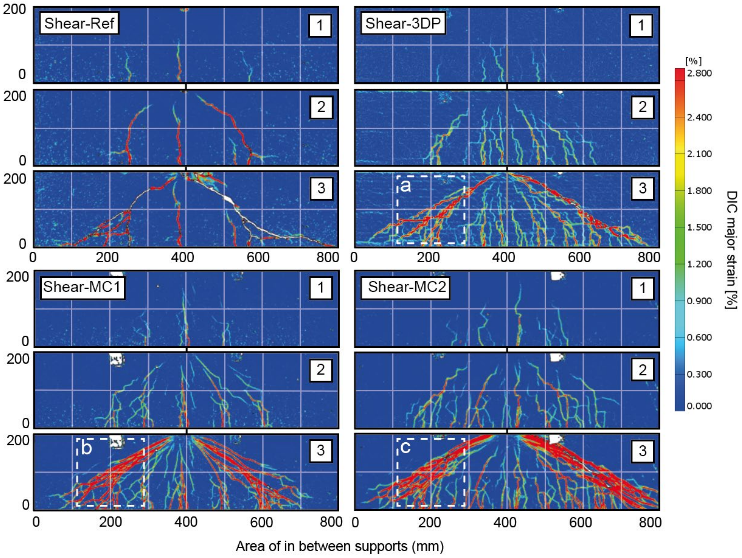

Figure 6.13: Crack pattern development of beams under shear at critical stages (i.e., flexural crack initiation, shear crack initiation and peak load)

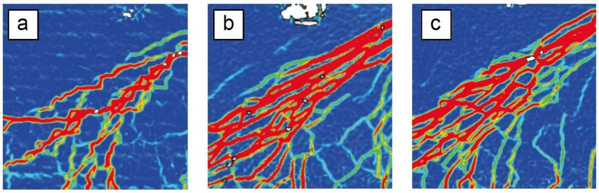

Figure 6.14: Local pattern of major shear cracks of (a) She-3DP, (b) She-MC1, and (c) She-MC2.

3.4 Crack propagation

To further investigate the impact of the cover in enabling the microcracking formation, the tested beams were sawed into smaller sections (Fig. 6.15a), which were subsequently epoxy impregnated for visualizing the crack path. From the cross-section of the beams (Fig. 6.15b), the cover and the core can be distinguished: due to the high slag content in the SHCC, the cover area appeared to be blueish/greenish. Furthermore, it is evident that concrete has densely filled the space between the shear keys, showcasing the successful implementation of the concept.

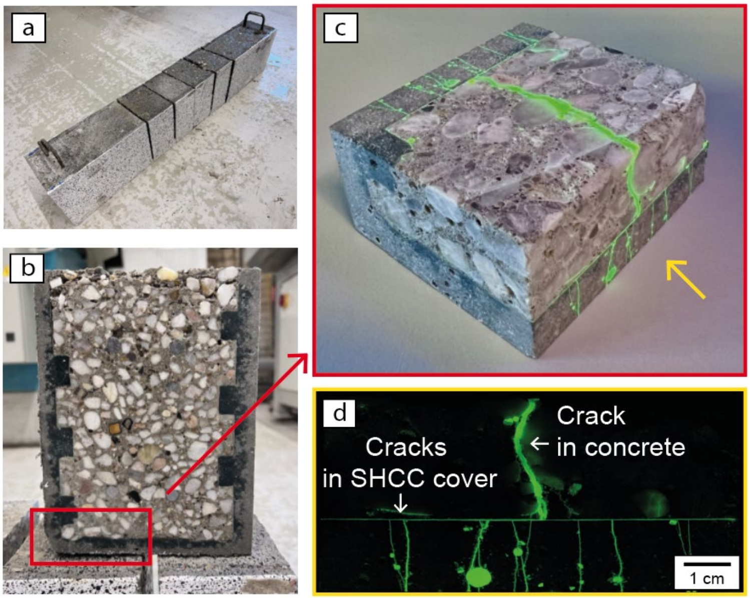

Figure 6.15: (a) A hybrid beam with mould-cast cover after sawing, (b) cross-sectional image of a section demonstrating the covered system, (c) corner piece cut from the beam section after epoxy impregnation, (d) front surface of the corner specimen under UV light to highlight the crack path.

To visualize how cracks propagate from the core to the cover, a corner piece was further cut out from the section. As can be seen from Fig. 6.15c, a major crack in the concrete core was successfully arrested and spread into multiple fine cracks both on the front and bottom sides of the cover. Upon closer examination of the cross-section depicting the crack path toward the bottom surface (Fig. 6.15d), it is evident that the entire section of the SHCC cover is engaged, with evenly distributed fine cracks forming beneath the primary crack in the concrete. By spreading the centralized deformation to the whole section, not only the crack width is reduced but healing can happen easier and faster. This concept is presented schematically in Fig. 6.16a. It has been demonstrated by many that cracks represent spatial discontinuities in which the transport of moisture and chlorides is significant and that the effect of cracking on durability is significantly dependent on the crack width [15–17]. Therefore, even the cover does not have a healing ability, only the reduction of effective crack width can increase the durability of the structural elements. It is also important to emphasize that assessing the effective crack width in hybrid structures becomes challenging. Interfaces introduce non-linear deformation that can redirect cracks into configurations where propagation becomes more challenging. As depicted in Fig. 6.16b and 16c, the ultimate failure crack in concrete was diverted within the cover, yet connected by a fine interfacial crack between the cover and the core. In future, the impact of interface opening on moisture and chloride ingress should be thoroughly investigated.

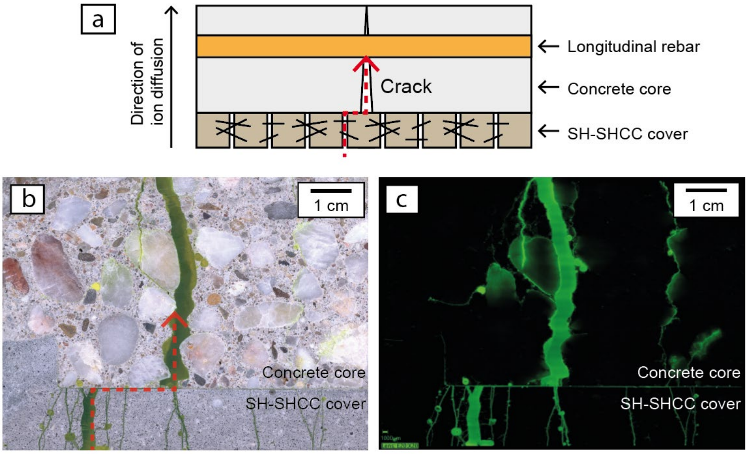

Figure 6.16: (a) Schematic illustration depicting how SHCC cover obstructs the pathway for external ions to reach the rebar, (b) optical microscope image of an epoxy impregnated specimen sawed from tested beams, and (c) the same specimen under UV light for highlighting the crack path.

Propagation of cracks from concrete core to 3D-printed cover exhibited different pattern compared to the scenario described above. In Fig. 6.17a, the cross-section of a hybrid beam with a 3D-printed cover post-epoxy impregnation is depicted. Subsequently, this piece was cut along the indicated dash lines to reveal the plane intersecting the primary crack in the concrete and the rebar (denoted by the red arrow in Fig. 6.17b). As illustrated in Fig. 6.17c, the major crack, which interests with the rebar and the bottom cover, exhibits branching into multiple finer cracks. However, owing to the relatively strong interfacial adhesion between the printed cover and the concrete core, only a limited amount of the cover beneath the major crack demonstrates activation. Fig. 6.17d presents another instance wherein a concrete crack extends into a bundle of fine cracks within the cover region, where again only crack branching was observed instead of saturated fine cracks in the whole cover as observed in mould cast cover (Fig. 6.15d). This observation elucidates why the crack width control capacity of the 3D-printed cover is less effective compared to that of the mould-cast cover (Fig. 6.10), wherein interface conditions was engineered.

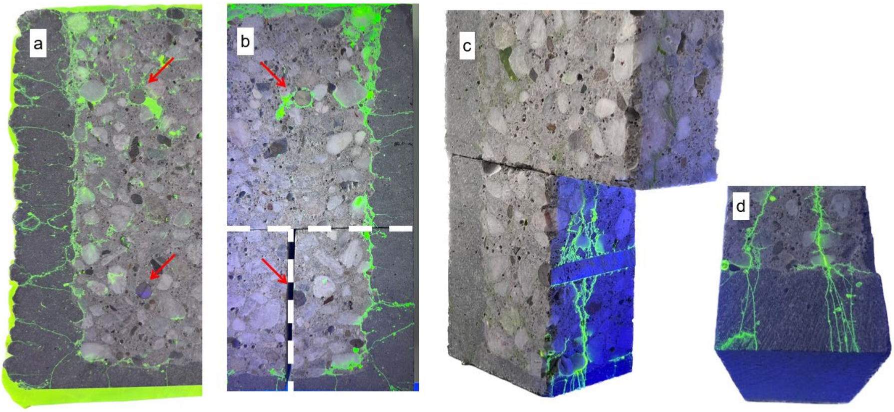

Figure 6.17: (a) cross-sectional image of a section of hybrid beam with 3D-printed cover, (b) cross-sectional image with indicative lines for further cutting, (c) cross-sectional imaging revealing the progressive propagation of cracks extending from the rebar to the bottom cover layer, (d) close-up depiction capturing the interface between the concrete and the cover.

3.4 Healing performance

Since the primary purpose of the U-shaped SH-SHCC cover is to facilitate self-healing, the healing effectiveness of the hybrid beams was evaluated. This involved examining a cracked beam segment before and after a one-month healing period under 95% relative humidity at a constant temperature of 20 °C. Fig. 6.18 presents a comparative analysis of the bottom surface of a beam segment before and after the healing process. Binary images, highlighting the crack patterns, accompany the original photos. To ensure fairness in comparison, identical thresholds were applied to generate the binary images. As can be seen, the results reveal significant healing of most cracks after a one-month period, indicating the effectiveness of the self-healing mechanism. However, it is evident that not all cracks fully healed within this timeframe. Larger cracks may require more time for complete recovery. Also, the random distribution of healing agents within the matrix may result in areas lacking sufficient amount of agents to facilitate healing. Consequently, healing in these regions relies on autogenous healing of SHCC and bacterial migration from other parts of the cracks, leading to prolonged healing durations. Nevertheless, since the diffusion rate of most ions depends on the crack width [18], even partially healed cracks are expected to contribute to an increase of durability.

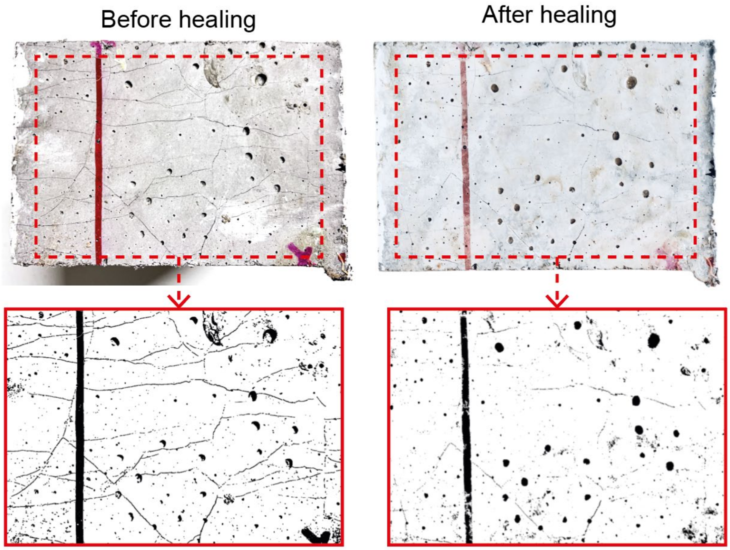

Figure 6.18: Visual comparison of crack patterns on the bottom surface of tested beams before and after healing.

It is important to emphasize that the healing agents utilized in this study are commercial products with a tailored particle size of approximately 1 mm. This design is specifically crafted to facilitate the healing of relatively large cracks commonly encountered in reinforced concrete structures.

Notably, when employing the SH-SHCC cover, as shown in this study, smaller crack widths at similar loads can be expected. Therefore, adjustments in the particle size of the healing agents possibly could be made accordingly. Decreasing the particle size of the healing agents would result in a higher number of particles per unit volume of concrete at the same dosage. Consequently, this increases the likelihood of cracks intersecting with healing agents, enhancing the overall healing efficacy.

In summary, this chapter demonstrates the successful activation of the healing function, alongside improvements in structural performance such as cracking behaviour, load-bearing capacity and ductility. This challenges the previous perception that incorporating healing might inevitably compromise concrete's mechanical properties. Through strategic deployment of the self-healing mechanism where it is most needed, this research presents a scalable and economically viable strategy for integrating self-healing concrete into standard construction practices.

6.4 Conclusions

An experimental study was carried out to investigate the structural behaviour of hybrid reinforced concrete beams with U-shaped covers made via mould-casting method and 3D printing method. Structural behaviour, surface crack pattern and crack propagation between the reinforced concrete core and U-shaped SHCC cover were studied. A qualitative assessment of the crack appearance before and after healing was also presented. The main findings of the current study are:

1. Hybrid beams with mould-casted SH-SHCC covers displayed an improved crack control capability compared to the control beam, enhancing crack sealing within the cover zone. This improvement in crack control was achieved without compromising other beam properties. Experimental results indicate that the hybrid beams possess either comparable or enhanced structural performance, including load capacity and ductility, under both flexural and shear loads.
2. Extrusion-based 3D printing methods provide practical solutions for efficiently manufacturing the U-shaped cover. The hybrid beams with 3D-printed covers demonstrate improved crack control abilities compared to the reference beam. However, the printed cover is slightly less effective than mould-cast covers. Additionally, the hybrid beams with printed covers exhibit higher load capacity and ductility under shear, which might be partially attributed to larger thickness of the side surface, but also the locally weak interfaces between printed layers that channelled nonlinear deformations. The mould-cast cover, with its intricately designed interface profile, necessitates multiple steps and the use of sophisticated moulds for production. In comparison, 3D printing offers a more efficient alternative for creating the U-shaped cover.
3. Both the shear-key profile in the mould-cast cover and the layered profile in the printed cover prove effective in arresting delamination. Interfacial opening larger than 1mm between the cover and core was not observed under both flexural and shear failure mode.
4. The mould-cast cover and printed cover exhibit distinct crack-arresting mechanisms. Analysis of the crack path from the concrete core to the printed cover reveals that the cover disperses a major crack into a branch of fine cracks. In contrast, the mould-cast cover not only disperses a major crack into multiple fine ones but also redirects crack paths, effectively blocking the main transport path. Despite these differences, in both

cases, dispersing a large crack into finer ones increases the likelihood of intersecting with the healing agent, while reducing the average crack width, thus facilitating easier healing.

5. Evident crack healing was observed after a period of 1-month moist curing. Despite that not all cracks had fully closed within this timeframe, those that remained were visibly shorter and smaller, indicating a positive progression of healing. While the current study primarily examined the structural behaviour and visually assessed the performance of healing, future studies are encouraged to explore the influence of healing on durability-related indicators of hybrid RC elements, such as the chloride ingress or carbonation induced corrosion.

References

[1] J.D. Birchall, A.J. Howard, K. Kendall, Flexural strength and porosity of cements, Nature 1981 289:5796 289 (1981) 388–390. https://doi.org/10.1038/289388a0.

[2] S. He, J. Qiu, J. Li, E.-H. Yang, Strain hardening ultra-high performance concrete (SHUHPC) incorporating CNF-coated polyethylene fibers, Cem Concr Res 98 (2017) 50–60. https://doi.org/10.1016/j.cemconres.2017.04.003.

[3] R. Ranade, V.C. Li, W.F. Heard, B.A. Williams, Impact resistance of high strength-high ductility concrete, Cem Concr Res 98 (2017) 24–35. https://doi.org/10.1016/J.CEMCONRES.2017.03.013.

[4] E. Cuenca, L. D'Ambrosio, D. Lizunov, A. Tretjakov, O. Volobujeva, L. Ferrara, Mechanical properties and self-healing capacity of Ultra High Performance Fibre Reinforced Concrete with alumina nano-fibres: Tailoring Ultra High Durability Concrete for aggressive exposure scenarios, Cem Concr Compos 118 (2021) 103956. https://doi.org/10.1016/J.CEMCONCOMP.2021.103956.

[5] S. Mustafa, S. Singh, D. Hordijk, E. Schlangen, M. Luković, Experimental and numerical investigation on the role of interface for crack-width control of hybrid SHCC concrete beams, Eng Struct 251 (2022). https://doi.org/10.1016/j.engstruct.2021.113378.

[6] K.M.A. Hossain, S. Hasib, T. Manzur, Shear behavior of novel hybrid composite beams made of self-consolidating concrete and engineered cementitious composites, Eng Struct 202 (2020) 109856. https://doi.org/10.1016/J.ENGSTRUCT.2019.109856.

[7] R. Zhang, P. Hu, X. Zheng, L. Cai, R. Guo, D. Wei, Shear behavior of RC slender beams without stirrups by using precast U-shaped ECC permanent formwork, Constr Build Mater 260 (2020) 120430. https://doi.org/10.1016/J.CONBUILDMAT.2020.120430.

[8] C.K.Y. Leung, Q. Cao, Development of Pseudo-ductile permanent formwork for durable concrete structures, Materials and Structures/Materiaux et Constructions 43 (2010) 993–1007. https://doi.org/10.1617/S11527-009-9561-4/FIGURES/17.

[9] Ł. Sadowski, Adhesion in Layered Cement Composites, 101 (2019). https://doi.org/10.1007/978-3-030-03783-3.

[10] M.A. Al-Osta, M.N. Isa, M.H. Baluch, M.K. Rahman, Flexural behavior of reinforced concrete beams strengthened with ultra-high performance fiber reinforced concrete, Constr Build Mater 134 (2017) 279–296. https://doi.org/10.1016/j.conbuildmat.2016.12.094.

[11] M. Luković, H. Dong, B. Šavija, E. Schlangen, G. Ye, K. Van Breugel, Tailoring strain-hardening cementitious composite repair systems through numerical experimentation, Cem Concr Compos 53 (2014) 200–213. https://doi.org/10.1016/J.CEMCONCOMP.2014.06.017.

[12] H.M. Tanarslan, Flexural strengthening of RC beams with prefabricated ultra high performance fibre reinforced concrete laminates, Eng Struct 151 (2017) 337–348. https://doi.org/10.1016/J.ENGSTRUCT.2017.08.048.

[13] Y. Chen, S. He, Y. Gan, O. Çopuroğlu, F. Veer, E. Schlangen, A review of printing strategies, sustainable cementitious materials and characterization methods in the context of extrusion-based 3D concrete printing, Journal of Building Engineering 45 (2022) 103599.

[14] A. Jipa, B. Dillenburger, 3D-printed Formwork for Concrete: State-of-the-Art, Opportunities, Challenges, and Applications, 3D Print Addit Manuf 9 (2022) 84–107. https://doi.org/10.1089/3DP.2021.0024/ASSET/IMAGES/3DP.2021.0024_FIGURE10.JPG.

[15] B. Gérard, J. Marchand, Influence of cracking on the diffusion properties of cement-based materials Part I: Influence of continuous cracks on the steady-state regime, 2000.

[16] M. Ismail, A. Toumi, R. François, R. Gagné, Effect of crack opening on the local diffusion of chloride in cracked mortar samples, Cem Concr Res 38 (2008) 1106–1111. https://doi.org/https://doi.org/10.1016/j.cemconres.2008.03.009.

[17] S. Jacobsen, J. Marchand, L. Boisvert, Effect of cracking and healing on chloride transport in OPC concrete, Cem Concr Res 26 (1996) 869–881. https://doi.org/https://doi.org/10.1016/0008-8846(96)00072-5.

[18] I.S. Yoon, E. Schlangen, Experimental examination on chloride penetration through micro-crack in concrete, KSCE Journal of Civil Engineering 18 (2014) 188–198. https://doi.org/10.1007/s12205-014-0196-9.

7

Perspectives on the incorporation of self-healing in design practice of reinforced concrete structures[5]

For the developed self-healing cover system to be applied in structures, it is necessary to consider the implications of healing during the design process. Only by doing so can the advantages of self-healing be realized, such as potentially permitting a larger allowable crack width or prolonging the service life of reinforced concrete structures.

This chapter thus aims to demonstrate the possibility of integrating self-healing concepts into the design practice of structural concrete. To facilitate the design of the developed self-healing cover system, emphasis is given to the role of self-healing in resisting chloride penetration into cracked concrete. In specific, the chapter first reviews related research progress and then suggests modifications to existing predictive models to accommodate various healing approaches. Additionally, it discusses the limitations and challenges that currently impede the standardization and broader application of self-healing technologies in the construction industry.

---

[5] Part of this chapter has been published in:

He, S., Sayadi, S., Patel, R. A., Schultheiß, A. L., Mihai, I. C., Jefferson, A., ... & Dehn, F. (2025). Perspectives on the incorporation of self-healing in the design practice of reinforced concrete structures. Structural Concrete.

7.1 Introduction

To explore the benefits of self-healing in real-world applications, efforts have been made to align infrastructure requirements with the self-healing functionality [1–4]. One of the proven examples is concrete structures in wet environments. Waterproof structures typically necessitate the elimination of cracking risks, or at the very least, the restriction of cracks to a width of 0.1 mm or smaller. Achieving such minimal crack formation requires the use of a large amount of steel reinforcement, which is not needed for load capacity but is there only for crack width control. If self-healing concrete is used, the design criteria of waterproof construction can be simply changed by allowing some larger cracks, since the water tightness of self-healing concrete can be ensured even when cracks are 0.2 to 0.4 mm wide [3]. The transition to crack management not only offers potential material savings and a diminished CO_2 footprint but also simplified construction processes. This is facilitated by a coarser reinforcement network, which mitigates the risk of execution-related complications. Several full-scale demonstrators have been constructed in the Netherlands with bacteria-based self-healing concrete for water-proofing purposes [3,5].

The integration of self-healing concrete in water-retaining structures exemplifies a scenario wherein the advantages of incorporating self-healing properties can be quantified during the design phase. This is possible because the effects of cracking are explicitly described in the standards used for the prediction of water tightness. Nevertheless, in the design of various other concrete properties, such as the estimation of corrosion initiation time, conventional service life models typically assume concrete to be intact and devoid of cracks. Therefore, integrating the advantages of healing requires an expansion of the current design models in use.

This chapter thus aims to discuss how self-healing can be considered in designing durability of reinforced concrete structures with appropriate modifications of existing models. The focus will be placed on exploring the incorporation of healing effects into the prediction of chloride resistance.

7.2. Effect of healing on chloride penetration in cracked concrete

7.2.1 Chloride ingress process altered by cracking and healing

Chloride-induced corrosion is a major deterioration factor in reinforced concrete structures, particularly affecting marine structures, road slabs, and parking facilities. In uncracked concrete, chloride penetration is slow, occurring mainly through diffusion. However, cracks in the concrete create additional pathways, allowing chloride ions to access deeper areas more quickly. Studies have demonstrated that once cracks exceed certain thresholds, notably the critical crack width, the diffusion coefficient of chloride increases linearly with the widening of cracks.

Self-healing of cracks in concrete can mitigate this process. Regardless of the chosen healing method—be it autogenous or autonomous—it tends to diminish the crack volume, consequently narrowing the effective pathway for aggressive ion transport. Previous research [6] has proven the effectiveness of crack healing in chloride-rich environments. Furthermore, studies have shown that crack healing can not only increase the critical crack width but also decrease the diffusion coefficient of chloride when the cracks are larger than the critical crack width [7].

Despite the evident effects of healing on resisting chloride ingress through cracks, it is challenging to calculate the benefits of healing in terms of service life extension of concrete structure. This is because, when determining the time to corrosion initiation, service life models, such as those in the *fib* Model Code for Service Life Design (hereafter referred to as *fib* chloride model) [8], consider concrete to be homogeneous and crack free. This assumption poses challenges in directly accounting for the impact of cracking and crack-healing. Recognizing this, this section will first review methods for incorporating pre-existing cracks within chloride ingress models. Furthermore, the influence of self-healing on chloride diffusion in cracked concrete will be explored within various scenarios. Finally, a proposal will be put forth to extend the model for accommodating healing effects in probabilistic service life prognosis.

7.2.2 Service life design of cracked concrete

Reinforcement corrosion in concrete occurs in two stages: initiation and propagation. During the initiation stage, concrete provides a protective alkaline environment that prevents corrosion by forming a passive oxide layer on the steel surface. Over time, aggressive agents like chlorides or carbon-dioxide combined with water penetrate the concrete, eventually breaking down this protective layer. This marks the end of the initiation stage and the beginning of the propagation stage, where active corrosion of the steel reinforcement starts. The end of corrosion initiation stage is usually considered as the end of service life in concrete infrastructure.

In the case of chloride ingress, passivation of reinforcement is widely considered to be lost when a critical concentration of chloride is present at the level of rebar surface. Under the assumption that concrete is crack-free, chloride ingress can be modelled based on Fick's 2nd law of diffusion and often Gauss error function (erf) based models are used to predict the chloride content as a function of concrete depth. An illustrative instance of this is the *fib* chloride model as presented below:

$$C_{crit.} = C(a,t) = C_0 + (C_{s,\Delta x} - C_0)\left[1 - erf\left(\frac{a - \Delta x}{2\sqrt{D_{app,c} \cdot t}}\right)\right] \tag{7.1}$$

where, $C_{crit.}$ is the critical chloride content, $C(a,t)$ is content of chlorides at rebar (a is concrete cover thickness) and at time t, C_0 is the initial chloride content, $C_{s,\Delta x}$ is the chloride content at a depth Δx (depth of convection zone), and $D_{app,c}$ is the apparent coefficient of chloride diffusion coefficient. $D_{app,c}$is a time-dependent variable that can be calculated based on:

$$D_{app,C} = k_e \cdot D_{RCM,0} \cdot k_t \cdot A(t) \tag{7.2}$$

which allows the calculation of apparent diffusion coefficient $D_{app,C}$ from chloride migration coefficient ($D_{RCM,0}$) determined from chloride ingress tests of uncracked concrete. This calculation also considers the impact of environmental alterations, represented by k_e, and the effects of material aging, represented by A(t). With these equations, the duration required for the chloride content at the cover depth 'a' to reach the critical chloride content $C_{crit.}$ can be determined. This calculated time can subsequently serve as an estimate for the predicted service life of the structure if the concrete is crack-free.

To consider the effects of cracking in chloride ingress process, different approaches to account for cracks in the erf solution can be found in the literature. Since cracks represent spatial discontinuities in which the transport of moisture and chlorides is significant, crack-altered chloride ingress process is usually modelled as an accelerated progress where the protecting effect of cover is diminished. Fig. 7.1 provides an overview of various methodologies for addressing cracks. Most proposed methods focus either on modifying the diffusion coefficient or to adapt the effective concrete cover depth. The discussed approaches all assume pre-existing cracks, which occur at the beginning of the service life~~.~~

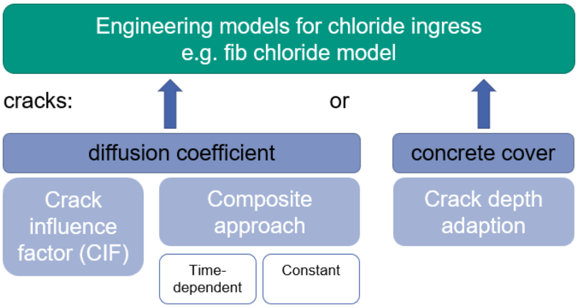

Figure 7.1: Methods to account for cracks in engineering models for chloride ingress [9]

If diffusion is assumed to be the dominant transport mechanism for chloride ions within cracks, the effects of cracking can be considered by using an adjusted diffusion coefficient in the erf-solution. Estimation of a smeared diffusion coefficient of cracked concrete can be done either by increasing the diffusion coefficient based on the cracking condition or by fitting the erf-solution to the chloride profiles of a cracked area (the composite approach). The obtained diffusion coefficient is usually expressed as a function of the crack width [10]. Another way of estimating an adapted diffusion coefficient involves calculating a crack influence factor (CIF), *i.e.*, the ratio of smeared diffusion coefficient of cracked concrete $D_{smeared}$ and diffusion coefficient of uncracked concrete D_{uncr}. For the use of CIF approaches, chloride profiles from structural sampling or experiments are extracted at the location of a specific crack. Then an apparent $D_{smeared}$ can be determined by fitting the erf-solution for a specific time [11].

When diffusion is not the main controlling mechanism, which happens when the crack width is so large that influence of capillary suction or convection cannot be ignored, cracks would provide direct channel of chloride ingress and thus render the cover useless until the tip of the crack. In this case, accounting for cracking can be done by adapting the convection zone. In the *fib* chloride model, the convection zone describes the surface of reinforced concrete structure, where the transport mechanisms are not mainly diffusion controlled due to its exposure to a frequent change of wetting and subsequent evaporation. To still describe the penetration of chlorides using Fick's 2nd law of diffusion, the resistance of the convection zone is thus neglected, and Fick's 2nd law of diffusion is applied starting at a depth with a substitute surface concentration. Since cracks could provide an immediate transport of liquid, the convection zone could be extended to the crack depth, to approximate the reduced effective depth of the concrete cover to resist chloride [9]. This approach is referred to as 'crack depth adaptation' in Fig. 7.1.

In addition to the engineering models outlined earlier, advanced multi-physics coupled numerical models have been devised to assess the impact of cracking on chloride diffusion in concrete [12–16]. These numerical models consider a wider array of factors, encompassing not only primary parameters like crack width and depth but also secondary influencing factors such as crack tortuosity, the interaction among various ionic species, and the chloride binding capacity of cracked surfaces. However, while numerical models offer a more accurate depiction of the impacts of cracking, estimating the effects of healing on factors beyond crack width and depth remains challenging. Consequently, investigations into the role of healing and design strategies will predominantly concentrate on primary crack parameters, such as crack width and depth.

7.2.3 Role of healing on service life design

Since healing involves changes in effective crack widths and depths, proposed models incorporating crack effects can also include healing effects. To gain deeper insights into the impact of various scenarios of healing events on chloride penetration resistance, a literature review was performed to survey studies with relevant results. The findings are presented in Table 7.1 (placed at the end of this chapter). The table provides details of each study on the employed healing mechanisms, degrees of damage, and their respective scenarios and key findings. In total, eighteen research papers were found to have observed healing-induced alterations in chloride resistance properties. Among these publications, thirteen studies focused explicitly on investigating the effects of self-healing, while the remaining five reported on observing healing when researching other subjects. Twelve papers reported quantitative data, such as smeared chloride diffusion or migration coefficients, suitable for developing models that account for the healing effect. The remaining studies reported a reduced penetration depth in chloride profiles due to healing but did not provide quantitative data.

One key finding from the literature review is that crack healing may not always completely restore cracked concrete to its original condition. This variability arises from how healing products fill the crack volume. Various forms of healing are pictured schematically in Fig. 7.2. As can be seen, depending on the healing method selected and the extent of the damage, some cracks may undergo complete restoration (Fig. 2a), regaining full resistance against aggressive substances, while others experience only partial healing, with healing products dispersed evenly throughout the crack depth (Fig. 2b) or aggregated in specific directions (Fig. 2c and 2d). The forthcoming discussion on the influence of healing on chloride transport in cracked concrete is thus structured according to each specific scenario.

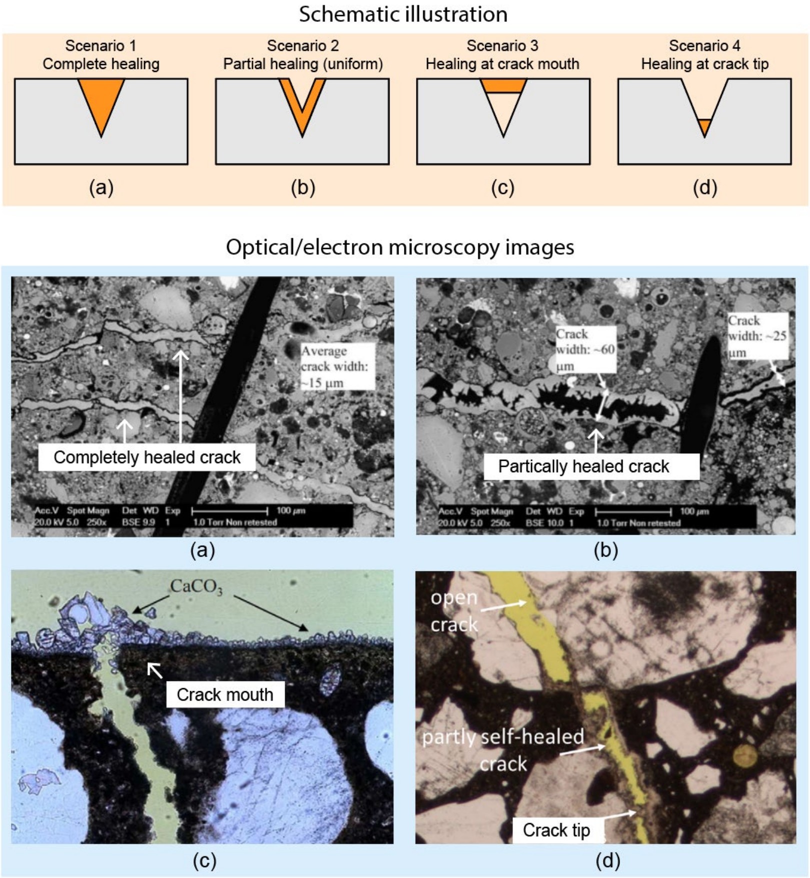

Figure 7.2: Illustration of different healing scenarios: (a) complete healing, (b) uniform partial healing [17], (c) healing at crack mouth [18] and (d) at crack tip [19].

7.2.3.1 Scenario 1: Complete healing

Under all healing approaches, complete crack healing is feasible when dealing with sufficiently small cracks. Even though healing products may be more porous than the matrix, research has shown that a fully healed crack can effectively regain its resistance against chloride ingress. Yoon and Schlangen [20] investigated the impact of microcracking on concrete. They found that the critical crack width for unhealed concrete is 15 μm, whereas prolonged autogenous healing raised this threshold to 40 μm. This establishes that cracks smaller than 40 μm have the potential for complete restoration. Maes et al. [21] studied specimens containing glass capsules filled with polyurethane as a healing agent. The results show that for crack widths of 100 and 300 μm, almost no chloride penetration was measured around the healed crack in 83 % and 67 % of the cases, respectively. Abro et al. [22,23] and Cuenca et al. [24] both conducted studies investigating the efficiency of crystalline admixture systems. Their research demonstrated that the crystalline system is capable of fully restoring chloride resistance in cracked concrete. Specifically, it was found that specimens with 100 µm cracks, after 56 days of healing, exhibited nearly identical diffusion coefficients to the uncracked specimens, irrespective of the specific mixture used.

7.2.3.2 Scenario 2: Partial healing (uniform)

Once a crack surpasses a certain width or encounters adverse conditions, complete healing becomes unfeasible, resulting in only partial recovery. The way partial healing occurs depends on the healing approach. The healing products can form either uniformly along the crack depth or aggregating towards either the crack mouth or tip. In instances of uniform partial healing, the effective crack width uniformly decreases within the crack. Self-healed specimens can be simply seen as specimens characterized by a reduced crack size. This means that if complete healing can happen at a crack width of 100 µm, then any cracks larger than this threshold can only be partially healed, with an effective crack width reduction of 100 µm. Uniform partial healing has been observed across various methods, including autogenous healing through ongoing hydration [20,25,26], stimulated autogenous healing via super-absorbent polymer [27] and autonomous healing utilizing encapsulated polyurethane [21] and crystalline admixture [24].

7.2.3.3 Scenario 3: Partial healing (crack mouth)

Analysing the healing effects becomes complex in cases of uneven partial healing, where healing products tend to form preferentially either at the crack mouth or tip. For instance, in self-healing bio-concrete, healing typically starts at the crack mouth [28]. This is because the healing in this case relies on the calcium carbonate precipitated by bacteria through aerobic metabolic conversion of organic compounds. Since this microbial activity relies on the availability of oxygen, the rate of precipitation is the highest at the crack mouth. Consequently, even if a crack closure is observed at the surface, the crack might remain largely unhealed along the crack depth. In a recent study by Rossi et al. [29], mortars embedded with bacteria-based healing agents were examined for their chloride penetration resistance. While a surface healing was evident, positive effects of the self-healing on the chloride penetration of cracked specimens were not observed. This was attributed to the thin layer of self-healing products formed at the crack mouth, offering minimal resistance to chloride penetration.

Nevertheless, calcite-precipitating bacteria may prove effective in impeding chloride penetration under specific conditions, particularly when the thickness of the healing product formed at the crack mouth reaches certain thresholds. In a recent study, He et al. [30] explored crack healing in a real-world setting, uncovering noteworthy distinctions from healing under controlled conditions (*i.e.*, moisture curing at constant temperature). Unlike the limited healing restricted to the crack mouth in controlled settings, a substantial healing process was observed throughout the entire crack depth in a realistic environment. However, this study did not measure transport properties.

When considering healing specifically at the crack mouth, estimating the transport properties of healed concrete based on the surface crack width is wrong. Many existing methods for healing detection which rely on the surface crack width measurement therefore are not applicable when this type of healing is expected. To address this, understanding the healed crack depth within a particular environment over a defined period of time becomes essential.

7.2.3.4 Scenario 4: Partial healing (crack tip)

Healing only at the crack tip exhibits a contrasting characteristic compared to the previous scenario. In this case, healing might has occurred without any discernible evidence upon surface inspection. This type of healing happens most commonly when the encapsulation technique is used. If the crack volume exceeds the volume of the healing agent released from the carriers, due to capillary forces only the area around the crack tip can be filled with the healing agent. This circumstance may also manifest in vascular-based self-healing systems if the vessels aren't sufficiently ruptured, thus limiting the release of the healing agent. In both instances, the viscosity of the released liquid is a crucial parameter dictating how deep the crack can be healed.

7.3 Incorporation of healing into design

Possible situations where the impact of healing on the chloride penetration resistance can be considered include: 1) the determination of maximum allowable crack width for a concrete structure with a known environment and intended service life, or 2) the estimation of remaining service life of a cracked concrete structure. In both cases, the effects of healing will be reflected through the adjustment of a parameter that characterizes a decelerated chloride transport process. Options for adjustment include adapting the critical crack width, the diffusion coefficient, or the cover depth. The following strategies are suggested depending on the healing scenario:

For healing scenario 1:

In situations where complete crack healing is expected, the cracked concrete can be treated as if it is intact, under the condition that the triggered healing process occurs at a significantly faster rate than the ingress of chloride. Prior research indicates that if the width of concrete cracks is below a certain threshold (*i.e.*, the critical crack width), the ion diffusion rate through these cracks equals that of uncracked concrete. Consequently, concretes engineered with self-healing capacity can exhibit an increased tolerance for crack widths, hereafter referred to as 'healable crack width' (illustrated in Fig. 7.3a). The difference between the 'critical crack width' and the 'healable crack width' is the net contribution from healing, which is expressed as Δw_{hl}. Healable crack widths, as related to various healing methods, are documented under 'Scenario 1' in Table 1, with specific values of 40 μm, 100 μm, and 300 μm corresponding to the autogenous healing, healing with crystalline admixture, and healing with polyurethane, respectively. It is essential to highlight that accurate determination of the 'healable crack width' requires chloride diffusion/migration tests to be conducted on healed concretes. The crack width threshold determined by surface observations of crack closure can be misleading, as a visually 'sealed' crack does not guarantee a complete restoration of the chloride resistance.

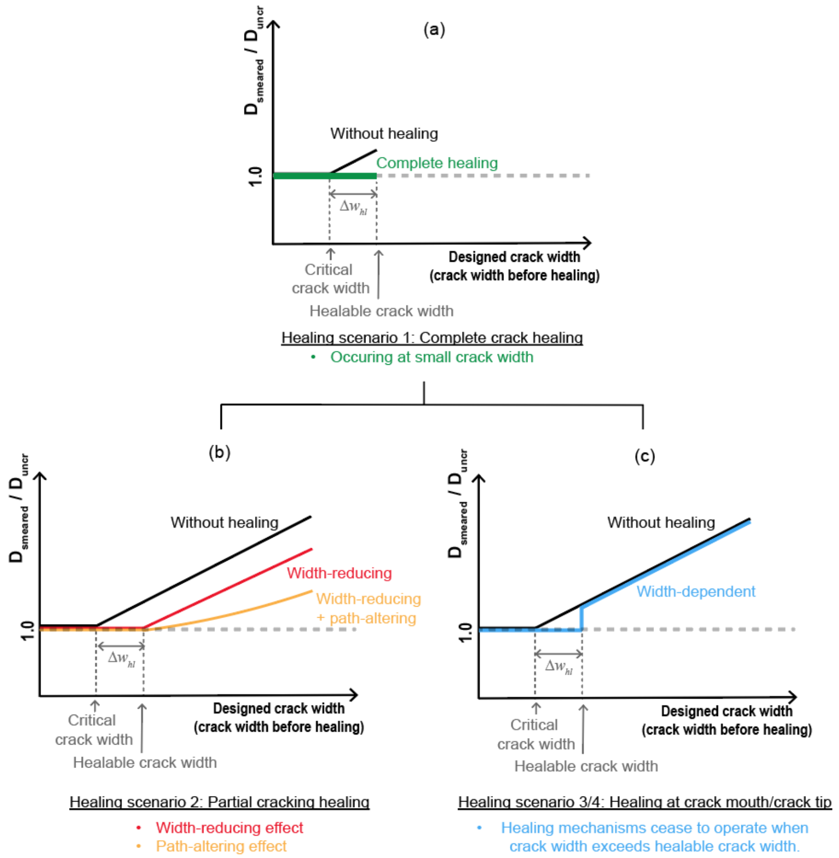

Figure 7.3: Schematic illustration of the relationship between diffusion coefficient and crack width for (a) complete healing, (b) partial healing, and (c) healing methods functioning only at small crack widths for rapid healing.

For healing scenario 2:

If the chosen method of healing aligns with partial healing, two situations emerge. In the first one, partially healed cracks can be simply considered as cracks with reduced openings. This indicates that only the crack width is affected by healing, while other characteristics such as roughness, tortuosity, and path connectivity remain unchanged. In this situation, healing only delay the increase of diffusion coefficient but does not affect the linear relation between the diffusion coefficient and the crack width, as illustrated schematically as 'width reducing' healing in Fig. 7.3b. Serval studies [23,25,31] provide supporting evidence for this situation. In this case, the effective crack width w_{eff} (the width after healing) can be determined by subtracting the healing contribution Δw_{hl} from the designed crack width w_d:

$$w_{eff} = w_d - \Delta w_{hl} \tag{7.3}$$

If the relationship between crack width and diffusion coefficient is known for a certain type of concrete, the diffusion coefficient of such concrete with healing capacity can be expressed as:

$$D_{cr,hl}(w_d - \Delta w_{hl}) = \begin{cases} D_{uncr}, & w_d - \Delta w_{hl} < critical\ crack\ width \\ f(w_d - \Delta w_{hl}), & w_d - \Delta w_{hl} \geq critical\ crack\ width \end{cases} \quad (7.4)$$

The advantage of employing this method is that it eliminates the need to test the diffusion coefficient of healed concrete. Existing databases containing the chloride diffusion coefficients of cracked concrete (with varying crack widths) are sufficient for the analysis.

For certain healing mechanisms, healing does not only reduce the crack width but also change the crack roughness and tortuosity. 'Path-altering' healing, depicted schematically in Fig. 7.3b, can lead to an additional recovery of the diffusion resistance of the partially healed concrete. To describe such effects, it is necessary to experimentally determine the diffusion coefficient of the partially healed concrete by carrying out chloride diffusion tests of healed concrete with different crack widths as reported in several studies [20,31].

For healing scenario 3&4:

If healing is expected to occur preferably at the crack mouth or crack tip, the effects of healing can be better predicted by applying the 'crack depth adaptation' method. Regardless of the healed location along the crack depth, the presence of healing products obstructs the effective diffusion paths for chloride ions to reach the reinforcement, which can be described by a reduced thickness of the convection zone. The depth of the healing can then be estimated by the amount of healing products formed/released. For example, in an encapsulated system, if the theoretical quantity of released healing agent can be estimated using the geometric dimensions of a crack (either measured or anticipated), then the calculated filling ratio could act as a parameter for predicting the extent to which the resistance to chloride diffusion can be restored. In systems employing calcite-precipitating bacteria, the quantity of healing products formed can be deduced from the duration of the healing process and the theoretical rate of formation of the healing agents in its depth direction. It should be noted that healing methods in this category (*e.g.*, bacteria-based and vascular-based) may cease to function when crack widths exceed certain thresholds. In bacteria-based self-healing concrete, small cracks allow nutrients to diffuse effectively throughout the damaged area, supporting bacterial growth and metabolism. However, larger cracks may have areas with limited nutrient availability, reducing healing efficiency. This limitation can result in abrupt changes in the diffusion coefficient, as shown in Fig. 7.3c. It was observed that the bacterial crack healing efficiency is limited when crack width exceeds 0.8 mm [32,33]. References [29,34] in Table 1 offer relevant data that may serve as guidance.

In previous scenarios, it is assumed that the effect of healing is not time dependent. They are applicable either when healing completes before the start of chloride exposure or when the rate of healing significantly outpaces the rate of the chloride ingress. Thus, alternative strategies must be considered when dealing with a healing process that operates at a slower pace. One way to determine the reduced smeared diffusion coefficient of cracked concrete due to slow-acting healing is by conducting chloride resistance experiments at different stages of the healing process. By repeating the same experiments for concrete with different crack widths, the modified diffusion coefficient can then be expressed as a function of time and crack width. Alternatively, to account for slow healing effects, one might adjust the 'ageing' factor in the *fib* chloride model as presented above in Eq. 7.2. This factor is considered in service life prediction models to reflect the increase in diffusion resistance as the concrete matures. This arises from ongoing hydration reactions and the formation of additional calcium silicate hydrate gel, which reduces the pore space for chloride ion penetration and acts similarly to healing.

7.4 Limitations and challenges

While the proposed methods hold theoretical validity, certain limitations persist. The first one is related to the sequence between healing action and chloride exposure. The preceding discussion concerning the design approaches assumes that the healing process initiates concurrently with the onset of chloride exposure. In some cases, healing occurs rapidly in relation to the chloride diffusion process, making it suitable for consideration as an instantaneous event. In cases of slow-acting healing, it may also be regarded as a time-dependent process, characterized by a gradual reduction in diffusion rate over time. However, experiments in literature usually ensured that healing took place before exposing the material to chloride. Even for healing processes that require more time, studies often allocated extended periods to allow complete healing, maximizing potential benefits. This approach renders the results from these studies impractical for real-world scenarios. Only 4 studies adopted simultaneous healing and chloride ingress as listed in Table 7.1. To date, no publication has provided a direct comparative analysis between the two procedures, *i.e.*, simultaneous healing and chloride ingress, and healing followed by chloride exposure.

Regarding the determination of the chloride penetration resistance, the relevant experimental method must be chosen carefully. Although it falls outside the scope of this study to determine the most appropriate test for evaluating chloride resistance properties of self-healing concrete, it is evident from the literature that outcomes differ based on the test employed. Two publications have specifically compared results obtained from various tests [29,34]. Both studies suggested that the efficacy of healing is more prominent when assessed through diffusion tests. Additionally, studies by Abro at al. [22,23] are directed towards developing a novel testing protocol to measure the chloride migration coefficient in cracked concrete after healing.

The durability of the healing products is another important factor that requires further investigation. Durability determines whether crack healing merely slows down chloride penetration or effectively stops its ingress over the long-term. If the healing/sealing products degrade over time, their effectiveness as barriers diminishes, leading to temporary impediments that only delay rather than permanently impede chloride penetration. Among the literature found, only the time dependent efficiency of super absorbent polymer (SAP) [27] and bacterial healing agents [29] were evaluated. In the case of SAP, a considerable reduction in chloride ingress was only observed in the first week of exposure. After exposure to aggressive media for five weeks, healed SAP specimens had a similar chloride ingress as reference specimens which have only autogenous healing capacity. A similar initial retarding effect was also observed for bacterial healing.

Another topic that received little attention is the reliability of healing, *i.e.*, the statistical probability that certain healing mechanisms can be activated and deliver the anticipated effect. The probability of healing mechanism activation was investigated only for the encapsulation system, where the number of capsules activated is calculated based on the likelihood of a crack intersecting the capsules [35,36]. Beyond assessing activation probability, understanding the success rate of non-failures that produce anticipated effects is also important. Studies from Maes et al. [37] revealed that despite placing a macro-capsule containing PU directly above a notch (for ensuring activation), healing was not observed in all specimens. This outcome is reasonable considering that crack healing relies on a sequence of successful events; and the heterogeneous nature of concrete means any reactions within it carry inherent uncertainty. While absolute certainty is not mandatory, having a measurable level of reliability is essential for application and development.

To summarize, it is evident from the published literature that self-healing processes, whether autogenous or autonomous, can mitigate chloride penetration in cracked concrete, thereby prolonging the service life of infrastructure and allowing more optimized design with respect to crack widths. By refining models to include the impact of cracks, it becomes possible to predict the healing effects under specific scenarios. However, in other situations, accurately assessing the healing effects remains a challenge. Although the incorporation of self-healing technologies into structural design codes and service life predictions is a feasible goal, it remains in its nascent stages, requiring extensive experimental data and real-world validations before it can be fully realized and effectively implemented.

7.5 Conclusions

This chapter study offered insights into impact of incorporating the self-healing on service life design of reinforced concrete structures. The focus was placed around one particular advantage of adopting self-healing concrete: its effectiveness in resisting chloride ingress within cracked concrete. Modifications to existing engineering models were proposed. Limitations and challenges that currently impede the standardization process were discussed. The main findings of the current chapter are:

1. Incorporating the influence of healing into the calculation of corrosion initiation duration poses a challenge, as current service life models typically assume concrete to be crack-free. Nevertheless, by appropriately adjusting parameters such as the diffusion coefficient and aging factor in these models, it becomes feasible to consider the healing process as a slowed chloride ingress phenomenon.
2. It is crucial to emphasize that determining the 'healable crack width' necessitates conducting performance tests, such as chloride diffusion/migration tests, on concrete before and after healing. Relying solely on surface observations of crack closure to establish the crack width threshold can be deceptive, as visual closure does not always ensure complete restoration of chloride resistance.
3. While the integration of healing mechanisms into service life predictions holds theoretical promise, it remains at an early developmental stage, requiring significant experimental data which is currently insufficient. Despite the abundance of studies in this field, data reflecting real-world conditions are scarce, emphasizing the crucial need for validation of healing processes in practical settings.

Table 7.1 Summary of studies reporting healing-induced alterations in chloride resistance properties.

	Year	Author	Damage type / crack width	Healing type / healing condition	Crack filling scenario	Tests performed/measured properties	Order between healing and chloride ingress.	Relevant results
1	1996	Jacobsen et al. [26]	Rapid freeze and thaw / crack width unknown	Autogenous healing / in lime water for 3 months	2	Rapid chloride permeability test AASHTO T 277-89/ chloride migration rate	Healing prior to chloride exposure	-Self-healing reduced chloride migration rate as compared to newly cracked specimen. - Chloride migration rate of healed specimen is still higher than undamaged concrete.
2	2007	Şahmaran et al. [38]	Mechanically induced cracks / crack width = 29 - 390 microns	Autogenous healing / in NaCl solution for 30 days	1 / 2	Ponding test AASHTO T259-80 / chloride diffusion coefficient	Simultaneously	- Self-healing accounted for the marginal effective diffusion coefficient of mortar observed with crack widths below 135 microns. - XRD shown formation of calcite as main healing products.
3	2008	Ismail et al. [39]	Mechanically induced cracks / crack width = 6 - 325 microns	Autogenous healing / in NaCl solution for 14 days	1 / 2	Modified chloride penetration test / chloride profile	Simultaneously	- Self-healing can impede chloride diffusion for cracks less than 55 microns when the specimen is young (at 28 days). - Two-year-old specimens have a smaller healable crack width, indicating diminished healing potential.
4	2014	Yoon et Schlangen [20]	Mechanically induced cracks / crack width = 25 - 200 microns	Autogenous healing Samples / in artificial sea water for 472 days	1 / 2	Modified ponding test (472 days immersion)/ chloride diffusion coefficient	Simultaneously	- Critical crack width due to healing can be increased from 0.015 to 0.4 mm. - Crack healing resulted in a slower increase of the chloride migration coefficient with widening cracks, signalling a decelerated chloride penetration process.
5	2014	Maes et al. [21]	Standardized cracks / crack width = 100 & 300 microns	Encapsulated polyurethane	1 / 4	Standard chloride diffusion test NT Build 443 (7 weeks immersion) / Chloride profiles and diffusion coefficient	Healing prior to chloride exposure	- Across various crack widths, the average diffusion coefficients surrounding a PU-healed crack are lower than those around an unhealed crack. - At a crack width of 100 microns, 50% of the healed specimens exhibit chloride profiles identical to those of uncracked specimens.
6	2016	Maes et al. [40]	Standardized cracks / crack width = 100 & 300 microns	Autogenous healing / In artificial sea water for 7 weeks.	1 / 2	Modified chloride diffusion (immersion for 7 weeks)/ chloride profiles	Simultaneously	- Crack widths lower than 105 microns can heal autogenously. Crack larger than 105 microns will also heal but not completely.

								- Samples with autogenously healed cracks have identical chloride profile as uncracked concrete after 7 weeks in a chloride solution.
7	2016	Darquennes et al. [25]	Mechanically induced cracks / crack width = 126 - 152 microns	Autogenous healing / immersion in tap water for 14 and 21 days	1 / 2	Modified chloride migration tests / chloride migration coefficients	Healing prior to chloride exposure	- Concrete mixes with blast-furnace slag display potent self-healing. After 21 days in water, their chloride migration coefficient nearly matches uncracked concrete. - A linear behavior is found for the evolution of the chloride migration coefficient of self-healed materials as function of the crack width.
8	2017	Van Belleghem et al. [41]	Standardized cracks / crack width = 300 microns	Encapsulated polyurethane	2 / 4	Standard chloride migration tests (NT Build 443) / chloride migration coefficient	Healing prior to chloride exposure	- Healing of cracks largely decreases the chloride content compared to unhealed cracks. - Perfect healing of the crack, so that the concrete would behave as uncracked, was not observed.
9	2018	Van Belleghem et al. [42]	Standardized cracks / crack width = 300 microns	Encapsulated polyurethane	1 / 4	Electrochemical measurement and modified chloride diffusion test (26 weeks)/ chloride profiles	Healing prior to chloride exposure	- The specimens healed with high viscosity polyurethane exhibited a chloride profile like that of cracked specimens without healing. - Autonomous crack healing with low viscosity polyurethane noticeably reduced chloride content compared to untreated cracked specimens.
10	2019	Van Mullem et al. [27]	Mechanically induced cracks / crack width = around 150 microns	Stimulated autogenous healing by super absorbent polymers/ wet-dry cycles for 28 days	2	Chloride diffusion test/chloride profiles	Healing prior to chloride exposure	- SAP stimulated autogenous healing, notably reducing chloride ingress during the initial week of exposure. - Yet, after five weeks in aggressive media, specimens healed with SAP exhibited similar chloride ingress levels to reference specimens healed without SAP.
11	2019	Abro et al. [22]	Mechanically induced cracks / crack width = 100-500 microns.	Crystalline and expansive admixtures / immersion in water for 28 and 56 days.	1 / 2	Modified migration test / diffusion coefficient	Healing prior to chloride exposure	- After 56 days of healing, specimens with a 0.1 mm crack showed diffusion coefficients nearly identical to uncracked specimens across all mixtures. - For larger crack widths, the reduction in the diffusion coefficients depended on the mixture.
12	2021	Abro et al. [23]	Mechanically induced cracks /	Crystalline and	1 / 2	Modified	Healing prior to chloride exposure	- Change of migration coefficient over cracks for different crack widths were reported.

			crack width = 200 -400 microns.	expansive admixtures / immersion in water for 28, 56 and 128 days		migration test / diffusion coefficient		- A linear relationship between migration coefficient and crack width is found. - The concept of equivalent crack width is proposed.
13	2021	Yoo et al. [31]	Mechanically induced cracks / crack width = 100 -300 microns	Autogenous healing / immersion in water for 28, 56 and 91 days	1 / 2	Modified migration test / diffusion coefficient	Healing prior to chloride exposure	- A linear relationship between migration coefficient and crack width is found. - The slope of diffusion coefficient to crack width decreases, as the reduction in diffusion coefficient is larger as the crack width increases.
14	2021	Cuenca et al. [24]	Mechanically induced cracks / crack width = 200-800 microns	Crystalline admixture/ Continuous immersion and wet-dry cycles in NaCl solution for 1, 3, 6 months.	2	Chloride diffusion test/chloride profiles	Simultaneously	- When crystalline admixtures are included in the mix, the chloride profile stabilizes at a depth considerably closer to the exposure surface compared to the reference mix. - Crystalline admixture proves more effective in specimens under constant immersion compared to those undergoing wet-dry cycles.
15	2022	Rossi et al. [29]	Mechanically induced cracks / crack width = 100-150 microns	Bacteria-based healing agent / immersion in water for 28 days	3	Chloride diffusion and migration test / Chloride diffusion and migration coefficients	Healing prior to chloride exposure	- The positive impact of self-healing is evident in chloride diffusion but not in chloride migration. - The healing products formed at the crack mouth can initially mitigate chloride diffusion, but their blocking effect diminishes in the long term.
16	2023	Cappellesso at al. [43]	Mechanically induced cracks / crack width = 300 microns	Crystalline admixture + bacteria-based healing agent / weekly wet-dry cycles for 3 months	2 / 3	Chloride diffusion test (immersion in a NaCl solution for 3 months) / chloride profiles	Healing prior to chloride exposure	Both types of healing agents had improved behaviour related to chloride ingress, while reference specimens had an ingress of about 1.5 times more than the self-healing concrete.
17	2024	De Brabandere et al. [34]	Standardized cracks / crack width = 300 microns	Crystalline, expansive, and bacterial healing agents	2 / 3	Diffusion test (immersion in NaCl solution for 6 and 12 weeks) and migration test / chloride profile	Healing prior to chloride exposure	- A higher sealing efficiency does not necessarily mean a higher resistance to chloride ingress. - All healing agents delivered a faster reduction as compared to autogenous healing. However, after 56 days of healing, all test specimens exhibited a chloride

						and migration coefficient		migration coefficient similar with the control specimens.
18	2024	Cappellesso at al. [6]	Mechanically induced cracks / crack width = 100 microns	Manual injection of water-repellent agent (WRA), sodium silicate (SS, and polyurethane (PU)/ air drying for 2 days	1/2	Diffusion test (immersion in NaCl solution for 140 days) / chloride profile and diffusion coefficient	Healing prior to chloride exposure	- Selected healing agents can all effectively reduce the rate of chloride ingress. - PU and WRA are more effective than SS. But SS is more desirable for resisting chloride ingress during freeze-thaw cycles.

References

[1] Z. Huang, E. Cuenca, L. Ferrara, Incorporation of self-healing of UHPC in structural design approaches through healable crack width threshold and kinetics: The case study of H2020 project ReSHEALience database, Developments in the Built Environment 18 (2024) 100388. https://doi.org/10.1016/J.DIBE.2024.100388.

[2] M. Roig-Flores, S. Formagini, P. Serna, Self-healing concrete-What Is it Good For?, Materiales de Construcción 71 (2021) e237–e237. https://doi.org/10.3989/MC.2021.07320.

[3] R.M. Mors, H.M. Jonkers, Bacteria-based self-healing concrete: evaluation of full scale demonstrator projects, RILEM Technical Letters 4 (2019) 138–144. https://doi.org/10.21809/RILEMTECHLETT.2019.93.

[4] A. Al-Tabbaa, C. Litina, P. Giannaros, A. Kanellopoulos, L. Souza, First UK field application and performance of microcapsule-based self-healing concrete, Constr Build Mater 208 (2019) 669–685. https://doi.org/10.1016/J.CONBUILDMAT.2019.02.178.

[5] M. RM, J. HM, Bacteria-Based Self-Healing Concrete: Towards Standardization, Research & Development in Material Science 10 (2019). https://doi.org/10.31031/rdms.2019.10.000732.

[6] V. Cappellesso, T. Van Mullem, E. Gruyaert, K. Van Tittelboom, N. De Belie, Enhancing concrete durability in chloride-rich environments through manual application of healing agents, Journal of Building Engineering 90 (2024) 109380. https://doi.org/10.1016/J.JOBE.2024.109380.

[7] V. Cappellesso, D. di Summa, P. Pourhaji, N. Prabhu Kannikachalam, K. Dabral, L. Ferrara, M. Cruz Alonso, E. Camacho, E. Gruyaert, N. De Belie, A review of the efficiency of self-healing concrete technologies for durable and sustainable concrete under realistic conditions, International Materials Reviews 68 (2023) 556–603. https://doi.org/10.1080/09506608.2022.2145747.

[8] P. Schiessl, S. Helland, C. Gehlen, L.O. Nilsson, S. Rostam, fib bulletin 34: Model code for service life design, 2006.

[9] A.L. Schultheiß, R.A. Patel, M. Vogel, F. Dehn, Comparative study of probabilistic modeling approaches for chloride ingress in concrete structures with macro-cracks, Structural Concrete 24 (2023) 345–358. https://doi.org/10.1002/suco.202200069.

[10] A. Djerbi, S. Bonnet, A. Khelidj, V. Baroghel-bouny, Influence of traversing crack on chloride diffusion into concrete, Cem Concr Res 38 (2008) 877–883. https://doi.org/10.1016/j.cemconres.2007.10.007.

[11] J. Pacheco Farias, Corrosion of steel in cracked concrete: Chloride microanalysis and service life predictions, (2015). https://doi.org/10.4233/UUID:BC726EAD-0999-4FE4-BAD1-5C26C0E50405.

[12] A.L. Schultheiß, R.A. Patel, F. Dehn, Probabilistic service life prediction of cracked concrete using numerical and engineering models, Ce/Papers 6 (2023) 1524–1533. https://doi.org/10.1002/CEPA.2958.

[13] D.P. Bentz, E.J. Garboczi, Y. Lu, N. Martys, A.R. Sakulich, W.J. Weiss, Modeling of the influence of transverse cracking on chloride penetration into concrete, Cem Concr Compos 38 (2013) 65–74. https://doi.org/10.1016/J.CEMCONCOMP.2013.03.003.

[14] T. Ishida, P.O.N. Iqbal, H.T.L. Anh, Modeling of chloride diffusivity coupled with non-linear binding capacity in sound and cracked concrete, Cem Concr Res 39 (2009) 913–923. https://doi.org/10.1016/J.CEMCONRES.2009.07.014.

[15] Q.F. Liu, J. Yang, J. Xia, D. Easterbrook, L.Y. Li, X.Y. Lu, A numerical study on chloride migration in cracked concrete using multi-component ionic transport models, Comput Mater Sci 99 (2015) 396–416. https://doi.org/10.1016/J.COMMATSCI.2015.01.013.

[16] L. Marsavina, K. Audenaert, G. De Schutter, N. Faur, D. Marsavina, Experimental and numerical determination of the chloride penetration in cracked concrete, Constr Build Mater 23 (2009) 264–274. https://doi.org/10.1016/J.CONBUILDMAT.2007.12.015.

[17] S. Qian, J. Zhou, M.R. de Rooij, E. Schlangen, G. Ye, K. van Breugel, Self-healing behavior of strain hardening cementitious composites incorporating local waste materials, Cem Concr Compos 31 (2009) 613–621. https://doi.org/10.1016/J.CEMCONCOMP.2009.03.003.

[18] K. Sisomphon, O. Copuroglu, E.A.B. Koenders, Self-healing of surface cracks in mortars with expansive additive and crystalline additive, Cem Concr Compos 34 (2012) 566–574. https://doi.org/10.1016/J.CEMCONCOMP.2012.01.005.

[19] T. Danner, U.H. Jakobsen, M.R. Geiker, Mineralogical Sequence of Self-Healing Products in Cracked Marine Concrete, Minerals 2019, Vol. 9, Page 284 9 (2019) 284. https://doi.org/10.3390/MIN9050284.

[20] I.S. Yoon, E. Schlangen, Experimental examination on chloride penetration through micro-crack in concrete, KSCE Journal of Civil Engineering 18 (2014) 188–198. https://doi.org/10.1007/s12205-014-0196-9.

[21] M. Maes, K. Van Tittelboom, N. De Belie, The efficiency of self-healing cementitious materials by means of encapsulated polyurethane in chloride containing environments, Constr Build Mater 71 (2014) 528–537. https://doi.org/10.1016/j.conbuildmat.2014.08.053.

[22] F. ul R. Abro, A.S. Buller, K.-M. Lee, S.Y. Jang, Using the steady-state chloride migration test to evaluate the self-healing capacity of cracked mortars containing crystalline, expansive, and swelling admixtures, Materials 12 (2019) 1865.

[23] F.U.R. Abro, A.S. Buller, T. Ali, Z. Ul-Abdin, Z. Ahmed, N.A. Memon, A.R. Lashari, Autogenous healing of cracked mortar using modified steady-state migration test against chloride penetration, Sustainability (Switzerland) 13 (2021). https://doi.org/10.3390/su13179519.

[24] E. Cuenca, F. Lo Monte, M. Moro, A. Schiona, L. Ferrara, Effects of autogenous and stimulated self-healing on durability and mechanical performance of UHPFRC: Validation of tailored test method through multi-performance healing-induced recovery indices, Sustainability 13 (2021) 11386.

[25] A. Darquennes, K. Olivier, F. Benboudjema, R. Gagné, Self-healing at early-age, a way to improve the chloride resistance of blast-furnace slag cementitious materials, Constr Build Mater 113 (2016) 1017–1028. https://doi.org/https://doi.org/10.1016/j.conbuildmat.2016.03.087.

[26] S. Jacobsen, J. Marchand, L. Boisvert, Effect of cracking and healing on chloride transport in OPC concrete, Cem Concr Res 26 (1996) 869–881. https://doi.org/https://doi.org/10.1016/0008-8846(96)00072-5.

[27] T. Van Mullem, R. Caspeele, N. De Belie, The influence of SAPs on chloride ingress in cracked concrete, in: Concrete Solutions-7th International Conference on Concrete Repair, 2019.

[28] S. He, Z. Wan, Y. Chen, H.M. Jonkers, E. Schlangen, Microstructural characterization of crack-healing enabled by bacteria-embedded polylactic acid (PLA) capsules, Cem Concr Compos 143 (2023). https://doi.org/10.1016/j.cemconcomp.2023.105271.

[29] E. Rossi, R. Roy, O. Copuroglu, H.M. Jonkers, Influence of self-healing induced by polylactic-acid and alkanoates-derivates precursors on transport properties and chloride penetration resistance of sound and cracked mortar specimens, Constr Build Mater 319 (2022) 126081. https://doi.org/https://doi.org/10.1016/j.conbuildmat.2021.126081.

[30] S. He, Z. Wan, Y. Chen, H.M. Jonkers, E. Schlangen, Microstructural characterization of crack-healing enabled by bacteria-embedded polylactic acid (PLA) capsules, Cem Concr Compos 143 (2023). https://doi.org/10.1016/j.cemconcomp.2023.105271.

[31] K.S. Yoo, S.Y. Jang, K.M. Lee, Recovery of chloride penetration resistance of cement-based composites due to self-healing of cracks, Materials 14 (2021). https://doi.org/10.3390/ma14102501.

[32] Y. Javeed, Y. Goh, K.H. Mo, S.P. Yap, B.F. Leo, Microbial self-healing in concrete: A comprehensive exploration of bacterial viability, implementation techniques, and mechanical properties, Journal of Materials Research and Technology 29 (2024) 2376–2395. https://doi.org/10.1016/J.JMRT.2024.01.261.

[33] M. Luo, C.X. Qian, R.Y. Li, Factors affecting crack repairing capacity of bacteria-based self-healing concrete, Constr Build Mater 87 (2015) 1–7. https://doi.org/10.1016/J.CONBUILDMAT.2015.03.117.

[34] L. De Brabandere, T. Van Mullem, J.H. Lee, J.-I. Suh, K.-M. Lee, N. De Belie, Comparative analysis of three different types of self-healing concrete via permeability testing and a quasi-steady-state chloride migration test, Constr Build Mater 411 (2024) 134288. https://doi.org/10.1016/j.conbuildmat.2023.134288.

[35] Z. Wan, Z. Chang, Y. Xu, B. Šavija, Optimization of vascular structure of self-healing concrete using deep neural network (DNN), Constr Build Mater 364 (2023) 129955. https://doi.org/10.1016/J.CONBUILDMAT.2022.129955.

[36] S. Sayadi, E. Ricketts, E. Schlangen, P. Cleall, I. Mihai, A. Jefferson, Effect of microstructure heterogeneity shapes on constitutive behaviour of encapsulated self-healing cementitious materials, MATEC Web of Conferences 378 (2023) 09004. https://doi.org/10.1051/MATECCONF/202337809004.

[37] B. Pan, K. Qian, H. Xie, A. Asundi, Two-dimensional digital image correlation for in-plane displacement and strain measurement: A review, Meas Sci Technol 20 (2009). https://doi.org/10.1088/0957-0233/20/6/062001.

[38] M. Şahmaran, Effect of flexure induced transverse crack and self-healing on chloride diffusivity of reinforced mortar, J Mater Sci 42 (2007) 9131–9136. https://doi.org/10.1007/s10853-007-1932-z.

[39] M. Ismail, A. Toumi, R. François, R. Gagné, Effect of crack opening on the local diffusion of chloride in cracked mortar samples, Cem Concr Res 38 (2008) 1106–1111. https://doi.org/https://doi.org/10.1016/j.cemconres.2008.03.009.

[40] M. Maes, D. Snoeck, N. De Belie, Chloride penetration in cracked mortar and the influence of autogenous crack healing, Constr Build Mater 115 (2016) 114–124. https://doi.org/10.1016/j.conbuildmat.2016.03.180.

[41] B. Van Belleghem, P. Van den Heede, K. Van Tittelboom, N. De Belie, Quantification of the service life extension and environmental benefit of Chloride Exposed Self-Healing Concrete, Materials 10 (2017). https://doi.org/10.3390/ma10010005.

[42] B. Van Belleghem, S. Kessler, P. Van den Heede, K. Van Tittelboom, N. De Belie, Chloride induced reinforcement corrosion behavior in self-healing concrete with encapsulated polyurethane, Cem Concr Res 113 (2018) 130–139. https://doi.org/10.1016/j.cemconres.2018.07.009.

[43] V.G. Cappellesso, T. Van Mullem, E. Gruyaert, K. Van Tittelboom, N. De Belie, Comparison of different types of self-healing concrete under extreme conditions, in: SMARTINCS'23 Conference on Self-Healing, Multifunctional and Advanced Repair Technologies in Cementitious Systems, EDP Sciences, 2023: p. 08005. https://doi.org/10.1051/matecconf/202337808005.

8

Application of SH-SHCC in Tram Line 19

This chapter documents a demonstrator project to apply the developed SH-SHCC in a full-scale construction project where stringent requirements for tensile performance and crack healing properties are essential.

The construction project entailed is the extension of tram line 19 from Delft station to TU Delft campus. Constructing of this tram line poses considerable technical challenges, since tram services can generate significant vibration and electromagnetic radiation, both of which can impact sensitive measuring devices used at the TU Delft campus. While vibration and radiation can be individually mitigated using established methods, addressing both issues simultaneously poses conflicting demands on the design of the tram track. One issue arises due to the electromagnetic reduction system (EMRs) applied to mitigate radiation, which necessitates the absence of magnetic materials in the tram track, except for the rails. Consequently, steel reinforcement cannot be incorporated into the concrete foundation, inevitably leading to concrete cracking. This, in turn, reduces the structural stiffness of the foundation, thereby elevating its vibration levels. To address this requirement, we seek fibre-reinforced concrete capable of bearing tensile stress independently of embedded steel. Also, since no concrete can be crack-free, concrete that can autonomously heal its cracks is chosen.

This chapter will detail the insights gained from scaling up the developed self-healing system for this project, which requires the casting of around 1,800 cubic metres of SH-SHCC. Technical considerations such as reducing the shrinkage of SHCC, optimizing the production method, and verifying its pumpability will be discussed. A documentation of the construction process of the SH-SHCC layer will also be provided at the end.

8.1 Tram line 19

Delft, situated in the heart of the Randstad, the densely populated urban area in the western Netherlands, is strategically positioned between major cities such as The Hague and Rotterdam. This prime location underscore Delft's historical prominence as a pivotal hub in the region's economic and transportation networks. Tram connection between Delft and The Hague traces its origins back to 1866, the first tram line in the Netherlands. Moreover, the city is home to a prominent technical university accommodating 27,000 students and 4,000 academic staffs. This sizable community further underscores the necessity and relevance of a robust public transportation link.

Being the second tram line connecting Delft and its neighbouring areas, tram line 19 has been planned since 2004 to connect TU Delft with Leidschendam via Ypenburg and Leidschenveen in The Hague. This line connects well with public transport in the region. Travelers can transfer from tram line 19 to about 20 city and regional buses, 3 rail lines and 4 tram lines. Construction on tram line 19 began in 2005. However, a series of delays pushed back the opening of the first section, running between Leidschendam-Voorburg and Delft station, until July 2010. The last leg of tram line 19, connecting Delft station to the TU Delft campus, faced a significant hurdle due to concerns about the Sebastiaans bridge's structural capacity to accommodate tram traffic. This led to the decision to replace the bridge entirely. After years of planning and construction, the new bridge was finally opened on June 12, 2022, enabling the completion of the final section of tram line 19 (Fig. 8.1).

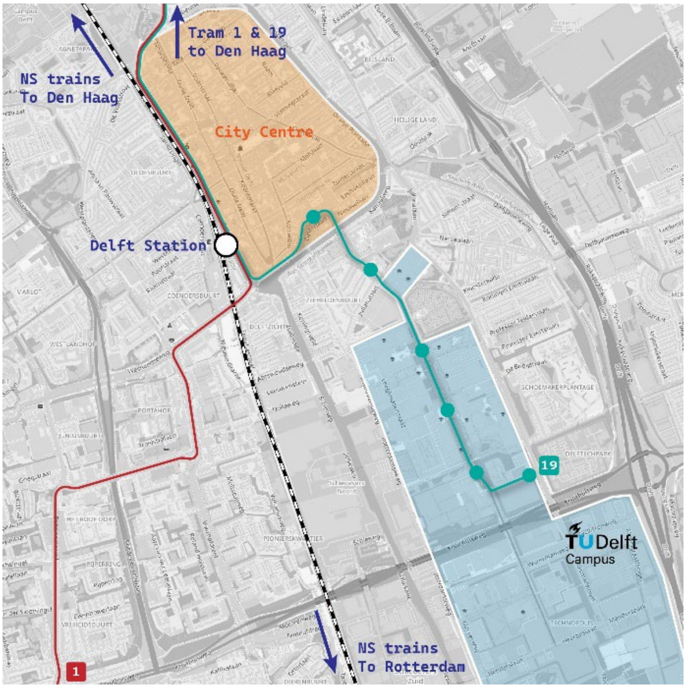

Figure 8.1: Map depicting the routes of tram 1 and tram 19 in Delft.

Since tram traffic generates vibration and variable magnetic fields, it is critical to make sure researchers at TU Delft can carry out research activities with as little disruption from the tram as possible. As part of the solution, roughly 1 km long of the tram track in the centre of TU Delft campus between Station Aula and Station Berlageweg (as shown in Fig. 8.2) must be designed with an Electromagnetic Reduction System developed to limit the electromagnetic fields generated by the tram traffic. However, this system necessitates the absence of magnetic materials in tram track, except for the rails. Consequently, steel reinforcement cannot be incorporated into the concrete foundation, inevitably leading to concrete cracking. Consequently, the stiffness of foundation decreases, resulting in higher vibration levels. To address this issue, a special type of concrete is required, capable of withstanding tensile stress without relying on embedded steel. Moreover, to maintain an effective damping effect, the concrete must remain free of cracks, as any cracking would diminish its damping properties.

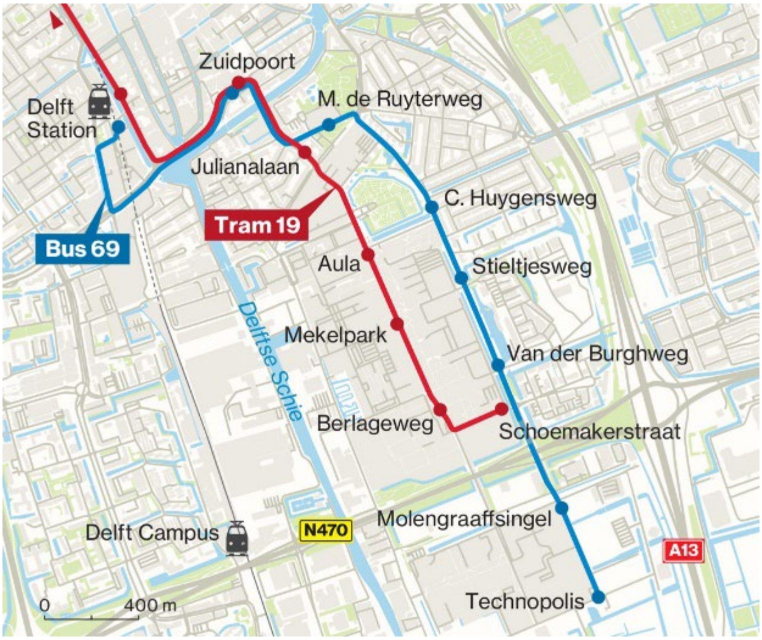

Figure 8.2: Map illustrating bus and tram routes connecting Delft Station to the TU Delft campus.

This justifies the need to use SH-SHCC in this particular section of the tram track. SH-SHCC fulfils the demand for withstanding tensile stress through polymeric fibres rather than steel rebars. Additionally, considering that concrete inevitably develops cracks under external strain, the self-healing capacity of SH-SHCC can aid in restoring some stiffness even in the presence of cracks.

This chapter will detail the process of upscaling SH-SHCC for application in the tram project. The total volume of the SH-SHCC required is around 1,600 m^3. Despite its considerable potential, several practical challenges persist. Specifically, the upscaling efforts will focus on optimizing the SH-SHCC mix design to accommodate the raw material availability at concrete plants and to reduce the shrinkage. Furthermore, various mixers and mixing protocols will be evaluated to determine the maximum production speed of SH-SHCC while maintaining its tensile properties. Additionally, the feasibility of pumping SH-SHCC will be demonstrated. Finally, prototypes simulating SH-SHCC segments over sub-layer concrete joints will be tested. Insights and knowledge gained at each stage will be shared.

8.2 Optimization of mixture composition

8.2.1 Backgrounds

The composition of the SH-SHCC developed in previous chapters features a significant proportion of binder, unlike normal concrete where fillers (*e.g.* sand and aggregates) typically dominate the volume. This design is made purposely to enhance the tensile properties of the SH-SHCC, since a larger binder portion ensures that the material is more homogeneous, and the distribution of fibres is more even [1,2]. However, one drawback of this approach is the decreased workability of the fresh concrete due to the larger surface area of all powdered materials. While this challenge is manageable in a laboratory setting with the application of advanced mixers, it poses significant difficulties in a concrete plant where production speed is paramount. Dealing with a sticky mix becomes particularly challenging, especially considering its adverse effects on concrete pumping. Furthermore, a large binder proportion typically lead to large shrinkage. For normal concrete, an ultimate drying shrinkage strain with magnitude of 400×10^{-6} to 600×10^{-6} is obtained under typical drying conditions of 20 °C and 60% relative humidity [3]. By contrast, the ultimate drying shrinkage strain of conventional SHCC is approximately 1200×10^{-6} to 1800×10^{-6} under the similar drying conditions [4,5]. Therefore, the 1st target of optimizing the mixture of SH-SHCC is to increase the filler content with the aim to reduce drying shrinkage strain.

The 2nd target relates to the type of filler. The fillers commonly used in SHCC, such as micro silica sand or finely ground limestone powder, are notably smaller in size compared to typical fine aggregates like river sand used in conventional concrete. While this poses no challenge in laboratory settings, it can present significant processing difficulties due to the large surface area in industrial production. Additionally, micro silica sands and limestone powder are not commonly stocked materials in concrete plant silos. Plant managers are typically hesitant to empty a silo for materials intended for a single project. Consequently, the filler type for SHCC should be adjusted to utilize fillers readily available in concrete plants.

The 3rd requirement concerns the replacement of silica fume. The SH-SHCC mixture contains silica fume to enhance the fibre/matrix bond by densifying the microstructure of the interfacial transition zone (ITZ) between the fibre and matrix [6]. However, the extremely fine particle size of silica fume powder, as much as 100 times finer than cement, greatly complicates handling of silica fume. For this reason, using silica fume at conventional concrete plants does come with some inherent risks, primarily related to worker health and safety as well as environmental considerations. One way to facilitate handling of silica fume is to blend it with water, making silica fume in a stable slurry form. However, this approach necessitates specialized infrastructure at concrete plants. Again, plant managers may be hesitant to invest in such facilities for a single project. Therefore, other fine materials that can be used to density the fibre/matrix interfacial zone are needed.

The 4th target is related to the amount of fibre. Since the construction of the tram track demand the casting of SH-SHCC to be executed at a relatively high speed, SH-SHCC must be transferred by a concrete pump to facilitate this casting process. However, SH-SHCC is essentially a fibre-reinforced concrete with an extremely high fibre content, which can potentially lead to increased wear on equipment, clogging, and higher pumping pressure. While there is no precise threshold for tolerable fibre content, minimizing it as much as feasible is advantageous for both performance and cost reduction for large scale construction projects.

Accordingly, the proposed modifications to the SHCC mixture entail:

1. Utilizing fillers readily accessible at concrete plants.
2. Identifying substitutes for silica fume.
3. Decreasing binder content.
4. Lowering fibre content.

These modifications should ensure that the two primary objectives for facilitating SHCC field application are met: (i) sustained high fluidity throughout mixing and (ii) volume stability.

8.2.2 Experimental results

8.2.2.1 Mixture analysis

Table 8.1 displays the composition of SH-SHCC mixtures before and after modification. The initial mixture, labelled as SHCC-Lab, represents the original laboratory-developed recipe utilized for preparing the SH-SHCC U-shape cover detailed in Chapter 6. This mixture acts as a foundational framework for formulating blends suitable for large-scale production at concrete plants. The subsequent two mixtures are refined formulations designed for concrete plant manufacturing. Both formulations maintain identical water-to-cement and filler-to-binder ratios. The differentiating factor lies in the choice between silica fume and micro-cement for enhancing the fibre/matrix bonding.

Table 8.1: Mixture composition of SH-SHCC for lab and plant production

Material	SHCC-Lab	SHCC-Plant-1	SHCC-Plant-2
CEM III/B 42.5 N	842	573	560
Silica fume	94	64	-
Micro-cement (Dyckerhoff Mikrodur®)	-	-	74
Limestone powder (Carmeuse Calcitec®)	468	318	317
Sand (0-4 mm)	-	954	904
PE fibre	10	10	12
Healing agent	10	10	10
Water	286	286	301
Superplasticizer	3.0	2.5	3.2

Fig. 8.3 illustrates the volume percentage of various constituents for both the original SHCC mixture and the refined version. In the original mixture, limestone exclusively serves as the filler, comprising 26% of the total volume. The binder, comprised of cementitious material and water, dominates the composition, constituting approximately 73% of the total volume. In contrast, the

mixture tailored for large-scale mixing comprises 56% filler. Within this filler component, 70% consists of 0-4 mm river sand, which boasts a significantly lower surface area compared to limestone. Consequently, this variation is expected to reduce shrinkage and to enhance workability due to its reduced surface area.

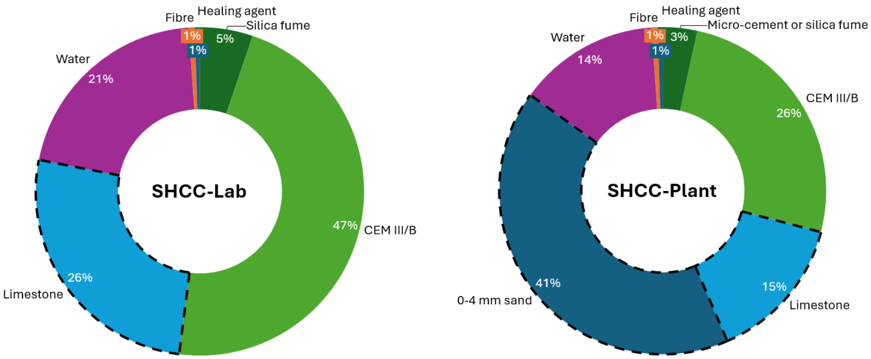

(a) (b)

Figure 8.3: Volume percentage of various constituents for (a) the original SHCC mixture and (b) the refined version for large scale application.

8.2.2.2 Material properties of SH-SHCC

Fig. 8.4 presents the findings from the drying shrinkage assessment conducted on both the initial SHCC and the optimized variant (SHCC-Plant-2). This evaluation involved subjecting a prismatic specimen (40 mm × 40 mm × 160 mm) to a controlled environmental condition (19 °C and 50% RH) and monitoring the length alterations over a 30-day period. As evident from the data, the shrinkage value after 30 days decreased notably from 1000 με to 600 με, aligning closely with the typical shrinkage values observed in conventional concrete. Moreover, it seems that drying shrinkage of SHCC-plant mix is reaching plateau which is not the case for SHCC-Lab mix. The observed reduction in shrinkage can likely be attributed to the higher filler content incorporated into the mixture.

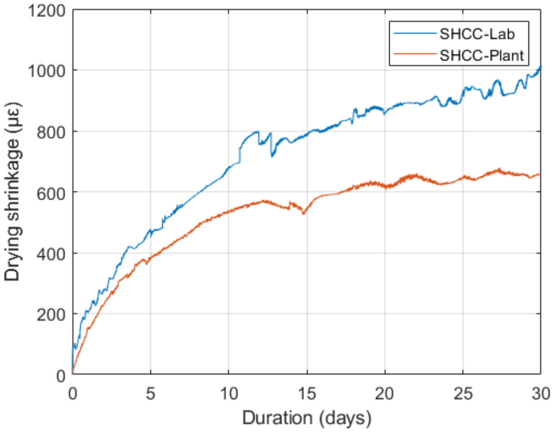

Figure 8.4: Comparison of drying shrinkage of the original SHCC and the optimized SHCC.

Fig. 8.5 illustrates the tensile stress-strain characteristics of the SH-SHCC formulations tailored for laboratory testing and large-scale production. Given the utilization of 0-4 mm sands in the SHCC mixture for large-scale production, dogbone specimens featuring a larger cross-sectional area (60 mm × 60 mm) were prepared, contrasting with the 10 mm × 30 mm cross-sectional area employed for the laboratory version of SHCC. The applied set-ups for testing the dogbones are presented next their respective tensile stress-strain curves.

As evident from the findings, both formulations displayed significant ductility under tensile loading. Despite the substantial inclusion of sands into the matrix, the optimized mixture still demonstrates a strain capacity of around 2%, albeit lower than that of the original SHCC mix. Also, in one sample, the first cracking resistance is significantly higher than the resistance at larger deformations. Given that stress transfer at large deformations (1-2% tensile strain) remains comparable to lab samples, this mix is considered suitable. Note that due to smaller cross-sectional area, lab samples have more preferential fibre orientation which also contributes to higher strain capacity. Furthermore, given that a 2% tensile strain still satisfies the criteria of the current study, the compromise on strain capacity is deemed acceptable. Fig. 8.6 shows the crack patterns of SHCC dogbones after test. The dogbone specimens crafted from SHCC-Plant showcased the development of numerous fine cracks, mirroring the characteristics observed in the dogbones created from SHCC-Lab.

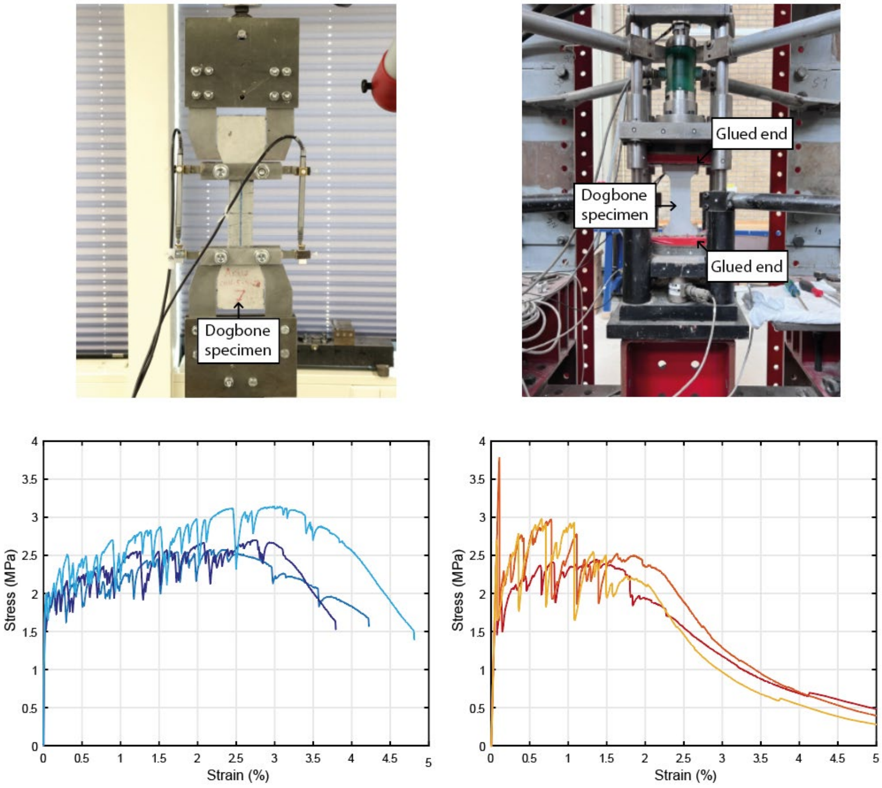

(a) (b)

Figure 8.5: Uniaxial tensile results of (a) original SHCC and (b) optimized SHCC for large-scale production.

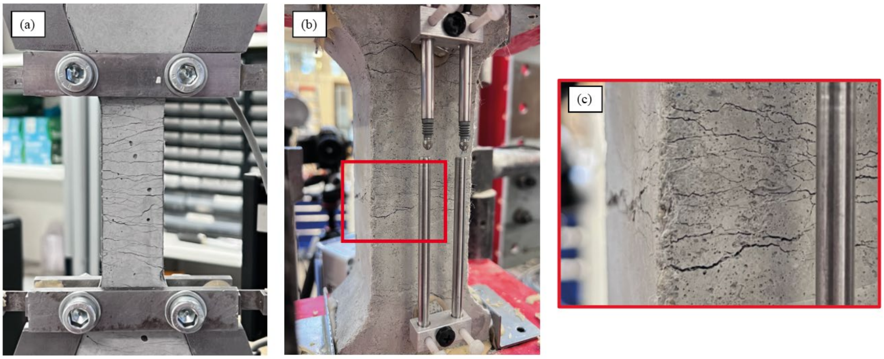

Figure 8.6: Crack pattern shown on tested dogbone specimen of (a) SHCC-Lab, (b) SHCC-Plant, and (c) zoom-in photo of a SHCC-Plant dogbone.

8.2.2.3 Structural performance of SH-SHCC beams

Beside dogbone specimens, beam specimens, cut from the SH-SHCC panel cast at the concrete batching plant, were also tested to assess their flexural performance. The beams were subjected to a 4-point-bending configuration (refer to Fig. 8.7), while DIC cameras were deployed to track the development of cracks during the test. The evaluation of the performance of the beam revolved around its ductility and cracking behaviour.

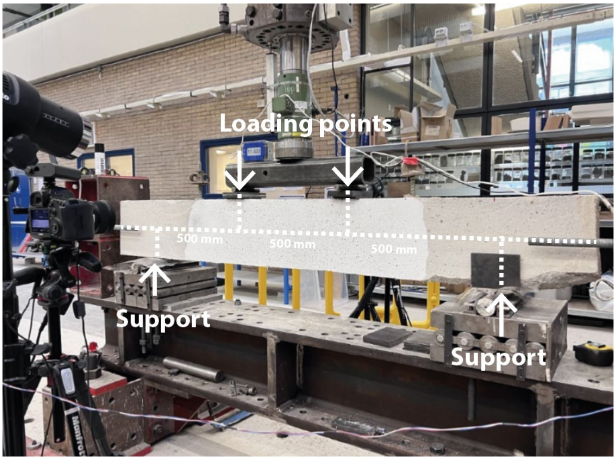

Figure 8.7: Experimental set-up for the 4-point-bending test.

Fig. 8.8 displays the load-deflection curve obtained, revealing three distinct stages in its behaviour. In the initial stage, the beam exhibited elastic deformation, characterized by a linear relationship between the applied load and the deflection. As the load increases further, the beam transitioned into the plastic deformation stage, marked by more pronounced deformation as cracks begin to form. Observable load drops during this stage indicate the initiation of new cracks. Subsequently, upon reaching the ultimate strength, the beam entered the post-failure stage, where the load-deflection curve demonstrates a steady decline as the beam experiences a ductile failure.

The beam displayed a significant deflection of 16 mm at peak load, a measure comparable to that of a conventional reinforced concrete beam with the same dimensions. This exceptional response in a plain concrete beam, without any rebars, demonstrates remarkable ductility, especially when compared to typical plain concrete beams that tend to fail suddenly with only a few millimetres of deflection. Moreover, what sets this beam apart is its pronounced 'hardening' behaviour, wherein the load-bearing capacity continued to increase with the deflection. This post-cracking characteristic is a direct result of using fibres in this special concrete mix.

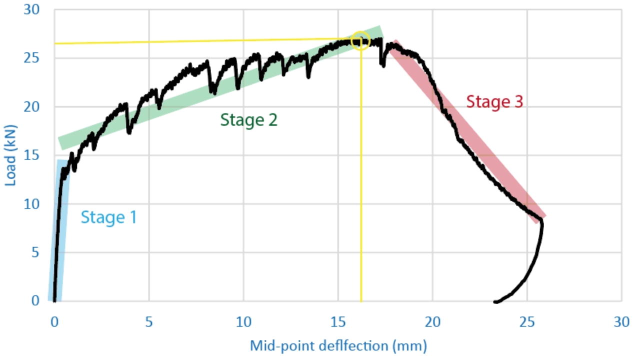

Figure 8.8: Load-deflection curve of the tested SH-SHCC beam.

Of great importance is that the beam exhibited multiple cracking behaviour, with the formation of many bands of micro-cracks. In Fig. 8.9, the crack pattern at peak load, as captured by cameras, is shown. Before the crack localization occurred, these micro-cracks were barely visible by naked eye. The formation of only small cracks in the SH-SHCC will prevent the occurrence of reflective cracks in the covering asphalt layer and will result in minimal stiffness reduction. Moreover, tight crack width can facilitate crack healing and promote the rapid recovery of the structural integrity, making it a significant advantage in terms of long-term durability and performance.

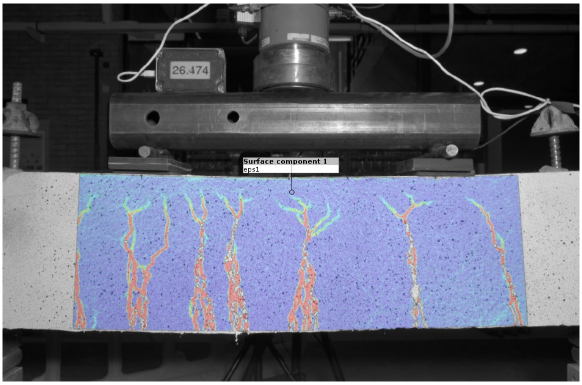

Figure 8.9: Crack pattern of the beam at peak load tracked by DIC camera.

8.3 Large scale mixing and pumping of SH-SHCC

8.3.1 Backgrounds

Once the mix design of the SH-SHCC is finalized, the subsequent stage involves assessing the feasibility of manufacturing these materials at concrete plants. This evaluation entails conducting SH-SHCC mixings at two concrete plants, utilizing different concrete mixers: one equipped with a pan mixer and the other with a reversing drum mixer, as depicted in Fig. 8.10.

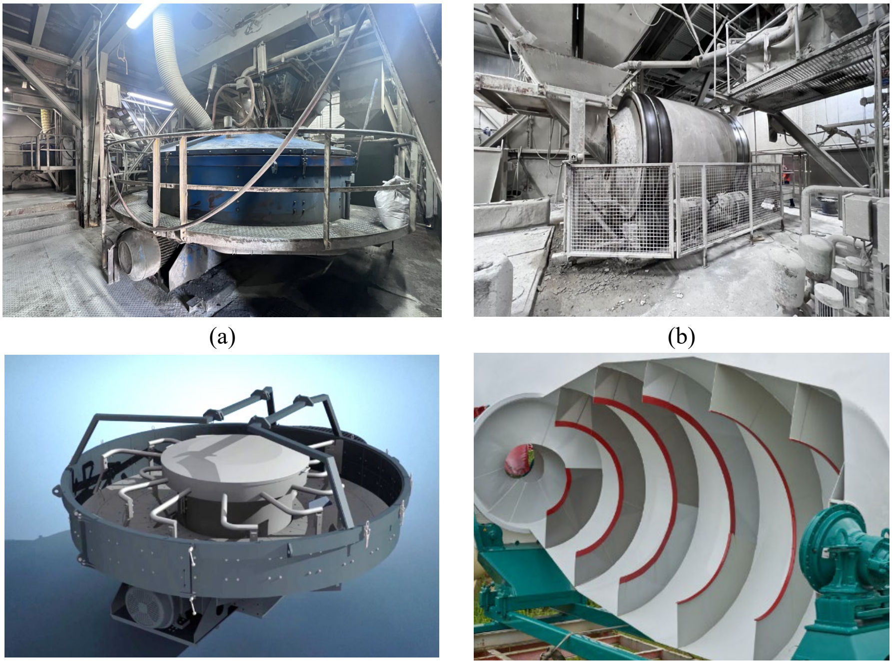

(a) (b)

(c) (d)

Figure 8.10: Photos of the mixers applied in the current study: (a) pan mixer and (b) reversing drum mixer. Inner structure of the two types of mixers is shown in (c) and (d)

A pan concrete mixer operates with a stationary pan or drum, typically made of steel, mounted on a fixed frame. Inside the pan, mixing blades or paddles, often attached to a central vertical shaft, rotate around the central axis. During operation, the pan remains stationary while the mixing blades revolve, lifting the concrete mixture from the bottom of the pan and causing it to cascade over the blades, ensuring thorough blending. Once mixing is complete, the concrete mixture can be discharged through a chute or gate at the bottom of the pan. Pan mixers are well-suited for small to medium-scale concrete mixing applications due to their efficient mixing action and relatively compact design.

The mechanism of a drum mixer involves a rotating drum that serves as the mixing vessel. During operation, the drum rotates in one direction to mix the materials inside, and then reverses its direction to discharge the mixture. Inside the drum, mixing blades or fins as shown in Fig. 8.10b facilitate the blending of materials as they are lifted and dropped during rotation. This simple yet effective mechanism allows for the thorough mixing of concrete and similar materials, making drum mixers a common choice for a wide range of construction projects. In common concrete trucks, a tilting drum mixer serves as the primary mixing mechanism.

When mixing fibre-reinforced concretes, planetary mixers and twin-shaft mixers are typically favoured for their ability to evenly distribute fibres throughout the concrete (Fig. 8.11). However, the choice of mixer is usually constrained by the need to minimize transportation distances to the construction site, as long journeys can escalate costs and degrade the concrete's quality. In the scenario of the current project, only two concrete plants are situated conveniently nearby. Consequently, despite the advantages of planetary and twin-shaft mixers, the pan mixer and the drum mixer were chosen due to their proximity and availability.

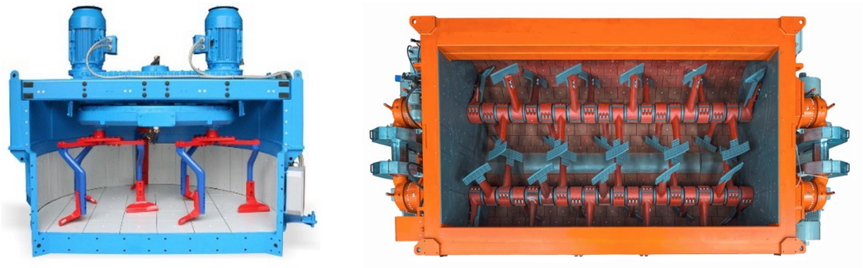
(a) Planetary mixer (b) Twin shaft mixer

Figure 8.11: Mixers preferred for mixing fibre reinforced concrete

Considering the diverse attributes of the two mixer types (*i.e.*, pan mixer and drum mixer), trial mixings were conducted to establish appropriate mixing protocols and validate the mechanical properties of the resultant materials. Subsequently, a decision was reached through a comprehensive evaluation encompassing both production efficiency and tensile strain capacity.

8.3.2 Experimental results

8.3.2.1 Mixing sequences

A comparison of the finalized mixing procedure between the two mixers can be found in Fig. 8.12. As observed, the pan mixer takes 18 minutes to produce one batch of SH-SHCC with satisfactory fibre distribution, whereas the drum mixer achieves the same quality in 8 minutes. The long duration needed for the pan mixer was primary due to the lack of a dedicated feeding system for adding fibres into the mixture. Consequently, the addition of fibres necessitated halting the mixing process, opening the mixer, and manually introducing the fibres. In contrast, the drum mixer features an open design that allows the ingredients to be added from the inlets during the mixing process, which largely simplifies the process. When using the drum mixer, two mixing sequences were also experimented. Method 1 involved initially dry-mixing aggregates and fibres to preliminarily disperse the fibres before incorporating cement and water. This approach aims to break the fibre chunks with the help of the aggregate. Conversely, Method 2 focuses on first creating a homogeneous cement paste and then adding fibres. This practice leverages the shear stresses in the fresh paste to enhance fibre dispersion. Both methods were found to be equally effective. Additionally, the pan mixer used has a smaller capacity, capable of producing only 1 m^3 per batch, compared to the drum mixer's 2 m^3. Consequently, the combination of smaller batch volume and longer mixing time results in a significantly lower hourly output from the pan mixer compared to the drum mixer. While the pan mixer is capable of producing only 3 m^3 per hour, the drum mixer can produce 12 m^3 per hour. Therefore, in terms of production speed, the drum mixer significantly outperforms the pan mixer.

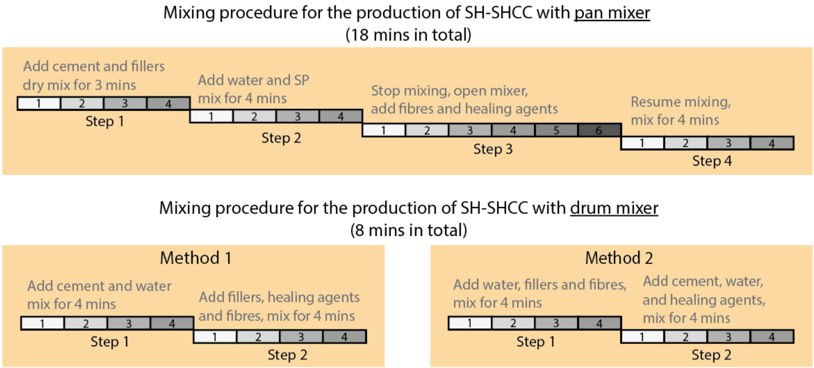

Figure 8.12: Mixing sequences developed at commercial concrete batching plants with pan mixer and reversing drum mixer.

8.3.2.2 Tensile properties of SH-SHCC produced by different mixers

Fig. 8.13 depicts the results of uniaxial tensile tests conducted on dogbone specimens manufactured by two distinct mixers. It is evident that although there are slight variations in tensile strength, both sets of dogbones exhibit a strain capacity exceeding 2%, meeting the requirements of the project. Furthermore, Fig. 8.14 illustrates the crack patterns observed in the dogbone specimens, revealing a consistent occurrence of multiple cracking phenomena across both series.

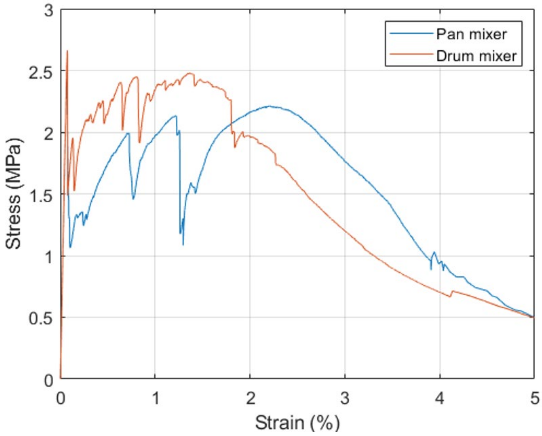

Figure 8.13: Tensile stress-strain curves of SH-SHCC dogbone specimens produced by the two types of mixers.

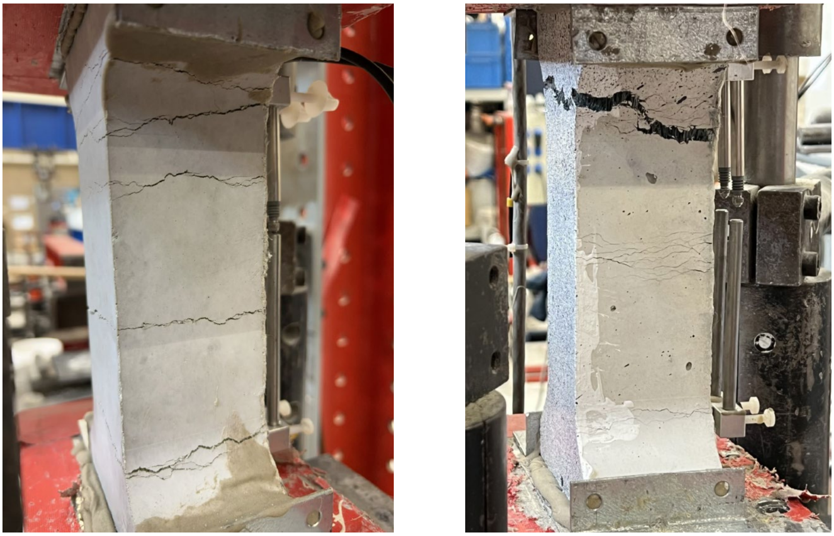
(a) (b)

Figure 8.14: Crack pattern of SH-SHCC dogbone specimens produced by (a) pan mixer and (b) drum mixer.

8.3.2.3 Demonstration of pumping feasibility

Since one of the requirements from the contractor is to transport the SH-SHCC by pump during the final pour, pumping trials were also carried out after mixing of large batches. Pumping trials were performed with a truck-mounted concrete pump (SCHWING S36x) capable of a pumping pressure of 85 bar and a maximum concrete output of 161 m^3/h. The trials all went successfully, and the monitored pressure level when pumping the SH-SHCC was constantly less than 30 bar. Fig. 8.15 shows some photos taken during one of the pumping trials. As can be seen, the fresh SH-SHCC can be easily discharged from a concrete truck to the hopper of concrete pump, and the fresh mortar pumped out demonstrated quite good workability. It can thus be concluded that both developed mixtures are compatible with pumping.

(a) (b)

(c) (d)

Figure 8.15: Photos taken during the pumping trial: (a) and (b) concrete truck discharging SH-SHCC into pump truck, (c) and (d) casting of an SH-SHCC panel from the pumped SH-SHCC

In conclusion, the findings of this section affirm that a drum mixer is more suitable for producing SH-SHCC at concrete batching plants compared to a pan mixer. The drum mixer facilitates a higher production rate while simultaneously ensuring that the fresh and hardened properties of SH-SHCC remain satisfactory.

8.4 Design of continuous SHCC layer over discrete concrete substrates

8.4.1 Backgrounds

Tram line 19 adopts an embedded ballastless track system which involves laying the tram tracks within the roadway surface rather than on top of it (Fig. 8.16). This system is designed to integrate the tram tracks seamlessly into the street, allowing vehicles to travel over them without disruption.

In the segment within TU Delft campus, the tram tracks are embedded in a 24 cm thick layer of SHCC. This layer of SHCC is supported by an underlying layer of concrete (27 cm in thickness) to provide structural support. On top of the SHCC, the surface will be overlaid with a layer of asphalt paving. The concrete layer beneath the SHCC incorporates expansion/contraction joints at intervals of 12.5 meters to accommodate temperature or shrinkage induced deformation. The SHCC layer itself remains continuous atop the discontinuous concrete layer, ensuring a seamless surface for paving asphalt.

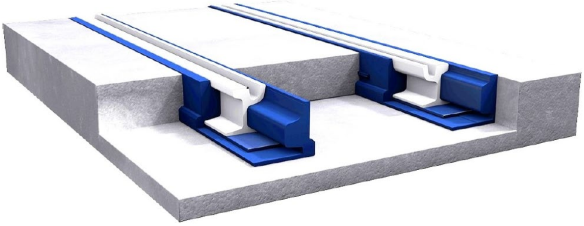

(b)

Figure 8.16: Schematic illustration of the embedded system

In this design, a critical aspect to consider is the area neighbouring the concrete joint, where the intentional gap between adjacent concrete slabs is anticipated to widen over time. This widening creates tensile stress and strain within the SHCC layer, leading to the formation of distributed multiple fine cracks.

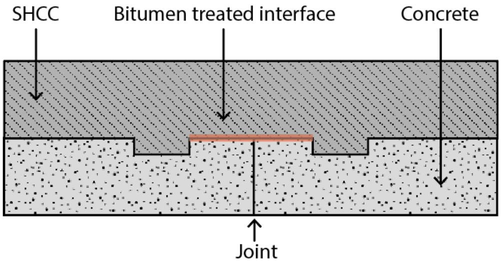

(a) before shrinkage

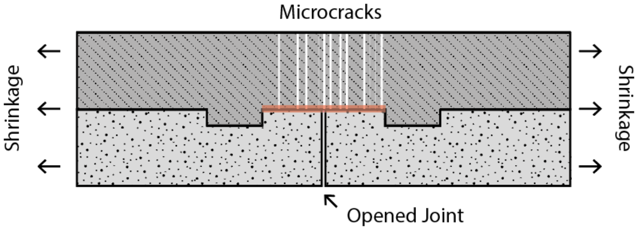

(b) After shrinkage

Figure 8.17: Schematic illustration of SH-SHCC overlay above concrete joint

As evident, the design objective entails that the SHCC layer effectively disperses localized deformation stemming from the joint into distributed fine cracks, thereby preventing the formation of reflective cracks in the asphalt layer and facilitating crack healing over time. This objective aligns with the concept of the SHCC cover for crack width control and crack healing as discussed in previous chapters (Chapter 4 and Chapter 6).

Hence, a specialized design inspired by the Vaseline-treated shear key method was implemented near the concrete joint. Illustrated in Fig. 8.17, this design incorporates indents on both sides of the joint within the concrete layer to enhance mechanical interlocking between the concrete and the SHCC layer. Additionally, bitumen will be applied at the interface to promote the activation of the SHCC. Experiments were thus designed and carried out to verify this concept.

8.4.2 Experimental results

Fig. 8.18 and Fig. 8.19 illustrate the experimental setup devised to validate the feasibility of using SH-SHCC to link adjacent concrete slabs. In this design, concrete beams with rectangular indents on their top surface were initially prepared, followed by the casting of SH-SHCC on top. The top surface of the concrete beam between the two indents was coated with a layer of bitumen prior to the casting of the SHCC. This step was taken to encourage debonding between the layers during the experiment. A gap between the two concrete beams was intentionally left to accommodate the insertion of a flat hydraulic jack. The purpose of the flat jack is to exert pressure, causing the two concrete beams to separate, simulating the expansion of the joint. The beams were refrained by steel frame at both ends to ensure that the middle segment of SH-SHCC would be subjected to pure tension.

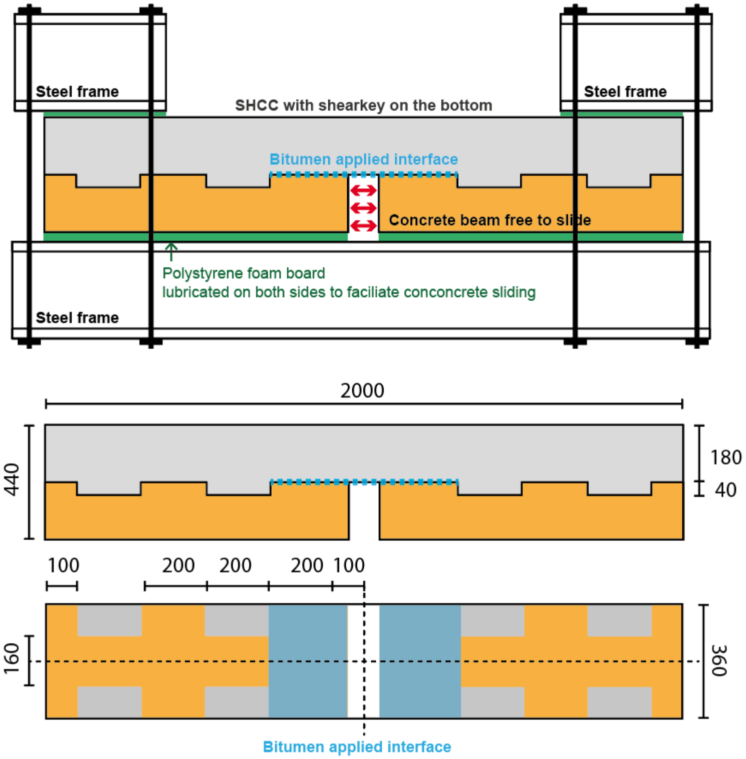

Figure 8.18: Experimental set-up for testing the performance of SH-SHCC over expanding joint

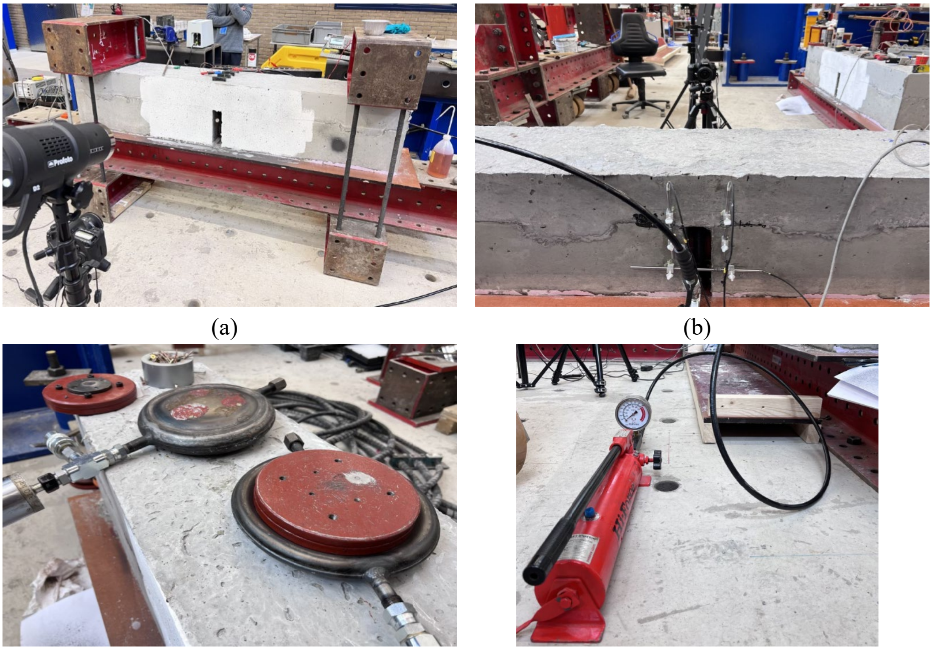

(a) (b)

(c) (d)

Figure 8.19: Photograph of (a) the overall test setup, (b) rear view of the beam with LVDT and hose for pump. (c) and (d) the flat jack and the hydraulic pump utilized during the test, respectively.

Fig. 8.20 shows the results obtained from the hydraulic pump and the LVDT applied to measure the opening of the joint. As observed, the SH-SHCC layer effectively withstood the tensile stress, displaying highly ductile behaviour. The crack pattern on the right side of the figure demonstrates the anticipated multiple cracking phenomena characteristic of SH-SHCC. Significantly, at an 8 mm opening, no reduction in pressure was observed. The test concluded at an 8 mm opening upon reaching the maximum deformation of the flat jack, suggesting that the SH-SHCC could withstand even greater deformation. Nonetheless, considering the debonded length of approximately 300 mm, the absence of load drop at this 8 mm opening signifies a strain capacity exceeding 2% in this structural configuration.

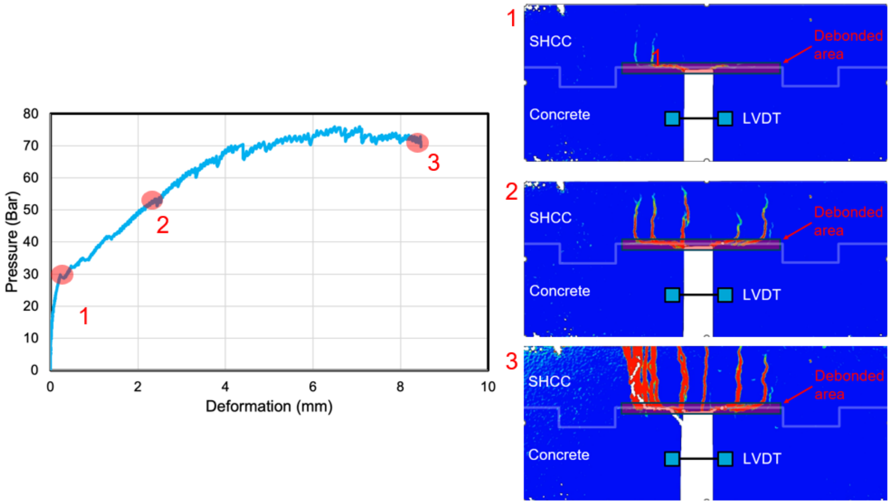

Figure 8.20: Experimental results

It is therefore concluded that a continuous layer of SH-SHCC can function as a link slab over concrete joints. The ductile SH-SHCC layer has the potential to effectively dissipate localized deformation stemming from the joint into distributed fine cracks, thereby preventing the formation of reflective cracks in the asphalt layer and facilitating crack healing over time. The process of crack healing will enhance the overall structural stiffness of the track, thereby augmenting its ability to dampen vibrations.

8.5 Conclusions

This chapter explored the feasibility of applying SH-SHCC in constructing the section of tram line 19 in the TU Delft campus. The overarching goal was to address the dual challenges of electromagnetic radiation and vibration mitigation, essential for the sensitive operational environment of TU Delft. The use of SH-SHCC was driven by its ability to withstand tensile stress independently of traditional steel reinforcement and its unique self-healing properties that mitigate crack propagation, which is critical in maintaining structural integrity and damping characteristics under operational conditions. At the same time, the challenge was to upscale this innovative material, its mix design and manufacturing to industrial level production without jeopardizing its tensile strain capacity.

Several key achievements and insights were highlighted through the project:

1. The transition from lab-based formulations to large-scale production posed significant challenges, particularly in terms of raw material availability and limited concrete mixing equipment selection. Adjustments in the material composition and production techniques were necessary to maintain the mechanical properties while ensuring the mixture was viable for large-scale processing. These adjustments included reducing the binder content,

modifying filler types, and optimizing fibre content to balance workability with mechanical properties.

2. The experimental results, including those from tensile and flexural tests, demonstrated that the optimized SH-SHCC mixtures for large scale production maintain satisfactory ductility under tensile stress. This is crucial for its application in tram tracks where it must endure dynamic loads and environmental factors that can facilitate cracking.
3. The successful large-scale mixing and subsequent pumping trials confirmed that SH-SHCC could be manufactured and applied in situ using conventional concrete batching and pumping equipment. This feasibility is essential for the practical implementation of such advanced materials in standard construction projects.
4. The design integration of SH-SHCC over discrete concrete substrates using the bitumen-treated shear key method illustrated the SH-SHCC layer can effectively dissipate localized deformation stemming from the joint into distributed fine cracks, thereby preventing the formation of localized reflective cracks in the asphalt layer and facilitating crack healing over time.

8.6 Documentation of construction process of the SH-SHCC layer

The photo above was taken before casting the SH-SHCC layer and provides an overview of the foundation layers beneath it. The foundation consists, from bottom to top, of a gravel layer, a foam concrete layer, and an unreinforced concrete layer that supports the sleepers. After positioning the sleepers and aligning the trials, the SH-SHCC layer will be cast over the concrete layer. At the end, the rails will be embedded within the hardened SH-SHCC layer.

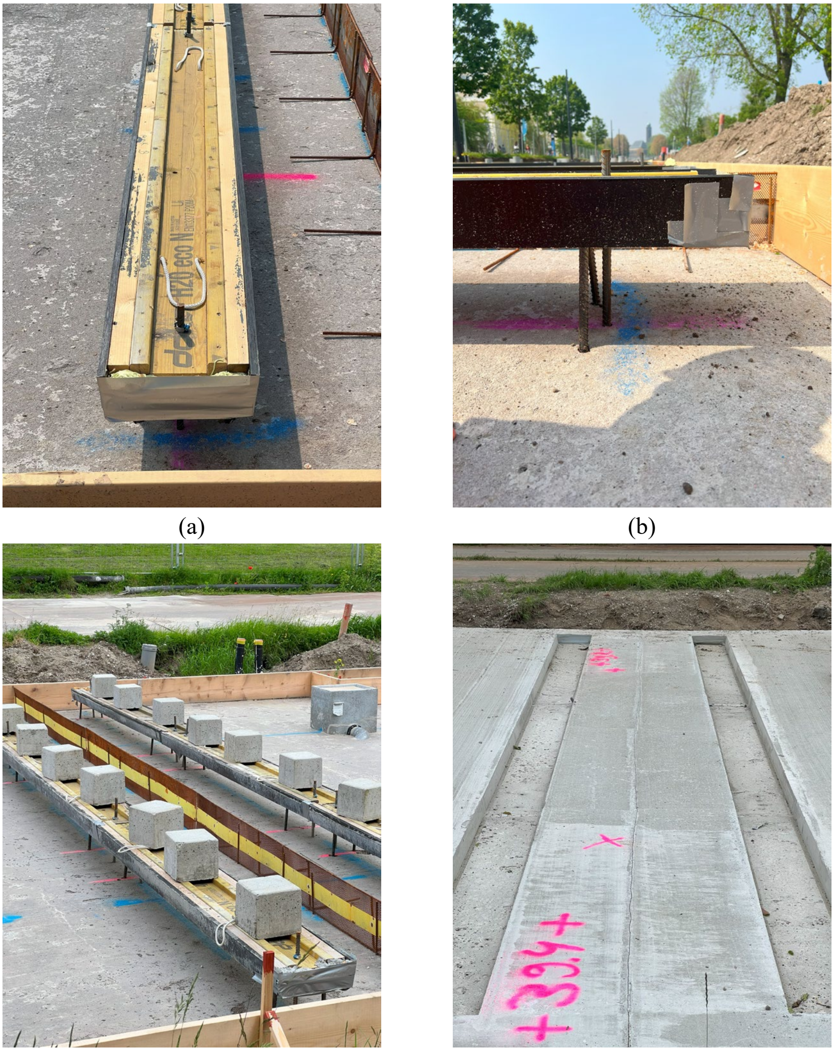

(a) (b)

(c) (d)

The photos above illustrate the preparation process for creating indents in the concrete layer. As outlined in section 8.4.1, this design incorporates indents on both sides of the joint within the concrete layer to enhance mechanical interlocking between the concrete and the SHCC layer. Prior to casting the concrete layer, specialized timber blocks (a, b) were prepared and installed on both sides of the joint. The indent depth was controlled using vertical steel bars, and additional weight was applied to prevent the timber blocks from rising during concrete pouring (c). The final photo (d) shows the appearance of the indents in the concrete layer after the timber blocks were removed. A crack at the joint can already been seen at this stage.

The photo above shows the preparation between two adjacent indents just before casting the SHCC layer. Bitumen was applied between the indents to create a debonded region between the concrete and SH-SHCC, ultimately aiming to promote multiple cracking behaviour in the SH-SHCC layer above the concrete joint

The first photo, taken during the first SH-SHCC casting on September 27, 2024, shows the fresh material being poured along the centreline of the track, allowing it to flow to both sides. This approach ensures the filling of gaps beneath the rail and sleepers. The SH-SHCC proved to be pumpable and highly workable, with manual levelling applied to achieve an even surface. The second photo was taken during an inspection carried out on Oct 18, 2024. It shows the hardened SH-SHCC with the embedded rail in place, and the final result has a clean and visually appealing finish.

During the inspection, small cracks, likely resulting from the shrinkage of the SH-SHCC itself, were observed. However, due to the presence of microfibers in the mixture, the crack widths were minimal, making them visible only when the surface of the SH-SHCC was damp. These small cracks have a high likelihood of self-healing within a couple of weeks. Additionally, bundles of microcracks were noted, demonstrating the occurrence of multiple cracking behaviour.

The photos above depict the preparation of the next section of the rail, awaiting the application of SH-SHCC. Each 60-meter section is cast with a continuous supply of SH-SHCC to prevent the formation of multiple cold joints, ensuring a consistent presence of fibres throughout the material. The casting of SH-SHCC along the entire length of the tramway at the TU Delft campus is expected to be completed by the end of 2024.

Acknowledgement

The successful implementation of SH-SHCC in Tram 19 was a collaborative achievement. The author would like to express sincere gratitude to all parties involved, with special thanks to TU Delft and the Metropolitan Region Rotterdam The Hague (MRDH) for their support in advancing this technology on the tramline. The author is also especially appreciative of the team at Dyckerhoff Basal for their invaluable insights into scaling up material production at batching plants and for their dedicated work in trial mixing and pumping. Further thanks go to colleagues at Royal HaskoningDHV for their contributions to the structural design discussions and to Dura Vermeer for their expertise and input on finalizing construction details.

Within TU Delft, the author extends gratitude to the project management team for coordinating effectively with all stakeholders in the planning, testing, and execution phases. Additional appreciation goes to the academic and technical staff from the Materials & Environment and Concrete Structures sections, whose prioritization and swift execution of many experiments and arrangements were vital to the success of the tram project.

References

[1] V.C. Li, S. Wang, C. Wu, Tensile Strain-Hardening Behavior of Polyvinyl Alcohol Engineered Cementitious Composite (PVA-ECC), Materials Journal 98 (2001) 483–492. https://doi.org/10.14359/10851.

[2] V.C. Li, D.K. Mishra, H.C. Wu, Matrix design for pseudo-strain-hardening fibre reinforced cementitious composites, Mater Struct 28 (1995) 586–595. https://doi.org/10.1007/BF02473191/METRICS.

[3] A.M. Neville, Properties of concrete, Longman London, 1995.

[4] E.-H. Yang, Y. Yang, V.C. Li, Use of high volumes of fly ash to improve ECC mechanical properties and material greenness, ACI Mater J 104 (2007) 620.

[5] M. Li, V.C. Li, Behavior of ECC/Concrete Layered Repair System Under Drying Shrinkage Conditions / Das Verhalten eines geschichteten Instandsetzungssystems aus ECC und Beton unter der Einwirkung von Trocknungsschwinden, Restoration of Buildings and Monuments 12 (2006) 143–160. https://doi.org/10.1515/RBM-2006-6040.

[6] Y.W. Chan, V.C. Li, Effects of transition zone densification on fiber/cement paste bond strength improvement, Advanced Cement Based Materials 5 (1997) 8–17. https://doi.org/10.1016/S1065-7355(97)90010-9.

9

Conclusions and outlook

This chapter presents a brief summary of the work reported in this PhD dissertation, followed by conclusions drawn from it. In addition, this chapter outlines specific topics the PhD candidate intended to investigate but had to forgo due to time constraints. General suggestions for future research directions are also provided.

9.1 Retrospection

Despite notable advancements in the research of self-healing concrete, the transition from laboratory to real-world applications encounters significant hurdles, particularly concerning efficiency, economic feasibility, and design integration. To tackle these challenges, this thesis aims to devise a method for implementing self-healing concrete exclusively within the cover zone. By focusing on the concrete cover zone, which crucially influences the durability of reinforced concrete structures, this approach maximizing the effects of healing agents by targeting the specific area in need, thereby enhancing efficiency and cost-effectiveness.

To develop a composite system comprising a reinforced concrete core and a self-healing cover zone, a self-healing SHCC suitable for the cover was initially developed in Chapter 2, with a specific emphasis on examining the influence of bacterial-embedded PLA capsules on the multiscale properties of SHCC. A dosage of 2.5% by weight of cement was found to be a balanced dosage for the capsules, considering their effects on the mechanical and fresh properties of SHCC. The healing behaviour of the developed material was then demonstrated in Chapter 3. It was found that bacteria-enabled healing can deliver faster and deeper crack closure compared to autogenous healing.

After studying the mechanical and healing performance of the developed material, Chapter 4 investigated the impact of applying such a cover on the structural response of beams subjected to flexural loading. A special interface profile was developed and found to be effective in ensuring the structural integrity of the system while promoting the most favourable crack pattern with small crack widths at the surface of the beams. Chapter 5 examined the behaviour of hybrid elements under shear loading. The study demonstrated that the developed interface profile can also effectively mitigate interfacial delamination under shear. Furthermore, it was observed that the inclusion of the cover enhanced both shear capacity and ductility. After confirming the efficacy of the developed cover system under both flexural and shear loading, Chapter 6 conducted a comparative analysis of hybrid beams with cover zones manufactured using various methods, including precast and 3D printing. The chapter concluded that 3D printing holds promise as a technique for producing the cover as lost formwork.

To facilitate the application of the developed technology, Chapter 7 proposed methodologies for incorporating the benefits of the self-healing cover into existing design codes. Finally, Chapter 8 presented attempts to scale up the technology into demonstrators and full-scale pilot projects. Insights into scaling up material production, designing its performance and validating its performance in the real scale application were reported. The conclusion drawn is that the developed material can be mass-produced in standard concrete plants at a reasonable production speed and requiring no specialized equipment.

9.2 Conclusions

Overall, the main findings obtained in the present work are summarized as follows:

1. *Robust and rapid healing can be achieved when bacteria-embedded polylactic acid (PLA) capsules are added in strain hardening cementitious composites (SHCCs).*

The synergy between self-healing and strain-hardening is evident. On one hand, the inclusion of PLA capsules enhances strain-hardening behaviour by introducing artificial defects and strengthening the fibre/matrix bond. On the other hand, since healing is most sensitive to crack width, the formation of multiple cracks with narrow crack widths facilitates faster and easier healing.

2. *Bacteria-enabled healing can deliver faster and deeper crack healing compared to autogenous healing*

When the assessment of healing goes beyond observation from surface, it can be found that the aerobic bacteria-mediated healing offers not only accelerated but also deeper recovery compared to autogenous healing. This is because autogenous healing due to, for example, carbonation is limited by the penetration of carbon dioxide, while the aerobic bacteria changed the controlling factor to oxygen.

3. *Long-term crack healing in realistic environment was observed to fundamentally differ from healing under short-term controlled conditions.*

Specimens containing PLA healing agent exhibited healing products mainly at the crack mouth after short-term healing. However, after long-term healing, no healing products were observed at the crack mouth, yet extensive healing was evident throughout the entire crack depth. It is likely that the environmental actions such as rainfall and freeze and thaw cycles may have worn away the healing products at the crack mouth and thus led to a deeper ingress of oxygen into cracks. Autogenous healing after long-term outdoor exposure was found to possess similar characteristics, with the depth of healing increased and a loss of healing products at surface.

4. *Vaseline-treated profiled interface offers a viable solution for connecting brittle concrete and ductile SHCC, preserving the distinctive characteristics of each material.*

A strong interfacial bond is not necessarily beneficial for the overall composite behaviour. In our current study, the desired characteristic of the material obtained from SHCC is its ability to exhibit multiple cracking behaviour. If the SHCC is perfectly bonded to the underlying concrete, it may not demonstrate this desired behaviour. Conversely, if the bond is weak, interfacial delamination can occur. In such cases, a chemically debonded but mechanically interlocked interface seems to offer a solution to these contradicting requirements.

5. *Both mould-casting and 3D printing are promising techniques in making the self-healing SHCC cover zone as lost formwork.*

In this study, experiments have demonstrated that mould-casted self-healing SHCC covers effectively enhance crack control and healing without compromising beam properties. They provide comparable or improved load capacity and ductility under various stresses. While 3D-printed covers exhibit slightly lower effectiveness in crack control, they still enhance overall performance and offer manufacturing efficiency advantages. Both types of covers effectively prevent delamination and disperse major cracks into finer ones, thereby facilitating rapid and robust crack healing.

6. *Although the incorporation of self-healing technologies into structural design codes and service life predictions is a feasible goal, it remains in its nascent stages, requiring extensive experimental data and real-world validations*

Incorporating the influence of healing into the calculation of corrosion initiation duration poses a challenge, as current service life models typically assume concrete to be crack-free. Nevertheless, by appropriately adjusting parameters such as the diffusion coefficient and aging factor in these models, it becomes feasible to consider the healing process as a slowed chloride ingress phenomenon. The challenges primarily stem from the availability of data required to accurately calibrate the parameters in these models. Despite the abundance of studies in this field, data reflecting real-world conditions are scarce, emphasizing the crucial need for validation of healing processes in practical settings.

7. *Large-scale production of self-healing SHCC at conventional concrete batching plants is possible.*

The transition from lab-based formulations to large-scale production posed significant challenges, particularly in terms of raw material availability and limited concrete mixing equipment selection. However, with proper adjustments in the material composition and production techniques, it is possible to maintain the properties of self-healing SHCC while ensuring the mixture was viable for large-scale processing. These adjustments included reducing the binder content, modifying filler types, and optimizing fibre content to balance workability with mechanical properties.

9.3 Recommendations for future research

<u>Specific advice for advancing the research presented in the current thesis:</u>

1. *Tailoring the particle size of healing agent for optimized healing performance.*

One factor influencing healing efficiency is the probability that a random crack intersects with a healing agent. If the crack exposes at least one healing agent, it can activate the embedded bacteria, thereby initiating the healing process. Therefore, the particle size of the healing agent should be minimized to allow a greater number of agents within a unit volume, thereby increasing the likelihood of crack intersection and activation. However, if the particle size is too fine, it results in a larger surface area, which can accelerate hydrolysis during the initial mixing process. These two effects highlight the need to research and determine the optimal particle size.

2. Optimization of the shear-key pattern

A key finding from the thesis is that a lubricated shear-key interfacial pattern can effectively bond brittle and ductile materials. It is important to note that this pattern was designed based on the engineering intuition of the author rather than iterative optimization, meaning it remains far from optimal. In theory, the spacing between each shear-key (representing the length of the debonded region) influences the amount of SHCC that can display multiple-cracking behaviour. Greater spacing can encourage more cracking, yet too sparse a pattern may lead to insufficient interfacial bonding. These competing effects, therefore, serious scientific investigation.

3. Verification of the performance of hybrid elements under imposed deformation.

All the hybrid beams presented in this thesis were tested under imposed load conditions (*e.g.*, 3-point bending and 4-point bending tests) rather than imposed deformation conditions (*e.g.*, freeze-thaw cycles, wetting-drying cycles, etc.). These conditions may be equally critical for the behaviour of this hybrid system, as the cover and the core have distinct compositions and different transport/mechanical properties related to the aforementioned processes. Future research should explore these aspects to deepen our understanding of hybrid beam performance in varying environmental conditions.

4. Durability assessment of RC beams with self-healing cover

Due to time constraints of the PhD program, the author was unable to explore the effects of the self-healing cover on the durability of reinforced concrete elements. Since many deterioration processes can be significantly accelerated by cracking, the self-healing cover could potentially delay their progression. Therefore, it would be valuable to investigate, for example, the corrosion behaviour of reinforced concrete elements with a self-healing cover. The results would not only validate the performance of the developed system but also provide meaningful data for its design.

5. Design self-healing cover for large structural elements.

In the current thesis, the volume ratio of the self-healing cover to the entire element is approximately 26%. This ratio is constrained by the requirement that the cover thickness must be at least 1 to 1.5 cm to ensure sufficient strength against various handling conditions. Additionally, the size of the beam elements (1 meter long) is limited by the testing methods and transportation facilities available in the lab. However, if larger elements are produced with the same cover thickness, a significantly lower volume ratio could be achieved. It would be worthwhile to investigate the performance of thin self-healing covers on full-scale structural elements for infrastructure applications.

General advice for self-healing concrete research:

The ability of self-healing concrete to autonomously repair cracks and damage highlights its potential in restoring diverse critical properties. This versatility, while valuable in a way, also poses a challenge in design, as different structural requirements demand different healing outcomes. For instance, microbial mineral precipitation effectively reduces chloride ingress but has limited impact on restoring stiffness. This discrepancy highlights the importance of prioritizing certain properties in the healing process. Research is thus needed to determine which concrete characteristics stand to gain the most from self-healing, taking into account practicality, economic viability, and sustainability. Focused enhancements will ensure more robust and efficient healing performance, providing greater motivation for industry adoption of this technology.

After identifying key properties, it is essential to evaluate how specific self-healing effects can inform structural design. Many have proposed the notion of a 'healable crack width', suggesting the relaxation of current crack width criteria for different exposure classes to allow for larger cracks to some extent. This approach offers potential benefits, including a reduction in the reinforcement needed for crack width control for certain applications, resulting in cost and environmental footprint savings. However, determining the healable crack width is essential. Emphasizing this point, it is crucial to note that establishing this value requires conducting performance tests, such as chloride diffusion/migration tests, on concrete before and after healing. Relying solely on surface observations of crack closure to establish the crack width threshold can be misleading, as visual closure does not always guarantee complete restoration of chloride resistance.

Challenges still persist in the availability of data. Approaches to the design for durability of reinforced concrete structures can be divided into two categories: prescriptive approaches and performance-based approaches. The former consists of simple rules usually presented as threshold values for different parameters, often derived from experience, that should be fulfilled to guarantee an expected service life, using ordinary materials and technologies. The latter consists in design procedures aimed at determining (or verifying) the service life as a function of the desired performance of the structure, allowing the quantification of the effect of all the parameters involved, including the use of innovative materials (*e.g.*, self-healing concrete). Obviously, for self-healing concrete, a performance-based approach is essential. However, a critical aspect of this approach is the need for reliable data on all input parameters. This requirement presents a significant challenge in incorporating the effects of healing into the modelling of degradation mechanisms. Despite numerous studies showing self-healing's positive impact on concrete durability, there is a notable lack of probabilistic assessments evaluating these effects. Future research focusing on investigating the reliability of self-healing concrete over a large sample size would be beneficial.

Shifting the focus from structural design back to material development, future research should also aim to enhance the robustness of the shortlisted self-healing mechanisms. Perhaps, the absence of probabilistic-based reliability assessments for self-healing concrete might be that the technology, in its current form, is not yet sufficiently reliable. Current research on self-healing concrete typically reveals its efficacy under controlled and ideal conditions. Yet, even in these favourable environments, the effectiveness of these systems has exhibited inconsistencies. For practical application in real-world structures, it is crucial that self-healing processes can reliably maintain their effectiveness under typical operational conditions of infrastructure. To this end, research should focus on enhancing the robustness of self-healing mechanisms in concrete. This could include developing new self-healing materials or refining existing ones to make them more effective and reliable.

APPENDIX A

Characterization of porosity in the interfacial transition zone (ITZ) between microfibre and cement paste

Understanding the interaction between the fibres and matrix is vital in developing fibre-reinforced composites. Many researchers have focused on studying the properties of the interface or interphase between the fibre and matrix, which govern this interaction. However, characterizing this region in cement-based materials around micro-polymeric fibres is challenging due to the small diameter of the fibres, making sample preparation difficult. To address this challenge, a new method has been developed to characterize this Interfacial Transition Zone (ITZ) and provide valuable insights for future engineering projects.

Since the study has already been published in an open-access format and does not directly relate to the topic of self-healing, only the abstract is presented during the upcoming session (also to save trees). Web link and QR code are provided for attendees to access the full paper online.

Title of the paper:

Distribution of porosity surrounding a microfiber in cement paste

Abstract:

This study investigates the microstructural changes of cement paste due to the inclusion of polymeric microfiber at different water-to-cement (w/c) ratios. A procedure to quantify the porosity of epoxy impregnated interfacial transition zone (ITZ) is also presented. Results show that the microstructures of the ITZ beneath and above a microfiber, with respect to the gravity direction, are largely different. Though the ITZ at both sides of the fibre are more porous than the bulk matrix, the porosity of the lower ITZ (*i.e.*, the ITZ beneath a fibre) is significantly higher than the upper side (*i.e.*, the ITZ above a fibre). This difference can be attributed to the combined effects of fibre on the initial packing of surrounding cement grains and on the settlement of the fresh mixture. The porosity gradients of the upper ITZs are found to be nearly identical for all the tested w/c ratios, while the porosity gradients of the lower ITZs become steeper when the w/c is higher. The lower side is also found to be the preferred location for the precipitation of calcium hydroxide crystals. Results of energy-dispersive X-ray spectroscopy (EDS) and nano-indentation analyses confirm that the chemical and mechanical properties of the ITZ are also asymmetric.

Download:

https://doi.org/10.1016/j.cemconcomp.2023.105188

QR code:

ACKNOWLEDGEMENT

In the many theses I've read, I always start with the acknowledgment, as it captures the essence of the authors and their journey. While the rest of the thesis is filled with factual and logical statements, the acknowledgment is where the author can finally release the emotions they couldn’t express elsewhere. It’s like an explosion in a lab.

As a PhD candidate, I often wonder about others' doctoral experiences, which is why I find myself reading acknowledgments — I was curious, and perhaps a little apprehensive, about how my own PhD would unfold. Fortunately, my experience has been incredibly rewarding, and this is due to the support of each and every person I will mention below.

First, as a formality, I would like to acknowledge the financial support from the European Union's Horizon 2020 research and innovation program, specifically through the SMARTINCS project. This funding made my research possible, and I am truly grateful for it. At the time of writing this, governments in both Europe and the U.S. are implementing large-scale budget cuts for scientific research. It is disheartening to see that, despite the undeniable role of science and innovation in addressing global challenges, research funding is increasingly being treated as a dispensable expense. What did researchers do wrong? Should we acknowledge harder?

Now the real part begins. In Chinese culture, it is believed that the deepest gratitude should not be expressed in words, as no words can truly convey it. Therefore, I will not say anything appreciative to my promotors, Erik Schlangen and Henk Jonkers. But I do want to say that I enjoyed every moment we spent together—in the office, in the labs, during travels, at conferences, and especially in bars. In the many discussions and meetings we had, I always left with less worry and more energy.

I feel the same way about my daily supervisor, Mladena Luković. I truly cherished her great mentorship, positive attitude, and always cheerful smile. I can't count how many emails I received late at night, making me wonder if I was somehow in China’s time zone. To be clear, those emails were never requests, but always offered support.

Besides my promoters and supervisors, I would like to express my gratitude to the chairperson and my committee members. Thank you for taking the time to review my thesis and for providing comments that helped improve this work. I am especially grateful to Prof. En-Hua Yang, who was my supervisor during my master’s studies, for traveling from Singapore to attend my defense. It was during my years in Singapore that I decided to pursue a PhD, and that’s where this journey began.

As a dedicated experimentalist, I believe that while professors are the flags and faces of the scientific community, the true backbone is the technicians. Therefore, I would like to acknowledge all the help I received from the technicians at both Microlab and Macrolab. In particular, I want to thank Ton, who happens to be my neighbour, for all the help with concrete casting and cutting, and John for the electrochemistry experiments we have long been discussing (but sadly have yet to execute). Also, Arjan, I'll miss the time we spent working together with SEM and CT, and our discussions about microscopes, lenses, and, more generally, perspectives on life. Last but not least, I would like to give special thanks to Maiko, who will be my paranymph during the defense—if a suitable white tie can be found—for not only the outstanding professional support but also the friendship. With Maiko as a friend, I always have someone to talk to, no matter what. I also appreciate the effort he put into organizing all the events to make Microlab feel like a family.

Colleagues are the most important source of support during a PhD study, as we mostly share the same enjoyment and suffering that come with this unique journey. I would like to particularly acknowledge my colleagues, with whom I worked together during the COVID-19 pandemic. These were truly unprecedented and challenging times, and it required a great deal of trust to continue gathering for meals and drinks frequently at each other's homes, knowing that any one of us could potentially bring the virus. Since this was not exactly a socially responsible act, I will not reveal any names here.

In addition, I appreciate all my colleagues who gave me the opportunity to participate in their research. Of the many projects and publications completed, few were my own initiative. I am grateful for the collaborative environment we had at Microlab and for every chance I had to work with and learn from you all. The PhD will end sooner or later for all of us, but the bonds we've formed will remain.

The colleagues I worked most closely with are the 15 ESRs from the SMARTINCS project. I am truly grateful for the time and effort we all dedicated to making this project a success. The experience of collaborating in a multidisciplinary team has been a constant source of motivation for me. I am especially grateful to our project coordinators, Prof. Nele De Belie and Prof. Liberato Ferrara. I also deeply appreciate Prof. Frank Dehn for hosting me at Karlsruhe Institute of Technology during my secondment. Special thanks go to Dr. Andrija Blagojevic for the multiple visits at Concrefy in Venlo and the many fruitful discussions we had. Lastly, I would like to thank Dr. Tim Van Mullem for his efficient management of the project.

Also, I would like to thank my colleagues at Witteveen+Bos. The final stages of completing this thesis coincided with the start of my work there, which was a challenging period for me. I truly appreciate the understanding and thoughtful support they provided throughout this process.

Of course, at the end I would like to express my deepest gratitude to my parents, but it feels a bit strange to thank them in a language they don't speak. Parents who support their children in pursuing a PhD (especially abroad) are truly admirable. A PhD takes at least three years, often much longer, during which life goes on around, or sometimes without, the individuals. When they are in the lab, they are not at home with family. The cost is very real. I am truly grateful for all the assurance they've given me throughout this journey.

Finally, I would like to thank the woman who was once my girlfriend and is now my wife. I originally planned to do the same as I did with my promoters — say nothing — but I know you'd prefer I express my gratitude openly. I am deeply thankful for your unwavering support. We met, fell in love, and were united in Delft, which makes this PhD journey even more meaningful. Throughout our time together, I've never felt alone in this journey. Thank you.

Delft, Mar 2025

Curriculum Vitae

He, Shan 何山

22-03-1993	Born in Tianjin, China

Education

2011 - 2015	BSc Civil Engineering Nanjing University of Aeronautics and Astronautics, Nanjing, China
2013 - 2014	Exchange Carleton University, Ottawa, Canada
2015 - 2017	MEng Civil Engineering Nanyang Technological University, Singapore
2019 - 2024	PhD Civil Engineering Delft University of Technology, Delft, The Netherlands

Employment

2017 - 2019	Energy Research Institute @ NTU, Singapore *Research Associate*
2023 (Feb – Mar)	Karlsruhe Institute of Technology, Karlsruhe, Germany *Guest Researcher*
From 2024	Witteveen+Bos BV, Utrecht, The Netherlands *Consultant*

Awards

1. DSTA Gold Medal Award (for top master graduates of NTU in 2017)
2. IA-FraMCoS Conference Young Researcher Best Paper Award (2019)
3. ICSHM2022 Conference Best Paper Award (2022)
4. Smartincs'23 Conference Outstanding Research Award (2023)
5. Chinese Government Award for Outstanding Self-Financed Students Abroad (2023)
6. Winner of Bain & Company Brussels PhD challenge (2023)
7. Materials and Structures Journal's Best Paper of the Year Award (2023)

LIST OF PUBLICATIONS

First-author journal publications:

1. **He, S.**, Qiu, J., Li, J., & Yang, E.-H. (2017). Strain hardening ultra-high performance concrete (SHUHPC) incorporating CNF-coated polyethylene fibers. Cement and Concrete Research, 98, 50–60.
2. **He, S.**, Li, Z., & Yang, E.-H. (2019). Quantitative characterization of anisotropic properties of the interfacial transition zone (ITZ) between microfiber and cement paste. Cement and Concrete Research, 122, 136–146.
3. **He, S.**, & Yang, E.-H. (2021). Strategic strengthening of the interfacial transition zone (ITZ) between microfiber and cement paste matrix with carbon nanofibers (CNFs). Cement and Concrete Composites, 119, 104019.
4. **He, S.**, & Yang, E.-H. (2021). Non-normal distribution of residual flexural strengths of steel fiber reinforced concretes and its impacts on design and conformity assessment. Cement and Concrete Composites, 123, 104207.
5. **He, S.**, Zhang, S., Luković, M., & Schlangen, E. (2022). Effects of bacteria-embedded polylactic acid (PLA) capsules on fracture properties of strain hardening cementitious composite (SHCC). Engineering Fracture Mechanics, 268, 108480.
6. **He, S.**, Chen, Y., Liang, M., Yang, E.-H., & Schlangen, E. (2023). Distribution of porosity surrounding a microfiber in cement paste. Cement and Concrete Composites, 105188.
7. **He, S.**, Mustafa, S., Chang, Z., Liang, M., Schlangen, E., & Luković, M. (2023). Ultra-thin Strain Hardening Cementitious Composite (SHCC) layer in reinforced concrete cover zone for crack width control. Engineering Structures, 292, 116584.
8. **He, S.**, Wan, Z., Chen, Y., Jonkers, H. M., & Schlangen, E. (2023). Microstructural characterization of crack-healing enabled by bacteria-embedded polylactic acid (PLA) capsules. Cement and Concrete Composites, 105271.
9. **He, S.**, Nuri, M., Jonkers, H. M., Luković, M., & Schlangen, E. (2024). Structural behaviour of reinforced concrete beams with self-healing cover zone as lost formwork. Developments in the Built Environment, 18, 100458.
10. **He, S.**, Sayadi, S., Patel, R. A., Schultheiß, A. L., Mihai, I. C., Jefferson, A., ... & Dehn, F. (2025). Perspectives on the incorporation of self-healing in the design practice of reinforced concrete structures. Structural Concrete.

Co-authored journal publications:

1. Qiu, J., **He, S.**, & Yang, E.-H. (2019). Autogenous healing and its enhancement of interface between micro polymeric fiber and hydraulic cement matrix. Cement and Concrete Research, 124, 105830.
2. Sonat, C., **He, S.**, Li, J., Unluer, C., & Yang, E.-H. (2021). Strain hardening magnesium-silicate-hydrate composites (SHMSHC) reinforced with short and randomly oriented polyvinyl alcohol microfibers. Cement and Concrete Research, 142, 106354.
3. Chen, Y., **He, S.**, Zhang, Y., Wan, Z., Çopuroğlu, O., & Schlangen, E. (2021). 3D printing of calcined clay-limestone-based cementitious materials. Cement and Concrete Research, 149, 106553.
4. Chen, Y., **He, S.**, Gan, Y., Çopuroğlu, O., Veer, F., & Schlangen, E. (2022). A review of printing strategies, sustainable cementitious materials and characterization methods in the context of extrusion-based 3D concrete printing. Journal of Building Engineering, 45, 103599.
5. Liang, M., Li, Z., **He, S.**, Chang, Z., Gan, Y., Schlangen, E., & Šavija, B. (2022). Stress evolution in restrained GGBFS concrete due to autogenous deformation: bayesian optimization of aging creep. Construction and Building Materials, 324, 126690.
6. Chen, Y., Chang, Z., **He, S.**, Çopuroğlu, O., Šavija, B., & Schlangen, E. (2022). Effect of curing methods during a long time gap between two printing sessions on the interlayer bonding of 3D printed cementitious materials. Construction and Building Materials, 332, 127394.
7. Wan, Z., Xu, Y., Zhang, Y., **He, S.**, & Šavija, B. (2022). Mechanical properties and healing efficiency of 3D-printed ABS vascular based self-healing cementitious composite: Experiments and modelling. Engineering Fracture Mechanics, 267, 108471.
8. Liang, M., Chang, Z., **He, S.**, Chen, Y., Gan, Y., Schlangen, E., & Šavija, B. (2022). Predicting early-age stress evolution in restrained concrete by thermo-chemo-mechanical model and active ensemble learning. Computer-Aided Civil and Infrastructure Engineering, 37(14), 1809–1833.
9. Chen, Y., Zhang, Y., **He, S.**, Liang, M., Zhang, Y., Schlangen, E., & Çopuroğlu, O. (2023). Rheology control of limestone calcined clay cement pastes by modifying the content of fine-grained metakaolin. Journal of Sustainable Cement-Based Materials, 1–15.
10. Chen, Y., Zhang, Y., **He, S.**, Liang, X., Schlangen, E., & Çopuroğlu, O. (2023). Improving structural build-up of limestone-calcined clay-cement pastes by using inorganic additives. Construction and Building Materials, 392, 131959.
11. Liang, M., Zhang, Y., **He, S.**, Chen, Y., Schlangen, E., & Šavija, B. (2023). On the chemo-mechanical evolution process of high-volume slag cement paste. Construction and Building Materials, 400, 132891.
12. Liang, M., Chang, Z., Zhang, Y., Cheng, H., **He, S.**, Schlangen, E., & Šavija, B. (2023). Autogenous deformation induced-stress evolution in high-volume GGBFS concrete: Macro-scale behavior and micro-scale origin. Construction and Building Materials, 370, 130663.

13. Liang, M., **He, S.**, Gan, Y., Zhang, H., Chang, Z., Schlangen, E., & Šavija, B. (2023). Predicting micromechanical properties of cement paste from backscattered electron (BSE) images by computer vision. Materials & Design, 229, 111905.
14. Zhang, S., **He, S.**, Ghiassi, B., van Breugel, K., & Ye, G. (2023). Interface bonding properties of polyvinyl alcohol (PVA) fiber in alkali-activated slag/fly ash. Cement and Concrete Research, 173, 107308.
15. Sayadi, S., Chang, Z., **He, S.**, Schlangen, E., Mihai, I. C., & Jefferson, A. (2023). An enhanced lattice beam element model for the numerical simulation of rate-dependent self-healing in cementitious materials. Engineering Fracture Mechanics, 109632.
16. Chang, Z., Liang, M., **He, S.**, Schlangen, E., & Šavija, B. (2023). Lattice modelling of early-age creep of 3D printed segments with the consideration of stress history. Materials & Design, 112340.
17. Wan, Z., Xu, Y., **He, S.**, Chen, Y., Xie, J., & Šavija, B. (2023). Direct ink writing of vascularized self-healing cementitious composites. Cement and Concrete Composites, 105295.
18. Wan, Z., Xu, Y., **He, S.**, Schlangen, E., & Šavija, B. (2024). The use of additive manufacturing in self-healing cementitious materials: A state-of-the-art review. Developments in the Built Environment, 17. https://doi.org/10.1016/j.dibe.2024.100334
19. Ji, X., Du, L., **He, S.**, van Zeijl, H., & Zhang, G. (2023). Microstructural and micromechanical characterization of sintered nano-copper bump for flip-chip heterogeneous integration. Microelectronics Reliability, 150.
20. Al-Obaidi, S., **He, S.**, Schlangen, E., & Ferrara, L. (2023). Effect of matrix self-healing on the bond-slip behavior of micro steel fibers in ultra-high-performance concrete. Materials and Structures/Materiaux et Constructions, 56(9).
21. NguyenDinh, N., Liu, Y., Qiu, J., Bawono, A. A., **He, S.**, Lechner, B., & Yang, E. H. (2024). Strain-hardening cementitious composites ultra-thin whitetopping (SHCC-PUTW) for rapid asphalt pavement rehabilitation. Construction and Building Materials, 412, 134252.
22. Liang, M., Xie, J., **He, S.**, Chen, Y., Schlangen, E., & Šavija, B. (2024). Autogenous deformation-induced stress evolution in cementitious materials considering viscoelastic properties: A review of experiments and models. Developments in the Built Environment, 17, 100356.
23. Gan, Y., Yang, S., **He, S.**, & Šavija, B. (2024). Experimentally-informed lattice model to simulate the fiber pull-out behavior at the microscale. Construction and Building Materials, 436, 136839.
24. Liang, M., Chang, Z., Holthuizen, P., Chen, Y., **He, S.**, Schlangen, E., & Šavija, B. (2024). Efficiently assessing the early-age cracking risk of cementitious materials with a mini temperature stress testing machine. Cement and Concrete Composites, 153, 105710.
25. Liang, M., Feng, K., **He, S.**, Gan, Y., Zhang, Y., Schlangen, E., & Šavija, B. (2025). Generation of cement paste microstructure using machine learning models. Developments in the Built Environment, 100624.

Conference:

1. **He, S.** and Yang, E.H. Development of high strength and high ductility cementitious composites incorporating CNF-coated polyethylene fibers. 4th International Conference on Strain-Hardening Cement-Based Composites (SHCC4), Dresden, Germany, 18-20 Sep, 2017.
2. Li, J., Qiu, J., **He, S.** and Yang, E.H. Micromechanics-Based Design of Strain Hardening Cementitious Composites (SHCC). 4th International Conference on Strain-Hardening Cement-Based Composites (SHCC4), Dresden, Germany, 18-20 Sep, 2017.
3. **He, S.** and Yang, E.H. Characterization of CNF-strengthened interface transition zone (ITZ) between polyethylene fiber and cement paste. 6th International Symposium on Nanotechnology in Construction (NICOM6), Hong Kong, China, 3-5 Dec, 2018.
4. **He, S.** and Yang, E.H. Anisotropic properties of fiber/matrix interface transition zone. 10th International Conference on Fracture Mechanics of Concrete and Concrete Structures (FraMCoS-X), Bayonne, France, 24-26 Jun, 2019.
5. Qiu, J., **He, S.** and Yang, E.H. Autogenous healing of _bre/matrix interface and its enhancement. 10th International Conference on Fracture Mechanics of Concrete and Concrete Structures (FraMCoS-X), Bayonne, France, 24-26 Jun, 2019.
6. **He, S.**, Van der Pauw, A., Schlangen, E. “Self-healing performance of strain hardening cementitious composite (SHCC) incorporating bacterial embedded polylactic acid (PLA) particles”. 8th International Conference on Self-Healing Materials ICSHM-MILANO 2022. Milan, Italy, 20-22 Jun, 2022.
7. **He, S.**, Sayadi, S., Chang. Z., Wan, Z., Jefferson, T., Schlangen, E. “Experimental validation of a discrete lattice model for simulating mechanical regains in a vascular self-healing cementitious material”. 8th International Conference on Self-Healing Materials ICSHM-MILANO 2022. Milan, Italy, 20-22 Jun, 2022.
8. **He, S.**, Liang, M., Yang, E.H., Schlangen, E. “A new method to quantitatively characterize the porosity of fiber/matrix interfacial transition zone (ITZ) via longitudinal cross-sections”. 5th International Conference on Strain Hardening Cementitious Composites SHCC5. Gifu, Japan, 11-13 Sep, 2022.
9. **He, S.**, Luković, M., Jonkers, H., Schlangen, E. “Structural performance of reinforced concrete beams with self-healing cover zone”. SMARTINCS’23 Conference on Self-Healing, Multifunctional and Advanced Repair Technologies in Cementitious Systems. Ghent, Belgium, 22-23 May, 2023.
10. **He, S.**, Luković, M., Schlangen, E. “Strain hardening cementitious composite (SHCC) in reinforced concrete cover zone for crack width control”. fib Symposium 2023. Istanbul, Turkey, 5-7 Jun, 2023.
11. **He, S.**, Chen, Y., Luković, M., Schlangen, E. “3D printed self-healing strain hardening cementitious composite as permanent formwork for self-repair of structural elements”. 4th International Conference on 3D Construction Printing (4-IC3DcP). Singapore, 19-21 Jul, 2023.
12. **He, S.**, Van Leeuwen, M., Luković, M., Schlangen, E. “Self-healing SHCC for Tram Line 19 in TU Delft Campus”. Concreep-12. Delft, The Netherlands, 5-7 Jun, 2024.

13. He. Y., **He, S.**, Liang, M., Schlangen, E. “Indentation splitting test of cement paste micro-cubes containing single microfibre” Concreep-12. Delft, The Netherlands, 5-7 Jun, 2024.
14. **He, S.**, Luković, M., Schlangen, E. “Self-healing strain-hardening concrete cover” 12th International Conference on Fracture Mechanics of Concrete and Concrete Structures (FraMCoS-12). Vienna, Austria, 23-25 Apr, 2025.
15. He, Y., **He, S.**, Luković, M., Schlangen, E. “Testing and modelling of fibre-matrix interface by microcube splitting” 12th International Conference on Fracture Mechanics of Concrete and Concrete Structures (FraMCoS-12). Vienna, Austria, 23-25 Apr, 2025.

If you, as the reader, have any questions or require further clarification regarding this thesis, or if you would like to engage in a discussion on the topic, please feel free to contact me at shanhe9918@outlook.com or +31 6 4402 1555.

THE END